Electronic and spintronic properties of the interfaces between transition metal oxides

Pierre Bruneel

université
PARIS-SACLAY

Electronic and spintronic properties of the interfaces between transition metal oxides

Thèse de doctorat de l'Université Paris-Saclay

École doctorale n° 564, Physique en Île-de-France (EDPIF)
Spécialité de doctorat : Physique
Unité de recherche : Université Paris-Saclay, CNRS,
Laboratoire de Physique des Solides, 91405, Orsay, France
Référent : Faculté des Sciences d'Orsay

Thèse présentée et soutenue en visioconférence totale, le 2 novembre 2020, par

Pierre BRUNEEL

Composition du jury :

Pascale FOURY-LEYLEKIAN Professeure, LPS Orsay	Présidente
David CARPENTIER Directeur de recherche, ENS Lyon	Rapporteur & Examinateur
Gervasi HERRANZ Chercheur titulaire, ICMAB Barcelona	Rapporteur & Examinateur
Manuel BIBES Directeur de recherche, UMR CNRS-Thalès (Saclay)	Examinateur
Marie-Bernadette LEPETIT Directrice de recherche, Institut Louis Néel (Grenoble)	Examinatrice
Marc GABAY Professeur, LPS Orsay	Directeur de thèse

Version du 19 novembre 2020, 16:35

Thèse de doctorat

NNT : 2020UPASP047

Version du 19 novembre 2020, 16:35

Cette thèse est dédiée à mon grand-père.

Version du 19 novembre 2020, 16:35

Version du 19 novembre 2020, 16:35

Table des matières

Remerciements

Ces remerciements sont un peu spéciaux dans la mesure où j'ai très peu vu certaines des personnes qui y sont mentionnées durant les derniers mois passés cloîtré dans mon appartement. Cette situation inédite dans le mauvais sens du terme permet de se rappeler combien le contact avec les autres est quelque chose d'important, et à quel point les petits riens du quotidien de ces trois dernières années ont pu disparaître rapidement. C'est grâce à toutes les personnes que j'ai eu la chance de côtoyer pendant ces trois dernières années que cette expérience a été aussi riche.

Je veux premièrement remercier mon directeur de thèse Marc Gabay, qui aura été d'un immense soutien sur tous les plans possibles : sur un plan scientifique, il a pu me guider et m'aider au gré des difficultés qui se sont présentées et de mes nombreux allers-retours dans les escaliers menant du premier au troisième étage. Sur un plan personnel, sa disponibilité pour discuter, sa bonne humeur et son bon humour légendaires ne sont plus à prouver. Je te remercie de m'avoir permis de travailler sur des sujets aussi variés et pour tes nombreux conseils avisés.

Un grand merci au groupe théorie du LPS, qui a su me supporter durant ces trois ans et quelques dans une ambiance agréable. Merci à Mark et Fred pour les innombrables pauses cafés assorties de discussions passionnantes et passionnées sur les sujets les plus divers (à 53 pourcents culinaires, 30 pourcents politiques et 17 pourcents scientifiques d'après une étude statistique personnelle menée sans aucune méthodologie). Un grand merci à Marie-France et Véronique qui ont su faire preuve de patience devant mon incompétence et ma mauvaise foi chronique dans ce qui concerne les démarches administratives.

Je remercie Manuel Bibes, Andrea Caviglia et Jean-Marc Triscone pour la confiance qu'ils m'ont accordée lors des collaborations dont j'ai eu la chance de faire partie durant ces trois

ans, qui à mes yeux ont été d'excellentes expériences et m'ont permis de confronter le travail de théoricien à la réalité des systèmes physiques et des expériences, une chose qui me tient particulièrement à coeur.

Je remercie Jonathan et Bruno pour m'avoir intégré et impliqué dans l'option d'enseignement de Méthodes Numériques. L'expérience d'enseignement a été très riche, et j'espère avoir un jour l'occasion de la réitérer (on ne sait pas de quoi la vie est faite) ! J'ai été très heureux de participer activement à l'élaboration et l'amélioration de cette option que j'ai adoré enseigner.

Je fais un grand coucou au groupe des thésards du laboratoire qui me manque au moment où j'écris ces lignes. Merci à Maxime pour avoir été là depuis le début du M2, et avoir été un compagnon d'échange sur tous les sujets lors de cette drôle d'expérience, ainsi qu'un bon voisin des (parfois très très) longs trajets de RER. Merci à Xin qui a été un excellent voisin de bureau, et avec lequel j'ai eu le plaisir de gribouiller de la physique au tableau. Je repars en ayant heureusement eu le temps de prendre une photo où tu fais la sieste. Je souhaite une bonne continuation à Ansgar, JB et Vivien que je n'ai finalement pas eu autant l'occasion de voir que je l'aurais voulu. Je dis un grand merci à tous mes compagnons indéfectibles de pause café Quentin, Brendan, Noémie, Julian, Marie, Manon, Marina, Aymeric et Jonas qui ont toléré de m'entendre raconter n'importe quoi lorsque je n'étais pas en train de me plaindre de ma journée. Je remercie Oscar, Alberto et Giuseppe pour leur aide indispensable dans l'apprentissage de l'utilisation du cluster, d'Unix et de la DFT.

Je mentionne (remercier est trop fort) la ligne de RER B dont les trajets m'auront souvent poussé à bout, et je remercie le site à l'oiseau bleu ainsi que les livres de poche qui m'ont permis de faire passer un peu plus vite les environ 33480 km (0.837 tours de la Terre) que j'y ai parcourus en environ un mois de temps cumulé. Mentions mineures à la porte de la ligne 6 que ma joue a eu finalement peu l'occasion de connaître, et à la montée menant au laboratoire et sa mythique pente de 21 pourcents qui m'a permis de renforcer mon jeu de jambes de boxeur et de me vautrer deux ou trois fois seulement lors d'épisodes de verglas.

Je remercie bien évidemment mes parents pour leur appui et leur écoute de mes questionnements personnels. Je dois aussi les remercier pour tous les bons repas que j'ai pu ingurgiter à l'oeil les dimanches ! Merci à ma soeur d'avoir accepté aussi souvent de se faire payer des restaurants japonais en ma compagnie, je me doute qu'il s'agissait d'un grand

sacrifice... Je remercie mon ancien coloc Hadrien d'avoir partagé ma conception stricte du ménage, ainsi que pour toutes les discussions (divagations ?) scientifiques qu'on a pu avoir, et enfin pour mise à disposition de sa Xbox 360 dans notre four à vapeur parisien. Je remercie Geoffroy, Charles et Félix pour les innombrables soirées belotes (dans la vie réelle ou en visio-conférence) et le super voyage en Argentine. Je remercie Thibaut, Fabien, Tom, Jules, Robin, Vincent et Olivier avec qui j'ai partagé ma passion pour les émissions mythiques du PAF...

Ultimes remerciements pour Hadrien, Félix et JB qui ont bien voulu m'aider dans la relecture de cet ouvrage.

Version du 19 novembre 2020, 16:35

List of symbols

Δ : gap in band structure, the nature of which is specified by indices or exponents.

T_c : critical temperature of a superconductor.

d_{xy}, d_{xz}, d_{yz} : t_{2g} orbitals. d^n_{xy} denotes the n^{th} d_{xy} subband, when several subbands are present in the system.

$\epsilon_\nu(k)$: eigenenergies relative to the band with index ν.

$|\nu, k\rangle$: eigenvectors of band ν with wavevector k. They are simply denoted $|\nu\rangle$ when k is implicit. Greek (α, β) and roman (n, m) letters denote states of orbital character (α, β) and subband indices (n, m).

Γ, X and M : special points of the 2D Brillouin Zone, denoting respectively $(0, 0)$, $(\frac{\pi}{a}, 0)$ and $(\frac{\pi}{a}, \frac{\pi}{a})$.

t : hopping amplitudes, an index can specify its nature.

$\mathcal{H}$: Hamiltonian.

$\vec{E}, \vec{B}$: electric and magnetic fields.

c : speed of light.

μ_B : Bohr magneton.

$\hbar$: reduced Planck constant.

$\vec{r}, \vec{v}, \vec{p}$: position, velocity and impulsion. The operators are denoted by adding a hat to the corresponding symbols.

$\vec{k}$: wavevector of a particle, its momentum is defined by $\vec{p} = \hbar\vec{k}$.

$\vec{L}, \vec{S}$: angular momentum and spin. $\hat{\vec{L}}, \hat{\vec{S}}$ are the respective quantum mechanical operators.

$\sigma_x, \sigma_y, \sigma_z$: 2x2 Pauli matrices verifying $\{\sigma_\alpha, \sigma_\beta\} = 2\delta_{\alpha\beta}\sigma_\alpha$ and $[\sigma_\alpha, \sigma_\beta] = 2i\epsilon_{\alpha\beta\gamma}\sigma_\gamma$ with δ the Kronecker symbol and ϵ the Levi-Civitta symbol.

λ_{SO} : amplitude of the atomic spin-orbit coupling.

γ_{OM} : amplitude of the orbital mixing.

m_e : bare mass of the electron ($= 9.1 \times 10^{-31}$ kg).

m^* : effective mass of an electron. Additional precision are contained in subscripts or superscripts if needed.

e : charge of the electron. $e = 1.6 \times 10^{-19}$ C is a positive quantity in our conventions.

Ai, Bi : Airy functions of the first and second kind.

V : electrostatic potential. V_g denotes gate voltages.

ρ : density of charge.

ε_0 : dielectric permittivity of the vacuum ($= 8.85 \times 10^{-12} F.m^{-1}$).

ε_r : relative permittivity of a medium .

$\varepsilon = \varepsilon_0 \varepsilon_r$: total permittivity.

$\vec{D} = \varepsilon \vec{E}$: displacement field.

$\vec{P}$: polarization field.

$\chi = \frac{dP}{dE}$: dielectric susceptibility $\chi = \varepsilon_r - 1$.

σ : electric conductivity of a material (unit $\Omega^{-1}.m^{-1}$).

σ_{xx}, σ_{xy} : longitudinal and transverse conductivities.

eV : electron-Volt, unit of energy. 1 eV $= 1.6 \times 10^{-19} J$.

E_F : Fermi energy.

$\delta(.)$: Dirac δ-function.

D_ν : Density of states of a band ν.

n_{2D} : 2D density of carriers.

τ : electron scattering time.

$\langle . \rangle$: mean value.

$f_{\nu,k}$: Fermi function for wavevector k and band index ν. $f_{\nu,k}(E_F) = \Theta(E_F - \epsilon_\nu(k))$.

Θ : Heaviside function. $\Theta(x) = 0$ for $x \leq 0$ and $\Theta(x) = 1$ for $x > 0$.

$\vec{a} \times \vec{b}$: cross product of vectors $\vec{a}$ and $\vec{b}$.

$\vec{a} \cdot \vec{b}$: scalar product of vectors $\vec{a}$ and $\vec{b}$.

ρ_{xx}, ρ_{xy} : longitudinal and transverse resistivities.

U : Hubbard constant.

$k_\pm = k_x \pm i k_y$: complex representation of the wavevector (k_x, k_y).

γ_ν : Berry phase of band ν.

$\vec{\mathcal{A}}_\nu$: Berry connection of band ν.

$\vec{\Omega}_\nu$: Berry curvature of band ν.

$\vec{\Omega}^z_\nu$: spin curvature of band ν (z polarization).

$\vec{j}, \vec{j_S}$: charge and spin current operators.

$\partial_u = \frac{\partial}{\partial u}$: partial derivative according to a variable u.

$\nabla_{\vec{R}} = [\partial_{R_1}, \partial_{R_2}, ...]$: canonical nabla operator for the coordinate system $\vec{R}$.

α_R : Rashba coefficient (unit eV.m^{-1}).

κ : Edelstein coefficient.

σ_{SH} : Spin Hall conductivity.

$\zeta = \frac{\Delta}{\lambda}$: ratio between the confinement energy and the atomic spin-orbit coupling.

$s = \sqrt{\zeta^2 + 2\zeta + 9}$.

$\omega_{\nu\chi}$: scattering rate between states ν and χ.

Version du 19 novembre 2020, 16:35

Overview

Semi-conductor heterostructures have been for a long time the standard to build electronic devices, the hallmark of this technology being the Si/SiO_2 heterostructures used to do MOS-FET transistors. Tremendous progress in the quality of the materials in terms of crystallinity and purity has allowed this technology to thrive : its performances have been following an exponential trend for decades, the Moore's law [1, 2]. Though the success of these technologies is not to be proven, new issues are emerging in addition to the decrease of the size of the devices, as for instance power consumption and the use of cleaner materials, providing opportunities to use other classes of materials to make heterostructures. Transition Metal Oxides (TMO) are interesting candidates because they are known to host a lot of interesting functionalities [3, 4, 5]. The cuprates, a very broad family of high-T_c superconductors, are maybe the most famous family among these systems. A complete zoology of these materials would be futile for they are so diverse and intriguing : $SrTiO_3$ is the most dilute superconductor known and also a quantum paraelectric [6], $LaAlO_3$ is a polar insulator, $LaTiO_3$ and VO_2 are Mott insulator and exhibit a metal to insulator transition [7, 8, 9]. Cobaltates [10, 11] and nickelates [12] have magnetic properties. The conduction band of these materials is mostly composed of d electrons which are more impacted by electronic correlations or effect such as spin-orbit coupling than the s or p electrons forming the conduction band of semiconductors. TMO also exhibit richer physics because of the multi-orbital nature of the d electron manifold and the multiple states of oxidization of their chemical components [5, 11]. One of the simplest crystalline structure of transition metal oxides is the perovskite structure, which is versatile for it can display distortions from the idealized cubic case, which can induce ferroelectricity or even more exotic effects due to electron-phonon coupling [4, 13].

TMO are indeed a very rich class of materials would it be only for their bulk properties.

But as Herbert Kroemer said in his Nobel lecture in 2000, "Often, it may be said that *the interface is the device*" [14]. In this respect, TMO heterostructures are a fascinating playground to study new electronic states of matter. The discovery in 2004 [15] that the interface between the two wide band-gap insulator $LaAlO_3$ (LAO) and $SrTiO_3$ (STO) becomes metallic if more than 4 LAO layers are put on top of an STO substrate opened the way for a new area of research called "oxitronics". Huge progress in the synthesis of these materials [16] allows to produce devices with mobilities matching the state-of-the art materials standards. Futhermore, it is possible to pattern nanostructures within a layer-to-layer accuracy [15, 17, 18]. New designs such as sandwiches [19] or superlattices [20, 21] composed of several oxide layers with a great regularity allow to tailor the property of the materials in situ, using each oxide as a building block for an artificial material with the targeted properties. The layered structure of these oxides can be used as a probe to study the effects of dimensionality on electronic properties : if interfaces behave as 2-dimensional objects, stacking enough layers of a material on top of a substrate can restore the bulk properties [22, 23].

The complex interplay between crystalline and orbital degrees of freedom can lead to unusual electronic properties. Far from the ideal picture of the free electron gas, exotic couplings can emerge from broken symmetries. The Nobel Prize of 2017 has been awarded to Kosterlitz, Thouless and Haldane for the discovery of topological phase transitions [24, 25, 26, 27]. The recent experimental proofs of the Quantum Anomalous Hall Effect (QAHE) and Quantum Spin Hall Effect (QSHE) [28, 29] have shed light on the dramatic effects of the geometry of the band structure on the ground state of a material. The case of Topological Insulators (TI) illustrates the change in the ground state due to this geometry : at the edges of these bulk insulators, conducting states emerge and carry a ballistic current immune to disorder [30, 31]. These phenomena are entangled with broken symmetries and are related to topological invariants of band structures [32, 33]. These new states of matter are of a great interest for applications because of both their robustness and their immunity to disorder. The QSHE is intimately related to nontrivial spin properties emerging from spin-orbit coupling and inversion symmetry breaking. In superconductors it is again the interplay between the quasi-particles and the spin-orbit coupling that may give rise to the appearance of Majorana fermions [34, 35, 36]. Transition Metal Dichalcolgenides (TMD), a class of 2d graphene-like materials with additional couplings, also provide a good example of systems where topological

effects are expected [37, 38]. TMO heterostructures gather all the usual suspects responsible for topological properties [39, 40, 41] : breaking of inversion symmetry, spin-orbit coupling, multi-orbital conduction band and sometimes magnetism or even superconductivity. They should provide a nice platform to study these topological effects.

The Quantum Spin Hall Effect belongs to the family of *spintronic* phenomena, yielding a mean to manipulate the spin of the electrons by acting on the charge sector. The objective of spintronics is to process information using the spin degree of freedom within microelectronic chips [42]. It is already a very successful area of research both academically and industrially : the discovery of Giant MagnetoResistance (GMR) led to the attribution of a Nobel Prize [43], and Magnetic Random Access Memory (M-RAM) is already produced on an industrial scale. Building spintronic devices using antiferromagnetic materials is on the roadmap of the ITRS (International Technology Roadmap for Semiconductors) to increase their performances [44]. Heavy metals such as Pt, W and Ta host interesting spintronic properties and are thus under active investigation to understand how to tame and engineer these effects [45, 46, 47, 48]. Magnetization dynamics and spin-orbit torques [49, 50] rule how to write and read the information with spin. It is reckoned that interesting spintronic effects emerge in systems displaying a Rashba spin-orbit coupling [51]. TMO interfaces, in particular STO-based, exhibit a gate-tunable Rashba interaction [52] and thus are a nice material platform to study these effects in detail. Recent experiments [53, 54, 55] have shown they present interesting spintronic effects : we explain two spin-to-charge conversion mechanisms and how these effects can be used to better characterize the multi-orbital characteristics of the TMO systems in general.

The organization of the thesis is the following :

In the first chapter, we study the electrostatic doping of transition metal oxide heterostructures. First, we review the essential experimental aspects pertaining to the physics of STO-based heterostructures. The origin of the metallicity of the LAO/STO interface is still under debate : the scenario of the polar catastrophe involves a mere transfer of electrons of the LAO layers while the scenario of oxygen vacancies involves the presence of defects inside the LAO layers. The LAO/STO interface becomes superconductive below a temperature $T_c \approx 300$ mK, and both the superconducting temperature and superfluid density can be tuned by electrostatic doping ; the nature of the pairing mechanism remains unknown

up to now. The multi-orbital nature of the conduction band is expected to have important effects on superconductivity. To a great surprise because these two effects are known foes, ferromagnetism has been observed in conjunction with superconductivity in some samples. Unusual magneto-resistance and localization properties of the LAO/STO interfaces hint at the presence of Rashba spin-orbit coupling. Its intensity can be tuned by electrostatic doping ; the change in the electrostatic properties of the interfaces and the presence of avoided crossings in the band structure are the main explanations invoked. Second, we provide the microscopic descriptions of the key ingredients we use to model the [001] and [111] oriented interfaces of STO. From their crystalline and chemistry properties, we derive a multi-orbital tight-binding model describing these interfaces, focusing on non-conventional terms : the compounded effects of atomic spin-orbit coupling and orbital mixing (due to surface distortions) induce splittings in the band structure and non-trivial spin-orbit textures. This model reproduces the ARPES measurements of STO interfaces. Third, we explain the main features of the Poisson-Schrodinger approach, which describes the electrostatic confinement near an interface by solving a self-consistent problem : the interaction between the spatial density of carriers and the electrostatic potential created by the interface. The presence of a confining potential creates subbands with a spatial extension related to its orbital character. Through this approach, we discuss the effects of temperature on the confinement and study features of the electrostatic doping of 2-dimensional electron gases (2DEG). Electrostatic doping can be done in two different geometries : top-gating and backgating. For top-gating, the electrostatic doping changes the density of the 2DEG, and the different subbands are not equally doped. In a back-gating geometry, the shape of the potential confining the 2DEG changes and differently impacts subbands : the levels which are less confined are more doped, and there exists a threshold of backgate voltage above which there can be a leakage of charge outside the well. We model electronic correlations to understand measurements of non-linear Hall effect in the [001] and [111] orientation of STO interfaces, and investigate the possibility of band inversions due to correlations and electrostatic doping.

In the second chapter, we introduce concepts of topology in the context of condensed matter theory. First, we describe paradigmatic systems where the topology of the band structure has a dramatic influence on electronic properties : topological insulators and the Quantum Spin Hall Effect. From these experimental discoveries we dive into the mathematical frame-

work underlying the concepts of topology in condensed matter physics. We unveil the key role played by the geometry of the wavefunctions inside the Brillouin Zone to explain the concepts of topological invariants, with a particular focus on the concept of Berry curvature. To continue our journey, we turn to more sophisticated topological invariants such as the spin curvature. We discuss the relationship between these geometrical quantities and the experimental probes available to observe them. Eventually, we discuss how to apply these concepts to metallic systems, which are our main interest in this work.

In the third chapter, we study the spintronic responses of transition metal oxides heterostructures. We begin with a description of two mechanisms of spin-to-charge conversion, namely the Edelstein Effect and the Spin Hall Effect, and discuss recent measurements in STO-based interfaces where these effects are found to be very large. Concepts of semi-classical transport allow us to compute transport properties from tight-binding models for STO-based interfaces and to fit experiments using realistic parameters. We further push our analysis of the generic model for STO interfaces and show that the multi-band structure of TMO is fundamental to explain the variations of the Edelstein response. The behavior of the system can be understood by a model we call Multiband Interfacial Spin-Orbit (MISO). Using analytical computations, we single out the important contributions to the spintronic responses using low-energy models around peculiar points of the band structure and show that the MISO induces winding spin textures of two different nature with a distinctive effect on the responses. Using perturbation theory, we detail these two contributions : if the former is analogous to the Rashba-Edelstein effect, the latter is peculiar to the multi-orbital nature of the conduction band and can be of the same amplitude. This dichotomy might provide an explanation for phenomena that are interpreted as a gate-tunable Rashba interaction or even more complex cubic Rashba interactions.

In the final chapter, we tackle the *capping problem* using ab initio computations. LAO/STO interfaces are known to become metallic above a critical thickness of 4 LAO layers on top of the STO substrate. It remains difficult to disentangle the respective roles of chemistry and electrostatics to explain the formation of the 2DEG at this interface. Recent experiments have shown that the 4 LAO layers can be replaced by m LAO + n STO layers, as long as $m + n \geq 4$. This observation, which is called the "capping problem", might help to unveil the mechanisms underlying the formation of 2DEGs and to better understand the different

effects at play. We use Density Functional Theory to study these capped heterostructures. After an analysis of the bulk and bare STO surfaces, we systematically probe the different m and n cases. The layer-resolved structure of the Density of States reveals how the Ti conduction and O valence bands are affected by the chemistry of the heterostructure. The metallicity criterion is obtained for known cases but fails to be fully explained. We discuss the introduction of defects in the heterostructures, which is a plausible explanation for this phenomenon.

To conclude, further developments into the problems of confinement, topology and magneto-transport provide interesting routes for future works.

If the confinement potential has known consequences on the spatial density and the band bending near the interface, the interplay of this potential with disorder leaves open questions. The presence of surface roughness and sparse oxygen vacancies in the bulk of TMO provides several non-equivalent disorder channels with different scattering properties. How orbitals and subbands are affected by disorder is of critical importance to evaluate their role in transport properties. The huge discrepancy between the number of carriers evaluated in ARPES and in nonlinear Hall effects is often explained by the presence of "frozen carriers". Why some carriers are seemingly muted in transport signatures is not yet well understood. A detailed treatment of disorder and its interplay with correlations may provide an explanation for the observation of magnetism in some STO samples [56].

As far as topological and magneto-transport properties are concerned, disorder should again be of the utmost importance. The Anomalous Hall Effect and Spin Hall Effect have contributions emerging from disorder : vertex corrections to the current operators yield the side-jump and skew-scattering contributions which are of the same order of magnitude as the intrinsic effect : it is acknowledged that these contributions may cancel the intrinsic contribution of the SHE in the linear Rashba model. Can the multi-orbital nature of TMO explain the survival of a SHE signal ? Can we understand the weak anti-localization and anisotropic magnetoresistance properties of STO interfaces using the framework of the MISO enriched with a more complete description of disorder ? The presence of several orbital in the conduction band of TMO heterostructures is a fundamental ingredient to understand their properties, and the numerous hints that it is possible to switch from single to multi-band transport upon electrostatic doping provides a mean to study multi-band transport

signatures and to understand the behavior of various complex physical phenomena in this context.

To put in a nutshell, Transition Metal Oxide heterostructures are fascinating systems with exotic transport properties and provide a rich playground to study complex phases of matter. They are strong contenders for building a next generation of electronic devices from materials with tailored functionalities.

Version du 19 novembre 2020, 16:35

Résumé en français

Les hétérostructures de semi-conducteurs constituent depuis longtemps un standard pour réaliser des dispositifs électroniques, le fer de lance de cette technologie étant les interfaces a base de silicium (Si) et d'oxyde de silicium (SiO_2) qui sont utilisées dans les transistors à effet de champ électrique (MOS-FET). Les très nombreux progrès relatifs à la cristallinité et la pureté des semi-conducteurs ont permis des progrès vertigineux : les performances des composants électroniques industriels ont suivi une croissance exponentielle pendant les quarante dernières années, suivant une célèbre tendance empirique, la loi de Moore. Bien que le succès rencontré par ces technologies ne soit plus à prouver, de nouvelles problématiques émergent en parallèle de la décroissance de la taille des composants (qui est l'un des principaux défis) : on pourra citer la consommation d'énergie et l'utilisation de matériaux moins nocifs pour l'environnement ou plus recyclables. Ces réflexions amènent à la fabrication d'hétérostructures à base d'autres matériaux. Les oxydes de métaux de transitions sont des candidats de choix car ils possèdent de nombreuses fonctionnalités. Les cuprates (oxydes de cuivre), large famille de supraconducteurs à haute température critique, forment certainement la plus célèbre sous-catégorie de ces oxydes. Faire une zoologie exhaustive de ces matériaux est compliqué car leurs propriétés sont très diverses. Pour citer quelques exemples : le titanate de strontium $SrTiO_3$ est le supraconducteur avec la plus basse densité de porteurs connue ainsi qu'un paraélectrique quantique, $LaTiO_3$ et VO_2 sont des isolants de Mott et traversent une transition métal-isolant lorsque la température évolue et les cobaltates (oxydes de cobalt) et des nickelates (oxydes de nickel) ont des propriétés magnétiques. La bande de conduction de ces matériaux est celle du métal de transition qui la compose. Cette bande de conduction est composée d'électrons appartenant à la couche électronique d, plus affectés par le couplage spin-orbite et les effets relatifs aux corrélations électroniques que les électrons des couches s

ou p, qui composent la bande de conduction des semiconducteurs traditionnels (Si, GaAs). Leur physique est également plus riche car la couche d est composée de plusieurs orbitales électroniques et les métaux de transition peuvent présenter plusieurs niveaux d'oxydation stables. L'une des structures cristallines les plus simples de ces oxydes est la structure perovskite (qui est le nom original du titanate de calcium $CaTiO_3$). Cette structure dérivée de la structure cubique est intéressante car elle peut se distordre et donner lieu à l'apparition de la ferroélectricité ou même d'effets plus exotiques liés au couplage électron-phonon.

Les oxydes de métaux de transition présentent déjà des propriétés très riches en phase cristalline. Mais comme l'a dit Herbert Kroemer dans la conférence suivant la remise de son Prix Nobel en 2000 : "Souvent, c'est en réalité l'interface qui constitue le dispositif". En ce sens, les hétérostructures d'oxydes sont un terrain de jeu fantastique pour étudier les nouveaux états électroniques de la matière. Il a été découvert en 2004 que l'interface entre l'aluminate de lanthane ($LaAlO_3$ ou LAO) et le titanate de strontium ($SrTiO_3$ ou STO), deux isolants à large bande interdite, pouvait être rendue métallique lorsque l'on dépose plus de quatre couches de LAO au dessus d'un substrat de STO. Cela a ouvert un nouveau domaine de recherche appelé "oxytronique". Les progrès dans la synthèse de ces matériaux permettent aujourd'hui de produire des composants avec des mobilités du niveau des meilleurs standards, et de produire des nanostructures avec une précision à la couche près. Cela permet de concevoir des structures en sandwich ou des super-réseaux composés de plusieurs oxydes et ainsi d'imaginer des matériaux artificiels avec des propriétés sur mesure, en utilisant chaque oxyde comme une brique élémentaire du matériau composite. La structure en couches successives de ces oxydes permet également d'étudier les effets de la dimensionnalité sur les propriétés électroniques : si les interfaces sont des objets bi-dimensionnels, en empilant suffisamment de couches au-dessus d'un substrat les propriétés volumiques du matériau supérieur finissent par être restaurées.

L'interaction entre les degrés de liberté cristallins et orbitaux peut amener des propriétés inattendues. Des couplages exotiques peuvent émerger de la brisure de certains symétries, nous éloignant de l'image idéale du gaz d'électrons libres. Le prix Nobel de 2017 a été attribué à Kosterlitz, Thouless et Haldane pour la découverte des transitions de phase topologiques de la matière. Des expériences récentes démontrant l'existence de l'Effet Hall Quantique Anormal (QAHE) et de l'Effet Hall Quantique de Spin (QSHE) ont mis en lumière le rôle

critique de la géométrie de la structure de bande sur l'état fondamental d'un système. Le cas des isolants topologiques illustre à merveille le lien entre cette géométrie et le changement de l'état fondamental du système : aux frontières de ces matériaux isolants de volume, des états métalliques peuvent se développer et donner lieu à une conduction ballistique, insensible au désordre de l'échantillon. Ces phénomènes sont intimement liés à certaines brisures de symétrie et à des invariants topologiques de la structure de bande. Ces nouveaux états de la matière sont d'un grand intérêt technologique en raison de leur robustesse et de leur immunité au désordre. Dans le cas du QSHE, ces états topologiques ont pour origine le couplage spin-orbite et la brisure de la symétrie par inversion. Dans les systèmes supraconducteurs on pense que c'est aussi l'effet du couplage spin-orbite sur les quasi-particules qui permettrait d'observer les fermions de Majorana. Les dichalcogénures de métaux de transition, matériaux bi-dimensionnels que l'on pourrait qualifier de graphènes augmentés, sont un bon exemple de matériaux où l'on s'attend à trouver des propriétés liées à la topologie. Les hétérostructures d'oxydes de métaux de transition rassemblent tous les ingrédients qui mènent à des propriétés topologiques : la brisure d'inversion de symétrie, le couplage spin-orbite, la présence de plusieurs orbitales et parfois du magnétisme ou de la superconductivité. Ils constituent donc une classe de matériaux intéressante pour étudier ces effets topologiques.

L'Effet Hall Quantique de Spin (QSHE) fait partie de la famille des phénomènes "spintroniques" car il fournit un moyen de manipuler le spin des électrons en agissant sur le secteur de charge. Le but de la spintronique est de stocker ou transmettre l'information en utilisant le degré de liberté de spin des électrons au sein de composants que l'on peut intégrer à des dispositifs électroniques. C'est un domaine de recherche déjà très abouti que ce soit au plan académique ou industriel : la découverte de la magnéto-résistance géante par Albert Fert lui a apporté un prix Nobel, et les mémoires M-RAM (Magnetic Random Access Memory) sont déjà produites à un échelon industriel. La possibilité d'utiliser des matériaux antiferromagnétiques pour réaliser des composants spintroniques figure sur la feuille de route de l'ITRS (International Technology Roadmap for Semiconductors) visant l'amélioration des performances des composants électroniques. Les métaux lourds comme le platine (Pt), le tungstène (W) et le tantale (Ta) ont démontré de bonnes propriétés de conversion du spin en charge et sont étudiés intensivement afin de comprendre comment maîtriser et optimiser ces effets. La dynamique de l'aimantation et les couples de spin-orbite dictent la manière

dont l'information de spin peut être écrite ou lue. Il est connu que les systèmes possédant un couplage spin-orbite de Rashba ont des propriétés spintroniques. Les interfaces d'oxydes de métaux de transition, et notamment celles à base de STO, ont une interaction de type Rashba qui peut être modulée par une tension de grille. Ils fournissent donc un bon cadre pour l'investigation de ces effets. Des expériences récentes montrent que les interfaces à base de STO présentent des effets spintroniques. Ces systèmes peuvent aider à comprendre des mécanismes de conversion du spin vers la charge. A l'inverse, ces effets spintroniques peuvent être utilisés pour mieux comprendre le caractère multi-orbital des oxydes de métaux de transition.

L'organisation de la thèse est la suivante :

Dans le premier chapitre, nous abordons le dopage électrostatique des interfaces entre oxydes de métaux de transition. Premièrement, nous passons en revue quelques-uns des résultats expérimentaux essentiels pour comprendre la physique des hétérostructures d'oxydes de métaux de transition. L'origine de la métallicité de l'interface entre LAO et STO est encore aujourd'hui sujette à débats : le scénario de la catastrophe polaire invoque un simple transfert des électrons de la surface du LAO alors que le scénario des lacunes d'oxygène implique de surcroît la présence de défauts dans la structure cristalline. L'interface LAO/STO devient supraconductrice en dessous de $T_c = 300$ mK, et cette température critique peut être modifiée par dopage électrostatique ; si la nature du mécanisme de liaison demeure inconnue, on s'attend à ce que la supraconductivité soit impactée par la nature multi-orbitale de la bande de conduction. Certains échantillons présentent des traces de ferromagnétisme en plus de leur supraconductivité, ce qui est surprenant car ces deux effets sont habituellement antagonistes. Les signatures de magnéto-résistance et de localisation non standards dans ces interfaces sont interprétées par la présence d'un couplage de spin-orbite Rashba. L'amplitude de ce couplage peut être modulé par dopage électrostatique ; ce phénomène est expliqué par le changement des propriétés électrostatiques au voisinage de l'interface ou par la présence de croisements évités dans la structure de bandes. Ensuite, nous fournissons une description microscopique des ingrédients essentiels à la description des interfaces de STO dans les orientations [001] et [111]. La structure cristalline et chimique de STO permet de construire un modèle de liaisons fortes à plusieurs orbitales. On détaillera la présence de termes spéciaux dans ces systèmes : le couplage spin-orbite atomique et le mélange orbital (du aux distorsions à la

surface des matériaux) induisent des croisements évités dans la structure de bandes et des textures de spin non triviales. Nous montrons que ce modèle reproduit les données fournies par les mesures ARPES sur les interfaces à base de STO. Puis, nous expliquons le modèle de Poisson-Schrodinger que nous utilisons afin de décrire le confinement proche de l'interface. Il s'agit d'une description auto-cohérente du confinement reliant la densité spatiale de porteurs et le profil du potentiel électrostatique créé par l'interface. Nous utilisons cette approche pour comprendre le dopage électrostatique de ces gaz bi-dimensionnels. Nous analysons pour cela deux types de géométrie de dopage électrostatique : la géométrie avec une grille au-dessus ou en-dessous. Lorsque la grille est au dessus de l'interface, le dopage change le nombre de porteurs qui se répartissent de manière différenciée entre les sous-bandes. Lorsque la grille est en dessous, la forme du potentiel électrostatique se modifie et celui-ci agit différemment sur chaque sous-bande : les niveaux les moins confinés sont les plus dopés. Nous discutions de l'existence d'un seuil de tension de grille qui peut amener à la fuite de certains porteurs en dehors du potentiel de confinement. Enfin, nous discutons l'effet des corrélations électroniques sur ces systèmes, en regard des résultats expérimentaux d'Effet Hall non linéaires réalisés sur les interfaces LAO/STO dans les orientations [001] et [111].

Le deuxième chapitre traite des effets de la topologie sur la physique de la matière condensée. Nous décrivons quelques exemples de systèmes dans lesquels la topologie de la structure de bandes a une influence profonde sur les propriétés électroniques des solides : les isolants topologiques et l'effet Hall Quantique de Spin. Fort de ces exemples nous nous plongeons dans le formalisme mathématique sous-jacent aux aspects topologiques de la matière condensée. Nous montrons le rôle joué par la géométrie des fonctions d'onde à l'intérieur de la zone de Brillouin pour expliquer le concept d'invariant topologique, en détaillant le concept de courbure de Berry. Pour continuer notre tour d'horizon, nous nous intéressons à des invariants plus sophistiqués tels que la spin courbure. Nous discutons des liens entre ces quantités géométriques et les mesures expérimentales disponibles pour mettre à nu ces effets. Enfin, nous essayons de transposer ces concepts aux cas métalliques, qui sont notre centre d'intérêt principal dans ce travail.

Le troisième chapitre a trait à la description des réponses spintroniques des hétérostructures d'oxydes de métaux de transition. Nous décrivons deux mécanismes de conversion du spin en charge, à savoir les effets Edelstein et Hall de Spin. Ces deux effets ont été mesurés

récemment dans des interfaces d'oxydes, où ils y battent des records d'amplitude. Nous expliquons comment évaluer ces réponses à partir de modèles de liaisons fortes, et montrons l'accord entre les expériences et les calculs numériques. Nous étudions ensuite de manière plus générique le modèle utilisé pour décrire STO, où la structure à plusieurs bandes est essentielle pour comprendre les variations d'amplitude de l'effet Edelstein. Nous construisons un modèle appelé MISO pour décrire la forme du couplage spin-orbite qui régit ces systèmes. Grâce à un traitement analytique de ce modèle à basse énergie, nous isolons les différentes contributions à la réponse spintronique du système au voisinage de certains points de la zone de Brillouin. Nous montrons que le MISO génère des textures de spin non triviales de deux natures différentes. La théorie des perturbations permet de déterminer leur rôle respectif sur les réponses spintroniques. L'effet du premier type de texture est de type Rashba-Edelstein, alors que le second est spécifique à la nature multi-orbitale du modèle et peut être d'une amplitude comparable voire plus importante que le premier. La distinction entre ces deux effets peut expliquer certaines interprétations relatives à l'existence d'un couplage Rashba modifiable par dopage électrostatique ou à la présence d'un couplage Rashba cubique.

Le dernier chapitre a trait à la modélisation du problème dit du "capping" à partir de calculs ab initio. En temps normal, les interfaces LAO/STO deviennent métalliques au-delà d'une épaisseur critique de quatre couches de LAO au-dessus d'un substrat de STO. Les rôles respectifs que remplissent la chimie et l'électrostatique de ces interfaces dans la création du gaz bi-dimensionnel sont encore mal compris. Des expériences récentes montrent que l'épaisseur critique de 4 couches de LAO peut être remplacée par m couches de LAO avec n couches de STO au-dessus (appelées couches de "capping"), si la condition $m+n \geq 4$ est remplie. Cette observation, appelée le problème du "capping", peut aider à comprendre davantage les mécanismes en jeu dans la formation des gaz bi-dimensionnels. Nous étudions ce problème à l'aide de la théorie fonctionnelle de la densité et modélisons les hétérostructures "cappées" pour essayer de résoudre ce problème. Après une analyse de STO dans ses formes volumique et de surface, nous modélisons systématiquement les hétérostructures pour les différentes valeurs de m et n. La structure couche par couche de la densité d'états montre l'impact de la chimie de ces hétérostructures sur les bandes de valence et de conduction. Si le critère de métallicité $m+n \geq 4$ est obtenu pour les cas les plus simples, il n'est pas expliqué dans son entièreté. Nous discutons enfin de l'introduction de défauts dans la structure.

Ce travail soulève de nouvelles questions dans l'étude des oxydes de métaux de transition, que ce soit en terme de confinement électrostatique, de topologie ou bien de magnétotransport.

Si le rôle du confinement électrostatique sur la densité de charge et sur la courbure de bandes est connue, la manière dont le potentiel électrostatique se comporte en présence de désordre laisse de nombreuses questions ouvertes. La présence de rugosité de surface et de lacunes d'oxygènes dispersées dans le volume fournissent plusieurs types de désordre susceptibles de produire des effets diffusifs de nature différente. La manière précise dont chaque orbitale et chaque sous-bande interagissent avec ce désordre dicte les propriétés de transport de ces systèmes. La différence d'un ordre de grandeur entre la densité de porteurs déterminée par l'interprétation des spectres ARPES et par l'Effet Hall non linéaire est souvent expliquée dans la littérature par la présence de "porteurs gelés". Les raisons pour lesquelles ces porteurs semblent ne pas participer au transport ne sont toujours pas bien comprises. Par ailleurs, une modélisation du désordre sous l'angle des corrélations électroniques pourrait fournir une explication au magnétisme observé de certaines surfaces de STO, même si cette observation expérimentale est encore sujette à débat.

En ce qui concerne les propriétés topologiques et le magnétotransport, le rôle du désordre est également de premier plan. Dans le contexte des Effets Hall Anormal et de Spin, les corrections de vertex aux opérateurs de courant (de charge ou de spin) produisent des contributions (side-jump et skew-scattering) qui sont du même ordre que la partie intrinsèque de la réponse. Dans le cas du modèle Rashba linéaire, il est dit que ces contributions peuvent occulter complètement la contribution intrinsèque à l'Effet Hall de Spin. La présence de plusieurs orbitales au sein de la bande de conduction peut-elle expliquer qu'un signal de SHE demeure ? Peut-on comprendre les propriétés d'anti-localisation faible et de magnétorésistance anisotropique des interfaces à base de STO en utilisant le modèle du MISO en incluant une description du désordre ? Il est clair que la nature multi-orbitale du gaz d'électrons aux interfaces d'oxydes de métaux de transition est essentielle pour comprendre ses propriétés. Les nombreuses observations démontrant la transition d'un à plusieurs types de porteurs par dopage électrostatique forment un excellent champ d'étude pour les propriétés des systèmes à plusieurs bandes. Cela permet aussi de comprendre comment certains phénomènes physiques complexes s'expriment en présence de plusieurs types de porteurs

électroniques.

En résumé, les hétérostructures d'oxydes de métaux de transition sont des systèmes fascinants qui offrent un excellent cadre pour étudier de nouvelles phases de la matière et des propriétés exotiques de transport. Ces matériaux sont des candidats pertinents pour le développement d'une nouvelle génération de composants électroniques possédant des propriétés ciblées.

I – Introduction to transition metal oxide heterostructures

> It is so difficult to find the beginning. Or, better : it is difficult to being at the beginning. And not to try to go further back.
>
> Ludwig Wittgenstein,
> *On Certainty*

I.1 An introduction to Materials Science

Materials Science intends to understand and predict the properties of materials (electronic, mechanic, chemical etc), and to discover new materials. If semi-conductors have been for long the ultimate standard to build electronic devices, Transition Metal Oxides (TMO) are strong contenders to build the next generation of devices for they are a big family of compounds with rich and various functionalities. While usual electronic devices are alloys of IV (C, Si), III-V (GaAs, GaN, BN) and II-VI (CdTe, ZnO) semi-conductors with p electrons in the valence/conduction band, TMO contain transition metals with a partially filled d-shell which determines the properties of the valence and conduction bands. d-shell electrons are known to have richer properties than s- or p-shell electrons, in particular regarding complex effects such as electronic correlations, spin-orbit coupling or magnetism. Materials for which the conduction and valence band is composed of s- and p-shell electrons are usually treated in the free electron picture : electron-electron interactions can safely be neglected because the Coulomb interaction between electrons is strongly screened. This model is called the

electron gas and has a parabolic dispersion

$$\epsilon_{EG}(k) = \frac{\hbar^2 k^2}{2m^*} \tag{I.1}$$

where k is the wavevector of the electron and m^* is the effective mass of the electron. This mass features corrections to the bare electron mass due to the periodic potential of the crystal and the electrostatic screening. This approximation holds for systems at very low filling and is also used to describe hole-like carriers. When the density of carriers increase, several effects have to be taken into account : the Pauli principle limits the filling of each orbital to two electrons (due to spin degeneracy) and imposes a finite bandwidth : at higher fillings, the dispersion and the effective mass deviate from the parabolic behavior. Above a certain threshold, the Fermi surface undergoes reconstructions : after a point called Van Hove singularity, the carriers change their nature, from electron-like to hole-like. The parabolic dispersion can be replaced by a cosine form $E_{TB}(k) = 2t(1-cos(ka))$ where t is the amplitude of the hopping and a is the lattice parameter. Around half-filling (one electron per unit cell), interactions can change the nature of the ground state from metallic to insulating. On-site interactions penalize so much double-occupancy of sites that the system goes towards a frozen charge state : this is called the Mott insulator. Other effects such as interactions between the electrons and spin waves or phonons can change the electronic properties of a material.

The geometry of a crystal has a strong influence on its electronic properties. The Linear Combination of Atomic Orbitals (LCAO) approximation treats electronic states as hydrogenoid orbitals located around the atoms of the unit cell. The overlap of these atomic orbitals can explain the formation of covalent bonds when electrons are shared between two neighboring atoms or metallic states when electronic states are no longer localized. The spatial distribution of the wavefunctions of the electronic states has an important interplay with the position of atoms inside the unit cell of the crystal : s orbitals have spherical symmetry, whereas p orbitals (p_x, p_y, p_z) are directional and have two lobes disposed along a common axis. The directionality of orbitals can either favor or penalize overlaps between neighboring atoms. The tight-binding approach helps to build effective models for materials from these principles enriched with symmetry considerations [57]. It allows to give a hierarchy of the hopping amplitudes and to model metallic states with a minimal number of terms

in the Hamiltonian. The parameters of a tight-binding Hamiltonian can be fitted to match experimental data or results of more sophisticated models such as *ab initio* computations.

I.2 Transition Metal Oxides

I.2.1 Oxides as functional materials

Transition Metal Oxides (TMO) constitute a vast class of materials known to display a lot of different functionalities [3, 4, 5]. The cuprates, a very broad family of high-T_c superconductors, are maybe the most famous family among these materials. A complete zoology of the functionalities of TMO would be futile for they are so diverse and intriguing : $SrTiO_3$ is the most dilute superconductor known and also a quantum paraelectric [6], $LaAlO_3$ is a polar insulator, $LaTiO_3$ and VO_2 are Mott insulators and exhibit a metal-to-insulator transition [7, 8, 9]. Cobaltates [10, 11] and nickelates [12] have magnetic properties. The conduction band of these systems is often composed of d electrons which are more impacted by electronic correlations or effects such as spin-orbit coupling than the s and p electrons of the conduction band of semi-conductors. They also exhibit richer physics because of the multi-orbital nature of the d-shell and to the multiple states of oxidization of their chemical components [5, 11].

I.2.2 Perovskite oxides : crystallography

"Perovskite" initially named calcium titanate $CaTiO_3$, but the term is now employed to name oxides with the general formula ABO_3. It condenses in a cubic structure with A ions on the corners, B ions in the center of the cube and O atoms in the center of the faces of the cube. The A ions usually are alkaline earth (Ca, Sr, Ba) or rare-earth (La, Nd, Eu) elements while the B ions are $3d$ (Ti, Co), $4d$ (Ru, Pd) or $5d$ (Ir, Ta) transition metals. The structure is stable for values of the Goldschmidt's tolerance factor $t_G = \frac{R_A+R_O}{\sqrt{2}(R_B+R_O)}$ in the range 0.75-1.0 [58, 59], where R_X is the ionic radius of species X. This condition comes from the steric constraint that the length of the diagonal of a face of the cube must be $\sqrt{2}$ times the length of one of its edge. For $t_G = 1$ the oxygens are in contact with both the A and B ions. For $t_G < 1$ the A ions have more space than needed in the interstices, leading to orthorombic

distortions, while for $t_G > 1$ the unit cell undergoes tetragonal distortions. These distorted structures lead to phenomena such as ferroelectricity (in $BaTiO_3$ where $t_G = 1.06$ [60]) or antiferrodistortive order (in $CaTiO_3$ where $t_G = 0.946$ [61]). The huge variety of compounds sharing this simple structure is an interesting playground to seek novel properties of matter. The A and B ions are building blocks that can bear functionalities : rare-earth atoms (Sm, Nd, Eu) host magnetic properties [62], while transition metals (Ti, Ta, W) display strong atomic spin-orbit coupling [63]. The interplay between the itinerant electrons of the *d*-shell, the crystal geometry and the chemistry yields a very rich environment to design new states of matter. The addition of defects such as atomic substitutions [64] or oxygen vacancies [65] allow to tailor the properties of bulk materials with even finer tools.

I.2.3 Making an interface

Perovskite oxides are fascinating if only for the properties of their bulk, but they turn out to be a very nice class of materials to build interfaces. The dimensions of the unit cell are similar for a large number of these compounds [66], allowing to make smooth interfaces of large dimensions while avoiding the proliferation of dislocations due to lattice mismatch. It is possible to design heterostructures with richer properties than those built from semiconductors thanks to the functionalities of TMO. Single interfaces can be modeled as 2-dimensional systems ; the application of strain, electric or magnetic fields can change their properties. Growing materials within a layer-resolved atomic precision allows to produce structures such as superlattices, and can be considered as synthesizing artificial materials with patterned crystalline structures. Interfacing perovskite oxides offers a new degree of freedom to design materials with novel properties : each material is a building block, and the stacking of these blocks offers new ways to study the interplay of different physical phenomena. These architectures yield means to harness the best properties of materials, or even to induce new physical effects proper to the patterned structures [19, 20, 21, 22, 23]. The main techniques used for the synthesis of perovskite oxides are molecular beam epitaxy, pulsed laser deposition, chemical vapor deposition and laser sputtering [16].

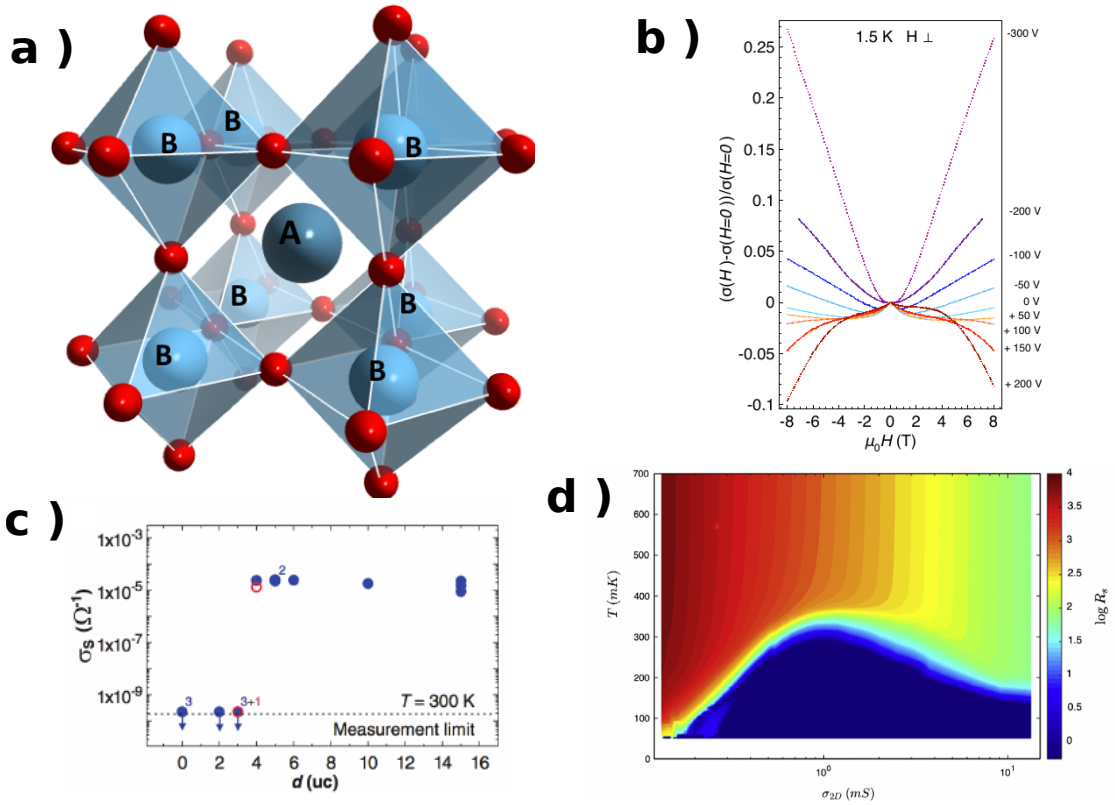

Fig. I.1 a) The perovskite structure ABO_3. b) Magneto-resistance of a LAO/STO interface under different backgate voltages, taken from [52]. c) Conductivity of LAO/STO interface as a function of the number of LAO layers on top of a STO substrate, extracted from [67]. A transition to a metallic state occurs above a thickness of four unit cells. d) Resistance map as a function of the temperature and of the conductivity. The superconducting transition displays a dome-like shape, taken from [68].

I.3 The LAO/STO heterostructure

I.3.1 Formation of the 2DEG

The paradigmatic example of perovskite heterostructure is the interface between $SrTiO_3$ (STO) and $LaAlO_3$ (LAO). It has been discovered in 2004 [15] that the interface between LAO and STO becomes metallic when more than 4 unit cells of LAO are piled up on top of a TiO_2-terminated STO substrate. This is unexpected because both LAO and STO are wide band gap insulators ($\Delta_{LAO} = 5.6$ eV and $\Delta_{STO} = 3.2$ eV). The metallic state at this interface is a 2-dimensional electron gas (2DEG), but contrarily to semi-conductor heterostructures, no extrinsic donors are to be added in order to create it. Several explanations have been proposed

to account for the formation of this 2DEG, two of them being the polar catastrophe and the presence of oxygen vacancies. Both these scenarios rely on a charge transfer between the topmost surface of LAO and the interface between LAO and STO. Indeed, the LAO part of the interface is composed of alternating layers of LaO and AlO_2, each carrying an opposite electrostatic charge (+1 for LaO and -1 for AlO_2). The stacking of these layers creates a linearly growing electrostatic potential which overcomes the gap between the two materials above a certain threshold. In the polar catastrophe scenario, this energy is relaxed by a mere transfer of electrons from the topmost LAO layer to the TiO_2 layer at the interface. It is computed that the critical thickness of LAO layers triggering the polar catastrophe is of four unit cells. A different theory to explain the emergence of this 2DEG relates the charge transfer to the formation of oxygen vacancies in the topmost layer of LAO. These empty oxygen sites are very common defects in perovskite crystals, and it is proposed that the accumulation of electrostatic energy thermodynamically favors the formation of these vacancies when there are more than four unit cells of LAO [69]. The formation of each vacancy is accompanied by the release of 2 electrons inside the system, to screen the effective charge left by the missing oxygen atom. The estimated critical thickness in this scenario is also around 4 unit cells of LAO. In both cases, the transferred charge shall be of 0.5 electron per unit cell to balance the electrostatic energy

I.3.2 Overview of the LAO/STO interface

The formation of the 2DEG at the interface of LAO and STO is not the end of the story : this interface hosts very intriguing properties such as superconductivity [70], magneto-resistance [71] and even ferromagnetism in some samples [56, 72]. Standard techniques in nanostructures make it possible to pattern Hall bars and to use gate voltages in order to dope the 2DEG. Its properties strongly varies with electrostatic doping : its superconducting temperature varies, displaying a dome-like shape analogous to the behavior of high-T_c superconductors [73], with a peak critical temperature of $T_c = 300mK$. Its magneto-resistance also depends strongly on temperature and electrostatic doping, displaying signatures of weak anti-localization which are interpreted as consequences of a gate-tunable Rashba spin-orbit coupling [52]. Hall effects measurements display nonlinear features typical of the presence of several types of carriers inside the 2DEG. Multi-band transport can hint at reasons why

superconductivity and ferromagnetism, which usually are antagonistic, are simultaneously observed on the same samples [56].

I.4 Organization of the thesis

In Chapter II, we provide microscopic descriptions of the key ingredients we use to model the STO [001] and [111] interfaces. From their crystalline and chemistry properties, we derive a multi-orbital tight-binding model describing these interfaces, focusing on non-conventional terms : the compounded effects of atomic spin-orbit coupling and orbital mixing (due to surface distortions) induce splittings in the band structure and non-trivial spin-orbit textures. This model reproduces the ARPES measurements of STO interfaces. Via the Poisson-Schrodinger approach, we explain the formation of subbands with a spatial extension related to their orbital character from the presence of a confining potential at the interface. We use this approach to understand the impact of temperature on the confinement and features of the electrostatic doping of these interfaces. Electrostatic doping can be done in two different geometries. For top-gating, the electrostatic doping changes the density of the 2DEG, and the different subbands are not equally doped. In a back-gating geometry, the shape of the potential confining the 2DEG changes and differently impacts subbands : the levels which are less confined are more doped, and there exists a threshold of backgate voltage above which there can be a leakage of charge outside the well. We model electronic correlations to understand measurements of non-linear Hall effect in the [001] and [111] orientation of STO interfaces and investigate the possibility of band inversions due to the compounded effects of interactions and electrostatic doping.

In Chapter III, we dive into the mathematical framework underlying the concepts of topology in condensed matter physics. We unveil the key role played by the geometry of the wavefunctions inside the Brillouin Zone in order to explain the concepts of topological invariants, with a particular focus on the concept of Berry curvature. To continue our journey, we turn to more sophisticated topological invariants such as the spin curvature. We discuss the relation between these geometrical quantities and the experimental probes available to observe these effects. Eventually, we discuss how these concepts can be applied to metallic systems, which are our main interest in this work.

The Chapter IV is devoted to the spintronic response of TMO heterostructures. We begin with a description of two mechanisms of spin-to-charge conversion, namely the Edelstein Effect and the Spin Hall Effect, and discuss recent measurements in STO-based interfaces where these effects are found to be very large. Concepts of semi-classical transport allow us to compute transport properties from tight-binding models for STO-based interfaces and to fit experiments using realistic parameters. We further push our analysis of the generic model for STO interfaces and show that the multi-band structure of TMO is fundamental to explain the variations of the Edelstein response. The behavior of the system can be understood by a model we call Multiband Interfacial Spin-Orbit (MISO). Using analytical computations, we isolate the important contributions to the spintronic responses using low-energy models around special points of the band structure and show that the MISO induces winding spin textures of two different natures with a distinct effect on the responses. Using perturbation theory, we detail these two contributions : if the former is analogous to the Rashba-Edelstein effect, the latter is peculiar to the multi-orbital nature of the conduction band and can be of the same amplitude. This dichotomy might provide an explanation for phenomena that are interpreted as a gate-tunable Rashba interaction or even more complex cubic Rashba interactions.

Chapter V is an *ab initio* study of the *capping problem* in LAO/STO heterostructures. LAO/STO interfaces are known to become metallic above a critical thickness of 4 LAO layers on top of the STO substrate. It remains difficult to disentangle the respective roles of chemistry and electrostatics to explain the formation of the 2DEG at this interface. Recent experiments have shown that the 4 LAO layers can be replaced by m LAO + n STO layers, as long as $m+n \geq 4$. This observation, which is called the "capping problem", might help unveil the mechanisms underlying the formation of 2DEGs and to understand better the different effects at play. We use Density Functional Theory to study these capped heterostructures. After an analysis of the bulk and bare STO surfaces, we systematically try the different m and n cases. The layer-resolved structure of the Density of States reveals how the Ti conduction and O valence bands are affected by the chemistry of the heterostructure. The metallicity criterion is obtained for known cases but fails to be completely explained. We discuss the introduction of defects in the heterostructures, which has only remained a possible explanation for this phenomenon.

II – Electrostatic doping of TMO heterostructures

> The non-physicist finds it hard to believe that really the ordinary laws of physics, which he regards as the prototype of inviolable precision, should be based on the statistical tendency of matter to go over into disorder.
>
> Erwin Schrodinger,
> *What is Life ?*

II.1 Introduction

Transition Metal Oxides (TMO) are a very rich class of materials if only for their bulk properties, so building heterostructures based on these materials provides a fascinating playground to study new electronic states of matter. The discovery in 2004 [15] that the interface between the two wide band-gap insulators $LaAlO_3$ (LAO) and $SrTiO_3$ (STO) becomes metallic if more than 4 LAO layers are put on top of an STO substrate opened the way for a new area of research called *oxitronics*. The huge progress in the synthesis of these materials [16] allows to produce devices with mobilities matching the state-of-the-art materials standards. Furthermore, it is possible to pattern nanostructures with a layer-to-layer accuracy [15, 17, 18]. New designs such as stacks [19] or superlattices [20, 21] composed with layers of different oxides and a great regularity allow to tailor the properties of materials in situ, using each oxide as a building block of artificial material with targeted properties. The laye-

red structure can be used to probe the effects of dimensionality on electronic properties : if interfaces behave as 2-dimensional objects, stacking enough layers of a material on top of a substrate can restore bulk properties [22, 23].

In this chapter, we provide the microscopic descriptions of the ingredients we use to model the STO [001] and [111] interfaces. From their crystalline and chemistry properties, we derive a multi-orbital tight-binding model describing these interfaces, focusing on non-conventional terms : the compounded effects of atomic spin-orbit coupling and orbital mixing (due to surface distortions) induce splittings in the band structure and non-trivial spin-orbit textures. We explain the main features of the Poisson-Schrodinger approach, which describes the electrostatic confinement near an interface by solving a self-consistent problem : the interaction between the spatial density of carriers and the electrostatic potential created by the interface. The presence of a confining potential creates subbands with a spatial extension related to its orbital character. Through this approach, we discuss the effects of temperature on the confinement and study features of the electrostatic doping of 2-dimensional electron gases (2DEG). Electrostatic doping can be done in two different geometries : top-gating and backgating. For top-gating, the electrostatic doping changes the density of the 2DEG, and the different subbands are not equally doped. In a back-gating geometry, the shape of the potential confining the 2DEG changes and differently impacts subbands : the levels which are less confined are more doped, and there exists a threshold of backgate voltage above which there can be a leakage of charge outside the well. We model electronic correlations to understand measurements of non-linear Hall effect in the [001] and [111] orientations of STO interfaces, and investigate the possibility of band inversions due to correlations and electrostatic doping. I thank the group of Andrea Caviglia for the collaboration I had the chance to take part of through the writing of [74] and the numerous discussions throughout the thesis.

II.2 Tight-binding modeling of TMO heterostructures

In this section, we detail the different terms of the tight-binding model which is used to describe the band structure of TMO heterostructures. We use this model to estimate the electronic spectrum of STO-based interfaces with different crystalline orientations and are

able to find a nice agreement with experimental results. This is a first step of validation of the model we use in the following of the thesis and it allows the determination of important parameters of materials (hopping amplitudes) from experiments.

II.2.1 Linear Combination of Atomic Orbitals and tight-binding approximation

A crystal is a periodic arrangement of atoms and can be represented by a unit cell and a basis of vectors, the periods of the crystal. This unit cell can contain several atoms and is repeated in all the directions of the crystal, and additional symmetries (inversions, rotations or other transformations) impact the electronic and mechanical properties of the crystal. In the ionic picture, electrons orbit around the nucleus in order to screen the charge of the nucleus. Electronic states are decomposed on the basis of the atomic levels of each species, and can be labeled by an index n. Translation invariance along the lattice vectors constrains the spatial form of the eigenfunctions inside a crystal : the Bloch theorem states they can be written $\psi_{n,k}(r) = e^{ikr}u_n(r)$ where u_n is a periodic function with the same periods as the crystal, k is the wavevector and n can be understood as a quantum number for the orbital or spin character of the electron. In the tight-binding formulation electrons are bound to atoms, and a natural basis to describe the electronic eigenstates in the crystal consists of hydrogenoid orbitals. Let us focus on the case of two atoms at a distance d with one electron each. When they are infinitely far from one another, the two electrons are not affected by their mutual electrostatic interaction. When they are brought closer, the wavefunctions of the electrons can overlap and form states that are not localized near only one atom : the bonding and anti-bonding states ; this model is used to explain chemical bonds in molecules. A solid consists in a very large number of atoms evenly spaced. If neighboring atoms can form chemical bonds, new possibilities emerge : in particular the existence of itinerant electrons, which are called metallic states. Contrarily to core levels or electrons forming covalent bonds, these metallic states can freely move inside the solid and are responsible for charge transport.

The shape of atomic orbitals impacts the characteristics of the conduction band and of the chemical bonds. The directionality of the p and d orbitals has dramatic effects on dispersion relations and orbital ordering of the bands, and depending on the geometry of the crystal, new energy splittings appear. For graphene, a 2-dimensional honeycomb lattice composed of carbon atoms, the s and p orbitals forms chemical bonds through sp^2 hybridization : the

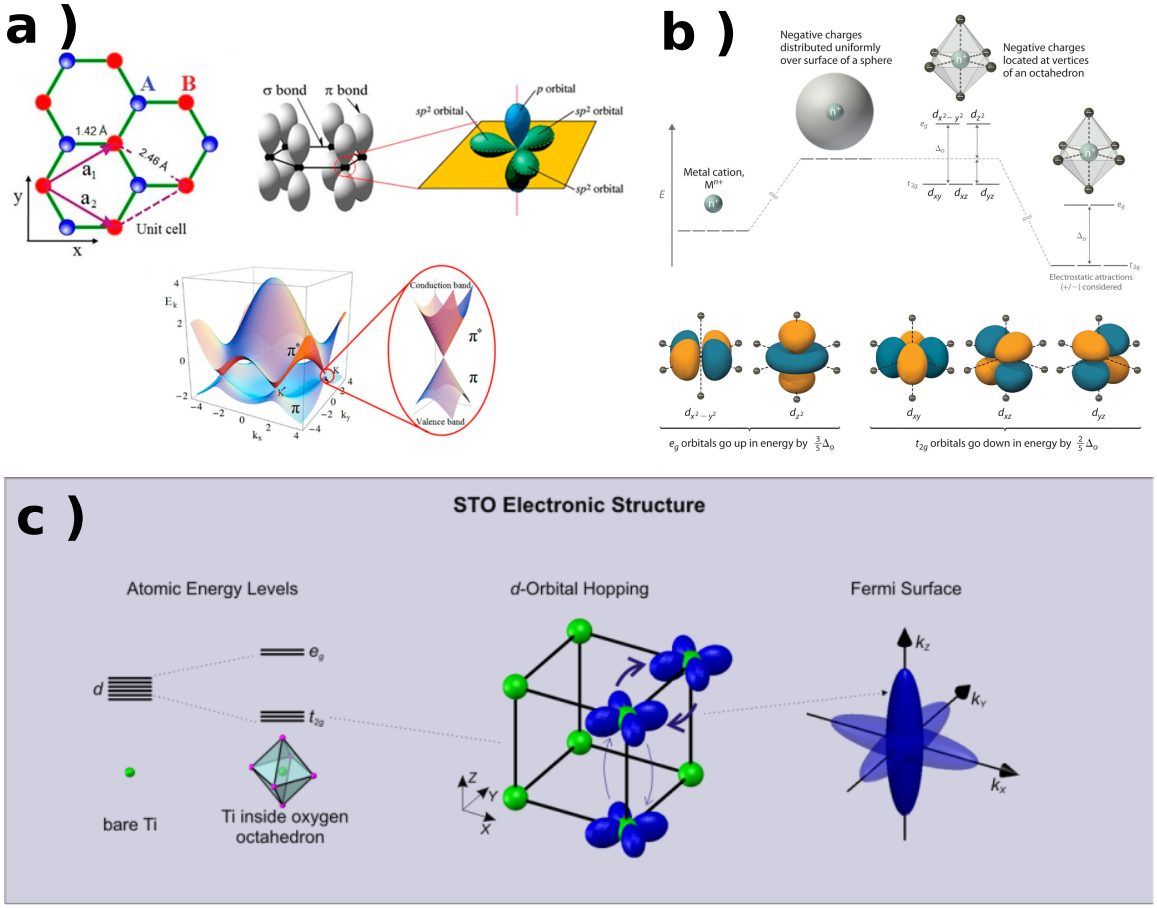

Fig. II.1 a) Graphene and sp2 hybridization, from [75]. b) Crystal field theory and d electrons : the $e_g - t_{2g}$ splitting, taken from [76]. c) Dispersion of t_{2g} orbitals in the perovskite crystal structure from [17].

$2s$ orbitals and $2p_{x,y}$ orbitals hybridize to constitute orbitals pointing in the direction of the neighboring atom to form σ-bonds, as shown in Fig. II.1 a. The remaining $2p_z$ orbitals of each atom points out of the lattice plane and hence do not form σ- but π-bonds by hybridizing with other $2p_z$ orbitals, producing bands split in energy from the bands made out of s and p orbitals. As there are two carbon atoms per unit cell, the $2p_z$ orbitals form two bands of bonding and anti-bonding states, leading to the peculiar semi-metallic band structure of graphene and the emergence of the famous Dirac cones. d orbitals in the perovskite environment are split into two manifolds by a crystal field : this is the $e_g - t_{2g}$ splitting. The t_{2g} orbitals of the transition metal ion do not directly point towards the negative charges surrounding, contrarily to the e_g orbitals as can be seen on Fig. II.1 b. This crystal field

splitting can be of several eV and determines the orbital nature of the conduction band of materials such as STO.

II.2.2 Kinetic terms

The conduction band of the system is mainly composed of the t_{2g} electrons of the Ti atoms, which can hybridize with their neighbor through an oxygen atom. The valence band of the oxygen is mainly composed of p orbitals. The $d-p$ hybridization is constrained in terms of orbital character and direction of hopping : to hybridize in the x direction, the p orbital involved must be either a p_y or a p_z orbital, and the d orbital respectively the d_{xy} or d_{xz} orbital (see Fig II.1 c). The same argument holds for the y and z directions, with a cyclic permutation of the x, y, z indices. Hopping between neighboring Ti atoms can also be direct, though this process is less likely for the overlap is smaller. Using these two principles, the d_{xy} orbital has a bandwidth t_1 in the x and y direction, and a bandwidth $t_2 << t_1$ in the z direction ; this smaller bandwidth means that electrons tend to be more localized. The dispersion relations of the d_{xy}, d_{xz}, d_{yz} bands in the bulk of STO are

$$\begin{aligned}
\epsilon_{xy}(k) &= 2t_1\left[1-\cos(k_x a)\right] + 2t_1\left[1-\cos(k_y a)\right] + 2t_2\left[1-\cos(k_z a)\right] \\
\epsilon_{xz}(k) &= 2t_1\left[1-\cos(k_x a)\right] + 2t_2\left[1-\cos(k_y a)\right] + 2t_1\left[1-\cos(k_z a)\right] \\
\epsilon_{yz}(k) &= 2t_2\left[1-\cos(k_x a)\right] + 2t_1\left[1-\cos(k_y a)\right] + 2t_1\left[1-\cos(k_z a)\right]
\end{aligned} \tag{II.1}$$

Where a is the unit cell parameter (for STO $a = 3.905\mathring{A}$), and the hopping amplitude t is inversely proportional to the effective mass of the electron $m_\alpha = \frac{\hbar^2}{2t_\alpha a^2}$. The fraction of the effective mass with respect to the bare electron mass is $\frac{m_\alpha}{m_e} \approx \frac{0.25eV}{t_\alpha}$.

a) [001] interface

The presence of an interface has dramatic effects on the band structure : it locally breaks inversion symmetry and induces an interfacial electric field. The t_{2g} orbitals are not equally impacted by this electric field which induces an energy splitting inside the t_{2g} manifold. If z is the name of the [001] direction, the d_{xy} orbital is lower in energy than the $d_{xz/yz}$ orbitals. The dispersion relations of the t_{2g} orbitals in the plane of the interface are not equivalent : the d_{xy} orbital has the same dispersion along the x and y directions, while the $d_{xz/yz}$ have anisotropic

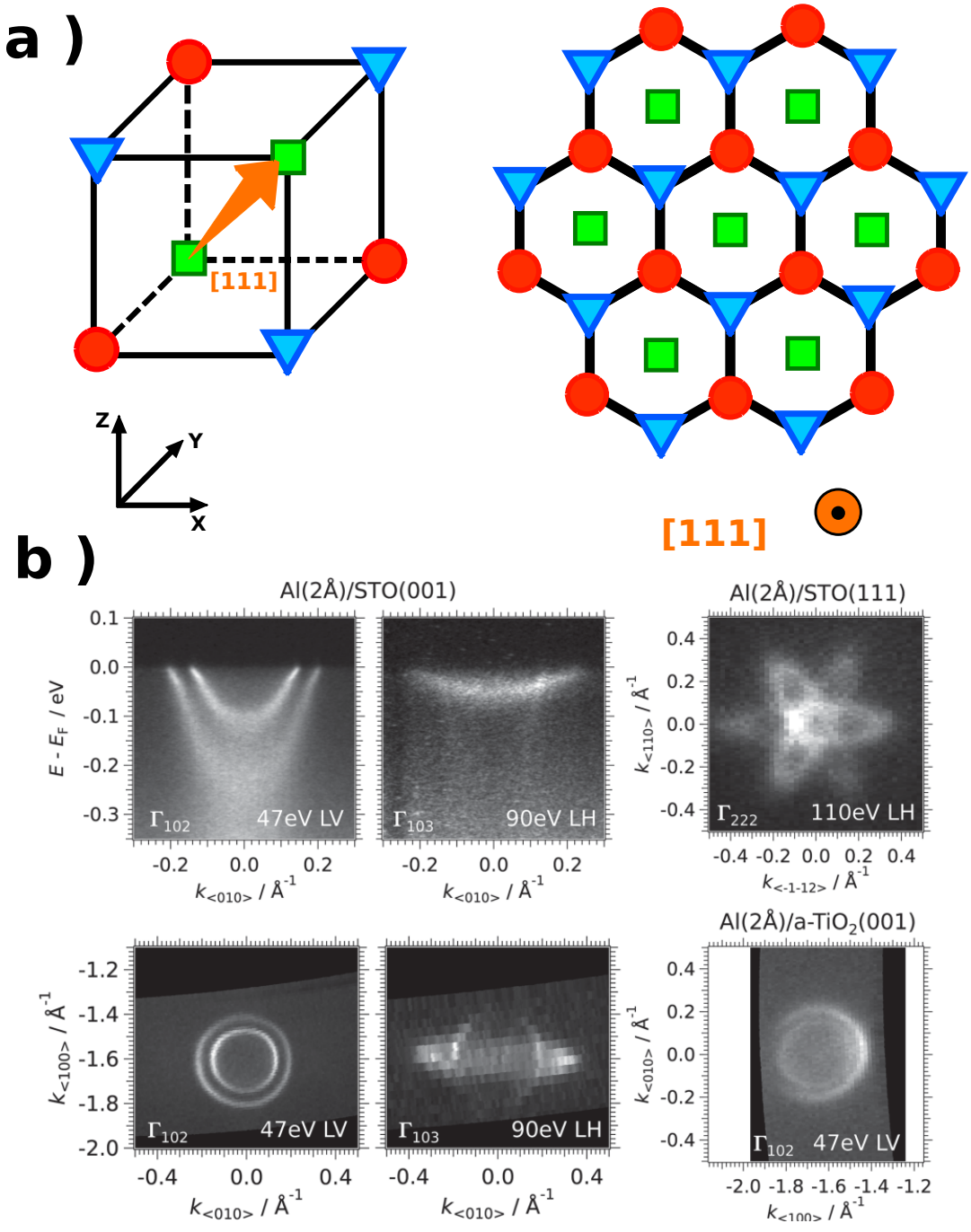

Fig. II.2 a) Cutting a cubic lattice perpendicularly to the [111] orientation yield a honeycomb lattice if only two layers are taken into account. b) Extracted from [77]. Left : spectrum of an AlOx/STO [001] interface with two different polarization and the corresponding Fermi energy cuts inside the BZ. The Fermi surface for Al/STO [111] interface is shown at the top right-hand corner while the Al/a-TiO_2 interface is shown at the bottom right-hand corner.

dispersion. This anisotropy stems from the fact that the electrons have a different effective mass along each of the crystal axis : m_1 is called the light mass and m_2 the heavy mass. For this reason, d_{xy} electrons are often called light carriers and $d_{xz/yz}$ electrons heavy carriers. The interface breaks translation invariance along the z direction, hence the quasi-momentum k_z is no longer a quantum number and states cannot be represented as plane waves in the z direction. Instead, confined states appear at the interface, forming discrete energy levels. The difference in bandwidth along the k_z direction affects the structure of this discrete spectrum, which is different for heavy and light orbitals. We make the approximation that this spectrum is decoupled from the dispersion in the plane of the interface. The discrete energy levels of heavy and light orbitals are respectively denoted $\Delta^n_{xz/yz}, \Delta^n_{xy}$, and the amplitude of this spectrum is discussed later. The dispersion relation of an interface along the [001] orientation becomes

$$\begin{aligned}
\epsilon^n_{xy}(k) &= 2t_1\left[1-\cos(k_x a)\right] + 2t_1\left[1-\cos(k_y a)\right] + \Delta^n_{xy} \\
\epsilon^n_{xz}(k) &= 2t_1\left[1-\cos(k_x a)\right] + 2t_2\left[1-\cos(k_y a)\right] + \Delta^n_{xz/yz} \\
\epsilon^n_{yz}(k) &= 2t_2\left[1-\cos(k_x a)\right] + 2t_1\left[1-\cos(k_y a)\right] + \Delta^n_{xz/yz}
\end{aligned} \tag{II.2}$$

With $\Delta^1_{xy} < \Delta^1_{xz/yz}$. We often use the notations $\Delta = \Delta^1_{xz/yz} - \Delta^2_{xy}$ and $\tilde{\Delta} = \Delta^1_{xz/yz} - \Delta^1_{xy}$ in the following to denote the energy splitting between the d_{xy} and d_{xz} subbands of the [001] orientation of the STO surface.

b) [111] interface

The [001] interface is perpendicular to one of the crystal axis, and the plane parallel to the interface can be described by the two minimal lattice vectors [100] and [010]. However, crystals can be cut perpendicularly to any of the lattice vectors : for the cubic lattice, the [111] direction (diagonal of the cube) is interesting because the surface orthogonal to this orientation will have a trigonal symmetry. Each atom of the bulk can be assigned to a plane perpendicular to the [111] direction, called [111] planes by simplicity. Fig. II.2 a shows the Ti atoms belonging to the same [111] planes decorated with the same symbol (circles or triangles). The two Ti atoms decorated with a square are separated by two [111] planes (containing the circles and triangles), far from one diagonal of the cube (one [111] vector),

represented by the full orange arrow. If we focus on the bi-layer composed of the triangle and the circle atoms, the neighborhood of each atom is the same as in a honeycomb lattice. The equivalent honeycomb lattice is also depicted, where the green squares are only put as a guide to the eye (they can be added to build a tri-layer model). The atoms represented by circles and triangles are not equivalent as they were in graphene because they do not lie in the same plane. It is possible to build a tight-binding model from this honeycomb lattice by assuming that electrons stay confined in the layers of the triangles and the circles. If the atoms are close to a [111] interface, they do not share the same electrostatic environment : the topmost layer is at the interface while the bottom layer is in contact with another STO layer. This has important effects at high fillings : at the levels of band crossings, Dirac points appear in this band structure and are split between the two sites by this energy difference [39].

Near the interface, we consider this bi-layer model as a two-dimensional tight-binding model. We build a unit cell with two lattice vectors (linking the neighboring blue triangles for instance), and define the reciprocal lattice with the dual basis of these vectors. The real hopping paths are along the x, y and z directions through oxygen atoms as in the bulk and respect the same orbital symmetries as bulk STO. The effective masses of the three orbitals are not equal along all crystalline directions : two directions are light and one is heavy. The details of the complete tight-binding model can be found in Appendix A.2 and [78]. As the fillings of these interfaces remain low, a low-energy model of the spectrum can be used to get a grasp on the shape of the Fermi surfaces.

After a rotation of the reciprocal space basis in order to respect the symmetry of the interface (details in the Appendix A.2), the kinetic energy can be split into the in-plane part (the corresponding reciprocal space vectors are k_1, k_2) and the out-of-plane part ($k_\perp$, parallel to the [111] direction). The effective mass of the three t_{2g} orbitals in the direction perpendicular to the interface is equal, so that we consider the confinement to be similar for the three orbitals, as is detailed later. If we focus on the in-plane kinetic energy, a dispersion

relation for the $d_{xy,xz,yz}$ orbitals at low k is

$$\begin{aligned}
\epsilon_{yz} &= t_1 a^2 \left(\frac{k_1}{2} + \frac{\sqrt{3}k_2}{2}\right)^2 + \frac{4}{3} t_2 a^2 \left(-\frac{\sqrt{3}k_1}{2} + \frac{k_2}{2}\right)^2 \\
\epsilon_{xz} &= t_1 a^2 \left(\frac{k_1}{2} - \frac{\sqrt{3}k_2}{2}\right)^2 + \frac{4}{3} t_2 a^2 \left(\frac{\sqrt{3}k_1}{2} + \frac{k_2}{2}\right)^2 \\
\epsilon_{xy} &= t_1 a^2 k_1^2 + \frac{4}{3} t_2 a^2 k_2^2
\end{aligned} \tag{II.3}$$

Where k_1, k_2 are two perpendicular directions of the hexagonal Brillouin Zone. The derivation of these formulas is given in Appendix A.2, where a tight-binding version is also detailed. As for the [001] orientation, in the [111] plane the t_{2g} orbitals have a light and a heavy direction, and the Fermi surface for each of the 3 orbitals can be obtained one from another via a rotation of $\frac{2\pi}{3}$. For the [111] orientation, one must add a trigonal crystal field, because the symmetry of the crystal is different in the vicinity of the interface. In the d_{yz}, d_{xz}, d_{xy} basis this term can be written

$$\mathcal{H}_{trig} = \Delta_{tcf} \begin{pmatrix} 0 & 1 & 1 \\ 1 & 0 & 1 \\ 1 & 1 & 0 \end{pmatrix} \tag{II.4}$$

The eigenvectors and eigenenergies of this operator can be found in Appendix A.3. In the direction perpendicular to the interface, as explained in the previous paragraph, all the orbitals have the same effective mass $m_\perp = \frac{3m_1m_2}{2m_2+m_1} \approx 0.9m_e$. Orbitals are not split in energy by the confinement contrarily to the [001] orientation of the surface, but will be split by additional terms such as the atomic spin-orbit coupling or the trigonal crystal field. If the orbital character is changed by these couplings, there is however no orbital dichotomy on the extension of the states due to a differentiated confinement. Local distortions of the structure might lead to such an effect but were not studied in this work.

In the following of the thesis, unless this is explicitly specified, we investigate the [001] orientation of STO interfaces.

II.2.3 Atomic spin-orbit coupling

The spin-orbit coupling is a relativistic interaction of the spin of a particle with its motion inside a potential. Let us sketch a semi-classical explanation of this phenomenon : in its rest frame, the electron undergoes an effective magnetic field $\vec{B}_{SO} = -\frac{1}{c^2}\vec{v} \times \vec{E}$ when it moves at a velocity $\vec{v}$ around the atom exerting an electric field $\vec{E}$ (c is the speed of light). This induces a Zeeman-like term $\mathcal{H}_{SO} = -\vec{m} \cdot \vec{B}_{SO}$, with $\vec{m}$ the magnetic moment of the electron, linked to its spin through $\vec{m} = -\frac{g_s \mu_B}{\hbar}\vec{S}$, with g_s the g-factor of the electron and μ_B the Bohr magneton. If the potential is spherical, the electric field is radial $\vec{E} = \frac{E}{r}\vec{r} = \frac{dV}{rdr}\vec{r}$. Using $\vec{p} = m_e\vec{v}$, an angular momentum $\vec{L} = \vec{p} \times \vec{r}$ emerges, and eventually $\mathcal{H}_{SO} = \frac{2\mu_B}{\hbar m_e c^2}\frac{1}{r}\frac{dV}{dr}\vec{L} \cdot \vec{S}$. If we replace the semi-classical vectors $\vec{L}, \vec{S}$ with quantum operators acting on the t_{2g} basis, due to symmetries the spin-orbit coupling Hamiltonian can be written in the (d_{yz}, d_{xz}, d_{xy}) basis as [79]

$$\mathcal{H}_{bulk}^{SOC} = i\lambda_{SO} \begin{pmatrix} 0 & \sigma_z & -\sigma_y \\ -\sigma_z & 0 & \sigma_x \\ \sigma_y & -\sigma_x & 0 \end{pmatrix} \tag{II.5}$$

Where λ_{SO} is the amplitude of the atomic spin-orbit and the σ operators are the Pauli matrices acting on the spin degree of freedom. This term entangles the spin and orbital degrees of freedom. The detailed form of the orbital operators $\hat{\vec{L}}$ and the derivation of the Hamiltonian can be found in Appendix A.1. The eigenvalues and eigenfunctions of this Hamiltonian can be found in Appendix A.3. The corresponding spin-orbit energy splitting is equal to $E_{SO} = 3\lambda_{SO}$; we chose to write the Hamiltonian using λ_{SO} instead of $\frac{E_{SO}}{3}$ in the following to simplify the formulas in Chapter IV. The spin-orbit energy of STO is often taken as $E_{SO} \approx 25$ meV, which is consistent with $\lambda_{SO} \approx 8$ meV.

II.2.4 Orbital mixing

The interface breaks inversion symmetry, and the interfacial layer has two neighbors of different nature. Reconstructions of the interface occur in order to relax the constraints exerted by this difference, possibly through a buckling of the surface due to a tilt in the bonds between the Ti and O atoms. Instead of having an angle of π for the (Ti-O-Ti) bond, the Ti atom goes lower in the direction perpendicular to the interface. This distortion and

the directional nature of the O p and Ti d orbitals allow new hoppings that were previously forbidden by symmetry. A detailed tight-binding model leads to the appearance of the orbital mixing term [80, 81, 82], here in the (d_{yz}, d_{xz}, d_{xy}) basis for the [001] orientation

$$\mathcal{H}_{OM} = \gamma_{OM} \begin{pmatrix} 0 & 0 & -2i\sin(k_x a) \\ 0 & 0 & -2i\sin(k_y a) \\ 2i\sin(k_x a) & 2i\sin(k_y a) & 0 \end{pmatrix} \tag{II.6}$$

Where γ_{OM} is the amplitude of the orbital mixing, which can come from two mechanisms : either an interfacial electric field or atomic displacements in the vicinity of the interface allow hoppings usually forbidden by symmetry. For low k, it can be rewritten $\mathcal{H}_{OM} = \gamma_{OM} a(\vec{L} \times \vec{k}) \cdot \vec{z}$ in the [001] orientation. This is analogous to the Rashba Hamiltonian with the orbital operator replacing the spin operator. If the interface has a [111] orientation, the orbital mixing has the form $\mathcal{H}_{OM} = \gamma_{OM} a(\vec{L} \times \vec{k}) \cdot \vec{u}_{111}$ for low k (where $\vec{u}_{111} = \frac{\sqrt{3}}{3}[1,1,1]$). We do not include the orbital mixing in the spectrum and Fermi surfaces shown in Fig. II.3 c,d because we talk extensively of the effects of the orbital mixing in Chapter IV.

II.2.5 Band structure of the t_{2g} model

Vacuum/STO and of AlOx/STO interfaces have been studied by Angular Resolved Photo-Emission Spectroscopy (ARPES). This experimental technique studies the emission of electrons upon irradiation of materials with photons : the angular and energy distributions of this process make it possible to evaluate the spectral function of a material and its electronic spectrum. Experimental results taken from [77] for the [001] surface of STO are presented in Fig. II.2 b, and show that there are two subbands of d_{xy} character split in energy and at least one group of heavy bands $d_{xy/xz}$-like orbital with anisotropic dispersion (with a characteristic flower-like Fermi surface). ARPES spectra of the [111] surface of STO [77, 83] display the 6-fold symmetry expected from the equivalence of all orbitals. The polarization of the photons irradiating the sample allows to probe the orbital character of the electrons : selection rules originating from symmetry considerations impact the amplitude of the ARPES response through terms called *matrix elements*. In Fig. II.2 b the Fermi surface in the bottom left looks isotropic as expected for d_{xy}-like orbitals, while the Fermi surface in the bottom right

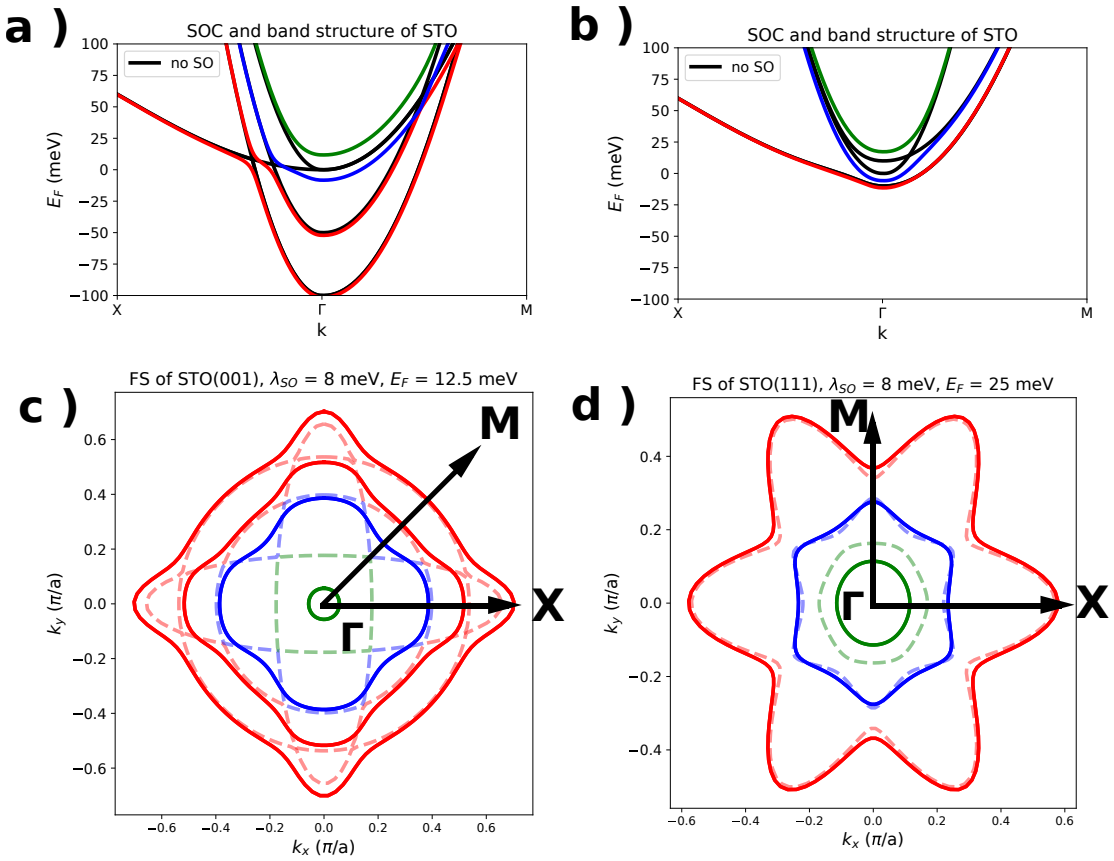

Fig. II.3 a,b) Band structure of the [001] and [111] orientations of the STO surface with (solid lines) and without spin orbit coupling (black lines). c,d) Corresponding Fermi surfaces with (solid lines) and without (dashed lines) atomic spin-orbit coupling. The parameters are $t_1 = 400$ meV, $t_2 = 30$ meV, $\Delta = 50$ meV, $\tilde{\Delta} = 100$ meV, $\lambda_{SO} = 8$ meV, $\Delta_{tcf} = 5$ meV and $\gamma_{OM} = \tilde{\gamma}_{OM} = 0$. The directions ΓX and ΓM are shown in the Fermi surface plots for the [001] and [111] orientations. The color code with red blue and green is the same between the band structure and the Fermi contours.

is more contrasted in the k_{010} direction ; this is not due to the absence of states in the k_{100} direction but to the response of the electrons to the light polarization : these anisotropies are typical of $d_{xz/yz}$ orbitals. ARPES experiments allow to determine characteristics of electronic systems such as gaps or effective masses, but also the carrier concentration through the area of the Fermi surfaces. The models presented for the [001] and [111] orientation of STO surface produce Fermi surfaces with the same symmetries as the ARPES spectrum, so they provide a good starting point to study these systems. Using polarized light, it is possible to perform Spin Resolved ARPES (SARPES). Experiments on STO surfaces [84, 85, 86] show that electronic states display properties of spin polarization consistent with a Rashba-like coupling. Although the resolution is not good enough to evaluate neither the intensity nor the exact form of the coupling, it suggests that a breaking of the spin degeneracy occurs. As we detail in Chapter IV, this Rashba-like coupling is a consequence of the compounded effect of the atomic spin-orbit coupling and the orbital mixing.

In the absence of spin-orbit coupling, due to the presence of a confinement gap, there are several band crossings in the band structure of the [001] surface of STO. In the ΓX (respectively the ΓY) direction, as the d_{yz} (respectively d_{xz}) subbands and the d_{xy} subbands do not have the same effective mass, they cross at a certain wavevector. The hierarchy of the subbands is changed before and after this wavevector and has an impact on the couplings between bands : band crossings are expected to have an important contribution to the amplitude of the Rashba coupling of STO-based interfaces [82]. Three-band crossings are also expected in the ΓM direction, where the d_{xz} and d_{yz} subbands have the same effective mass but a different effective mass as the d_{xy} subbands. These three-band crossings have been studied in [87, 88], where they are linked to topological properties. The band crossings for the [001] orientation of STO interfaces are the yellow circles shown in Fig. II.4 a and c. In the [111] orientation of the STO surface, three-band crossings are also expected, and come in two configurations, as shown in yellow circles in Fig. II.4 b and d. Near these points, the multi-orbital character of the conduction band is maximal and the form of the couplings between orbitals and subbands has a strong influence on the energy splittings and on the nature of the wavefunctions that emerge. This can lead to special responses in transport and spin properties of the system as we detail in Chapter IV.

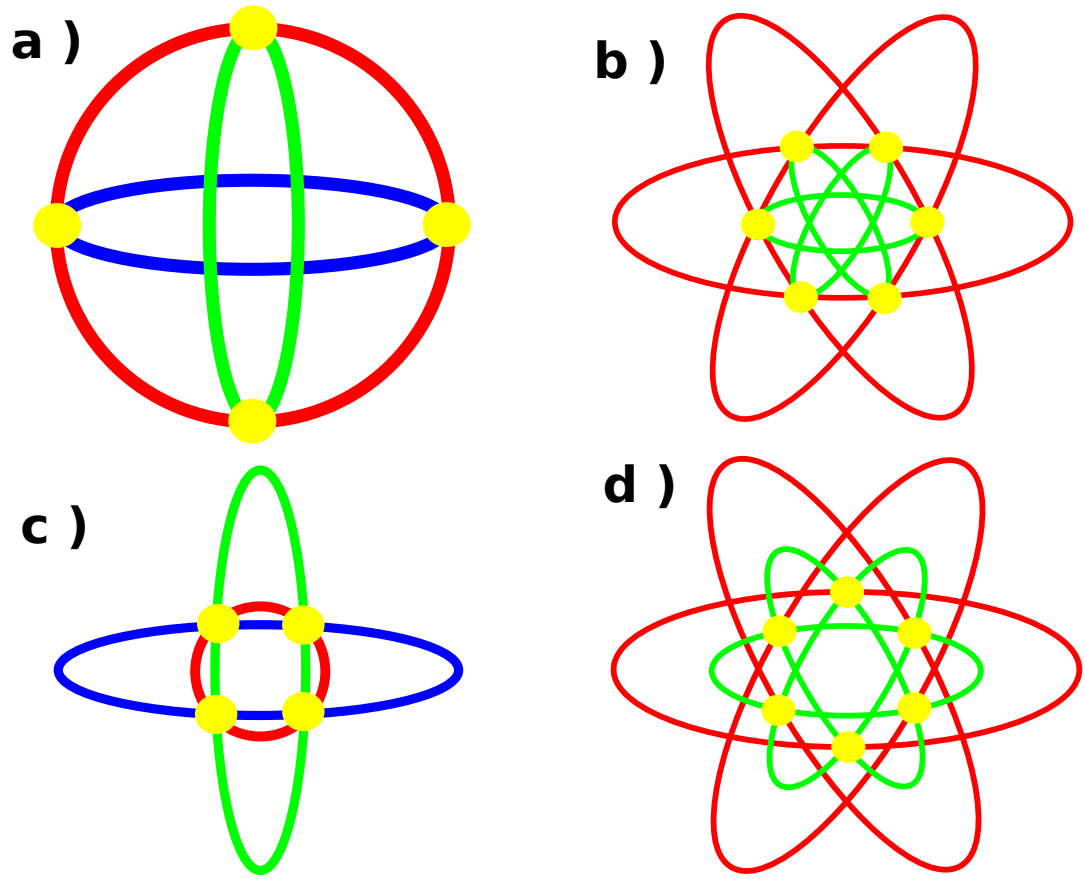

Fig. II.4 a) The avoided and c) "Topological" band crossings in the band structure of the [001] orientation of the STO surface. b,d) show the two types of triple crossings possible in the [111] orientation of STO

II.3 Electrostatic confinement near an interface

Due to electrostatic effects, the 2DEG at the LAO/STO interface is confined in a region which is a few nanometers thick. Confinement lowers the number of dimensions of the system : if the bulk of a material can be considered as a three-dimensional object, the electron gas at the interface behaves as a quasi two-dimensional object. The [001] interface breaks translation invariance along the z direction, resulting in the emergence of quantized, localized states near the interface. Eq. II.2 shows that confinement impacts the hierarchy of the bands near the interface, puts a gap in the spectrum, and determines the spatial extension of the 2DEG.

In this section, we model both the electrostatic confinement and the quantization of

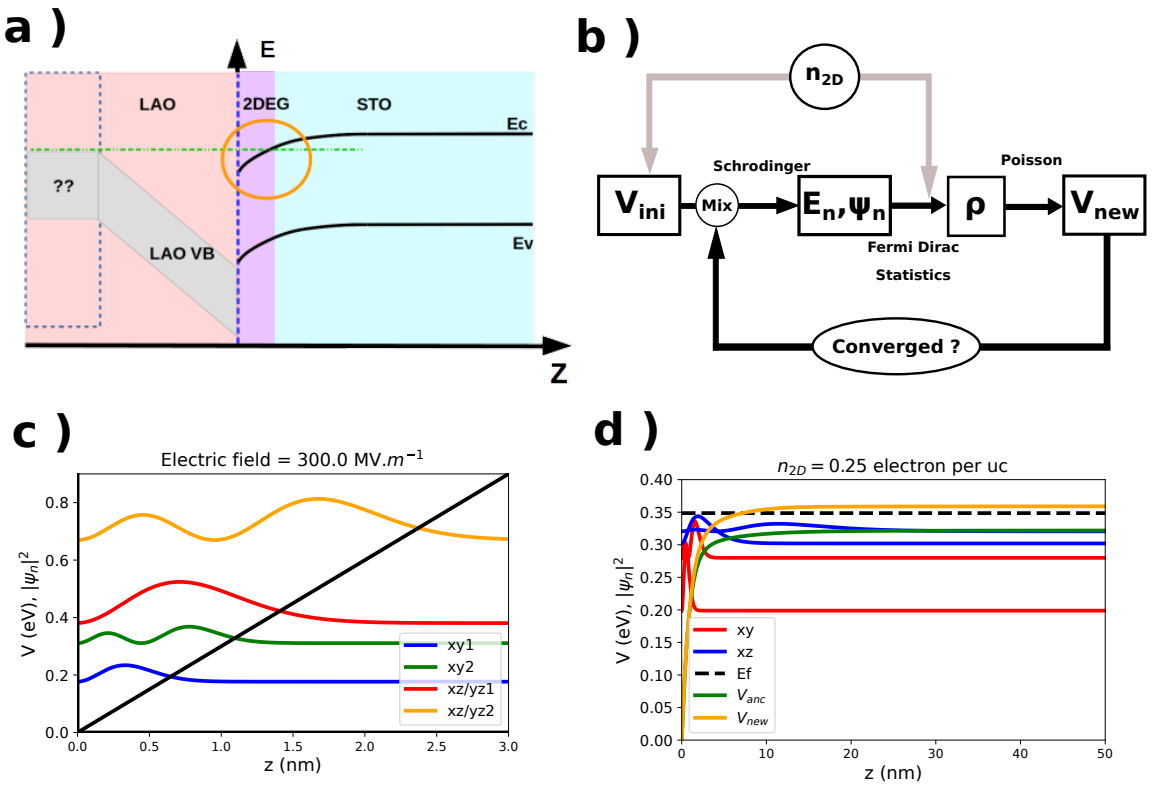

Fig. II.5 a) Band bending at the interface of LAO/STO. b) Flowchart of the Poisson-Schrodinger algorithm. c) Wavefunctions and eigenenergies of a triangular quantum well with an electric field of 300 MV.$^{-1}$. d) 10^{th} iteration of the Poisson Schrodinger loop for an electronic density of 0.25 electron per unit cell.

levels near the interface in order to understand the electrostatic doping of these interfaces and the extension of the 2DEG. We detail the Poisson-Schrodinger approach and the physical ingredients which composes it. We explain how to estimate physical quantities such as the spatial extension of the gas from this framework and study the effect of temperature on the gas from the variation of the dielectric constant of STO upon temperature and electric field.

II.3.1 Electrons in a quantum well

The particle-wave character of electrons has a dramatic effect on its properties when they are confined : as the electromagnetic modes inside a cavity or the acoustic modes of a pipe, a confining potential leads to the emergence of discrete modes with quantized energies. The density $\rho_n(z) = |\psi_n(z)|^2$ of the n^{th} mode is the modulus of the wavefunction ψ_n, solution of

the Schrodinger equation

$$-\frac{\hbar^2}{2m}\partial_z^2\psi_n + V(z)\psi_n(z) = E_n\psi_n \tag{II.7}$$

Where m is the mass of the particle, E_n is the energy of the mode and V is the confining potential of the quantum well. The "particle-in-a-box" problem is a paradigm for quantum wells, and models the spectrum of a particle of mass m inside a 1-dimensional box of length L. The potential is defined by $V(z) = 0$ for $0 < z < L$ and infinite barriers at the boundary $V(0) = V(L) = \infty$, enforcing hard boundary conditions $\psi(0) = \psi(L) = 0$. The solutions of this problem are $E_n = \frac{\hbar^2\pi^2n^2}{2mL^2}$ and $\psi_n(z) = \frac{\pi}{L}\sin(\frac{n\pi z}{L})$ $(n \geq 1)$. Boundary conditions at each extremity of the box can be loosened by replacing the infinite energy barrier with a finite value $V(z) = V_0$ for $z > L$ for instance. In this case, there are only a finite number of solutions determined by the respective values of L and V_0. Another simple model of quantum well is the triangular well with hard boundary conditions at the origin $V(0) = \infty$ and $V(z) = -Fz$ for positive z, with F the amplitude of the electric field associated to the potential. This problem can be solved exactly using the Airy function Ai (details can be found in Appendix A.4), and yields the energies $E_n \approx c_nK$, and eigenfunctions $\psi_n(z) \propto Ai(\frac{z-z_n}{C})$ where $K = \left(\frac{\hbar^2e^2F^2}{2m}\right)^{1/3}$, $C = \frac{2}{3}\left(\frac{\hbar^2}{2meF}\right)^{1/3}$, and $z_n = \frac{E_n}{eF}$ are linked to the zeros of the Airy function $c_n \approx \left(\frac{3\pi}{2}(n-\frac{1}{4})\right)^{2/3}$. The typical energy scales like $(\frac{n^2F^2}{m})^{1/3}$ while the typical length scales like $(\frac{n^2}{mF^2})^{1/3}$: the stronger the electric field, the more confined the electrons are. Electrons with larger masses are more confined by the well, and high-energy levels live away from the interface. The energies and eigenfunctions of the first modes of a triangular well with realistic parameters for the [001] STO surface are shown in Fig. II.5 c, and indeed display the $d_{xy} - d_{xz/yz}$ energy splitting.

II.3.2 The band bending model

The two previous models reveal two important features of electrons in quantum wells : the former has a finite number of bound states and the latter introduces an electrostatic potential smoothly varying in space, allowing to define an electric field. However, there is no notion of screening in these models, making the triangular model unrealistic : the electrostatic potential grows boundlessly as one goes away from the interface. In reality, the electrostatic

potential created by the electronic cloud screens the confining potential, leading to a zero electric field away from the interface : the bulk behaves as in the absence of interface. In semi-conductor heterostructures this phenomenon is called *band bending* [89]. The Poisson equation links the charge density $\rho(\vec{r})$ to the electrostatic potential $V(\vec{r})$ through

$$-\Delta V = \frac{\rho}{\epsilon} \tag{II.8}$$

The electronic cloud screens the electric field $E(z = 0)$ of the interface over a region located near the interface. Away from this region, the density of charge and electric field vanish. Near the interface the bands are bent, meaning their energy is lower than in the bulk, and the charges are trapped in this area.

II.3.3 The Poisson-Schrodinger approach

The Poisson-Schrodinger approach combines two fundamental equations of physics : the Poisson equation relates the density of charge to the electrostatic potential and the Schrodinger equation allows to find the eigenmodes of particles inside an energy potential. The Poisson-Schrodinger approach is suitable to compute the properties of particles trapped in an electrostatic potential : as charged particles create their own potential, they screen the interfacial electrostatic potential and impact the amplitude of their confinement. This problem is solved self-consistently using the algorithm depicted in the flowchart of Fig. II.5 b. We fix the total density of charge n_{2D} of the 2DEG, thus imposing an initial shape for the electrostatic potential of the interface. The Schrodinger equation gives the shape of the wavefunctions and the energies of the states confined by this potential. The Fermi-Dirac distribution and the knowledge of the total 2D density n_{2D} determine the 3D density $\rho(z)$ of electrons away from the interface. Plugging this density back into the Poisson equation determines the electrostatic potential created by the 2DEG to screen the potential of the interface. This new potential is used as a starting point to go back to the first step of the loop. The algorithm is stopped when a convergence criterion is reached (usually a converged potential profile). This problem was initially described in [90] to study Si-based interfaces. It is a standard tool to compute properties of semi-conductor heterostructures [91] and has been used successfully to model the electronic properties of STO-based heterostructures [92, 93, 94].

a) Decoupling of the problem

To tackle the screening of the potential by the 2DEG, the Poisson-Schrodinger approach uses a self-consistent description of the electrostatic potential and the density of the electron gas. It is approximated that the dispersion in the plane of the interface and the confinement of the electrons are decoupled, so that the eigenfunctions of the electrons can be factored

$$\psi^{\alpha}_{n,\vec{k}_{\parallel}}(\vec{r}) = e^{i\vec{k}_{\parallel}\cdot\vec{r}_{\parallel}} u^{\alpha}_{n}(z) \tag{II.9}$$

The $\parallel$ index stands for directions in the plane of the interface. The α and n indices denote respectively the orbital and subband index : for each orbital there are several sublevels confined in the well. The total energy of an eigenstate $|\alpha, n, \vec{k}_{\parallel}\rangle$ is $\epsilon^{\alpha}_{n}(k_{\parallel}) = \epsilon^{\alpha}_{kin}(\vec{k}_{\parallel}) + \epsilon^{\alpha}_{n}$. The n index is analogous to a discrete wavevector in the z direction. The kinetic energy is independent of the subband index n. It can either be computed using a model of free electrons like Eq. I.1, a tight-binding approach like Eq. II.2, or even more refined approximations. The confinement problem can either be solved using a continuum model or a discrete model to determine the spectrum ϵ^{α}_{n} and eigenfunctions u^{α}_{n} inside the well. From the eigenstates of the Hamiltonian $\mathcal{H}_0 = \mathcal{H}_{kin} + \mathcal{H}_{conf}$, we build effective models to include additional contributions $\mathcal{H}_1$ (next-to-nearest neighbor hopping, atomic spin-orbit coupling...). The total Hamiltonian is $\mathcal{H}_{tot} = \mathcal{H}_0 + \mathcal{H}_1$. Its eigenenergies and eigenfunctions are respectively $\epsilon_{\nu}(\vec{k}_{\parallel})$ and $\psi_{\nu,\vec{k}_{\parallel}}(z)$. The ν index has no reason to be of pure orbital or subband character : the eigenfunctions are now generic spinors in the basis of orbitals, subbands and spin of the model. The orbital, subband and spin nature of the level designed by ν can vary with $k_{\parallel}$, which remains a quantum number, and is noted k.

b) Density of States (DOS)

The energies and eigenstates determine the ground state of a system of non-interacting particles. It is mainly composed of the electronic states ν with an energy ϵ_{ν} lower than the Fermi energy E_F, and has the following density matrix $\hat{\rho} = \sum_{\nu,k} f_{\nu k}(E_F)|\nu, k\rangle\langle\nu, k|$, where $f_{\nu k}(E_F) = \frac{1}{1+e^{(\epsilon_{\nu}(k)-E_F)/k_B T}}$ is the Fermi Dirac distribution. At $T = 0$ K, we replace it by the Heaviside function $f_{\nu k}(E_F)_{T=0} = \Theta(E_F - \epsilon_{\nu}(k))$, and in the ground state is only composed

of states with an energy less than E_F. The mean value of an operator $\hat{A}$ is

$$\langle A \rangle = Tr(\hat{\rho}\hat{A}) \tag{II.10}$$

Where the trace is taken over the full Hilbert space. The total number of carriers is computed by taking $\hat{A} = \hat{\mathbb{I}}$, yielding $n_{2D}(E_F) = \frac{1}{a^2} \sum_{E_\nu(k)<E_F} 1 = \frac{N(E_F)}{a^2}$, with $N(E)$ the total number of carriers. In the Poisson-Schrodinger algorithm, we fix the density of carriers n_{2D}. The Fermi energy is chosen so that it matches this density.

The Density of States (DOS) at the Fermi energy is the derivative of the total number of states with respect to the Fermi energy $D(E) = \frac{dN(E)}{dE}$. At $T = 0$ K, it is $D(E) = \sum_{\nu,k} \delta(\epsilon_\nu(k) - E)$ with δ the Dirac δ-function. We define the density of states of band ν as

$$D_\nu(E_F) = \sum_k \delta\left(\epsilon_\nu(k) - E_F\right) \tag{II.11}$$

The Local Density of States (LDOS) is the local version of this quantity $D_\nu^{loc}(E_F, z) = \sum_k \delta\left(\epsilon_\nu(k) - E_F\right) |\psi_{\nu,k}(z)|^2$. Integrating the energy gives the spatial profile of the density as a function of the Fermi energy, noted

$$\rho(E_F, z) = \sum_\nu \int_{-\infty}^{+\infty} D_\nu^{loc}(E, z) f(E_F - E) dE \tag{II.12}$$

Where $f(x) = \frac{1}{1+e^{-x/k_B T}}$ is again the Fermi function. The Fermi energy, the eigenenergies and the eigenfunctions determine the spatial density of the 2DEG in the direction perpendicular to the interface.

The DOS can be computed with various levels of approximation : for a 2DEG with a parabolic dispersion such as Eq. I.1, it is $D_{2DEG}(E) = \frac{\pi\sqrt{m_x^* m_y^*}}{\hbar^2}\Theta(E - \epsilon_0)$, where m_x^* and m_y^* are the effective masses of the gas in the x and y directions, Θ is the Heaviside function and ϵ_0 the energy of the bottom of the band. For free electrons with a pure orbital character, this formula is both correct and easy to use ; effects such as atomic-spin orbit coupling mix the orbital character of bands, and the analytical expression of the dispersion relation no longer has the parabolic form $\epsilon(k) = \frac{\hbar^2 k_x^2}{2m_x} + \frac{\hbar^2 k_y^2}{2m_y}$: Fermi surfaces in the presence of spin-orbit coupling are presented in II.3 c,d. At high fillings, tight-binding energy cut-offs appear and

deform the dispersion relation, leading to Van Hove singularities or other deviations from D_{2DEG} [95]. To compute the DOS of complicated band structures, one samples the BZ with a K-mesh, computes the energies and numerically estimates the density function of these energies. This procedure requires a clever choice of both the density of the K-mesh and of the energy step used to compute the distribution function. A robust method to compute the density of states of a 2-dimensional model at low k uses polar coordinates to describe the Fermi surface with a polar wavevector $k_F(\theta)$. The total density of electrons is equal to the area enclosed by the Fermi surface $n_{2d} = \frac{1}{4\pi^2} \int_0^{2\pi} d\theta \frac{k_F^2(\theta)}{2}$ and the density of states is obtained by differentiating this quantity over E_F. The effective mass of a band ν can be defined by $m_\nu^* = \frac{\hbar^2}{\pi} D_\nu$, yielding a robust definition for bands with complicated and/or anisotropic dispersion. This formula can be easier to evaluate in numerical computations.

c) Poisson equation and screening

The Poisson equation relates the electrostatic potential and the density of charge of the 2DEG. For continuous media, the dielectric constant $\epsilon_r(z)$ can vary with the position, leading to the following form of the Poisson equation

$$\begin{aligned} \partial_z D(z) &= \rho(z) \\ D(0) &= \epsilon_0 \epsilon_r(0) E(0) = -e n_{2D} \end{aligned} \tag{II.13}$$

where $\vec{D}(z) = \epsilon_0 \epsilon_r(z) \vec{E}(z)$ is the displacement field, ϵ_0 is the dielectric constant and ϵ_r the relative permittivity of the material. The displacement field vanishes away from the interface in the absence of any residual electric field (the presence of a backgate voltage is discussed in Section II.4). These two boundary conditions determine the full profile of the potential $V(z)$ as a function of the spatial profile of the density of the 2DEG [96].

d) Self-consistency

To solve the full problem we start from a triangular profile $V(z) = -E_0 z$ with E_0 fulfilling Eq. II.13. The Schrodinger equation determines the density $\rho(z)$ from the initially fixed value of n_{2D}. The Poisson equation determines a new electrostatic potential $V_{new}(z)$. We mix this potential with the former version of the potential to get the new starting point

for the loop through a process called Anderson mixing [97] to avoid numerical instabilities : $V = (1-\xi)V_{anc}+\xi V_{new}$ with $\xi = 0.4$ for the first steps and $\xi = 0.2$ when closer to convergence. The loop stops when the variation of the potential between consecutive iterations is lower than a chosen threshold.

e) Number of bound states

In the band bending picture, the potential flattens when going away from the interface, to the point that it is constant in the bulk of the system, as shown by Fig. II.5 d. In the Poisson-Schrodinger approach, the difference in energy between high-energy levels becomes negligible, and the states cannot be considered as bound states as they extend very far from the interface. The tail of the gas is difficult to model for it is not very affected by the presence of the interface, and its shape depends both on the number of bound states determined at each step of the Poisson-Schrodinger loop and on the system size. Increasing the number of levels or the size of the system is detrimental to the simplicity of the numerical computations, and does not guarantee the accuracy of results. We limit to two or three subbands for each orbital in order to focus on the properties near the interface, studying levels clearly seen in the ARPES measurements of the bare surface of STO. We do not try to realistically compute the shape of the tail of the gas, and make a short discussion about this tail in Section II.4.3. [98] estimates the decay of the tail using the Thomas-Fermi approximation to treat screening away from the interface.

II.3.4 Dielectric constant of STO

Eq. II.13 uses a space-varying dielectric constant. STO is a quantum paraelectric : it behaves as a ferroelectric material with an aborted transition at low temperature due to quantum fluctuations, and its dielectric constant ranges from 24000 at $T = 0K$ to 300 at room temperature. It is proposed that it depends on the electric field inside STO. Near the interface, this electric field can take huge values and have a great impact on the dielectric constant. We use the Landau-Devonshire formalism to model this change of dielectric constant [99]. It assumes that the free energy associated to the electrostatic polarization P has the form

$$F = F_0 + A(T)P^2 + B(T)P^4 \tag{II.14}$$

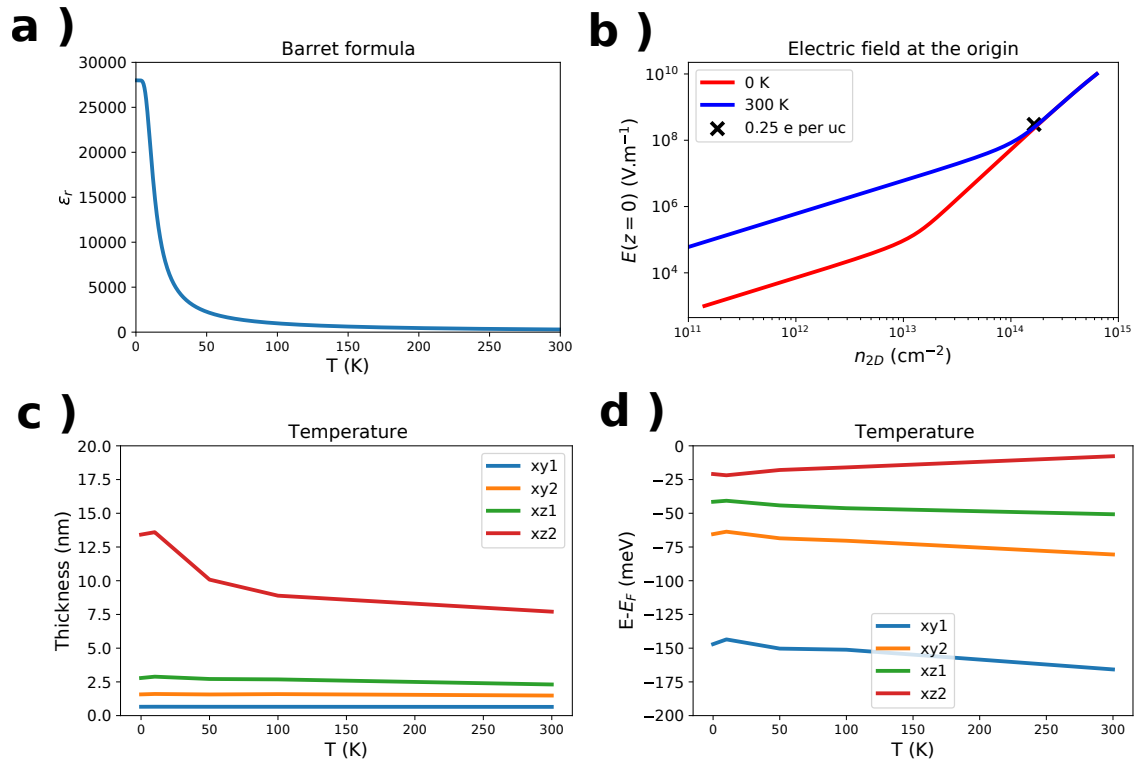

Fig. II.6 a) Dielectric permittivity of STO vs temperature. b) Electric field at the origin as a function of the doping at $T = 0$ K and $T = 300$ K. The density of $n_{2D} = 0.25$ electrons per uc is put as a guide for the eye. c,d) Variations of the thickness and energies $(\epsilon_\nu - E_F)$ of the states with respect to temperature at a fixed density of 0.25 electron per unit cell.

The electric field E is defined by $E = \partial_P F = 2AP + 4BP^3$ and the dielectric susceptibility χ is defined by $\frac{1}{\chi} = \partial_P E = 2A + 12BP^2$. In the $P \to 0$ limit, $\chi \approx \frac{1}{2A(T)}$ only depends on temperature. For large values of P we get $E \approx 4BP^3$ and $\chi(E) \propto E^{-2/3}$. To interpolate between these two limits we take the following susceptibility

$$\chi_{LD}(E,T) = \frac{\chi_0(T)}{\left[1 + \left(\frac{E}{E_0(T)}\right)^2\right]^{1/3}} \tag{II.15}$$

With $\chi_0(T) = \frac{1}{2A(T)}$ and $E_0(T) \propto \sqrt{\frac{A(T)^3}{B(T)}}$. The relative permittivity ϵ_r of the material is $\epsilon_r(E,T) = 1 + \chi_{LD}(E,T)$. The shape of $A(T)$ must respect the aborted ferroelectric transition : a more detailed treatment of the quantum effects involves a quantum-mechanical

$\langle z \rangle$ (nm)	$\langle z \rangle_{gas}$	d^1_{xy}	d^2_{xy}	$d^1_{yz/xz}$	$d^2_{yz/xz}$
[001]	5	0.7	1.6	3	14
[111]	8	3.9	19	3.9	19

Table II.1 Spatial extension of the wavefunctions of the gas for two different orientations at a density of 0.25 electron per unit cell, $T = 0$ K. The column corresponding to $\langle z \rangle_{gas}$ is the mean value $\langle z \rangle_{gas} = \frac{\int dz \rho(z) z}{\int dz \rho(z)}$ with ρ the density of the gas.

treatment of the polarization and can be found in [100], yielding the Barret formula [101]

$$\epsilon_r(T, E = 0) = 1 + \chi_0(T) = 1 + \frac{M}{\frac{T_1}{2} \coth\left(\frac{T_1}{2T}\right) - T_0} \tag{II.16}$$

A good fit for the formula is obtained for $M = 8.4 \times 10^4$, $T_0 = 14K$ and $T_1 = 36K$, yielding $\epsilon_r(T = 0, E = 0) \approx 24000$ and $\epsilon_r(T = 300, E = 0) \approx 300$ as measured in experiments. If B does not depend on the temperature, we estimate the characteristic field $E_0(T) = E_0(T = 0)\left(\frac{\chi_0(T=0)}{\chi_0(T)}\right)^{3/2}$; [92] uses $E_0(T = 0) = 80kV.m^{-1}$. We assume that the form of the dielectric constant is the same for the [001] and [111] orientations for simplicity, though [102] indicates different values at $T = 0$. The evolution of the electric field at the origin is depicted on Fig. II.6 b for two temperatures, where it displays a strong non-linearity above a density threshold depending on the temperature. Fig. II.6 c shows the evolution of the mean spatial extension of the states and of their energies as a function of temperature extracted from Poisson-Schrodinger computations with values of χ_0, E_0 given by Eq. II.16. Only the levels extending away from the interface feel the change in the dielectric constant : near the interface, the electric field does not depend on temperature and the first levels are not affected by the change of temperature.

Using Poisson-Schrodinger computations [103], we compute the spatial extension of each state in the direction normal to the interface using $\langle z \rangle_n = \frac{\langle \psi_n | z | \psi_n \rangle}{\langle \psi_n | \psi_n \rangle}$ and the mean thickness of the whole gas $\langle z \rangle_{gas} = \frac{\int z \rho(z) dz}{\int \rho(z) dz}$ in the [001] and [111] orientations for the same density of $n_{2D} = 0.25$ electrons per unit cell. The results are reported in Table II.1 : the gas is thicker for the [111] orientation, consistently with the lower out-of-plane effective mass of the carriers. Experimentally, the thickness of the gas for the [001] orientation has been estimated to be less than 7 nm by [104] using a conducting-tip atomic force microscope. The thickness of the gas in the [111] orientation is estimated indirectly through a superconducting

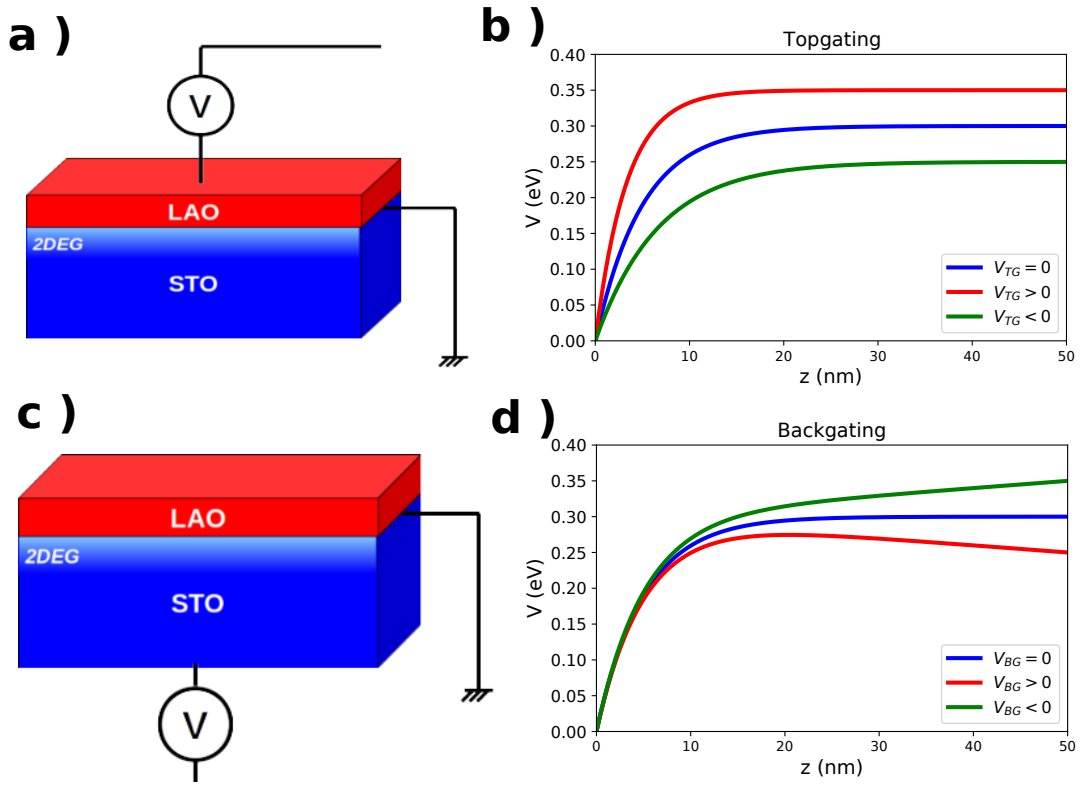

Fig. II.7 a,b) Top gating doping and the corresponding shape of the electrostatic potential. c,d) Backgating doping and the corresponding shape of the electrostatic potential.

length and is around 10 nm [105, 106]. In [107] they estimate the thickness of the gas at the LAO/STO interface at room temperature using inline electron holography : they estimate the thickness to 1 nm for the [001] orientation and to 3 nm for the [111] orientation ; our numerical estimations are consistent with experimental results. It has to be noticed that the thickness of the gas is lower than the thickness of the higher-energy levels because they are less populated. The mean value $\langle z \rangle$ of the gas only describes an average property, but the multi-band nature of the electron gas implies a non-negligible fraction of the carriers can live at a further distance away from the interface.

II.4 Electrostatic doping of TMO heterostructures

In this section, we are interested in modeling the doping of the 2DEG in STO-based interface. For this purpose, we analyze the different geometries which are used in experiments

and we use the potential-density formulation given by the Poisson Schrodinger framework in order to investigate the effects of the doping on the band structure and on the extension of the gas. We also investigate the problem of the leakage of the gas in the back-gating geometry.

II.4.1 Top- and back-gating geometries

Electrostatic doping is often modeled as a mere shift of the Fermi energy, with the underlying assumption that doping the system does not affect its band structure. However, this is not always true : in correlated systems, band structure can change upon doping. In the experiments presented in Fig. II.9, doping is achieved by electrostatic means, using a gate voltage. This can be done in two different geometries : the gate can be on top of the interface, close to the electron gas (as in regular MOS-FET devices), or can be under the bulk of the substrate, away from the gas. The two geometries and associated potentials are shown on Fig. II.7. In the top gate geometry, the voltage modifies the electric field at the origin. This changes the boundary conditions of Eq. II.13 and thus the density of charge of the electron gas n_{2D}. Fig. II.8 a-b shows the effects of top gating on the band structure and the spatial extension of the gas. The gaps between subbands change with doping and so does the population of these bands : the lower energy levels are more affected. The thickness of the states also diminishes with doping, and this effect is enhanced for states extending away from the interface.

The backgating geometry is more complicated to model [108]. In this configuration, the voltage can go up to several hundreds of volts. Depending on the sign of this backgate voltage, the topology of the electrostatic potential changes. For negative voltages, the slope of the potential is positive away from the interface, so the confined charges are only in the region near the interface. For positive backgate voltages the slope of the potential is negative when going away from the well. In a band bending picture, the charges are not guaranteed to be confined : the tunnel effect suggests that charges might escape outside of the well. The leakage of charge affects more the states composing the tail of the 2DEG, which live away from the interface. Experiments show that there remains a 2DEG under the application of a positive backgate voltage, though some leaking is indeed likely [93]. We model the application of a backgate voltage on the potential landscape and the density of the 2DEG using the Poisson-

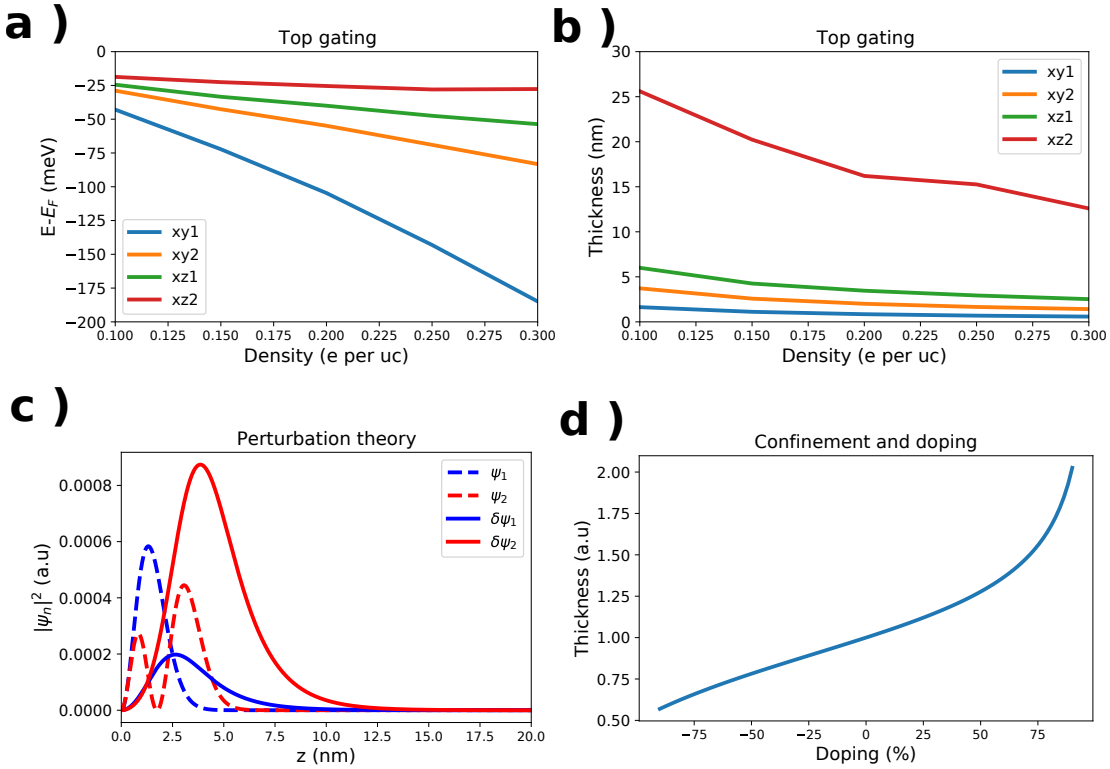

Fig. II.8 a,b) Thickness of the gas and energy of the subband minimum as a function of the density of the gas when doping in a top gating geometry. c) Perturbation of the eigenfunctions on a backgating configuration, due to bound states (plain lines) or continuum states (dashed lines). d) Thickness of the gas as a function of the percentage of doping.

Schrodinger approach. Bound states stay confined at least for reasonable gate voltages. We treat the backgating problem using two complementary approaches : one treats backgating as a perturbation to the Poisson Schrodinger approach and the other studies the stability of a 2DEG under the application of a backgating voltage.

II.4.2 Perturbation theory

We model the backgate voltage by adding an extra potential $V_g(z) = -F_g z$ to the potential of the well. Without it, the well is described by $V(z)$, a total density of the 2DEG n_{2D}, and levels $(E_n^\alpha, \psi_n^\alpha)$. Perturbation theory yields the following corrections to the energies

$$\delta E_n^\alpha = eF_g \langle z \rangle_{\alpha,n} \tag{II.17}$$

Where $\langle ... \rangle_{\alpha,n}$ denotes the mean value for the state with orbital and subband indices (α, n). Different orbitals and subbands are not equally affected by the backgate voltage : states living away from the interface are more impacted is it in term of energies or eigenfunctions. The variations of eigenstates are

$$\delta|\alpha, n\rangle = eF_g \sum_{(\beta,m)\neq(\alpha,n)} \frac{\langle \beta, m|z|\alpha, n\rangle}{E_n^\alpha - E_m^\beta}|\beta, m\rangle \tag{II.18}$$

Summing over both confined states and unfilled bulk states that belong to the conduction band. To evaluate the impact of these states, we consider that the states are particles in a box of length $L >> l_{well}$ (eigenenergies and eigenfunctions are described in Section II.3.1). Corrections of the energy and thickness of the states are proportional to the backgate voltage. Different orbitals and subbands are not affected equally by the electric field, showing that electrostatic doping is not a mere shift of the Fermi energy, but also affects the band structure of the 2DEG. A key quantity to streamline this behavior is the mean value of the position with respect to the interface. The corrections to the wavefunctions are shown in Fig. II.8 c. For a thickness $d = 10$ nm, a backgate voltage $V_g = 200$V and a thickness of the substrate $L = 0.5$ mm, the correction in energy is $E_{pert} = \frac{200\times10^{-8}}{5\times10^{-4}}eV = 4$ meV, while for states with an extension of around 1 nm the correction is lower than 1 meV. If the Fermi energy remains constant, the states living away from the interface are more doped by the application of a backgate. These corrections assume that the additional electric field created by the backgate voltage is constant over the whole STO part, while it might be changed in the vicinity of the interface.

For the [001] orientation, we compute the corrections to the wavefunctions from Eq. II.18 and the corrections for the states d^2_{xy} and d^1_{xz}, which are close in energy. Two types of terms emerge from perturbation theory : one the one hand, the corrections coming from the overlap between these two states are shown in dashed line in Fig. II.8 c. On the other hand, the corrections due to the overlap with bulk states are plotted using solid lines, and have a similar amplitude to the inter-subband contribution. States living away from the interface are more affected by states of the continuum. The computations are done for a backgate voltage of $V_g = 200$ V : even with this large value, the corrections to the wavefunctions are weak (the order of magnitude of $\frac{\delta\psi^2}{\psi^2}$ is 10^{-3}). They are significantly enhanced for the highest

level d^2_{xz} (not shown), to the point that perturbation theory is not valid anymore. The same situation occurs for the second subband in the [111] orientation, meaning that perturbation theory is not valid in this setting either.

II.4.3 Stability of the gas

We study the stability of the gas against backgating. The leakage of carriers has been measured and modeled in [93]. If high-energy levels can indeed flee due to the backgate voltage, the 2DEG is not emptied from its carriers. From the band bending approach, we understand that the 2DEG screens the polar imbalance due to the interface. If the backgate voltage indeed imposes a negative slope of potential away from the interface, the presence of the 2DEG close to the interface guarantees that the charge is indeed screened. The leakage of charge due to the shape of the potential is only a first level of approximation : this flee would be compensated by feedback effects on the gas. Using the parametric form $\rho(x) = Q\lambda x e^{-\lambda x}$ for the density, we compute the electrostatic energy associated with the presence of the well (details of the computation can be found in Appendix A.6). The thickness of the gas increases with electrostatic doping in a controlled way : in Fig. II.8 d we show the evolution of the thickness as a function of the percentage of excess charge brought by backgating. It increases smoothly with doping upon reaching the limit of 100 percents doping, where the gas breaks down and charge completely leaks. For the LAO/STO interface, this process affects primarily the high-energy levels, which reach the threshold of leakage quicker than the lower levels which remain in a stability range of doping.

II.5 Hall measurements in STO heterostructures

In this section, we are interested in the interpretation of Hall measurements in TMO heterostructures, in the light of our previous discussion of the band structure in terms of subbands and multi-orbital conduction band. We first review the principle of Hall measurements, before explaining the role of quantities such as the mobilities and density of states in the computation of the longitudinal and Hall resistances. From the estimation of these quantities in the multi-band case, it is possible to make comparisons with the 2-band model interpretation of Hall experiments. We try to explain the unusual behavior of the Hall

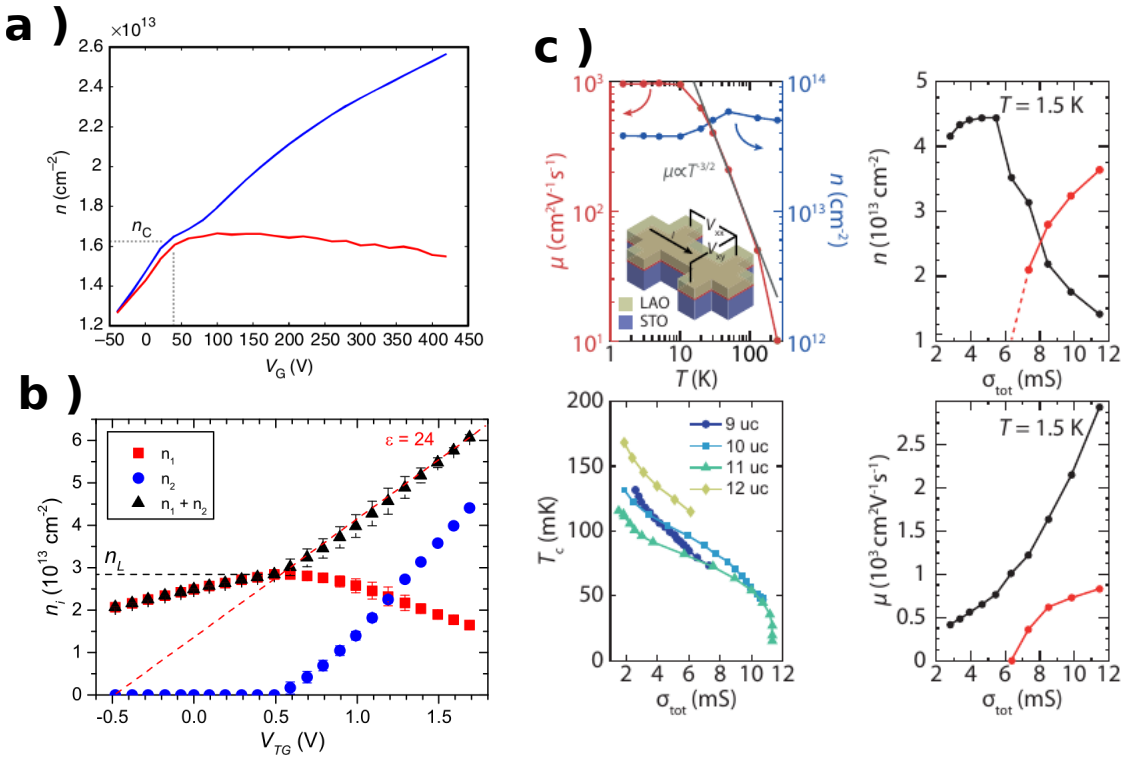

Fig. II.9 a) Evolution of the populations of carriers with respect to backgate voltage extracted from Hall data on the [001] orientation of the LAO/STO interface (taken from [109]). A Lifshitz transition occurs above a certain threshold. b) Hall data on the [001] orientation of LAO/STO, top gating, extracted from [94]. c) Hall measurements on the [111] orientation of LAO/STO, extracted from [74].

measurements in TMO heterostructures upon doping by a discussion on the scattering time and the multi-orbital character of the conduction band. Another explanation of this unusual behavior is sketched in the next section and involves interaction at the mean-field level.

II.5.1 Experiments

The Hall Effect is the creation of a transverse current in a conductor under the application of both a voltage difference and a magnetic field to a material. The Lorentz force exerted by the magnetic field deviates the trajectory of electrons and induces a transverse conductivity. In standard Hall Effect experiments, the longitudinal and transverse resistance of a Hall bar (the geometry is shown in Fig. II.9 c) are measured as a function of an out-of-plane magnetic field. The variations of these two resistances with the magnetic field can be traced back to

the number of carriers and to the mobilities of the electrons of a 2DEG using simple models for the band structure. In a 2DEG, the longitudinal and transverse resistances of a sample as a function of the magnetic field read

$$\begin{aligned} \rho_{xx} &= \frac{1}{nq\mu} = \frac{1}{\sigma_0} \\ \rho_{xy} &= \frac{B}{nq} \end{aligned} \tag{II.19}$$

Where n is the number of carriers, q is the charge of the carriers (positive for holes and negative for electrons), and μ is the mobility of the carriers, defined by $\vec{v} = \mu\vec{E}$. A derivation of the formulas of this section can be found in Appendix A.5. The slope of the Hall resistance $\rho_{xy}(B) = \rho_H(B)$ yields an estimation of the number of carriers. Although deviations from a linear behavior can occur in multiband systems, non-linear signatures in the Hall resistance can be fitted using a two-band model [92]

$$\begin{aligned} \rho_{xx} &= \frac{(\sigma_1^0 + \sigma_2^0) + (\sigma_1^0\mu_2^2 + \sigma_2^0\mu_1^2)B^2}{(\sigma_1^0 + \sigma_2^0)^2 + (\sigma_1^0\mu_2 + \sigma_2^0\mu_1)^2B^2} \\ \rho_{xy} &= \frac{(\sigma_1^0\mu_1 + \sigma_2^0\mu_2) + (\sigma_1^0\mu_2 + \sigma_2^0\mu_1)\mu_1\mu_2B^2}{(\sigma_1^0 + \sigma_2^0)^2 + (\sigma_1^0\mu_2 + \sigma_2^0\mu_1)^2B^2}B \end{aligned} \tag{II.20}$$

Where $\sigma_i^0 = n_i q_i \mu_i$ is the conductivity of the band i, populated by n_i carriers with a charge q_i and a mobility μ_i. A simultaneous fit of $\rho_{xx}(B), \rho_{xy}(B)$ yields the mobilities and number of carriers of each species. A simpler analysis takes the two limits of small and large magnetic field : for small magnetic fields, only the high mobility carriers participate to the Hall Effect while at high magnetic fields, all the carriers are bringing their contributions. The low-mobility carriers are defined as the difference between results at high and low field.

As the metallic interface is buried below the LAO layers, ARPES measurements of the LAO/STO interface have a bad resolution and are hard to interpret [110]. Hall measurements probe the characteristics of the carriers and allow to see whether the t_{2g} model accurately describes it. The ability to change the number of carriers via electrostatic doping in a Hall bar configuration gives a knob to probe the system at different fillings. Hall measurements on the [001] [111, 109, 92, 112, 94] and [111] [74, 106] orientations of the LAO/STO interface show signatures of multi-band transport. In particular, [109] reports a Lifshitz transition in the [001] orientation of LAO/STO. Fig. II.9 a shows that the number of carriers as a

function of backgate voltage changes of behavior above a voltage threshold : the number of high-mobility carriers is the red curve while the total number of carriers is the blue curve, and one can see that they move away from one another above a voltage $V_G \approx 50V$. Measurements on various samples lead to different voltage thresholds : to compare different samples it is better to use quantities such as the density of carriers or the sheet conductivity. Similar measurements for a top gating configuration are shown on Fig. II.9 b and are extracted from [94]. Experiments on the [111], orientation taken from [74], are shown on Fig. II.9 c. They also show the emergence of a second species of electrons above a critical voltage in a backgating configuration. We first apply simple models to match these behaviors, but in these experiments it seems that the doping of the system with a new type of carriers is made at the expense of the first population of carriers : the number of high mobility carriers decreases with doping, which is unexpected as doping the system should only bring new carriers. For the [001] orientation, the presence of electronic correlations has been suggested to explain this behavior [113]. We perform a similar analysis for the [111] orientation to try and understand the measurements of [74].

II.5.2 Mobility of a 2DEG

The electronic mobilities are affected by disorder through a scattering time τ. Mathiessen rule states that the scattering mechanisms are additive in terms of rate $\omega = \omega_{disorder} + \omega_{e-e} + \omega_{e-ph} + ...$ meaning $\frac{1}{\tau} = \sum_{scat} \frac{1}{\tau_{scat}}$. For random impurities, the Born approximation allows to estimate the scattering time $\tau^{-1} = \frac{2\pi}{\hbar} n_i V_0^2 D(E_F)$, with n_i the density of impurities, V_0^2 the square of the amplitude of the disorder potential and $D(E_F)$ the density of states at the Fermi energy. As the DOS is proportional to the effective mass of the electrons, the scattering time should be shorter for heavy electrons. This gives a result which is consistent with the Drude model $\mu = \frac{q\tau}{m^*}$ where τ is the scattering time and m^* is the effective mass of the electron. Because of the interface, a special form of disorder, called surface roughness, emerges from the compounded action of disorder and confining potential in the vicinity of the interface. A simple model for this phenomenon can be found in [114] : the mobilities scale with the inverse of the square of the mean electric field the states feel. Using the results of Section II.3.1, mobilities scale like the cube of the mean position of the state, significantly lowering the mobilities of the lowest subband which lives close to the interface. In the LAO/STO system,

$d_{xz/yz}$ electrons live away from the interface and have a notoriously longer scattering time.

II.5.3 Numerical results

We compute the band structure of a simplified 6-band t_{2g} model and infer the density of carriers and mobilities of the bands. In this simplified model, in order to understand the effects of bands with a different orbital character on the Hall response, we ignore the contribution of the lower d_{xy} subband : due to disorder, it has a lower mobility and its contribution is smaller. If the three bands are independent with a single relaxation time, one gets $n_\nu(E_F) = \frac{\pi m_\nu}{\hbar^2}\Theta(E_F - \epsilon_\nu)(E_F - \epsilon_\nu)$ at low fillings, $\mu_\nu = \frac{e\tau_\nu}{m_\nu}$, with $m_\nu = \sqrt{m_\nu^x m_\nu^y}$ the DOS effective mass, ϵ_ν the bottom of the band ν and τ_ν its scattering time. Unfortunately, this approximation does not explain the measurements presented in Fig. II.9 since all the populations increase when doping the system. This model can be refined by adding spin-orbit coupling and estimating the mobilities using $\mu_i = \frac{e\tau_\nu}{m_\nu^*}$ with $m_\nu^* = \frac{\hbar^2}{\pi}\frac{dn_\nu}{dE_F}$ and a constant scattering time $\tau_\nu = \tau_0$. This yields the curves in Fig. II.10 a-c for the [001] orientation : the black curve represents the total quantities (or mean mobility), while the red, blue and green curves are the first, second and third groups of spin-degenerate bands. Above the Lifshitz transition, a new species of electrons appears, and the variations of the population of the red band with Fermi energy changes of slope, corresponding to the enhanced DOS of the heavy carriers. The mobilities, computed with the constant relaxation time approximation $\mu_\nu = \frac{e\tau_0}{m_\nu^*}$, show that the system switch from high to low mobility because the DOS mass of the $d_{xz/yz}$ is heavier. It is unclear whether the decrease of the total conductivity above the Lifshitz transition is a physical characteristic of the system or is revealing flaws of this simple numerical model. In particular, the scattering time due to surface roughness is expected to be different for each orbital because they do not live at the same distance from the interface, and the mobilities shall be changed. Estimating μ_ν is complicated since it involves various mechanisms and can also be influenced by anisotropy effects : heavy bands have anisotropic dispersion relations which complicates the computation of scattering time. Interband couplings can also change the total scattering time of a band : the mixed orbital nature of bands (due to atomic spin-orbit coupling for instance) can mix the scattering time of the orbitals involved and further complicate the estimation of mobilities.

An analysis involving several types of carriers requires a substantial difference between

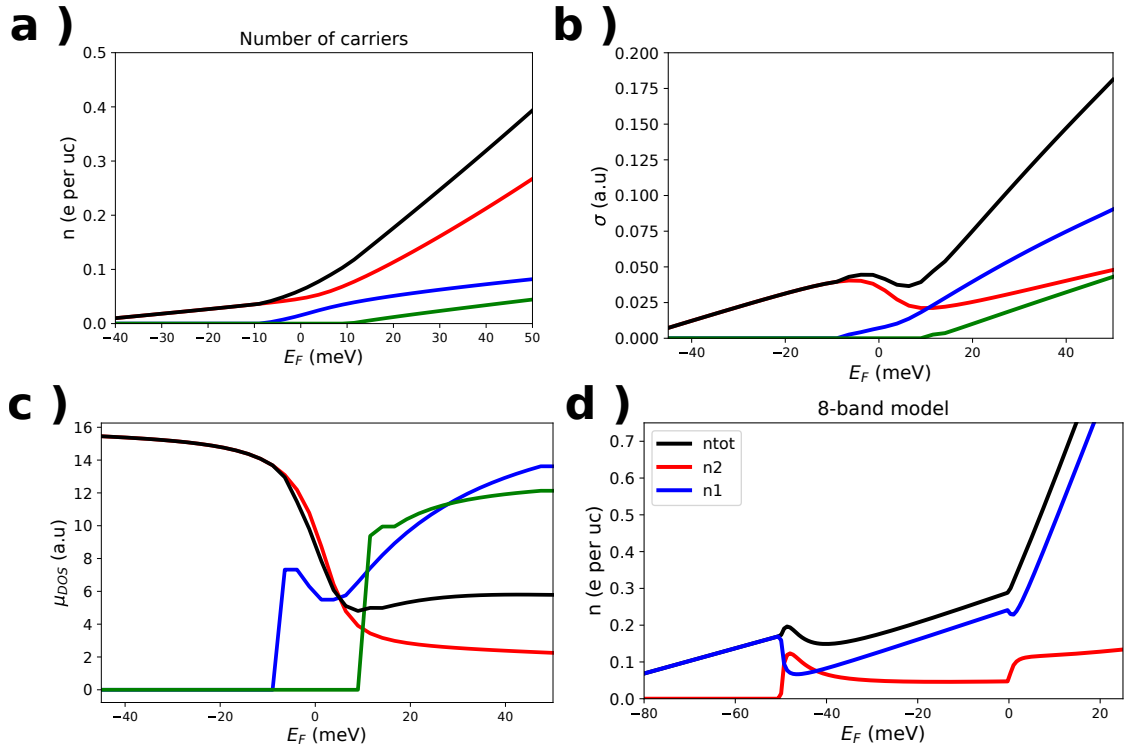

Fig. II.10 a-c) Number of carriers, conductivity and mobilities as a function of the Fermi energy for a 6-band model of the [001] interface of STO. The red blue green color code is similar to the colors of the band structure depicted on Fig. II.3 a. d) Computations of the density of carriers via non linear Hall effect of a simplified 8-band model of the [001] interface of STO.

the mobilities to precisely observe the transition to the nonlinear regime. The characteristic magnetic field of this transition verifies $B_c\mu_2 \approx 1$ if μ_2 is the lowest mobility. It corresponds to the transition from the highly diffusive regime $B\mu = \omega_c\tau << 1$ to a regime in which the electrons move following cyclotron orbits $\omega_c\tau >> 1$. The typical order of magnitude used to describe mobilities is $10^3 cm^2V^{-1}s^{-1}$, corresponding to a magnetic field of $B_c = 10$ T. In systems with several types of carriers, to observe the response of a band, the magnetic field must exceed this critical field, hindering the observation of very low mobility carriers and the resolution of fine structure in the distribution of mobilities. It can also be difficult to interpret measurements in terms of high and low mobility if there are more than two types of carriers. We discuss other limitations to the interpretations of Hall experiments in Appendix A.5. [115] partially discusses some corrections for the [111] interface ; the multi-

orbital nature of the wavefunctions should affect the mobility. In STO, using a scattering time of order $\tau = 0.5ps$ [52] and $m^* = 0.7m_e$ gives $\mu \approx 120cm^2.V^{-1}s^{-1}$ for d_{xy} carriers ($B\mu \approx 0.12 << 1$ for $B = 10$ T), while the mobilities for $d_{xz/yz}$ levels is expected to be higher by one or two orders of magnitude.

There are known discrepancies between the density of carriers determined by ARPES and by non-linear Hall experiments. ARPES estimates a density of carriers of around $1.6 \times 10^{14}cm^{-2}$ (0.25 electrons per unit cell [83]), while Hall measurements only yield densities of several $10^{13}cm^{-2}$. This discrepancy is often explained by the presence of frozen carriers that do not participate in the transport. Surface roughness can explain why the orbital and subband character of the states affects transport properties. Fig. II.10 d shows the results for an 8-band model (2 d_{xy} and 1 $d_{xz/yz}$ levels times spin degeneracy) with parabolic dispersion for each band : the two sets of d_{xy} subbands respectively begin at $E_F = -100/-50$ meV, while the $d_{xz/yz}$ begin at $E_F = 0$ meV. The effective masses are $m_{xy} = 0.7m_e$ and $m_{xz/yz} = \sqrt{0.7 \times 14} \approx 3m_e$, and the corresponding mobilities are $\mu^1_{xy} = 70cm^2V^{-1}s^{-1}$, $\mu^2_{xy} = 700cm^2V^{-1}s^{-1}$, $\mu_{xz/yz} = 3 \times 10^4cm^2V^{-1}s^{-1}$. Using formulas from Appendix A.5, we compute the corresponding Hall conductivity $\rho_{xy}(E_F, B)$ for B ranging up to 10 T. We then determine $n_{tot} \propto \frac{1}{\frac{dR_{xy}}{dB}}(B = 10T)$ (total density) and $n_1 \propto \frac{1}{\frac{dR_{xy}}{dB}}(B = 0T)$ (high mobility carrier density). $n_2 = n_{tot} - n_1$ is the low-mobility carrier density. The results show that the contributions of new bands with a higher mobility dramatically change the determination of the total density of carriers. In particular, the density associated with the low mobility carriers of the lowest d_{xy} subband is vastly underestimated. The situation is similar after the Lifshitz transition, which can be explained by the values of the mobilities compared to the maximum magnetic field : for the 2 d_{xy} levels, the criterion $\mu B > 1$ is not fulfilled, and the mobility of the lowest energy level is generally as low as $\mu B << 1$. For instance, when $B = 10$T, we have $\mu^1_{xy}B = 7 \times 10^{-2} << 1$, $\mu^2_{xy}B = 7 \times 10^{-1} < 1$ and $\mu_{xz/yz}B = 3 >> 1$. This might help explain the discrepancy between ARPES and Hall experiments.

II.6 Electronic interactions in TMO heterostructures

Electron-electron interactions can change the ground state of the system : in a Mott insulator, the ground state goes from metallic to insulating at half-filling, where the correlations

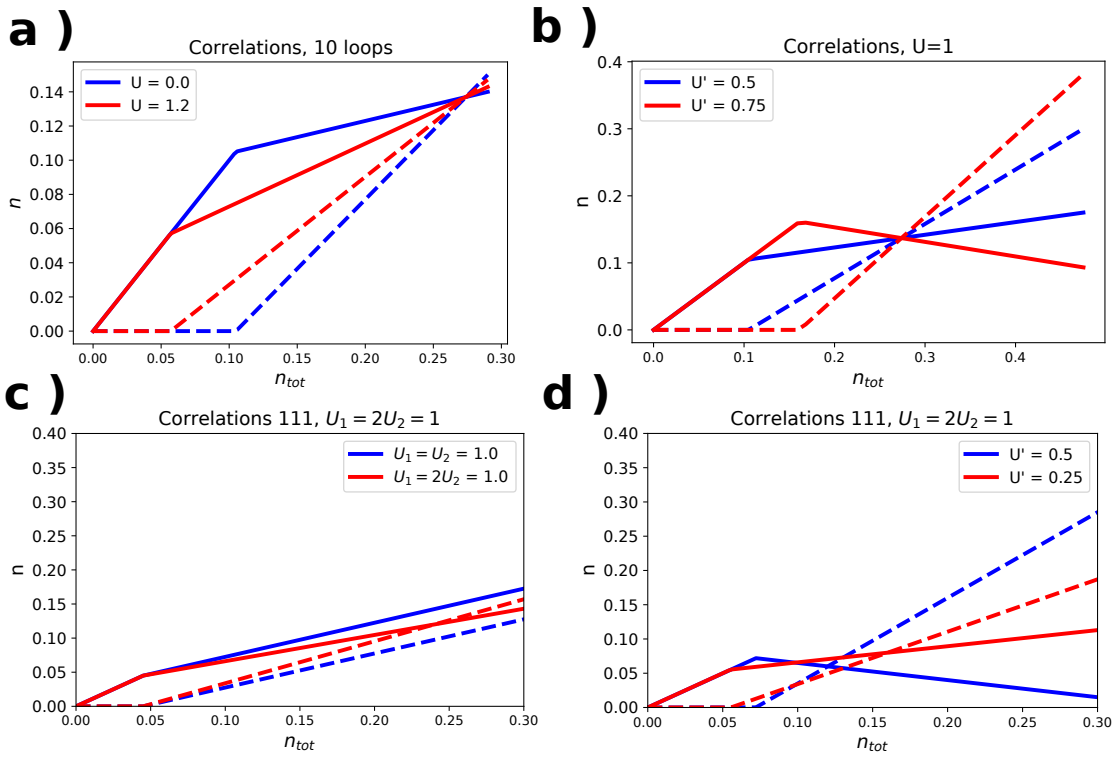

Fig. II.11 a) Density of d_{xy} (solid lines) and $d_{xz/yz}$ (dashed lines) carriers as a function of the total density of the gas in the presence and absence of a Hubbard-like interaction U, for a [001] orientation of the surface of STO. b) Effect of the introduction of an interband Hubbard interaction U' in the [001] orientation. c) [111] orientation and the effects of a differentiated interaction $U_1 = 2U_2$ on the populations of the subbands. The solid and dashed lines respectively represents the first and second subbands. d) [111] orientation and the effects of an interband interaction U'.

become so strong that it forbids a double occupancy of sites and freezes charge transport. Mott insulators differs from regular insulators : if the charge sector is completely frozen, fluctuations due to the spin degree of freedom are still allowed. Correlations can induce pairing of electrons inside the system : forming Cooper pairs, materials become superconducting, and charge transport occurs without dissipation. Interactions are described as a purely local on-site effect using the following Hubbard Hamiltonian

$$\mathcal{H}_{int} = U \sum_i n_{i,\uparrow} n_{i,\downarrow} \tag{II.21}$$

Where $n_{i\sigma}$ is the density operator at site i of spin species σ and U is the Hubbard constant, which represents the amplitude of the interactions. This Hamiltonian cannot be exactly solved in realistic problems, and a number of approximations are used to understand its properties.

In this Section, we focus on a mean field treatment of interactions in order to evaluate their impact in the LAO/STO interface, because interactions are thought to be weak. The filling of the systems we consider are very low : 0.5 electron per unit cell is an overestimation of the highest filling of these systems, and the electronic population is shared by different subbands and orbitals, so that the individual filling of each band is very low. We consequently stay at the mean field level in the following treatment of electronic interactions. We do not include an exchange term J in the following analysis because we do not try to understand magnetic properties. The effect of the confinement of the wavefunction in the direction perpendicular to the interface on the amplitude of the interaction is discussed in the Appendix A.7. This section formulates an interpretation of the experiments of [74] presented in the previous section under the light of a simplified model of electronic correlations in STO-based systems.

II.6.1 Interactions in the [001] orientation

It has been proposed in [94, 113] that interactions are responsible for the inversion of the populations of carriers occurring when doping the system. Using a model the [001] orientation of STO including take two d_{xy} and one $d_{xz/yz}$ subbands with the confinement gaps and effective masses of STO, we compute the effects of the electronic correlations on the filling of the system. We compare the fillings of subbands with and without the addition of a Hubbard interaction, using parabolic dispersion relations. To do so, we compute the population of each subband in the absence of interactions n_ν^0, add the interaction energy $E_\nu^{int} = Un_\nu^0$ to each band, compute the renormalized Fermi energy E_F and corrected populations of the subbands n_ν^1, so that the total population n_{2D} is equal to the one without interactions $\sum_\nu n_\nu^0 = \sum_\nu n_\nu^1$. This procedure must be achieved in a self-consistent manner to get subband densities, so that the densities n_ν^U in the presence of interactions are consistent with the interaction energies Un_ν^U ; this is achieved using a self-consistent loop and a Anderson mixing scheme. Fig. II.11 a shows the effect of a the Hubbard interactions : the solid lines show the density

of d_{xy} carriers while the dashed lines show the density of $d_{xz/yz}$ carriers as a function of the total density of the gas, for $U = 0$ and $U = 1.2$. In the presence of correlations, the $d_{xz/yz}$ subbands are populated earlier, lowering the energy of the Lifshitz transition, and the renormalization of the slope might be interpreted as a renormalization of the effective masses of the bands. No decrease in the density of the d_{xy} carriers can be observed with only an intraband Hubbard term, and the addition of an interband Hubbard term U' as in [113] is necessary to observe a decrease. This model is a variation of the Hubbard-Kanamori Hamiltonian [116], a multi-orbital version of the Hubbard model whose form is detailed in Appendix A.7. The presence of this inter-orbital Hubbard term U' and the difference in the effective masses of the orbitals play in concert to induce a decrease of the density of the d_{xy} band above a certain threshold. The addition of the term U' can lead to the decrease in the density of the d_{xy} orbitals, as shown in Fig II.11 b, and can be explained by a mean field treatment of the Hubbard-Kanamori Hamiltonian detailed in Appendix A.7.

II.6.2 Interactions in the [111] orientation

[113] assumes that the Hubbard U does not depend either on the orbital nor on the subband index. In Appendix A.7 we derive that interactions can have an orbital and subband selective effect in quasi-2DEG. States living closer to the interface are more impacted by electronic correlations than those living away from it : in the [001] orientation of the crystal, the d_{xy} orbitals are more penalized than the $d_{xz/yz}$ ones. Subbands live at a different distance from the interface, changing the impact of electronic correlations : the closer the state lives from it, the more it is penalized by the interaction energy. For the [111] orientation, the orbitals have the same effective masses and are all equally affected by the electrostatic confinement. As the amplitude of electronic interactions is affected by the proximity of the electronic states from the interface, the effects of interactions vary depending on the distance from the interface. As explained in Appendix A.7, interactions can have a differentiated impact on subbands, since they do not spread over the same distance away from the interface. Fig. II.11 c shows the effect of interactions with a different Hubbard constant on each subband, taking $U_2 = \frac{U_1}{2}$. This model has two subbands sharing the same effective mass and split by an energy gap, ignoring the multi-orbital nature of the 2DEG. If $U_1 = U_2$, there can be no inversion of subband populations : the correlations merely change the value of the gap

between subbands. Taking different values for the Hubbard constant of subbands allows for an inversion of the population of subbands. However, as in the [001] orientation, one cannot observe a decrease of the population of the lower subband as in the experiments shown in II.9 c from [74]. Only the addition of a U' term as in [113] can induce a decrease in the population of the lower subband, as shown in Fig. II.11 d, where we take $U_1 = 2U_2 = 1$, and U' takes two different values : for the lowest values, there is no decrease in the populations, but if it is large enough, a decrease can be observed. Why the inversion involves distinct values of U_1 and U_2 is explained in Appendix A.7. If this effective model indeed induces an inversion of the bands consistent with the experiments, the likelihood of the values of the U parameters is debatable.

The decrease of the population of the lower subband might also linked with the short-lived electronic states near the interface : in the highly diffusive regime $\mu B = \omega_c \tau << 1$, the non-linear Hall signature is less clear and the observation of the low-mobility carrier is blurred by disorder, yielding wrong estimations of transport parameters. The arrival of a new population of carriers in the experiments can either be due to a new subband or to the trigonal and spin-orbit split levels inside one of the subbands. In [115], the authors propose that the [001] orientation is more affected by electronic correlations and that that the unusual transport properties of the [111] orientation are due to the strong anisotropy of dispersion : a model of the scattering time in the six-fold symmetric Fermi surface might indeed lead to very distinct scattering times inside the same confinement level. The factor 5 between the mobilities of the bands in Fig. II.9 is also consistent with the presence of multiple levels in the well, using a surface roughness model for the mobilities of the subbands.

III – Topological properties in condensed matter

> I call our world Flatland, not because we call it so, but to make its nature clearer to you, my happy readers, who are privileged to live in Space.
>
> Edwin Abbott Abbott,
> *Flatland : A Romance in Many Dimensions*

III.1 Introduction

The complex interplay between crystalline and orbital degrees of freedom can lead to unusual electronic properties. Far from the ideal picture of the free electron gas, exotic phases can emerge because of broken symmetries. The Nobel Prize of 2017 has been awarded to Kosterlitz, Thouless and Haldane for the discovery of topological phase transitions [24, 25, 26, 27]. The recent experimental observations of the Quantum Anomalous Hall Effect (QAHE) and Quantum Spin Hall Effect (QSHE) [28, 29] have shed light on the dramatic effects that the geometry of the band structure can have on the ground state of a material. The concept of Topological Insulators (TI) illustrates such a geometry-driven change of nature of the ground state : at the edges of these bulk insulators, conducting states can emerge and carry a ballistic current immune to disorder [30, 31]. These phenomena are a consequence of broken symmetries and are related to topological invariants of band structures [32, 33]. These new states of matter are of a great interest for applications because of both their robustness and

their immunity to potential (non-magnetic) disorder. The QSHE is intimately related to non-trivial spin properties emerging from spin-orbit coupling and inversion symmetry breaking. In superconductors it is again the interplay between the quasi-particles and the spin-orbit coupling that may give rise to the emergence of Majorana fermions [34, 35, 36]. Transition Metal Dichalcolgenides (TMD), which are 2d graphene-like materials with additional couplings, also provide a nice example of systems where topological effects can be expected [37, 38]. TMO heterostructures gather all the usual suspects leading to topological properties [39, 40] : inversion symmetry breaking, spin-orbit coupling, multi-orbital properties and sometimes magnetism or even superconductivity. They should provide a nice platform to study these topological effects.

First, we describe two of the paradigmatic systems where the topology of band structures has a dramatic influence on the electronic properties of solids : the Chern insulator and the Quantum Spin Hall Effect. From these experimental discoveries, we dive into the mathematical framework underlying the concepts of topology in condensed matter physics. We unveil the key role played by the geometry of the wavefunctions inside the Brillouin Zone to explain the concepts of topological invariants, with a particular focus on the concept of Berry curvature. To continue our journey, we turn to more sophisticated topological invariants such as the spin curvature. We discuss the link between these geometrical quantities and the experimental probes available to observe these effects. Eventually, we discuss how these concepts can be applied to the case of metallic systems, which are our main interest in the rest of the thesis.

III.2 Topological insulators and Quantum Hall Effect

Topological insulators are hard to define since they look like standard insulators : their bulk is insulating with a finite energy gap separating their valence and conduction bands. To appreciate what makes them special, *topological*, one has to consider interfaces between a topological and a *trivial* insulator. Something dramatic indeed happens in this case : the boundaries of the topological insulator (TI) become metallic and host conductive states behaving as ballistic particles which do not feel disorder. These peculiar states only reside close to the edges of the sample and quickly decay inside the insulating bulk of the material.

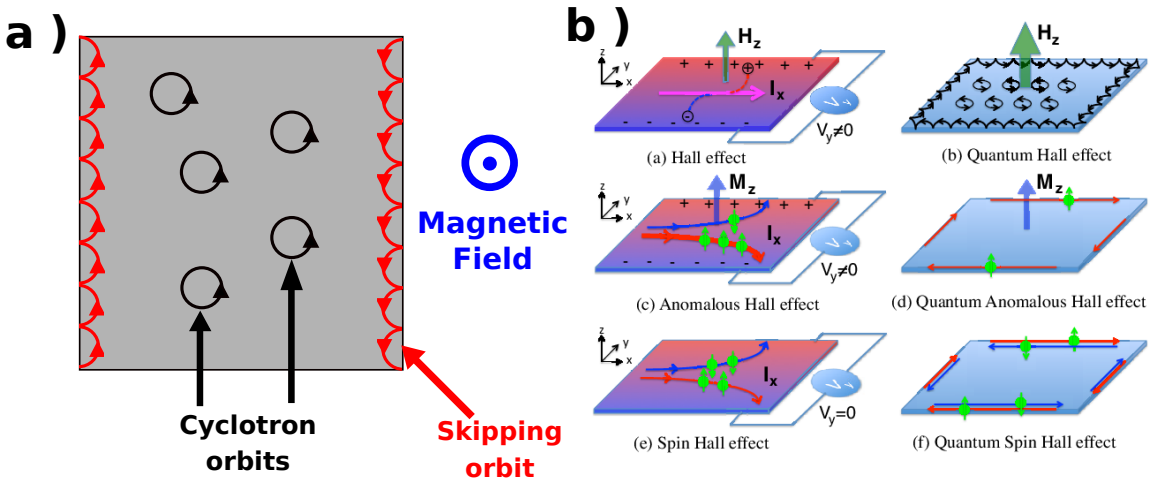

Fig. III.1 a) Cyclotron and skipping orbits in the case of the QHE. b) Different forms of Hall Effects from [117].

The Quantum Hall Effect (QHE) is a nice paradigm of this behavior [118]. In the presence of a strong magnetic field, the bulk of a metal does not conduct anymore as the electrons move following cyclotrons orbits. However, at the edges of the system electrons can conduct via skipping orbits [119, 120], shown in Fig. III.1 a. These ballistic channels of conduction are not impacted by disorder : the skipping orbits bounce forward on scattering centers as they bounce on walls, and both their size and number are controlled by the strength of the external magnetic field. Topological Insulators can display the Quantum Anomalous Hall Effect (QAHE), which is similar to the QHE but in the absence of an external magnetic field. Electrons experience a pseudo-magnetic field, internal to the material ; for ferromagnetic insulators, it can be the magnetization [121]. Topological edge states can appear without any net bulk magnetization inside the material, in the presence of spin-orbit coupling, leading to an effect called the Quantum Spin Hall Effect (QSHE) : the edge states are named *helical* for their spin and momentum are entangled. For a finite 2-dimensional rectangular slab, the topological states move along the edges in a direction locked to the polarization of their spin : clockwise for spin up and counterclockwise for spin down without leading to any charge current at the edges but to a net spin current. The two conduction channels are protected against potential disorder because spin conservation forbids back-scattering events. The different versions of the Hall Effects are presented in Fig. III.1 b from [122].

III.3 Geometry of a band structure

Now that we have reviewed some examples of topological phases of matter, we explain what topology means in the context of condensed matter physics. In general, topology is concerned with the properties of a geometric object that are preserved under continuous transformations, such as stretching, twisting, crumpling and bending, but not tearing and gluing [123]. If we put on "topological glasses", a soccer and a football look the same, but not a donut for it possesses a hole. It is possible to define classes of objects with similar topological properties, which bear the same topological invariants. The topology of simple objects like a donut or a football explicitly appears to the eyes as it is encoded directly in their spatial shape. For materials, the topological properties are of a different nature : they are encoded in the action of the Hamiltonian on the states of the system, and for crystals the space in which this topology dwells is usually the reciprocal space. In the following, we build the Berry phase, connection and curvature for a general Hamiltonian. The following derivations are largely inspired by [124].

III.3.1 Adiabatic evolution and Berry phase

We consider a Hamiltonian $\mathcal{H}(\vec{R})$ parameterized by a set of parameters $\vec{R}(t)$ which can evolve with time, following an adiabatic evolution along a path $\mathcal{C}$ in parameter space. For each value of the parameters, the Hamiltonian can be diagonalized using the eigenenergies $\epsilon_\nu(\vec{R})$ and the eigenvectors $|\nu(\vec{R})\rangle$ which verify $\mathcal{H}(\vec{R})|\nu(\vec{R})\rangle = \epsilon_\nu(\vec{R})|\nu(\vec{R})\rangle$. The eigenvectors $|\nu(\vec{R})\rangle$ are only defined up to an arbitrary phase factor. In a gapped system, the quantum adiabatic theorem [125] states that a system initially in one of the eigenstates $|\nu(\vec{R(0)})\rangle$ will remain an eigenstate of the Hamiltonian $\mathcal{H}(\vec{R}(t))$ throughout the process, so that we can write this eigenstate as

$$|\psi_\nu(t)\rangle = e^{i\gamma_\nu(t)} e^{\frac{i}{\hbar}\int_0^t du \epsilon_\nu(\vec{R}(u))} |\nu(\vec{R(t)})\rangle \tag{III.1}$$

The integrated phase in the exponential is named the dynamical phase factor and emerges from the Schrodinger equation : in a static case, it corresponds to the phase $e^{-\frac{i\epsilon_\nu t}{\hbar}}$. Inserting Eq. III.1 into the time dependent Schrodinger equation gives $i\hbar\partial_t|\psi_\nu(t)\rangle = \mathcal{H}(\vec{R}(t))|\psi_\nu(t)\rangle$.

Multiplying by $\langle\nu(\vec{R(t)})|$ on the left, one gets

$$\gamma_\nu = \int_{\mathcal{C}} d\vec{R} \cdot \vec{\mathcal{A}}_\nu(\vec{R}) \tag{III.2}$$

This phase is called the Berry phase and is linked to the integral of the vector field

$$\vec{\mathcal{A}}_\nu(\vec{R}) = i\langle\nu(\vec{R})|\nabla_{\vec{R}}|\nu(\vec{R})\rangle \tag{III.3}$$

along the path $\mathcal{C}$. This vector field is called the Berry connection, and changes upon a gauge transformation ζ of the eigenvector phase $|\nu(\vec{R})\rangle \to e^{i\zeta(\vec{R})}|\nu(\vec{R})\rangle$ according to $\vec{\mathcal{A}}_\nu(\vec{R}) \to \vec{\mathcal{A}}_\nu(\vec{R}) - \nabla_{\vec{R}}\zeta(\vec{R})$. If $\mathcal{C}$ is a closed path in parameter space, the Berry phase is a gauge-invariant quantity depending only on the geometrical properties of the band structure, contained inside the Berry connection. In crystals, the parameters $\vec{R}$ are the quasi momentum $\vec{k}$ of the electrons, and the curve $\mathcal{C}$ is a closed path in the Brillouin Zone.

III.3.2 Berry connection and curvature

The Berry connection is indeed a connection in the sense of differential geometry : it quantifies the evolution of the direction of the eigenvectors with the parameter $\vec{R}$ due to the algebraic structure of the Hamiltonian. The concept of Berry connection is analogous to the vector potential in electromagnetism : it is used to define the derivative operator with respect to the wavevector $(D_k)_\nu = \partial_k - i\vec{\mathcal{A}}_\nu$, while the vector potential in electromagnetism is used to define a corrected momentum $\Pi = \vec{p} - eA$. Using $\hat{r} = i\nabla_k$, one can see that the Berry connection can be interpreted as a correction to the position operator. Considering $\vec{\mathcal{A}}_\nu(\vec{R})$ is analogous to the vector potential in electromagnetism, we can define the associated magnetic field, called the Berry curvature

$$\vec{\Omega}_\nu(\vec{R}) = \nabla_{\vec{R}} \times \vec{\mathcal{A}}_\nu(\vec{R}) = i\langle\nabla_{\vec{R}}\nu(\vec{R})| \times |\nabla_{\vec{R}}\nu(\vec{R})\rangle \tag{III.4}$$

Where $\times$ is the cross-product. Due to the Stokes theorem, $\gamma_\nu = \int_{\mathcal{C}} d\vec{R}\cdot\vec{\mathcal{A}}_\nu = \iint_{\mathcal{S}} d\vec{S}\cdot\vec{\Omega}_\nu$, where $\mathcal{S}$ is a surface internal to the curve $\mathcal{C}$, in analogy with formulas involving magnetic fluxes. In a crystal, the parameter space is the reciprocal space ; as can be shown using perturbation

theory, in a non-degenerate case the Berry curvature writes

$$\Omega_\nu(k) = \hbar^2 \sum_{\chi \neq \nu} Im \left[\frac{\langle \nu | \hat{v}_x(k) | \chi \rangle \langle \chi | \hat{v}_y(k) | \nu \rangle - (x \leftrightarrow y)}{(\epsilon_\nu(k) - \epsilon_\chi(k))^2} \right] \tag{III.5}$$

Where ν, χ are band indices and $\hat{v}_\alpha(k) = \frac{1}{\hbar} \partial_{k_\alpha} \mathcal{H}(k)$ is the velocity operator in the direction k_α of the BZ. The Berry curvature has the dimensions of the square of a length.

III.3.3 Chern number

In a band insulator, the valence band and the conduction band are split by an energy gap, and it can be shown that the integral of the Berry curvature of a band over the whole Brillouin Zone is quantized to $2\pi C$, where $C \in \mathbb{Z}$ is the Chern number of the band (it is a consequence of the Gauss-Bonnet theorem and related to the TKNN invariant [126]). A band is said to be trivial when its Chern number is 0 and topological if it is nonzero. A simple two-band Hamiltonian yielding a nonzero topological invariant is the Chern insulator $\mathcal{H}_{CI} = \vec{h}(k) \cdot \vec{\sigma}$, with σ the 2×2 Pauli matrices and $\vec{h} = [k_x, k_y, m]$. This model has two energy branches $\epsilon_\pm = \pm h = \pm\sqrt{k^2 + m^2}$ with a finite gap $2|m|$ between the two bands, and its eigenvectors are $|\pm\rangle = \frac{1}{\sqrt{2h(h-m)}} \left[m \pm \sqrt{k^2 + m^2}, k_x - i k_y \right]$. The components of its Berry connection are $\mathcal{A}_x = -\frac{k_y}{2h(h+m)}$ and $\mathcal{A}_y = \frac{k_x}{2h(h+m)}$, and its Berry curvature is $\Omega = \frac{m}{2(k^2+m^2)^{3/2}}$. When the valence band is completely filled and the conduction band is empty, one gets $C = \pm\pi sign(m)$. This Chern number is half-quantized because of a regularization problem : the model should be put on a lattice with a tight-binding cut-off in order to get an integer value. Depending on the sign of the mass the Chern number changes from a constant, quantized value : a topological phase transition occurs and is associated with a closure of the gap. Between these two phases, the transverse conductivity changes by a quantized value. If the Fermi energy lies inside the gap, the transverse conductivity is the integral of the Berry curvature over filled states, and is proportional to the Chern number. If the Fermi energy is not inside the gap of the system, the integral of the Berry curvature is no longer quantized : it decays to zero on a certain energy scale depending on the mass when filling the system.

III.3.4 Spin Chern number

Unfortunately, the model presented before is not very realistic in terms of materials. Indeed, the Berry curvature is odd under Time-Reversal Symmetry and even under inversion symmetry, so that in systems presenting these two symmetries it vanishes for all the wave-vectors k. It can also be shown that $\sum_{\nu \in band} \vec{\Omega}_\nu(\vec{k}) = \vec{0}$, so the properties linked to the Berry curvature critically depend on the filling. The Chern insulator can be seen as a spinless two orbital model. Its spinful version is the celebrated Bernevig-Hughes-Zhang (BHZ) model [29]

$$\mathcal{H}_{BHZ} = \begin{bmatrix} m & Ak_- & 0 & 0 \\ Ak_+ & -m & 0 & 0 \\ 0 & 0 & m & Ak_+ \\ 0 & 0 & Ak_- & -m \end{bmatrix} \tag{III.6}$$

Where $k_\pm = k_x \pm ik_y$. This Hamiltonian is composed of two copies of the Chern insulator Hamiltonian which are time-reversed partners, and the four orbitals composing the basis can be labeled $(A\uparrow, B\uparrow, A\downarrow, B\downarrow)$. Due to the global Time-Reversal invariance of the Hamiltonian the total Chern number of the system is zero. However, each spin species has a nonzero Chern number of opposite sign : in the language of edge states, the spin up and the spin down states propagate in opposite directions. The overall charge current cancels but the overall spin current does not : this is called the Quantum Spin Hall Effect, and it is associated with the spin Chern number $C_z = \frac{C_\uparrow - C_\downarrow}{2}$. If the Fermi energy lies inside the gap, the spin Chern number is equal to the spin resolved conductivity because as the z component of the spin is conserved by the Hamiltonian, the spin Chern number is simply the difference between the Chern number of the up spin and the one of the down spin. The edge states are said to be helical : they come by pairs with opposite spin and velocities and like an helix or a screw, the direction of their propagation is associated with a direction of spin.

III.4 Topology and transport

The topological invariants play an explicit role in transport properties as one can see through two important examples : the emergence of edge states and the anomalous velocity.

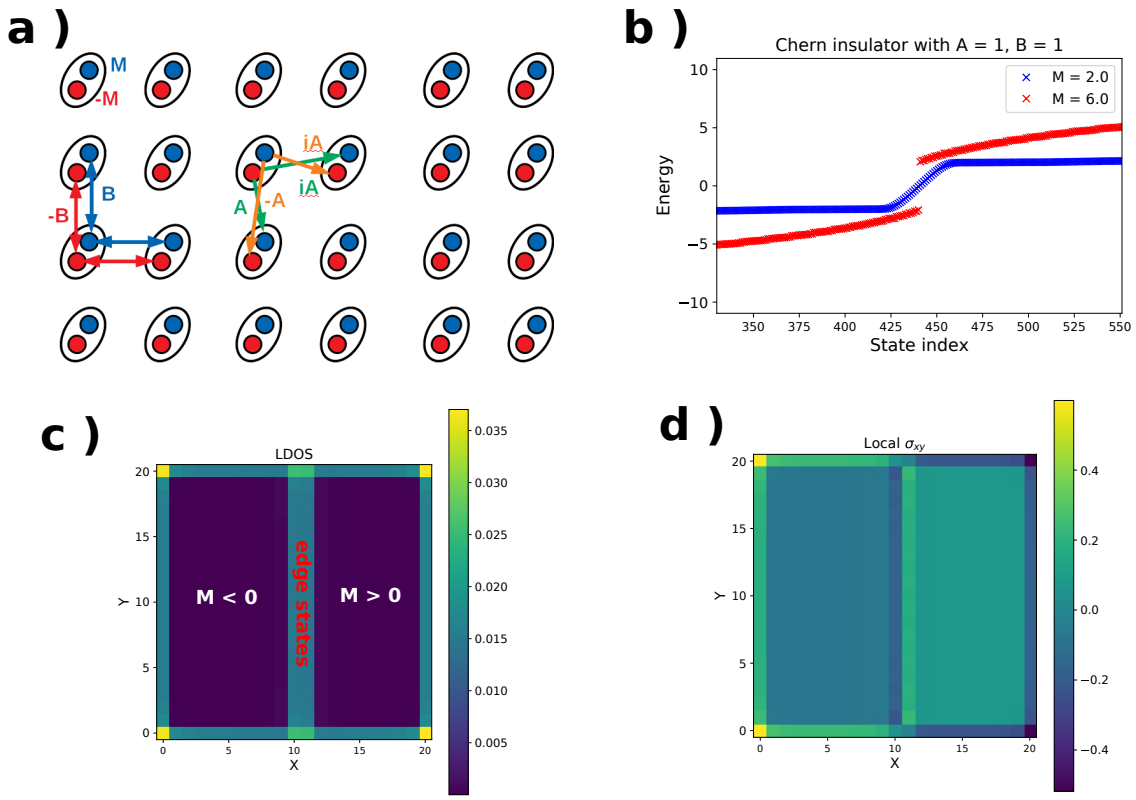

Fig. III.2 a) Tight-binding model for the Chern insulator. b) Spectrum of a Chern insulator on a lattice for two values of the mass M. For $M = 2$, the system is in the topological regime and has edge states in the gap while for $M = 6$ there are no states inside the gap. c) local density of states of a junction between two Chern insulators with opposite masses $M = \pm 2$ at the two sides of the junction. Edge states can be observed at the junction and at the border of the samples. d) Map of the corresponding local transverse conductivity marker at $E_F = 0$

III.4.1 Edge states

At the interface between materials with distinct topological invariants, topological edge states can emerge. They have the interesting property of being immune to disorder, making them interesting for applications, be it to build long lived symmetry protected qubits or to transport information without dissipation. In a two-dimensional slab of Chern insulator, chiral edge modes develop : they can only propagate in one direction (clockwise or anti-clockwise) and are protected against back-scattering on disorder because they can only scatter towards a state with similar energy. As their counterpart lives on the other edge of the insulator, scattering events are very unlikely (the bulk is insulating), hence their transport

is ballistic. Fig. III.2 a details the tight-binding from of the Chern insulator Hamiltonian of Section III.3.3. We put this model in a 21x21 square lattice and show its spectrum for two different values of the gap in Fig. III.2 b. For $M = 2$ (topological regime), there is a continuum of levels inside the gap while for $M = 6$ (normal regime) there is a gap ; the topological phase transition of this model occurs at $M = 4$. We compute the Local Density of States (LDOS) at $E_F = 0$ in the topological regime ($M = 2$) of a junction between two Chern insulators with an opposite mass M on each side. The LDOS, shown in Fig. III.2 c, is zero inside the bulk in both sides of the junction, but peaks at the edges of the slab and near the junction, at places where the topological phase transition occurs : the interface between the topological insulator and vacuum (borders) and between topological insulators of distinct invariants (junction).

III.4.2 Anomalous velocities

Under the application of an electric field $\vec{E}$ and of a magnetic field $\vec{B}$, the motion of a charged particle undergoes the Lorentz force $\vec{F} = q(\vec{E} + \vec{v} \times \vec{B})$. Using a wavepacket description where the position and momentum of the wavepacket are $(\vec{r}_c, \hbar\vec{k}_c)$, one gets

$$\begin{aligned} \partial_t \vec{r}_c &= \frac{1}{\hbar}\vec{\partial}_{k_c}\epsilon_{k_c} - \partial_t \vec{k}_c \times \vec{\Omega}_k \\ \hbar\partial_t \vec{k}_c &= -e\vec{E} - e\vec{\nabla}V - e\partial_t \vec{r}_c \times \vec{B} \end{aligned} \tag{III.7}$$

Where it appears that the Berry curvature is indeed the analog of a magnetic field for the position operator, and the anomalous velocity reads $\vec{v}_{an} = e\vec{E} \times \vec{\Omega}_k$.

III.4.3 Kubo formula and Berry curvature

The role of the Berry curvature and the geometry of the wavefunctions can be derived from a fully quantum-mechanical perspective. In a periodic crystal, the Bloch theorem states that a single-particle state can be described by a pseudo-momentum k inside the Brillouin Zone and other internal degrees of freedom, producing n bands of energies. In a single-particle approach, the Hamiltonian is block-diagonal in the reciprocal space and acts on this n-dimensional subspace, giving a total Hamiltonian $\mathcal{H} = \sum_k \mathcal{H}_k$. Each of the operator $\mathcal{H}_k$ is hermitian : the spectral theorem states that there exists eigenenergies $\epsilon_\nu(k)$ and an

orthonormal basis of eigenvectors $|\nu k\rangle$ such that $\mathcal{H}_k|\nu k\rangle = \epsilon_\nu(k)|\nu k\rangle$.

Upon the application of an electric field across a sample, the Hamiltonian is no longer transitionally invariant since a new term $\mathcal{H}_E = -e\vec{E}\cdot\hat{\vec{r}}$ appears, and the eigenvectors are no longer the $|\nu k\rangle$. The correction $\delta|\nu k\rangle$ of the eigenvectors due to the electric field is $\delta|\nu k\rangle = \sum_{\chi\neq\nu} \frac{\langle\chi k|e\vec{E}\cdot\hat{\vec{r}}|\nu k\rangle}{\epsilon_\nu(k)-\epsilon_\chi(k)}|\chi k\rangle$. In the wavevector basis, the position operator can be written $\hat{\vec{r}} = i\vec{\nabla}_k$, and perturbation theory in the non-degenerate case gives $\langle\chi|\nabla_k|\nu\rangle = \hbar\frac{\langle\chi|\vec{v}_k|\nu\rangle}{\epsilon_\nu(k)-\epsilon_\chi(k)}$. The mean value of an operator $\hat{A}$ for a band ν under the application of an electric field is obtained after taking the trace over the occupied states of the band ν

$$\langle A\rangle_\nu = ie\hbar\vec{E}\cdot\sum_k\sum_{\chi\neq\nu} f_{\nu k}\frac{\langle\nu k|A|\chi k\rangle\langle\chi k|\vec{v}_k|\nu k\rangle}{(\epsilon_\nu(k)-\epsilon_\chi(k))^2} \tag{III.8}$$

For the transverse conductivity, the operator is $A = e\hat{v}_y$ for an electric field $\vec{E} = E_x\vec{u}_x$. This formula relates the Anomalous Hall Conductivity (AHC) to the total Berry curvature of the filled states $\sigma_{AH} = \frac{e^2}{\hbar^2}\sum_\nu \int d^2k f_{\nu k}\Omega_\nu(k)$ [127]. This approach straightforwardly shows the emergence of the anomalous term, and that the topological effects concern the filled states. In a topological insulator, only the valence band is filled, leading to a quantized conductivity related to the Chern number of the bands. In a semi-classical transport approach, only scattering events can lead to conductivity, which forbids this topological term : this correction gives a simple origin for the anomalous term. This approach can also be applied to metals where the intrinsic terms is computed over the filled states. In a metal, it has no longer any reason to be quantized. However, scattering processes need to be considered in their entirety to estimate correctly physical quantities in metals (see Appendix B.6).

III.4.4 Local description of the curvature

Following [128, 129], it is possible to build a local Berry marker to interpret the Berry curvature in real space tight-binding models. Writing $\mathcal{P}_k = \sum_{\epsilon_\nu(k)\leq E_F}|\nu k\rangle\langle\nu k|$ the projector on occupied states for the wavevector k, the Berry curvature is $\Omega_{\alpha\beta} = iTr\left(\mathcal{P}_k\left[\partial_\alpha\mathcal{P}_k, \partial_\beta\mathcal{P}_k\right]\right)$. This equation can be transformed in real space

$$\Omega_{xy}(r) = i\langle r|\mathcal{P}\left[\left[\mathcal{P},\hat{X}\right],\left[\mathcal{P},\hat{Y}\right]\right]|r\rangle \tag{III.9}$$

Where $\mathcal{P} = \sum_{\epsilon_\nu \leq E_F} |\nu\rangle\langle\nu|$ is the projector on occupied states of the real space Hamiltonian and $\hat{X}, \hat{Y}$ are the coordinate operators. A color map of this quantity is shown for the previous simulations in Fig. III.2 d inside the gap of the system ; the response is carried in majority by the edge states and is opposite for the two sides of the junction. The same observations can be done for $\Omega_{xx}(r) = \langle r|\mathcal{P}\left[\mathcal{P}, \hat{X}\right]\left[\mathcal{P}, \hat{X}\right]|r\rangle$, in analogy with the longitudinal conductivity. The situation is more complicated for spin currents, where the definitions of the currents are already ambiguous [130]. Numerical computations of the "local spin curvature" for a 2D lattice version of a Rashba model on a slab show that the quantity is distributed inside the slab ; whereas for a 2D lattice version of the BHZ model in the Quantum Spin Hall regime, the major contribution to this quantity is located at the 1D edges of the slab when the computation is performed inside the energy gap : the spin Hall signature is carried by the helical edge states.

III.5 Topology and Transition Metal oxides interfaces

Topological properties of matter usually emerge from symmetry breaking and coupling between bands of different orbital character. The presence of an interface, the multiband character of the conduction band and the atomic spin-orbit coupling suggest that topological properties can be expected in TMO heterostructures. In [87], a BHZ-like effective Hamiltonian is derived near special band crossings of the band structure of the LAO/STO interface. The exact nature of these crossings and the algebraic form of the splitting are of crucial importance in order to determine which type of topology can emerge from these couplings. Since the conduction band of STO is composed of the three t_{2g} orbitals (doubled by a spin index), geometrical effects involving up to three bands can be expected (even up to six bands if the spin degree of freedom is taken into account).

In Chapter IV, we focus on the geometry of the in-plane spin vector field and derive the effect of such a geometry on spintronic responses : one can see the influence of the couplings of the bands between one another and observe strong multiband effects, and an analogy with the geometrical tools introduced in this Chapter is made. Since the effective model we use to describe STO interfaces is Time-Reversal symmetric, we do not expect to observe effects such as Anomalous Hall Conductivity in these interfaces. We introduce the Kubo-Streda formula

in Eq. III.8, which is used in the next chapter to describe the Spin Hall Conductivity. If it is difficult to disentangle the different contributions to this response, which is dominated by Rashba-like behavior, some of the response can be linked with unusual geometry. The observation of effects related to the topology of the band structure may be hindered by the metallicity of the system : the detection of edge states or of unusual transport signatures can be drowned by scattering processes or large contributions the conductivity.

IV – Spintronic properties of TMO heterostructures

> At such times I felt something was drawing me away, and I kept fancying that if I walked straight on, far, far away and reached that line where the sky and earth meet, there I should find the key to the mystery, there I should see a new life a thousand times richer and more turbulent than ours.
>
> Fedor Dostoievski,
> *The Idiot*

IV.1 Introduction

The Quantum Spin Hall Effect (QSHE) belongs to the family of *spintronic* phenomena, allowing one to manipulate the spin of the electrons by tuning the charge. The objective of spintronics is to process information using the spin degree of freedom within microelectronic chips [42]. It is already a very successful area of research both academically and industrially : the discovery of Giant MagnetoResistance (GMR) led to the attribution of a Nobel Prize [43], and Magnetic Random Access Memory (M-RAM) is already produced on an industrial scale. The possibility to build spintronic devices using antiferromagnetic materials is on the roadmap of the ITRS (International Technology Roadmap for Semi-conductors) to further improve the performances of devices [44]. Magnetization dynamics and spin-orbit torques [49, 50] rule how it is possible to write the information. Heavy metals such as Pt [131, 132, 45], W [47] and Ta [48] host interesting spintronic properties and are thus under active investigation

to understand how to tame and engineer these effects [46, 133]. Devices using Transition Metal Dichalcogenides (TMD) also exhibit interesting spintronic properties [134] and can be used to induce spin-orbit coupling in graphene [135]. It is observed that noteworthy spintronic effects emerge in systems displaying a Rashba spin-orbit coupling [51]. TMO interfaces, in particular STO-based, exhibit a gate-tunable Rashba interaction [52] and as such are a nice platform to study these effects. Recent experiments [53, 54, 55] have shown they present interesting spintronic effects : we explain two spin-to-charge conversion mechanisms and how these effects can be used to better characterize the multi-orbital characteristics of the TMO systems in general.

We begin with a description of two mechanisms of spin-to-charge conversion, namely the Edelstein Effect [136] and the Spin Hall Effect [51], and discuss recent measurements in STO-based interfaces where these effects are found to be very large. Concepts of semi-classical transport allow us to compute transport properties from tight-binding models for STO-based interfaces and to fit experiments using realistic parameters. We further push our analysis of the generic model for STO interfaces and show that the multi-band structure of TMO is fundamental to explain the variations of the Edelstein response. The behavior of the system can be understood by means of a property we call Multiband Interfacial Spin-Orbit (MISO). Using analytical computations, we isolate the important contributions to the spintronic responses using low-energy models around special points of the band structure and show that the MISO induces winding spin textures of two different natures with a distinct effect on the responses. Using perturbation theory, we detail these two contributions : the former is analogous to the Rashba-Edelstein effect and the latter is specific to the multi-orbital nature of the conduction band and can be of the same amplitude. This dichotomy might provide an explanation for phenomena that are interpreted as a gate-tunable Rashba interaction or even more complex cubic Rashba interactions. I want to express my gratitude to Manuel Bibes and his group for letting me participate to the projects of [55] and [54] ; this whole chapter is build on these two major experimental results regarding the spintronic responses, and the theoretical work we did on [137], presented in this chapter, was only possible through a detailed analysis of these two works.

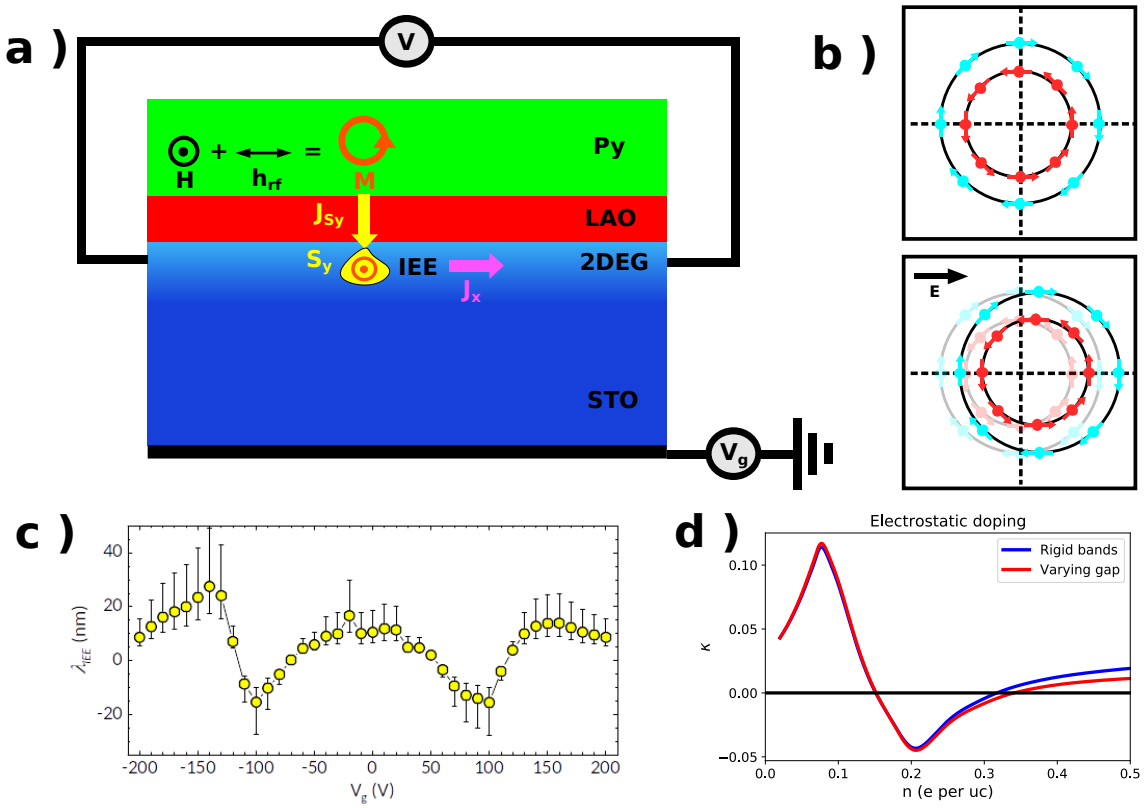

Fig. IV.1 a) Spin-pumping experiment. b) Spin texture of a Rashba model in equilibrium and under the application of an electric field in the x direction. c) Amplitude of the IEE as a function of the gate voltage for AlOx / STO taken from the experiments of [55]. d) Variations of the amplitude of the EE with electronic density for a 6-band model of STO. The parameters are $t_1 = 388$ meV, $t_2 = 30$ meV, $\Delta = 50$ meV, $\lambda = 8$ meV and $\gamma_{OM} = 20$ meV. The results are presented with and without corrections of the band structure relative to doping.

IV.2 Spin-to-charge conversion

IV.2.1 Experiments

a) The spin-pumping experiment

The Edelstein Effect (EE), or spin-galvanic effect, is the creation of a net spin polarization inside a material under the application of an electric field [136]. The Inverse Edelstein Effect (IEE), its counterpart, is the creation of an electric field in a material experiencing a spin imbalance, for instance via spin injection. Fig. IV.1 a shows the spin-pumping experiment which allows to detect and measure the IEE. A slab of ferromagnetic material (Permalloy Py

is another name for alloys of Ni and Fe) is driven towards ferromagnetic resonance via the application of a static magnetic field H and of a microwave field h_{rf} [138]. The precession of ferromagnetic moments iside Permalloy induces a DC spin-polarized current which is pumped into the STO 2-DEG below the LAO spacer and creates a net spin polarization in a given in-plane direction. The insulating spacer layers allow to inject only spin and to forbid charge diffusion between the ferromagnet and the 2DEG. This spin polarization creates an electric field and a charge current inside the 2DEG through the IEE, and the spin-galvanic response of the material is the ratio between the amplitude of the spin injection and the electric current.

This effect has been observed in semi-conductors [139, 140], and was recently detected in LAO/STO [53] and AlOx/STO samples [55], where the response is particularly large and presents interesting variations with electrostatic doping, which can be reproduced on a qualitative level using tight-binding models. The non-monotonicity of the IEE with doping comes from the presence of multiple bands in the system, and the large efficiency of the conversion makes it very appealing for applications. It is of interest to understand which parameters impact the amplitude of this conversion in order to choose the best materials to engineer new devices. In particular, the amplitude of the spin-orbit coupling can be tuned by using atoms with heavier nuclei : $5d$ electrons experience a greater atomic spin-orbit coupling than $3d$ electrons.

b) Nonlocal voltage measurements

While the Hall Effect is the creation of a transverse charge current under the application of a charge current, the Spin Hall Effect (SHE) is the creation of a transverse spin current under the application of a charge current. The SHE can be detected experimentally using the Hanle effect : measurements of a non-local voltage sensitive to magnetic fields hint towards the presence of spin currents [141, 142, 143]. The variations of these spin currents with respect to the direction of the magnetic field can discriminate between different spin-to-charge conversion mechanisms. The presence of non-local voltage can occur through different mechanisms ; we focus on two possibilities : one coming from the EE and the other from SHE. In the first scenario, a charge current J_c along the x direction in one arm of the Hall bar is converted into a spin accumulation polarized along the y axis due to the EE. Spin diffusion

inside the material transforms this spin density into a spin-polarized current diffusing towards another arm of the Hall bar. The second scenario involves a direct conversion from charge current to spin current through the Spin Hall Effect, and results in this case in the creation of a transverse spin current polarized in the z direction. At the other arm of the Hall bar the spin current can be converted back into a charge current through the respective reciprocal processes, leading to a non-local voltage detection in the set-up presented on Fig. IV.2 a,b. The efficiency of the spin transport between the two arms of the Hall bar determines the amplitude of the non-local voltage. The spin signal can be reduced by disorder effects (scattering on magnetic impurities, D'yakonov-Perel and Elliot-Yafet mechanisms), or by the application of a magnetic field. The relative direction between the magnetic field and the spin of the electron determines the impact of the magnetic field on the spin transport. A magnetic field perpendicular to the direction of spin polarization induces the precession of the spins of the electrons and the signal exhibits a signature proper to the Hanle effect : the amplitude of the non-local voltage decreases with the magnetic field. This Hanle analysis has been performed for the two in-plane directions of the magnetic field, and the similarity of the results in the two directions indicates that the out-of plane component of the spin polarization is non-zero and drives the non-local voltage. This type of symmetry hints towards a SHE scenario.

The variations of the non-local resistance with the length of the sample and the magnetic field can be fitted using formulas relative to the Hanle Effect [54]. This allows to independently determine the three parameters $\gamma, \lambda_s, \tau_s$, which are respectively the Spin Hall angle $\gamma = \frac{\sigma_{SH}}{\sigma_{xx}}$, the spin diffusion length and the spin scattering time. These experiments are performed at various backgate voltages V_g in order to observe the variations of the non-local resistance upon electrostatic doping. The variations of the SH angle with V_g are large and non-monotonic with a peak value of around 40% when $V_g \approx 30V$ in both directions of the magnetic field, as shown in Fig. IV.2 c. This value of backgate voltage is consistent with the occurrence of a non-linearity in the Hall resistance, suggesting the advent of a new species of carriers, which is most likely the first heavy $d_{xz/yz}$ band. The increasing of λ_s and τ_s with backgate voltage above this threshold is consistent with the high mobility of heavy bands. The link between the spin scattering time and the mobility is typical of an Elliot-Yafet mechanism of relaxation [144, 145, 146], which can describe the spin relaxation

of heavy bands.

IV.2.2 The Rashba model

The Linear Rashba model is a 2-dimensional, 2-band model exhibiting spin-to-charge conversion properties

$$\mathcal{H}_R = \frac{\hbar^2 k^2}{2m} + \alpha_R(\vec{k} \times \vec{\sigma}) \cdot \vec{z} \tag{IV.1}$$

Where m is the effective mass of the electrons and α_R is called the Rashba coefficient. Its spectrum is $\epsilon_\pm = \frac{\hbar^2 k^2}{2m} \pm \alpha_R k$. The two bands, labeled $+$ and $-$, have circular Fermi surfaces. A particularity of this model is its winding spin textures as the two bands undergo spin-momentum locking : the direction of the spin $\vec{S}$ of the electron is perpendicular to the direction of its wavevector $\vec{k}$. The textures of the bands labeled as $+$ and $-$ are winding in opposite directions as shown by Fig. IV.1 b. As the Fermi surface is circular, these textures do not induce any net spin polarization in equilibrium. Under the application of an in-plane electric field the two Fermi surfaces are shifted in a common direction and induce a spin imbalance polarized perpendicularly to the direction of the electric field. This is the Rashba-Edelstein effect. In a semi-classical approach, the application of a static electric field changes the wavevector of the electron, and the spin-momentum locking constrains electrons to perform vertical transitions and to relax producing a transverse spin-polarized current : this is the universal Intrinsic Spin Hall Effect described in [51].

IV.2.3 Generic band structure

The EE and SHE response of a generic band structure can be computed using the Boltzmann and Kubo-Streda formalism [49, 147, 148].

a) Direct and Inverse Edelstein Effect

The Edelstein tensor $\kappa_{\alpha\beta}$ represents the creation of a spin density along the β axis in response to an electric field along the α axis, and κ_{xy} denotes the Edelstein coefficient in the following. This spin-galvanic response is due to scattering events and can be evaluated as a

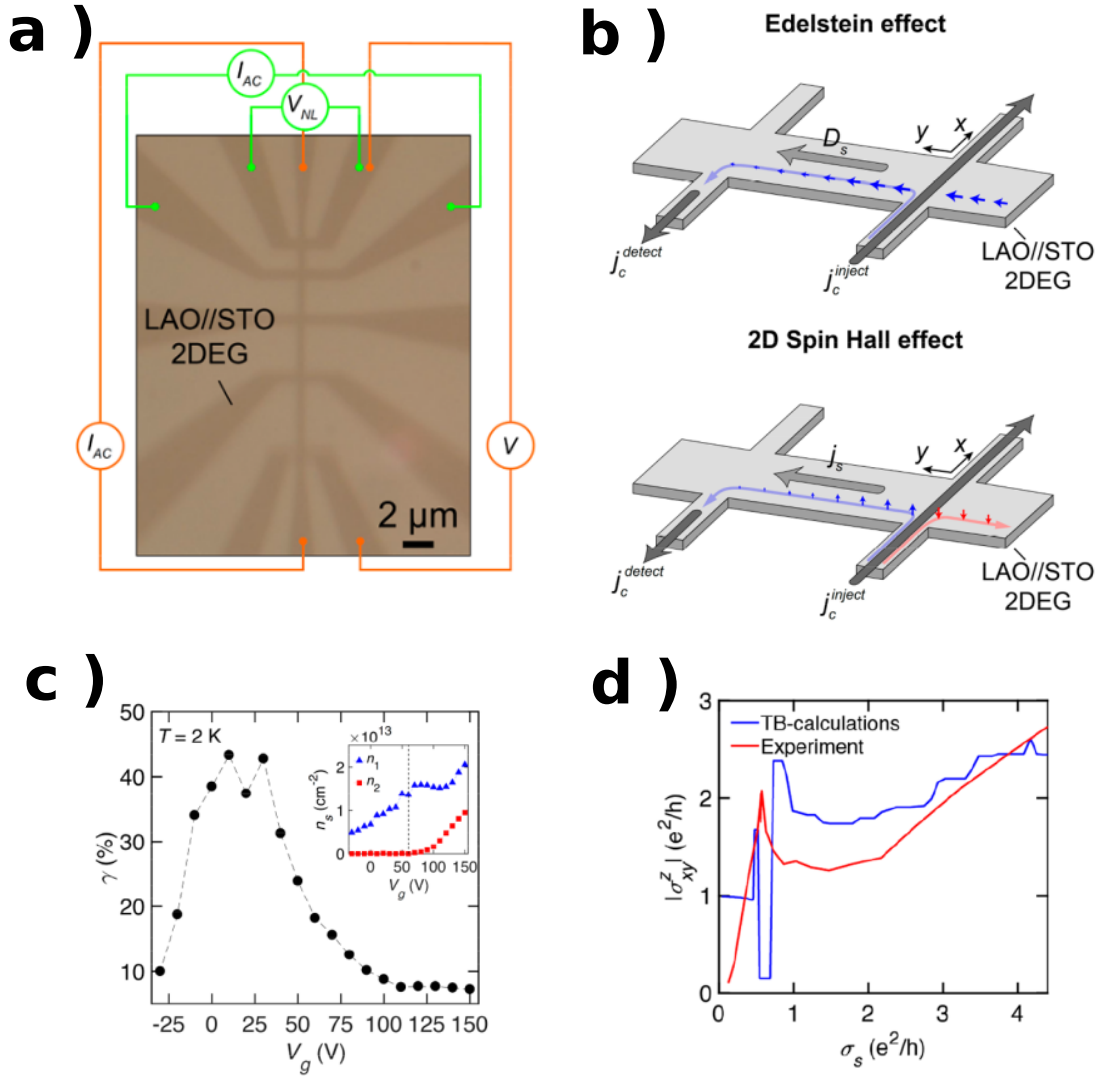

Fig. IV.2 a) Nonlocal voltage measurements on a LAO/STO sample, according to [54]. b) The two possible mechanisms for the creation of this non-local voltage, through Edelstein Effect of Spin Hall Effect. c) Spin Hall angle as a function of the back-gate voltage. d) Spin Hall Conductivity (SHC) as a function of the sheet conductivity : comparison of experiments and results of the tight-binding model of [54].

response of the Fermi surfaces, similarly to the electrical conductivity [149, 150] :

$$\kappa_{xy}(E_F) = \frac{e}{N_k a^2} \sum_{k,\nu} \tau^{\nu}(k) v_x^{\nu}(k) \langle S_y^{\nu} \rangle(k) \delta(\epsilon_\nu(k) - E_F) \tag{IV.2}$$

where τ is the scattering time, v_x the velocity along the x axis, $\langle S_y \rangle$ the mean value of the spin operator along the y axis, δ is the Dirac δ-function and E_F is the Fermi energy. The superscript ν is a band index, k is the wavevector and $\epsilon_\nu(k)$ the energy of band ν. $\frac{1}{N_k a^2}$ is a normalization factor for the sum which depends in the size of the K-mesh. Using the symmetries of the problem and making approximations detailed in Appendix B.2, the Edelstein response can be rewritten

$$\kappa(E_F) = \frac{e\tau_0}{h} \sum_{\nu} \int_0^{2\pi} k_F^{\nu}(\theta) S_\nu^t(\theta) d\theta \tag{IV.3}$$

Where S_ν^t is the mean value of the projection of the spin on the direction tangential to the Fermi surface of the band ν, and k_F^ν the Fermi wavevectors defined by the equations $\epsilon_\nu(k_F^\nu) = E_F$. τ_0 is the scattering time, assumed equal for all bands. Eq. IV.3 is useful to determine the Edelstein response : we compute the Fermi wavevectors k_F^ν for angles $\theta_j = \frac{2\pi j}{N_\theta}$ with $j \in [0..N_\theta - 1]$, compute the eigenvectors and the matrix elements, and then sum the contributions to the angular integral of Eq. IV.3. This method is both more accurate and faster than the use of an evenly spaced K-mesh because it avoids the problems of a bad sampling of the Fermi surface. It can however fail in the case of very complicated band structure with both electron and hole-like carriers. Using the Stokes theorem Eq. IV.3 can be recast in

$$\kappa(E_F) = \frac{e\tau_0}{h} \sum_{\nu} \iint_{BZ} d^2k f_{\nu k}(E_F) (\vec{\nabla}_k \times \vec{S}_\nu) \cdot \vec{z} \tag{IV.4}$$

With $\vec{S}_\nu$ the mean value of the spin operator for band ν. This alternative writing shows that the Edelstein response is a consequence of the spin textures and their vorticity inside the Brillouin Zone. It is analogous to the Berry curvature framework in the sense that the formula contains a rotational and that the integral is over a surface, and shows that the Edelstein Effect is linked to the geometry of the spin vector field. However, it is less useful for numerical purposes as rotational operators are not numerically stable.

b) The intrinsic Spin Hall Effect

Various processes can lead to the creation of a Spin Hall response inside a material. Using Boltzmann's theory of transport, they can be classified into two broad families : *extrinsic* when they emerge from scattering on disorder or *intrinsic* when they are present even in the absence of scattering. In the second case, their amplitude does not depend on the amount of disorder but only on specific quantities linked to the geometry of the eigenvectors and the band structure. We focus on the intrinsic part to study the SH response of TMO-based systems since it does not depend on the details of the modeling of disorder. However, as explained in various references [142, 151, 152, 153, 154], the extrinsic parts of the response, though only present in the disordered case, can have a contribution independent of the disorder strength. A full treatment of the extrinsic SHE is very complicated both numerically and theoretically, and crucially depends on the definition of operators, disorder and quantities to be observed. We report to Appendix B.6 a discussion of some of the extrinsic terms. The intrinsic SHE can be computed using Eq. III.8 with $A = \vec{j}_S$ the spin current operator. It is encoded in the spin-curvature of the system, which is determined by coherent processes involving vertical transitions between bands. The spin curvature of band ν is given by

$$\Omega_\nu^\alpha(k) = \hbar^2 \sum_{\chi \neq \nu} Im \left[\frac{\langle \nu | \hat{v}_x^\alpha(k) | \chi \rangle \langle \chi | \hat{v}_y(k) | \nu \rangle - (x \leftrightarrow y)}{(\epsilon_\nu(k) - \epsilon_\chi(k))^2} \right] \tag{IV.5}$$

Where $|\nu\rangle, |\chi\rangle$ are eigenvectors of the Hamiltonian (k is implicit). The velocity operators are defined by $\hat{v}_\beta(k) = \frac{1}{\hbar}\partial_{k_\beta}\mathcal{H}(k)$, and the spin velocity is defined by $\hat{v}_\beta^\alpha = \frac{1}{2}\{\hat{v}_\beta, \hat{\sigma}_\alpha\}$. The intrinsic part of the Spin Hall Conductivity (SHC) is obtained by summing this quantity over the occupied states

$$\sigma_{SH}^z(E_F) = \frac{e}{\hbar} \sum_n \int d^2k f_{\nu k}(E_F) \Omega_\nu^z(k) \tag{IV.6}$$

Where E_F is the chemical potential and $f_{\nu k}$ is the Fermi function of band ν. To prevent numerical divergences, we add a small cut-off η^2 to the denominator of Eq. IV.5. This is useful at points where bands are degenerate, and can be seen as a way to include some effects of disorder, while removing non-physical divergences of the quantity under scrutiny ; computations without this cut-off give divergences scaling with the size of the K-mesh,

Material	t_1 (meV)	t_2 (meV)	Δ (meV)	λ_{SO} (meV)	γ_{OM} (meV)
STO	338	30	100/50	8	20/20
KTO	580	30	490	123	20
CTO	240	17	90	-	20

Table IV.1 Parameters of the tight-binding model of Chapter II for some Transition Metal Oxides. For STO the presence of two values for Δ and γ_{OM} correspond to the coefficients for the lower and upper d_{xy} subbands. For CTO there are no reliable estimations of λ_{SO}.

confirming these divergences are mere numerical artifacts. We also take the antisymmetric part of the tensor in Eq. IV.5 with respect to the index x and y as for the Edelstein Effect. This is not a necessity for the computation but is interesting in numerics in order to take advantage of the symmetries of the problem. Indeed, in a four-fold or spherical symmetric band structure, this removes some of the angular dependence of the effect and avoids the errors due to the inhomogeneous sampling of the filled states. For numerical computations, we can switch to polar coordinates $d^2k = kd\theta dk$. As we are interested in interband transitions, it is important to sample the wavevectors that are between the bands. To do so, we compute the Fermi wavevectors for a regular grid of θ_j and then sample the radial wavevectors between the different bands so that we have the same number of wavevector in all the intervals between consecutive bands. This lowers the number of wavevectors necessary to perform the computation and gives clean numerical results.

IV.2.4 Numerics for STO-based heterostructures

We compute the two aforementioned quantities for the tight-binding model described in Chapter II. The values of the parameters of the model for several TMO are presented in Table IV.1. For STO-based systems, the numerical simulations are able to reproduce the non-monotonicity of the two quantities and reveal that the presence of several bands has a clear signature on the responses. The variations of the amplitude of the IEE of AlOx/STO heterostructures with respect to gate voltage are presented in Fig. IV.1 c and are extracted from [55]. They are compared to numerical computations for a 6-band model of STO yielding the Edelstein response as a function of the chemical potential E_F in Fig. IV.3 d. Changing the gate voltage or the chemical potential indeed affects the electrostatic doping of the system by adding new carriers. However, as explained in Section II.4 the two are not equivalent :

in multi-band systems, backgating can modify the effective chemical potential of the levels differently, making non-rigid changes in the band structure. In Fig. IV.1 d we estimate the effects of the change in the band structure on the EE and see that it does not change qualitatively the results, bringing only minor corrections to the response. The value of the gate voltage is complicated to interpret for another reason : for the same type of devices the characteristic voltages can vary depending on extrinsic and sample-specific parameters such as the amount of disorder, the quality of contacts, the chemical nature of contacts, etc. It is usual to present the results as a function of the electric conductivity σ_{xx} of the sample to avoid these problems and to allow comparisons.

ARPES spectra show that for the bare surface of STO there are two d_{xy} subbands and only one of the $d_{yz/xz}$ type. This can be included in the model by adding a second d_{xy} state with a different confinement gap $\tilde{\Delta}$. Fig. IV.3 d shows that the EE variations with E_F for the 8-band model track its counterpart for the 6-band model, using the parameters $t_1 = 388$ meV, $t_2 = 30$ meV, $\lambda_{SO} = 8$ meV, $\Delta = 50$ meV, $\tilde{\Delta} = 100$ meV, and $\gamma_{OM} = \tilde{\gamma}_{OM} = 20$ meV ($\tilde{\gamma}$ is the amplitude of the orbital mixing between the lower d_{xy} subband and the $d_{xz/yz}$ subbands). As the two d_{xy} subbands are not coupled, their contributions to the responses are additive, leading to a vertical shift of the 8-band curves as compared to the 6-band ones. The same analysis can be applied to the SHE and shows that the contribution of the first d_{xy} level is merely added to the response of the 6-band model : apart from a shift of 1 unit, the two results are almost identical. The lowest energy d_{xy} subband lies closest to the interface and disorder should affect it most, to the point that its contribution to SHC might be washed out by disorder. For this reason we focus on the 6-band model in the rest of the chapter as it contains the main features of the phenomena we want to discuss.

IV.3 Spin textures and spin-galvanic response

Eq. IV.3 establishes that the Edelstein coefficient is a direct consequence of spin textures inside the Brillouin Zone. For a Linear Rashba Model (LRM), these spin textures are simple : two arrow fields whirling in opposite directions around Γ, with an arrow length independent of the wavevectors and band index. The total Edelstein coefficient is the sum of the moment arms of the arrow fields with the Fermi wavevector. As the two arrow fields are of opposite

direction and of the same length for each orientation of the Fermi wavevector k, the total Edelstein coefficient is the moment arm of the arrow field times the difference in Fermi wavevector between the two bands. For a LRM in the regime where the two bands are occupied, the difference of Fermi wavevector is independent of the Fermi energy and is equal to $\delta k = \frac{2m\alpha_R}{\hbar^2}$, and the Edelstein response is therefore a constant. This is a good toy model to understand the microscopic origin of the Edelstein response, but is insufficient to describe STO-based heterostructures, where the amplitude of the response varies with the chemical potential. The form of Eq. IV.3 is analogous to the computations of a moment arm. In this analogy, the in-plane spin operator is analogous to a force $\vec{S} \equiv \vec{F}$, the wavevector to a position $\vec{k} \equiv \vec{r}$ and the Edelstein response to a torque $\kappa \equiv \mathcal{T}$. Besides, the Edelstein response is often considered in the discussions about spin torques [50].

We want to understand the role of the spin textures in the evolution of the EE and SHE of the TMO interfaces with the Fermi energy. To do so, we come back to the tight-binding model described in Chapter II and rewrite it in order to explicitly show the presence of spin-momentum locking and the underlying spin textures. Two different mechanisms lead to the creation of these spin textures, allowing to decompose them in two parts. In the absence of orbital mixing, the 6-band model used to describe the physics of the t_{2g} orbitals can be decomposed into three pairs of bands split by the kinetic energy, the confinement energy and the atomic spin-orbit coupling. The orbital mixing induces two types of couplings : a Rashba-like coupling internal to each pair, and terms which couple different sets of bands through complex inter-orbital terms. These two types of couplings induce spin textures of different natures that we respectively call intraband and interband. We compute the shape of these textures at the bottom of each pair of bands and identify their distinct signature in the evolution of the Edelstein response with the filling of the system. Using perturbation theory, we can quantitatively evaluate the role of these two types of texture in the Edelstein response near peculiar points of the band structure. Fig. IV.3 a shows these points : A (●), B (◆) and C (■) are located at the bottom of bands L, N and U. D (▲) and E(▼) are the avoided and topological band crossings. At low fillings, the response is dominated by the intraband part, while the interband part dominates at higher fillings. For one of the bands, the intraband part can be neglected in front of the interband part, and only emerges due to the anisotropy of the model. The multi-orbital nature of the system is responsible for the unusual variations

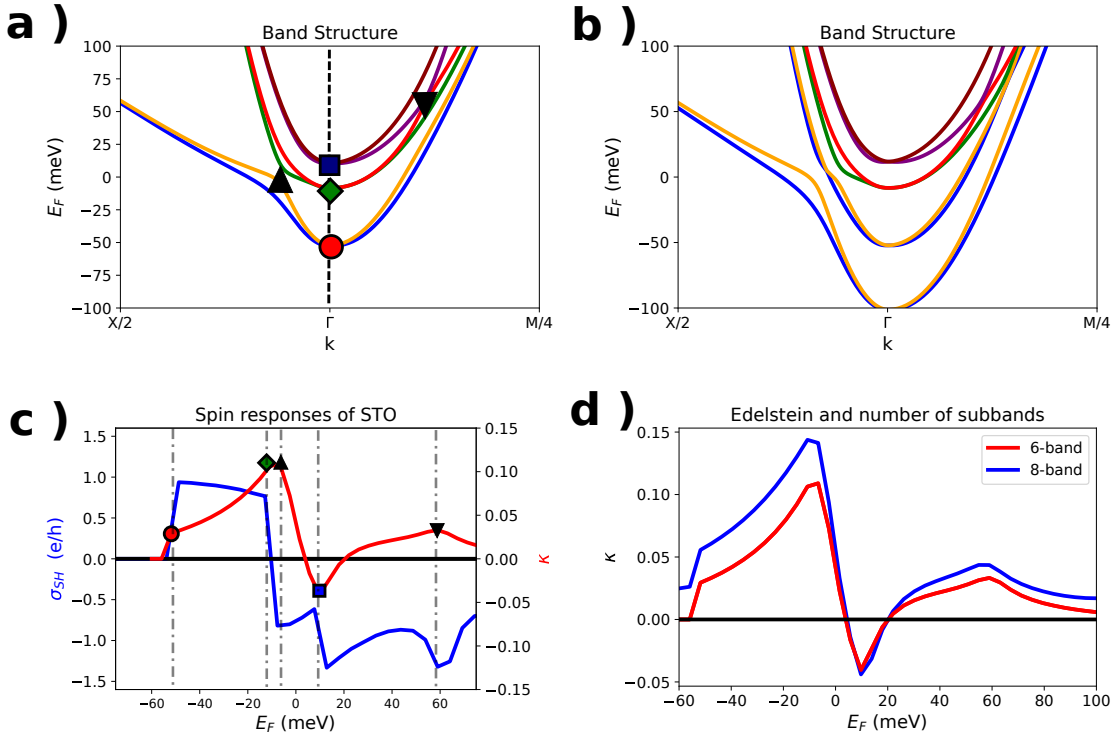

Fig. IV.3 a) Band structure of the 6-band model for STO. b) Band structure of the 8-band model of STO. The parameters are $t_1 = 388$ meV, $t_2 = 30$ meV, $\Delta = 50$ meV, $\tilde{\Delta} = 100$ meV, $\lambda_{SO} = 8$ meV and $\gamma_{OM} = \tilde{\gamma}_{OM} = 20$ meV. c) Edelstein and Spin Hall response as a function of the Fermi energy. Special points of the band structure are depicted with the same symbols as in a. A (●), B (◆) and C (■) are located at the bottom of bands L, N and U. D (▲) and E(▼) are the avoided and topological band crossings. d) Evolution of the Edelstein response with the Fermi energy in a 6- or 8-band model.

of the response. The emergence of complex spin textures is a common feature to the oxides and the amplitude of the expected response can be linked to the quantity $\zeta = \frac{\Delta}{\lambda_{SO}}$, the ratio between the atomic spin-orbit coupling and the confinement gap.

IV.3.1 MISO Hamiltonian

As explained in Chapter II, the Hamiltonian for TMO heterostructures can be split into four parts :

— Kinetic energy, coming from the tight-binding approximation and including nearest-neighbor hopping.

— Electrostatic confinement, splitting the t_{2g} orbitals according to their symmetry with respect to the interface.

— Atomic spin-orbit coupling, entangling the orbital momentum and the spin of the electron.

— Orbital mixing, entangling the orbital character and the wavevector of the electron.

The compounded effects of the orbital mixing and of the atomic spin-orbit coupling induce a spin-momentum locking of the electron : indeed, the orbital character and the spin are entangled by the atomic spin-orbit coupling, while the orbital character and the wavevector are entangled by the orbital mixing. The kinetic energy and the confinement gap induce an orbital polarization of the system and influence the amplitude of the response ; these quantities change inside the band structure, which is why the properties of the material vary with filling. In the following, we explain the origin of the spintronic properties of the model. We start by rewriting the Hamiltonian in a form displaying explicit spin-momentum locking terms. To do so, we make a low-energy expansion of the Hamiltonian in the vicinity of Γ, using extensively the low-k expansions $1-\cos(ka) \approx \frac{k^2a^2}{2}$ and $\sin(ka) \approx ka$. Near Γ the eigenenergies and eigenvectors can be analytically determined. We then compute the action of the orbital mixing and kinetic energy on these states away from Γ.

Because of Time-Reversal Symmetry, there are three doubly degenerate eigenstates at the Γ point that we label by a band index L, N or U and a spin index $\uparrow,\downarrow$. The eigenenergies are

$$\begin{aligned}
\epsilon_N &= -\lambda_{SO} \\
\epsilon_L &= \frac{1}{2}\left(-\Delta + \lambda_{SO} - \sqrt{\Delta^2 + 2\Delta\lambda_{SO} + 9\lambda_{SO}^2}\right) \\
\epsilon_U &= \frac{1}{2}\left(-\Delta + \lambda_{SO} + \sqrt{\Delta^2 + 2\Delta\lambda_{SO} + 9\lambda_{SO}^2}\right)
\end{aligned} \tag{IV.7}$$

With Δ the confinement gap and λ_{SO} the atomic spin-orbit coupling. We call the basis of these eigenvectors $\mathcal{B}_0 = (N\uparrow, N\downarrow, L\uparrow, L\downarrow, U\uparrow, U\downarrow)$. They are explicitly written in Appendix B.1. The letters N, L and U stand respectively for Neutral, Lower and Upper bands. For $\Delta > -\lambda_{SO}$, the L bands are the lowest in energy. We use this basis as an approximation of the eigenvectors of the full Hamiltonian, and treat the kinetic terms as a perturbation, splitting them in two parts : an isotropic and an anisotropic part, denoted

using $t_0 = \frac{t_1+t_2}{2}$ and $\delta t = \frac{t_1-t_2}{2}$. The isotropic part of the kinetic energy is $(t_0 + \delta t)a^2k^2$ for the d_{xy} orbital and $t_0a^2k^2$ for the $d_{xz/yz}$ orbital. The anisotropic part of the kinetic energy is 0 for the d_{xy} orbital and $\delta t a^2k^2\cos(2\theta)$ (respectively $-\delta t a^2k^2\cos(2\theta)$) for the d_{yz} orbital (for the d_{xz} orbital), where θ is the polar angle of the wavevector. The isotropic part has a diagonal part in the orbital space $t_0a^2k^2$, and a part that can be integrated in the confinement gap to produce an effective gap $\Delta_k = \Delta - \delta t a^2k^2$. We later discuss the impact of the k-dependence of Δ and first neglect its variation, and also neglect the anisotropies in order to understand the effect of the orbital mixing on the Hamiltonian. The diagonal part of the dispersion must be kept to get a correct shape for the Fermi surface. In the basis $\mathcal{B}_0$, the Hamiltonian $\mathcal{H}_{MISO} = \mathcal{H}_{kin}^{diag} + \mathcal{H}_{conf} + \mathcal{H}_{SO} + \mathcal{H}_{OM}$ reads

$$\begin{bmatrix} E_N & 0 & -B_L a k_- & 0 & 0 & -B_U a k_- \\ 0 & E_N & 0 & B_L a k_+ & B_U a k_+ & 0 \\ -B_L a k_+ & 0 & E_L & -iA_L a k_- & iCak_- & 0 \\ 0 & B_L a k_- & iA_L a k_+ & E_L & 0 & -iCak_+ \\ 0 & B_U a k_- & -iCak_+ & 0 & E_U & -iA_U a k_+ \\ -B_U a k_+ & 0 & 0 & iCak_- & iA_U a k_- & E_U \end{bmatrix} \tag{IV.8}$$

Using the notations $B_L = \sqrt{1 + \frac{1+\zeta}{s}}\gamma_{OM}$, $B_U = \sqrt{1 - \frac{1+\zeta}{s}}\gamma_{OM}$, $A_L = A_U = \frac{4}{s}\gamma_{OM}$ and $C = \frac{\sqrt{2}(\zeta+1)}{s}\gamma_{OM}$. The quantity $\zeta = \frac{\Delta}{\lambda_{SO}}$ is the ratio between the confinement energy and the atomic spin-orbit coupling, and $s = \sqrt{\zeta^2 + 2\zeta + 9}$ is the ratio of the gap between the L and U band at Γ and the atomic spin-orbit coupling. E_N, E_L, E_U are the kinetic energies of bands N, L and U and contain the energy at Γ given by Eq. IV.7 and $E_0 = t_0a^2k^2$. Eq. IV.8 shows that the L and U bands host a Rashba-like coupling, whose intensities are equal $A_L = A_U$. These two sets of bands are also coupled with one another and to the N bands through terms proportional to the orbital mixing intensity and the wavevector that can involve a change of the spin character of states. The N bands have no direct coupling between one another but are coupled to the L and U bands. These two forms of coupling influence the spin textures : couplings proportional to $k_\pm = k_x \pm ik_y$ involving a spin flip look like Rashba couplings, and are indeed responsible for the spin-momentum locking of the electrons.

IV.3.2 Intertwining of spin textures

The complex spin-orbital character of the MISO Hamiltonian given by Eq. IV.8 produces a superposition of spin textures inside the Brillouin Zone. In the absence of orbital mixing, there are three energy levels : L, N and U. In order to analytically compute the spin textures, we approximate that the bands keep the orbital nature they have at Γ with no orbital mixing nor anisotropy, meaning that $\mathcal{B}_k = (L_k, N_k, U_k) \approx \mathcal{B}_0$. This amounts to neglecting the change of the confinement gap when going away from Γ. The orbital mixing produces terms that either couple states belonging to the same level (intraband couplings) or states of distinct levels split in energy (interband couplings). Both these couplings produce winding spin textures with opposite directions between the bands they couple. If we focus on the (L,N) manifold, there are four bands to consider (L_+, L_-, N_+, N_-). The intraband term for the L bands induces a relative texture between L_+ and L_- (winding in an opposite direction between the two bands), while the terms coupling the L and N bands induce a relative texture within the subsets (N_+, L_+) and (N_-, L_-). The direction of this interband texture is opposite between the N and L bands, but both the L_+ and L_- bands have their interband texture winding in the same direction, creating an overall non-zero interband texture for the L bands.

To generalize this notion of intraband and interband texture, terms such as the orbital mixing or the anisotropy are treated as perturbations for low k. A band ν of the total Hamiltonian keeps a dominant character of one the bands L, N or U. We split the unity operator into the different band projectors $\mathbb{I} = \sum_{A=L,N,U} P_A$ where $P_A = \sum_{\sigma=\uparrow,\downarrow} |A\sigma\rangle\langle A\sigma|$ and decompose the expectation value of the spin operator for band ν as

$$\begin{aligned}\langle \vec{S} \rangle_\nu = \langle \nu | P_A \vec{S} P_A | \nu \rangle &+ \sum_{B \neq A} \langle \nu | P_B \vec{S} P_A + P_A \vec{S} P_B | \nu \rangle \\ &+ \sum_{B,C \neq A} \langle \nu | P_B \vec{S} P_C + P_C \vec{S} P_B | \nu \rangle\end{aligned} \tag{IV.9}$$

Here A is the dominant band character of ν in the $\mathcal{B}_0$ basis. The first term in the sum is what we call the intraband contribution to the spin and is responsible for the Rashba-Edelstein effect. The second term takes into account the transitions between A and another set of bands : it is a first order perturbation on the orbital mixing term, and is related to

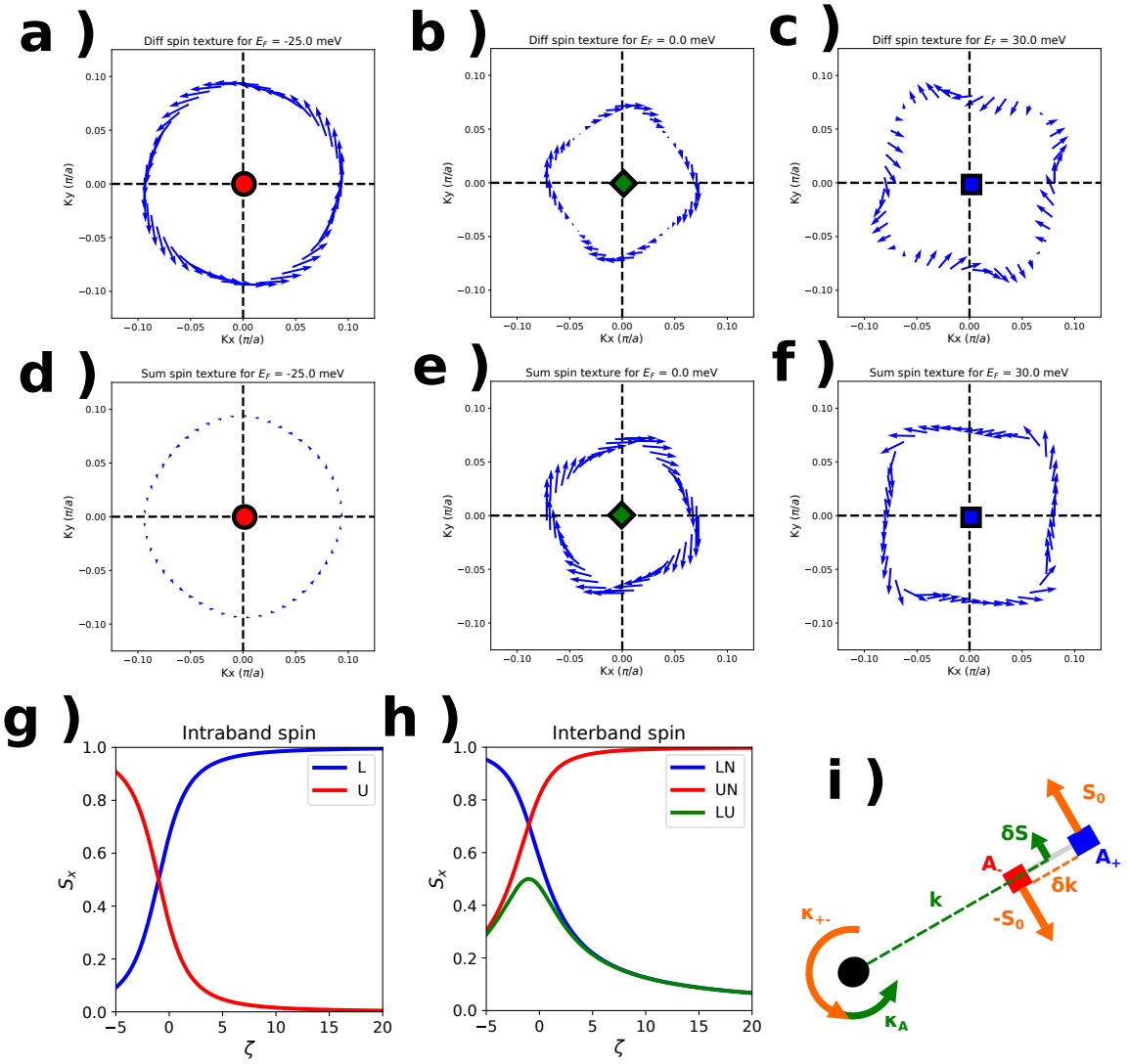

Fig. IV.4 a-c) Intraband and d-f) interband spin textures for the L, N and U pairs of bands near the bottom of the bands. The scale of the arrow for the interband spin textures has been magnified compared to the intraband spin textures. The symbols put at the Γ point are similar to the symbols of Fig. IV.3 a. g-h) length of the intraband and interband spin texture in the ΓM direction as a function of ζ. i) Depiction of the intraband (κ_{+-}) and interband (κ_A) contribution to the Edelstein tensor in a lever arm picture.

the geometry of the bands relatively to the form of the orbital mixing. The third term is a second order perturbation of the orbital mixing so we neglect it. To evaluate Eq. IV.9, we compute the spin operator in the $\mathcal{B}_0 = (N\uparrow, N\downarrow, L\uparrow, L\downarrow, U\uparrow, U\downarrow)$ basis. Noting $\zeta = \frac{\Delta}{\lambda_{SO}}$ and $s = \sqrt{\zeta^2 + 2\zeta + 9}$, we have

$$S_x = \begin{pmatrix} 0 & 0 & iv & 0 & 0 & iz \\ 0 & 0 & 0 & iv & iz & 0 \\ -iv & 0 & 0 & u & x & 0 \\ 0 & -iv & u & 0 & 0 & x \\ 0 & -iz & x & 0 & 0 & y \\ -iz & 0 & 0 & x & y & 0 \end{pmatrix} \tag{IV.10}$$

With $u = \frac{1}{2}\left(1 + \frac{1+\zeta}{s}\right)$ and $v = \frac{\sqrt{2}}{2}\sqrt{1 - \frac{1+\zeta}{s}}$, $x = \frac{\sqrt{2}}{s}$, $y = \frac{1}{2}\left(1 - \frac{1+\zeta}{s}\right)$, $z = \frac{\sqrt{2}}{2}\sqrt{1 + \frac{1+\zeta}{s}}$. S_y has a similar form to S_x.

Fig IV.4 a-c show the intraband textures of respectively the L, N and U bands near Γ while Fig. IV.4 d-f show the interband spin textures of the same bands. For the L bands, the intraband spin texture is typical of a Rashba-like model, while the interband part can barely be seen. It is however non-zero in STO and is small because the interband textures of bands L induced by the bands N and U almost cancel each other for this set of parameters. For the N bands, the intraband part is smaller than the interband part. The intraband part varies with the direction of the wavevector, and cancels at the angles $\pm\frac{\pi}{4}, \pm\frac{3\pi}{4}$, whereas the interband texture length is more homogeneous with the direction of the wavevector. The Fermi surface of the N bands is anisotropic and has a diamond-like shape. For the U bands, the length of the intraband and interband spin texture is comparable, and the Fermi surface has a square-like shape. The intraband texture presents variations with the direction of the wavevector, and looks like an anti-vortex with π-domains in the ΓM direction. The L and U textures wind in the same direction, opposite to the one of the N band. This explains why the Edelstein response of STO goes either up or down at the arrival of new bands.

Fig. IV.4 g and h show the amplitude the matrix elements of the S_x operator (g for the intraband and h for the interband) as a function of ζ. In the STO interface, $\zeta \approx 12$ for the lower d_{xy} subband and $\zeta \approx 6$ for the higher d_{xy} level ; the lower subband contributes less to

the Edelstein response and its effect can be neglected on a qualitative level. The L and U intraband part have opposite variations. As shown by the spin textures, the interband part for the L bands nearly cancel due to the almost equal values of the LN and LU interband part, while this is not the case for the UN/LU interband parts. Using the framework of Eq. IV.9 and IV.3, the Edelstein response can be rewritten as a sum of two contributions for any sets of bands

$$\kappa = \kappa_R + \kappa_{MB} = \frac{e\tau_0}{h} \int d\theta \left[\delta k_F^\theta S_0(\zeta, E_F, \theta) + k_F^\theta \delta S_0(\zeta, E_F, \theta) \right] \tag{IV.11}$$

Where δk_F^θ is the splitting of the Fermi wavevector between the two bands of the set, k_F^θ is the mean Fermi wavevector of this set, and $S_0(\zeta, E_F, \theta), \delta S_0(\zeta, E_F, \theta)$ are respectively the intraband and interband part of the spin texture for the set of bands. All these quantities depend on the polar angle of the wavevector θ. For the L bands the θ-dependence can be neglected as the system is essentially isotropic : one gets a nice approximation of κ by taking the value of the integrand corresponding to $\theta = \frac{\pi}{4}$ (the ΓM direction). The Rashba-Edelstein response κ_R is the main contribution very close to A, but it becomes dominated by the multiband contribution κ_{MB} upon increasing the filling even slightly, because then $\delta k << k$. The multiband contribution κ_{MB} is a distinctive signature of the MISO term. The Rashba-like winding textures of S_0 that one gets for band L is intraband, and the textures of δS_0 resulting from matrix elements between bands L and N , L and U and N and U are interband. The multi-band response is a feature of the interband couplings and is proportional to k_F. Eq. IV.11 can be explained in the light of the analogy with torques and moment arm developed in Section IV.3 by decomposing the system into subgroups of bands. The intraband response is the torque coming from the forces internal to a subset of bands while the interband response is the torque emerging from forces external to a subset of bands applied to its center of mass. This principle is depicted in Fig. IV.4 i : the torque κ_{+-} exerted by the orange arrow on the black dot axis is due to the lever arm separating $A+$ and $A-$ while the torque κ_A exerted by the green arrow is applied to the center of mass of the system $A+/A-$.

For a Rashba model, $k_F \approx \sqrt{\frac{2mE_F}{\hbar^2}}$ while $\delta k = \frac{m\alpha_R}{\hbar^2}$ so $\delta k << k$ only as long as $E_F << \frac{m\alpha_R^2}{\hbar^2} = E_R$, which is typically a small energy scale. However, in such a model the interband spin texture is zero, explaining why its effects are not usually seen. In physical systems,

the interband spin texture might be non-zero but still have negligible effects compared to the intraband response. Using [155, 79], ζ can be estimated for usual semi-conductors : $\zeta(AlP) \approx 30$, $\zeta(GaAs) \approx 15$, $\zeta(InSb) \approx 12$, which are bigger than $\zeta(STO) \approx 6$, so the aforementioned effects shall be smaller to non-existent.

Contributions due to the couplings of L to N and U are encoded in κ_{MB}. Within each band, spin textures of the time-reversed Kramers branches wind in opposite direction. The total winding in each branch is a superposition of two patterns : the intraband described by S_0, and the interband described by δS_0. For the two Kramers partners, the intraband pattern winds in opposite directions, while the interband pattern winds in the same direction. This decomposition of the EE response in two parts is valid for all bands, and also holds in the presence of several subbands. For E_F between A and B, Eq. IV.11 can be analytically evaluated using an isotropic approximation and cast in the form

$$\kappa = \frac{e\tau m^*}{\hbar^3}\gamma_{OM} a g(\zeta, E_F) \tag{IV.12}$$

Where τ is the scattering time, m^* the effective mass and $g(\zeta, E_F)$ is a band structure dependent factor taking into account both intraband and interband effects. Eq. IV.12 may be interpreted as the Rashba-Edelstein response of a system with an effective Rashba coefficient $\alpha_{eff} = \gamma_{OM} a g(\zeta, E_F)$ that depends on E_F. It is commonly stated that the LAO/STO interface is subject to an effective Rashba coupling, the intensity of which strongly varies with the chemical potential in the vicinity of avoided crossings in the band structure [82]. This approach points to an alternative explanation where spin textures play a prominent role, and the spin-orbital structure of the eigenfunctions is critical to explain the variations of α_{eff} with E_F.

IV.3.3 Evolution of the Edelstein effect with filling

a) Before the Lifshitz transition

We study the evolution of the Edelstein response of the system between point A (the bottom of the L bands) and B (the Lifshitz transition, bottom of the N bands), which is the region where only two bands are populated. It is often argued that due to the complex multiband nature of the STO system, its Rashba coefficient varies [52, 156, 157]. Eq. IV.8

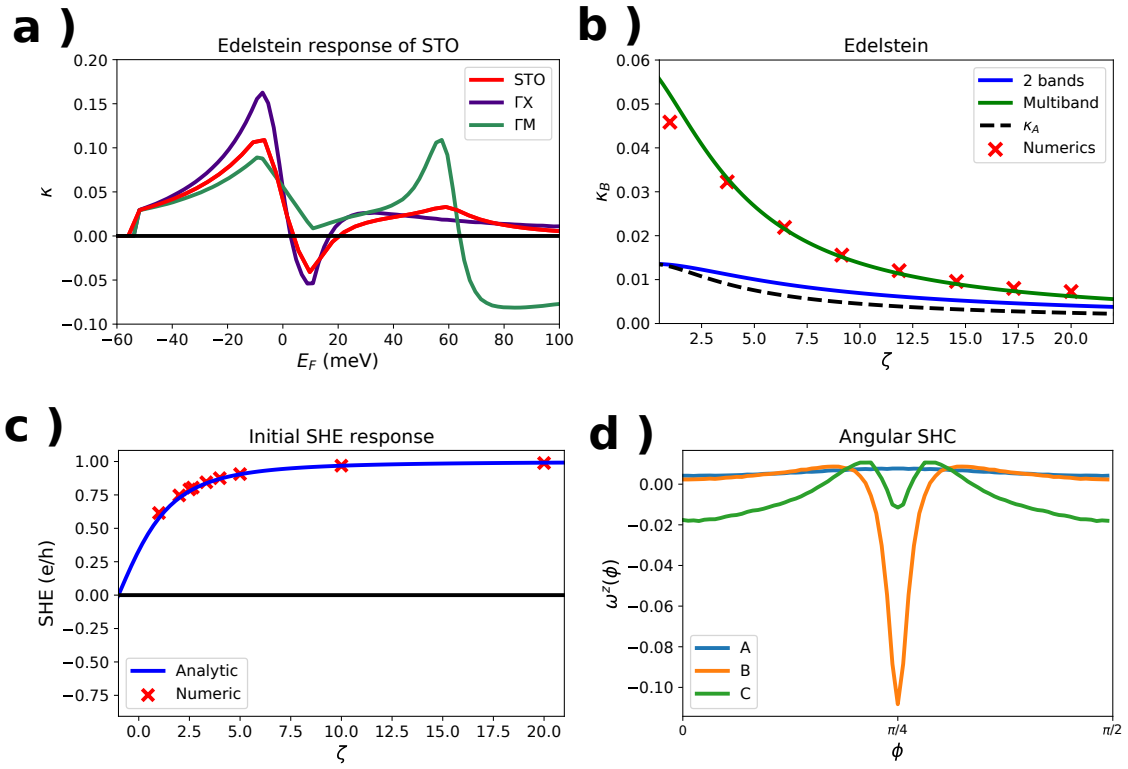

Fig. IV.5 a) Edelstein response of STO estimated from single directions inside the BZ, compared to the full Edelstein response (in red). b) Variation of the amplitude of the Edelstein value at point A and point B (the Lifshitz transition), as a function of ζ. The parameters are the same as in Fig. IV.3, only the value of λ_{SO} is changed to vary ζ in b and c. c) Amplitude of the first plateau of the SHE as a function of ζ. Numerical results are compared to the analytical form derived from Eq. IV.13. d) Angular variation of the SHC near special points of the band structure.

and IV.10 show that the Rashba-like coupling of the L bands and the expected value of the S_x operator indeed vary with ζ. To estimate the effects of this varying band structure, we rewrite $\zeta \to \zeta - \frac{\delta t a k^2}{\lambda_{SO}}$ in order to take into account the distinct dispersion of the t_{2g} orbitals. We compute the effect of the variation of ζ on the Rashba-like part of the response to gauge whether it can account for the increase of the EE between A and B. As the L bands mainly remain of d_{xy} orbital character near Γ, they have a nearly isotropic dispersion relation for low k. Near A, we perform a low-energy expansion of the Hamiltonian with an isotropic dispersion and use Eq. IV.11 to analytically evaluate its intraband part. These corrections are insufficient to reproduce the value of κ at point B as shown by Fig. IV.5 b. The numerical

value κ_B, displayed in red crosses, is compared to the intraband response at B along ΓM given by the first part of IV.11 in blue, and to the full multiband response at B along ΓM in green. The intraband response is not significantly changed between A and B while the full multiband response reproduces well the response. This seems to indicate that the system cannot be considered as a Rashba model with a varying Rashba coefficient (which would correspond to a full intraband response), but rather that multiband terms play a prominent role in the spin-orbit coupling, as a direct consequence of the form of the MISO. The values of the Edelstein response at point A and point B depend on ζ and are typical of the amplitude of the response, and are maximal for low ζ, when the spin-orbit coupling dominates the confinement energy. The big increase of the Edelstein Effect between A and B for a wide range of ζ shows that the interband spin texture can be the driving force of the amplitude of the Edelstein Effect, even though the length of the interband spin texture is small.

b) The N bands and the role of anisotropy

Fig. IV.5 a shows the variations of the Edelstein response with the Fermi energy given by Eq. IV.11. The full response of STO is compared to the value of the integrand for the directions ΓX and ΓM : between A and B, the Edelstein response is well described by an isotropic approximation, but above B the ΓX direction becomes of importance and further terms of the model have to be taken into account. We understand the Edelstein response for the N bands using the same approach of low-energy Hamiltonian. The absence of intraband matrix elements of the S_x operator inside the N levels in Eq. IV.8 seems to contradict the presence of an intraband spin texture in Fig. IV.4 b. In the ΓM direction the intraband part is indeed zero, but the intraband texture presents anisotropy, so that the intraband texture of the N bands is driven by the anisotropy of the band structure. We treat the anisotropy of the dispersion as a perturbation to the Hamiltonian of Eq. IV.8, and infer a 2-band model for the N bands to compute the intraband contribution to the Edelstein Effect. After tedious algebra, detailed in Appendix B.3, one finds $\kappa_N^{intra} \approx \frac{2ze\tau}{\hbar a}\frac{t_\alpha^2 B_U}{t_0^3}\frac{(E_F-E_N)^2}{D^2}$, where $D = E_U - E_N$ is the gap between N and U and $t_\alpha = \frac{\sqrt{2}}{2}\sqrt{1+\frac{1+\zeta}{s}}\delta t$. On the other hand, the interband part of the spin texture does not depend on the presence of anisotropy and is driven by transitions to the U bands as hinted by Fig. IV.4 h. Using perturbation theory, we get $\delta S_x = -\delta S_y = \delta S = -\frac{2zB_U ak}{D}$, and find $\kappa_N^{inter} \approx \frac{2ze\tau}{a\hbar}\frac{B_U}{t_0}\frac{(E_F-E_N)}{D}$: the interband part

dominates the intraband part at low fillings for the N bands. They have a different behavior from the L bands and are strongly affected by the multi-band nature of the Hamiltonian. The intraband part of the Edelstein response is zero in the absence of the anisotropy.

c) Higher fillings and band crossings

At higher fillings, the U bands begin to be populated and to add their contribution to the Edelstein response, which is positive because of the direction in which its texture winds. The band crossings produce a complicated form of spin-orbit coupling in their vicinity and impact the spin textures of the bands, at least locally in k-space, explaining why there are saturating values in their vicinity. As these contributions are localized in k-space it is difficult to find relevant low-energy models to evaluate their impact on the Edelstein response ; the interband/intraband language becomes irrelevant as many bands are involved.

IV.4 Intrinsic Spin Hall Effect

IV.4.1 Plateaus of the intrinsic SHE in STO

Fig. IV.3 c shows that the amplitude of the SHE presents important variations in the vicinity of the special points of the band structure A, B, C, D and E, corresponding to the symbols of Fig. IV.3 a : A (●), B (◆) and C (■) are located at the bottom of bands L, N and U. D (▲) and E(▼) are the avoided and topological band crossings. Between these points, the response smoothly varies. The apparent jumps in the SHC are due to the small energy scale of its variations : for a Linear Rashba Model (LRM), the SHC reaches a plateau in a scale of energy $E_R = \frac{m\alpha_R^2}{\hbar^2}$; for STO this energy is of the order of $m^* \frac{\gamma_{OM}^2 a^2}{\hbar^2}$, which is too small to be resolved compared to the other energy scales of the band structure. Taking $m^* = m_e$, $\gamma_{OM} = 20meV$ and $a = 3.905\mathring{A}$, one gets $E_R \approx 0.5meV$, a negligible energy compared to the sensitivity of experiments. Contrarily to the case of the LRM, the value of the first plateau of the SHC (the response of the L bands around point A) is less than 1 in units of $\frac{e}{\hbar}$. Fig. IV.5 c shows the computed SHC for various values of the spin-orbit coupling in order to track the variations of the SHC with respect to ζ (the other parameters are the same as STO, detailed in Table IV.1). The amplitude of the plateau can be related to the properties

of the z component of the spin operator : the S_z operator in the $\mathcal{B}_0$ basis reads

$$S_z = \begin{pmatrix} 1 & 0 & 0 & 0 & 0 & 0 \\ 0 & -1 & 0 & 0 & 0 & 0 \\ 0 & 0 & w & 0 & 0 & r \\ 0 & 0 & 0 & -w & -r & 0 \\ 0 & 0 & 0 & -r & w & 0 \\ 0 & 0 & r & 0 & 0 & -w \end{pmatrix} \tag{IV.13}$$

With $w = \frac{1+\zeta}{s}, r = \frac{2\sqrt{2}}{s}$. Fig. IV.5 c shows w as a function of ζ, and matches the numerical values obtained of the SHC near A. The amplitude of the SHC near A comes from the incomplete projection of the S_z operator which is due to the form of the spin-orbit coupling. The S_z operator does not couple the N bands with the L and U bands, while the L and U bands are coupled between them through a term r. The partial spin projections of the L and U bands are equal so the amplitude of the jump in SHC at point C is the same as at point A. For the L and U bands, the mechanism producing the SHC is the same as in a Rashba model, at least regarding the presence of plateaus. For N bands, the detailed form of the eigenvectors in the presence of anisotropy and orbital mixing are required in order to be able and evaluate the height of the plateau, and computations presented in Appendix B.4 show that the value of the plateau associated to the N bands is equal to -1, independently of the value of ζ, roughly matching with numerics. In the region near the Lifshitz transition, the band structure becomes very complicated due to the anisotropies and to the presence of band crossings very close ; as the U bands are close to the N bands in energy, it is hard to disentangle contributions one from another. The energy scale in which the approximations are valid is very narrow. The SHC signature around point D and E seem to indicate effects linked to band crossings. However, as for the EE, it is difficult to build effective models for these special contributions represent only a small fraction of the BZ, and the complex band structure produces a very complicated domain for the integration of the Spin curvature.

Fig. IV.5 d shows the angular dependence of the SHC around peculiar points of the band structure (the parameters are $t_1 = 388$ meV, $t_2 = 30$ meV, $\Delta = 50$ meV, $\lambda_{SO} = 8$ meV and $\gamma_{OM} = 20$ meV) through the quantity $\omega^z(\theta)$ defined by $\omega^z(\theta) = \sum_\nu \int k dk \Omega^z_\nu f_{\nu k}(E_F)$, with θ

the direction of the wavevectors ; it is the partial integration of Eq. IV.6 over the bands and the modulus of the wavevectors. The angular dependence is shown at Fermi energies lying just above the points A, B and C of the band structure, and is only shown for θ between 0 and $\pi/2$ because there is a four-fold symmetry. Around point A the SHC is nearly isotropic, while strong anisotropic features emerge near B. In particular, the response of the N bands peaks in the $\theta = \frac{\pi}{4}$ direction (ΓM), consistently with the analytical computations of the Appendix B.3. After point C the situation is more complicated, but new contributions are more homogeneous.

IV.4.2 Extrinsic SHE

The effects of disorder on SHE are still debated in the literature, as they are already difficult to quantify in the study of the AHE [152, 154, 151]. The two main extrinsic mechanisms with a significant impact on the SHE are the side-jump and the skew-scattering. Both are linked to scattering events ; however their net contribution can be independent of the scattering time, while their amplitude is comparable to the intrinsic part. For the Rashba model, it is expected that the side-jump part is exactly opposite to the intrinsic part and cancels it. These two mechanisms come from vertex corrections to the current operator. A scattering event changes the wavevector k_0 of an electron to k_1 without impacting the other quantum numbers for a simple scattering potential $\hat{V}$ diagonal in the band space, and the resulting eigenstate at wavevector k_1 is no longer guaranteed to be an eigenstate of the Hamiltonian. The mixed nature of the eigenstates after scattering events produces additional interband terms to the operators, called the vertex corrections. They depend on the details of the scattering mechanisms, which are unknown apart from some elementary approximations. The side-jump contribution comes from the lateral displacement of electrons between collisions, while the skew-scattering is an effect due to asymmetry in scattering mechanisms of the electrons. These terms are detailed in Appendix B.6 and they are derived in [158, 151]. In Appendix B.5, we show the role of the presence of a decay rate that in the denominator of Eq. IV.5 defining the spin curvature, suggesting that that the intrinsic contribution is diminished by disorder for a Rashba model. For STO-based interfaces, surface roughness should impact more the states closer to the interface (lower in energy), to the point that the contribution to SHC of the first d_{xy} band might be washed out by disorder.

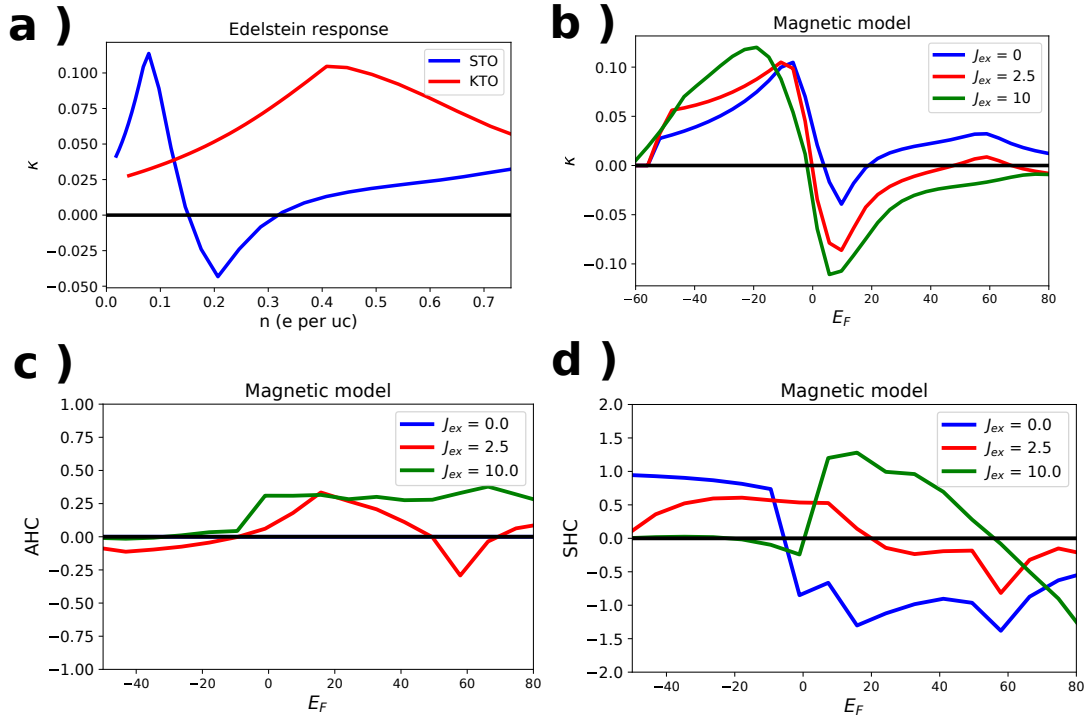

Fig. IV.6 a) Edelstein response as a function of the density of electrons for STO and KTO. Parameters are taken from Table IV.1. b,c,d) Edelstein, Spin Hall and Anomalous Hall response of a magnetic STO model as a function of the Fermi energy, the parameters are the same as in the whole chapter, with the addition of an exchange field J_{ex}.

IV.5 Response of other Transition Metal Oxides

IV.5.1 The case of another oxide : $KaTaO_3$

The same model can be applied to other oxides to see whether the spintronic responses present the same features. This is useful for applications in order to determine which oxides can yield the biggest response. Using the values of the parameters detailed in Table IV.1, we compute the Edelstein response for $KaTaO_3$ (KTO) as a function of the density of carriers and compare it with the response of STO. KTO is an interesting oxide because it has a very large spin-orbit coupling. The Edelstein responses of both materials are shown in Fig. IV.6 a : the response of STO is more tunable, as it can take positive and negative values in a small regime of doping, while for KTO we only see an increase and the beginning of a

decrease of the amplitude of the Edelstein response. The amplitudes are similar but this is partly due to the value of the orbital mixing which is considered equal for STO and KTO (it is difficult to independently determine this quantity and it is not accurately known). These results show that the amplitude of the conversion through the mechanism of textures is of similar amplitude for STO and KTO, though the spin-orbit coupling of KTO is higher by one order of magnitude. Increasing the orbital mixing would increase mechanically the Edelstein response.

IV.5.2 Magnetic oxides

We do the same computations for a simple magnetic model to see the effect of a net spin polarization on the amplitude EE and SHE. For magnetic oxides, the presence of AHE is also expected. Magnetism is modeled by the addition of an exchange term $\mathcal{H}_{ex} = J_{ex}\sigma_z$ to the previous model as in [159]. Exchange fields of $J_{ex} = 2.5, 10$ meV are added to the model of STO to see what it changes in term of EE, SHE and AHE, and the results are displayed in Fig. IV.6 b-d. The Edelstein response is not qualitatively changed by the addition of this exchange field (the system stays in a weak exchange limit, though $J_{ex} = 10$ meV is more than the atomic spin-orbit coupling). AHC is expected as soon as an exchange field appears : it starts to be non zero above the Lifshitz transition, and it is more stable for a higher exchange field. The SHC signal is strongly impacted by the presence of an exchange field, and the shape of the curve is largely deformed with increasing the exchange field : for $J_{ex} = 10$ meV, the first plateau of SHC is destroyed.

Version du 19 novembre 2020, 16:35

V – The capping problem : a DFT study

> To doubt everything or to believe everything, are two equally convenient solutions ; both dispense with the necessity of reflection.
>
> Henri Poincaré,
> *Science and Hypothesis*

V.1 Introduction

LAO/STO interfaces are known to become metallic when there are more than four layers of LAO on top of the STO substrate. However, the respective roles of chemistry and electrostatics in the formation of the 2DEG at this interface or in other TMO heterostructures are hard to disentangle. Recent experiments [160, 161] show that the critical thickness of 4 LAO layers can be reduced with the addition of STO capping layers : if m LAO layers are put on top of the surface, the addition of n STO layers turns the system metallic provided the condition $m+n \geq 4$ is fulfilled. This observation, which we call the "capping problem", might help to unveil the mechanisms triggering the formation of 2DEGs at TMO interfaces. Indeed, the origin of the conductivity in the capped configuration is unclear : the additional STO capping layers are not polar and should not add any electrostatic field to the one created by the LAO layers in the polar catastrophe scenario. The oxygen vacancy scenario also fails to provide a clear explanation : there is no reason why the additional STO layers should favor

the creation of oxygen vacancies, let alone why the number of capping layers should have an influence. A last scenario which is often invoked to explain the creation of the gas at the interface is cation intermixing : the interfacial layer could be of mixed chemical composition, inducing some local defects to the structure which can have an electronic effect. If the first STO(bulk)/LAO interface is n-type, the topmost interface is p-type (is it LAO or STO terminated). It is recognized that these p-type interfaces are insulating and only the first n-type interface is metallic. Can the other interfaces play a role in these heterostructures ? In all, this problem stands as a good laboratory to test the different scenarios proposed to explain the formation of the 2DEG.

We address the capping problem using Density Functional Theory (DFT) and model the capped heterostructures in order to understand this behavior. After an analysis of the bulk STO and of the bare STO surface, we systematically try the different m and n cases. The layer-resolved structure of the DOS reveals how the Ti conduction and O valence bands are affected by the chemistry of the heterostructure. In particular, the LAO layers accumulate polar energy and the topmost STO layer provide an additional shift of the Fermi energy. The metallicity criterion is obtained for the 4+0 and 3+1 cases but fails to be explained in the cases 2+2 and 1+3. Moreover, the role of the number of STO layers is not clear. Lastly, we discuss the addition of defects in the heterostructures : if they indeed make the system metallic, they also raise new questions and do not allow us to explain all the features of this complex system. I would like to thank the group of Jean-Marc Triscone for the nice discussions about this project and the explanations of the experimental data [160].

V.2 Experiments : the capping problem

Fig. V.1 a is extracted from [67] and shows the evolution of the conductivity and number of charge carriers of a LAO/STO interface when n layers of LAO are put on top of a TiO_2-terminated STO substrate. The metal-to-insulator transition is clearly observed above the critical thickness of $m = 4$ unit cells of LAO, in agreement with the original discovery of [15]. It was also shown that the LAO/STO interface can be made metallic with only three unit cells of LAO on top of a STO substrate if the top surface is exposed to an additional electric field : using a tip, it is possible to pattern conductive paths on the top surface of LAO [162].

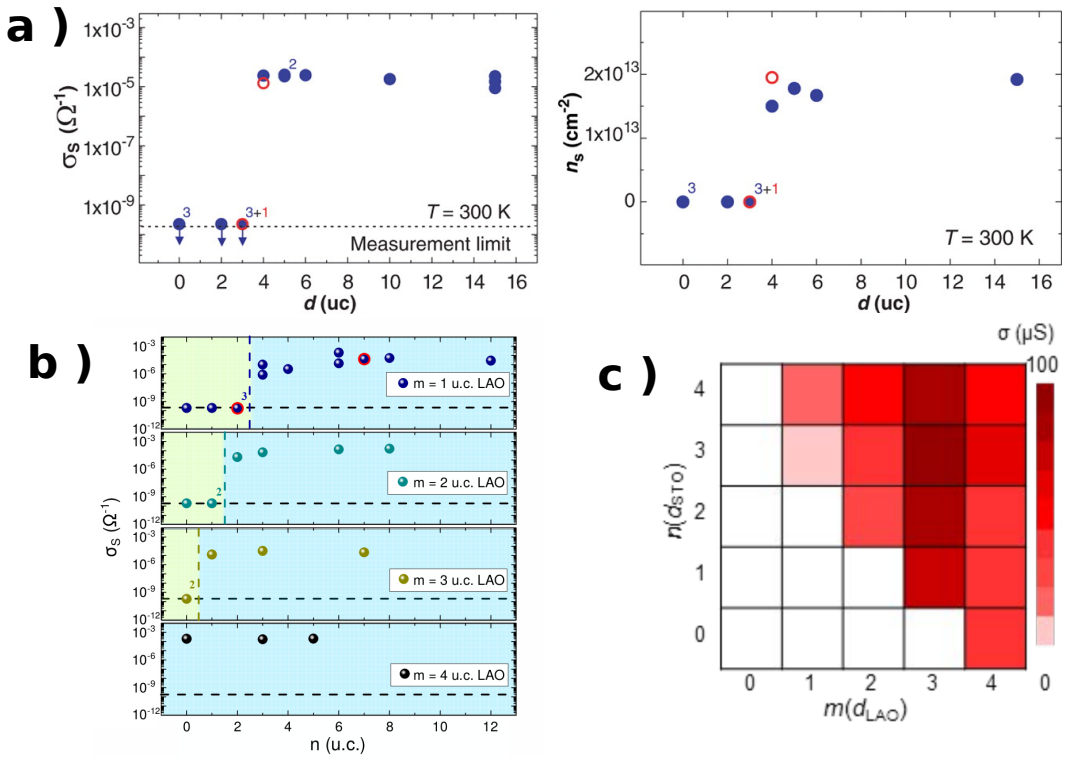

Fig. V.1 a) Sheet conductance and number of carriers in a LAO/STO heterostructures as a function of the number of the LAO layers from [67]. b) Sheet conductance of $STO_{bulk}/LAO_m/STO_n$ heterostructure as a function of the number n of STO capping layer for different values of the number m of LAO layers. The metal-to-insulator transition is represented by the dashed lines [160]. c) Map of the sheet conductance of $STO_{bulk}/LAO_m/STO_n$ heterostructure as a function of m and n. The white part corresponds to insulating behavior while the intensity of the red color represents the amplitude of the conductivity of the metallic state [161].

Additional capping layers of different materials on top of 3 unit cells of LAO can drive the sample towards a metallic state [163, 164, 165, 166]. In [167] they experimentally observe the formation of a 2DEG in the 2+2 case, and highlight a significant difference between the 2+1 and 2+2 case, depending on whether we refer to the experimental data or the DFT computations. Additional Hall experiments hint at the presence of simultaneous electron and hole transport, which are interpreted to occur in the different interfaces [167].

Recent experiments [160] shown in Fig. V.1 c reveal that the heterostructures $STO_{bulk}/LAO_m/STO_n$ become metallic if the criterion $n+m \geq 4$ is fulfilled. This result can also be found in [161], as shown in Fig. V.1 d, where the system is indeed metallic above the $n+m \geq 4$ condition.

If the cases $4+0$ and $3+1$ are more or less understood, it is not the case for the $2+2$ and $3+1$ cases ; they can reveal the role of chemistry and polarity in the emergence of a metallic phase. New experiments also show that heterostructures involving several LAO/STO interfaces can host electron gases in different parts of the structure [168]. These capped heterostructures thus are an interesting playground to design new devices ; finding out which mechanism triggers the metallicity can provide interesting insights to understand better the role of chemistry and polarity in the formation of a 2DEG at these interfaces.

V.3 Ab initio computations

V.3.1 Density Functional Theory

We briefly introduce the Density Functional Theory (DFT) approach that we use in order to study the capping problem via ab initio computations. Ab initio methods aim at the prediction of the properties of solids from their chemical formula, modeling individual atoms and their electronic cloud using electrostatics and quantum physics. The DFT scheme of approximation comes from the Hohenberg-Kohn theorem [169], which states that the energy of the ground state of a quantum system is a function of its electronic density, so that the ground state and its energy are uniquely defined by this density through the minimization of the energy

$$E[\rho(r)] = F[\rho(r)] + \int dr V_{ext}(r)\rho(r) \tag{V.1}$$

Where F denotes the electronic energy coming from both the kinetic energy and the interactions between electrons, and the second term denotes the energy from external potentials included in V_{ext} (from atoms, external electromagnetic fields etc). To find the electronic ground state, one must solve Eq. V.1, which is analogous to solving the many-body Schrodinger equation. As it is not possible to solve this problem exactly, various schemes of approximations are proposed in order to obtain numerical results in this framework. They primarily focus on the use of ansatz for the density functional F, which include both the electron-electron interactions and the kinetic energy. There are dozens of different functionals, among which the most popular are the Generalized Gradient Approximation (GGA), which can be enriched with a local Hubbard-like term (GGA+U).

V.3.2 Methods

The computations presented in this section were performed using the CRYSTAL code [170, 171], using the exchange functional WCGGA [172] and the correlation functional PBE [173]. The CRYSTAL code uses local, Gaussian orbitals to do the computations. It is a LCAO-like approach, contrarily to other software such as the Vienna Ab initio Simulation Package (VASP) which uses the Projector Augmented Wave (PAW) approach. The LCAO approach is more suitable to compute properties of insulators while the PAW approach is better suited for metallic states. The computations presented in this part use the same functionals as in several studies of LAO/STO heterostructures [174, 175, 110, 176, 177].

It is possible to compute the band structure along a given path in the Brillouin Zone. For the bulk of STO (which is 3-dimensional), we follow the Γ-X-M-W-Γ path, which represents all the high-symmetry directions of the Brillouin Zone for a cubic system (Γ = [0,0,0], X = [1/2,0,0], M = [1/2,1/2,0] and W = [1/2,1/2,1/2] in units of $\frac{\pi}{a}$). Heterostructures are 2-dimensional systems, so we study their band structure along the path Γ-X-M-Γ. The band structure is computed a posteriori using a finer K-mesh than the one used to compute the ground state of the system. The shrinking factor used to build the K-mesh of the 1x1 slabs with the Pack-Monkhorst method is 6, and 12 to determine the Fermi energy of the systems. It is also possible to compute the Density of States (DOS) and Partial Density of States (PDOS) of the system. The PDOS is the DOS projected on a single atom, or even a single orbital of one of the atoms. It is a very interesting quantity to study heterostructures since it allows to see where the weight of the electronic density is located and to resolve the orbital nature of the conduction and valence bands. As the heterostructures are modeled as symmetric slabs, we show the PDOS for positive values of z only.

V.3.3 Previous analysis of the capping problem

The capping problem has been studied using DFT in previous theoretical studies. In [167, 163] the authors focus on the case of 2 LAO layers and reproduce the metallic transition when 2 STO capping layers are put on top of the LAO. The addition of a first STO layer reduces the gap but not enough to induce metallicity, while the addition of a second layer overcomes the remaining gap and produces metallicity. Their study uses a GGA functional,

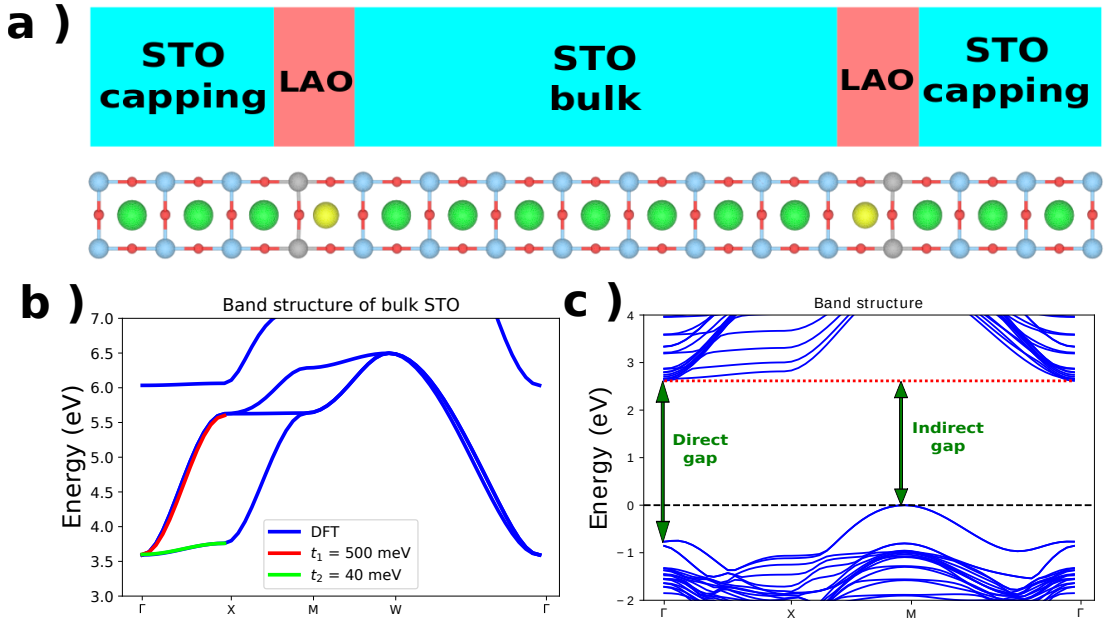

Fig. V.2 a) Geometry of the capping problem with 1 layer of LAO and 3 layers of STO capping. b) Band structure of the conduction band of the bulk of STO (lateral size 1x1x1) obtained from DFT. One can observe the e_g-t_{2g} split in energy and the tight-binding fit of the dispersion of the t_{2g} orbitals. The red curve is a cosine fit corresponding to $t = 500$ meV while the green fit is with $t = 40$ meV. The indirect gap is of 3.6 eV. The points forming the path in the Brillouin Zone are Γ = [0,0,0], X = [1/2,0,0], M = [1/2,1/2,0] and W = [1/2,1/2,1/2] in units of $\frac{\pi}{a}$. c) Band structure of the bare surface of STO in a 1x1 configuration.

which is known to underestimate the gap of oxide materials. In [161], they tackle the full capping problem using again a GGA functional and find the metallicity criterion. However, the gap of the capped structure linearly scales with the number of STO capping layer, which is unexpected for the STO layers should not add any polar energy. In [177], the problem is studied using hybrid functionals and additional oxygen vacancies defects. Though some interesting insights are gained into the role of the number of LAO layers on the reduction of the gap, a clear reason for the metallicity criterion is not found.

V.3.4 Geometry of the problem

In order to compute the electronic properties of a structure using DFT, we must specify the positions of the atoms (atoms are frozen in the Born-Oppenheimer approximation) and define a unit cell : the computation is extrapolated on an infinite crystal using periodic

boundary conditions. The unit cell must be tall enough so that it includes the relevant properties of the crystal. If a one-dimensional chain is known to present dimerization, it is necessary to put at least two atoms in the unit cell of the chain to observe the dimerization. Interfaces are not periodic in one of the directions. This is usually taken into account by adding a certain thickness of vacuum on top of the system. The system is made periodic in the direction perpendicular to the surface with this additional vaccuum layer : if the free surfaces are sufficiently far apart, they should not be affected by the presence of periodic copies, as long as there are no stray electric fields. The CRYSTAL code allows to fully take into account the 2-dimensional nature of the computation : there is no need for the additional vacuum. To avoid the presence of such fields in polar structures, it is advisable to take symmetric slabs of materials in order to cancel them. The positions of the atoms are fixed at each step of the computations. Once the solution to the electronic problem has converged, the code can try to modify the positions of the atoms in order to reduce the mechanical forces internal to the structure. On top of solving the electronic problem, the system also optimizes the crystal structure. This stage is fundamental for heterostructures which are not homogeneous systems : junctions between materials with different unit cell parameters and free surfaces induce distortions of the ideal case.

Fig. V.2 a shows the geometry of the capping problem for $STO_{bulk}/LAO_1/STO_3$. The bulk is taken wide enough in order to avoid that the two STO_{bulk}/LAO interfaces are influenced by one another. Fig. V.3 shows the PDOS of heterostructures with various m and n. Far from the interface, the Partial Density of States (PDOS) is similar through the STO layers, indicating that there are enough layers of STO to separate the interfaces and to consider that the middle behaves as the bulk of STO.

V.4 Electrostatics of interfaces

V.4.1 Bulk and surface STO

We first compute the electronic structure of the bulk of STO in order to compare with the results obtained in heterostructures. STO is cubic at room temperature, the linear size of its unit cell being $a = 3.905\mathring{A}$. The optical gap of STO is $\Delta = 3.2eV$ [178], and its direct gap is around 3.75 eV. Fig V.2 b shows the band structure obtained for a unit cell of STO.

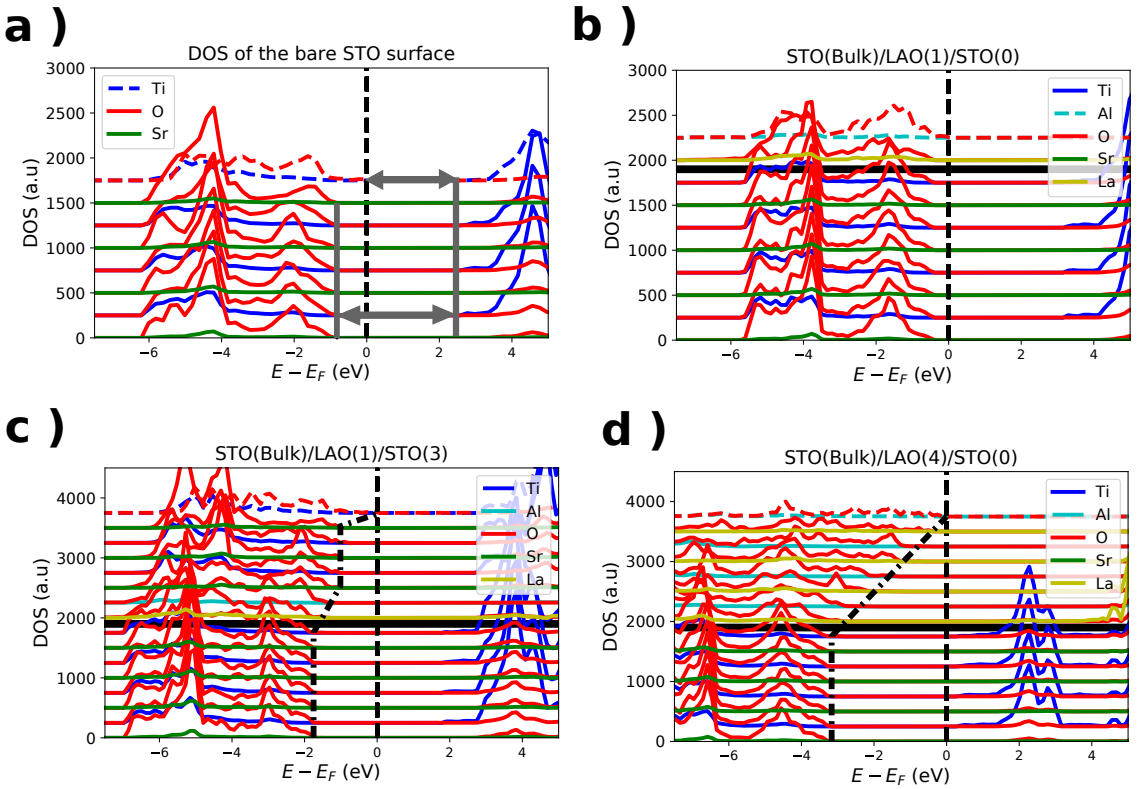

Fig. V.3 PDOS of several $STO_{bulk}/LAO_m/STO_n$ capped heterostructures for several values of m and n. a) bare STO surface ($m = 0, n = 0$). b) $m = 1$ LAO layer, $n = 0$ no capping STO layer. c) $m = 4$ LAO layers, $n = 0$ no capping STO layer. d) $m = 1$ LAO layer, $n = 3$ STO capping layers. The thick horizontal black line represents the interface between the bulk of STO and LAO, and the PDOS of the atoms belonging to the topmost interface are shown in dashed lines.

After geometrical optimization, the unit cell parameter is $a_{DFT} = 3.88\mathring{A}$ and the computed gap is around 3.6 eV. The computed lattice parameter is lower than in experiments, which in principle favors metallicity since it increases overlaps between orbitals ; this value is determined by various factors (the choice of the functional, of the basis and of the optimization scheme), so it is not surprising that the value slightly differs from the experimental value. In particular the WCGGA functional is known to underestimate the values of the unit cell parameter. One can observe the e_g/t_{2g} splitting and the t_{2g} structure of the conduction band. Indeed, the bands are not equivalent in the ΓX direction : two bands have a tight-binding dispersion with $t_1 \approx 500$ meV while one band disperses with $t_2 \approx 40$ meV. It is in agreement with the tight-binding description of t_{2g} orbitals in a perovskite environment presented in

m LAO	x	0	1	1	1	1	2	2	3	3	4
n STO	bulk	0	0	1	2	3	0	2	0	1	0
Gap (eV)	3.5	2.6	3.1	2.2	1.8	1.8	2.3	0.8	1.3	x	0.3

Table V.1 Table of the computed gap values for the different $m + n$ scenarios.

Chapter II. The corresponding effective masses are 0.5 and 6.2 in units of the electron mass are consistent with the experimental values determined by ARPES and the values used in Chapter II and IV. Results obtained with larger unit cells (2x2x2 and 2x2x4) of bulk STO are similar to the computations for a 1x1x1 unit cell. We did not try to model the tetragonal distortion of the bulk of STO that should occur below 105 K [179], though this step shall be important to correctly grasp the band structure of such bigger cells.

Fig. V.2 c shows the band structure of a slab of STO with lateral size 1x1. It is a symmetric slab of 7 layers of STO with a TiO_2 termination on both sides. The band structure displays an indirect gap of 2.6 eV and a direct gap of 3.4 eV. The cluster of bands at the bottom of the conduction bands is due to the layered structure of the system : each layer can participate to the conduction band, and small energy splittings emerge between the bands coming from each layer. The confinement gap can be estimated between 40 and 50 meV by looking at the energy levels at the Γ point. Fig. V.3 a shows the layered and atomically resolved PDOS of the bare surface of STO. Each layer is separated by a constant shift in the vertical axis for the sake of readability. The color code for each atom shows the alternating nature of SrO and TiO_2 layers in the structure. The conduction band is composed of the electrons of the Ti atoms while the valence band is composed of the electrons of the O atoms of the topmost layer. The direct gap matches the PDOS gap of the bulk STO layers of the system.

V.4.2 Varying n and m

We compute the electronic properties of the $m + n$ heterostructures with a 1x1 lateral size. The central STO part is 7 unit cells thick (2 x 3.5) with a TiO_2 termination. m LAO layers and n STO layers are put on top of the STO bulk (symmetrically on the bottom). The total slab is then terminated either by a TiO_2 free layer (if $n \neq 0$) or by an AlO_2 layer (if $n = 0$). A full mechanical relaxation of the structures is allowed during the optimization process before computing the band structure and the PDOS. The band structure and PDOS

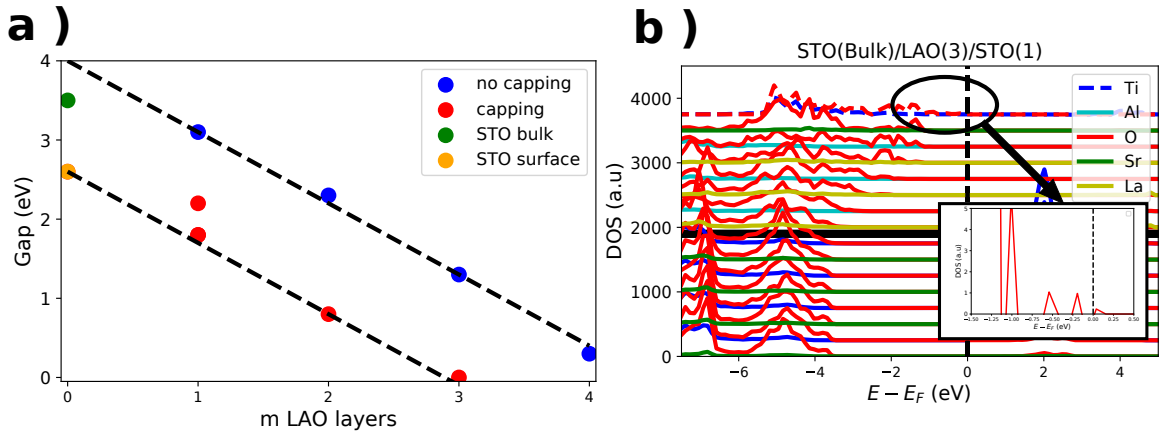

Fig. V.4 a) Gap of the $m+n$ heterostructures obtained via DFT. The red dots are with at least one layer of STO capping while the blue are for bare LAO surface. The values of the gaps are extracted from table V.1. The black dotted lines represent the linear approximation V.2. b) Atomically and layered resolved DOS for the $STO_{bulk}/LAO_3/STO_1$, found to be metallic. The thick horizontal black line represents the interface between the bulk of STO and LAO, and the PDOS of the atoms belonging to the topmost interface are shown in dashed lines. The inset shows the PDOS of the oxygen of the topmost layer near the Fermi energy.

of the heterostructures present a lot of similarities, in particular regarding the properties of the central STO part. The values of the gap as a function of m and n are reported in the Table V.1. Fig. V.4 a shows the gaps as a function of the number m of LAO layers. The points are given two different colors depending on whether there is a capping layer ($n \neq 0$). The two black dashed lines are a linear model for the gap as a function of m

$$E_{gap} = E_0 - E_{surf} - mE_{LAO} \tag{V.2}$$

Where E_0 is a constant, E_{surf} is the energy shift due to the presence of a free STO layer at the topmost interface and E_{LAO} is the energy shift due to one LAO layer. This linear model can be understood in the language of the polar catastrophe. Each LAO layer brings a polar energy of around 0.9 eV to the structure. The presence of a free STO layer on top gives an additional electrostatic energy. Indeed, the topmost TiO_2 layer lying at the free surface has an asymmetric ionic environment, so that the Ti and O atoms composing it are not feeling the same electrostatic force from below and above. This can promote distortions of the unit cell in the topmost layers and create an electric polarization to relax mechanical

constraints. This electrostatic energy may explain the shift in energy $E_{surf} = 1.4$ eV. There are few differences between the cases $n = 1, 2, 3$ for $m = 1$, suggesting that only the free interface plays a role in the energy shift. The additional STO capping layers do not play a role (as long as there is at least one) : the polarization induced by the LAO layers is almost entirely compensated in the first STO layer as shown by Fig. V.3, where the energy shifts are concentrated in the LAO layer and in the topmost STO layer. This is at odds with the results of the computations presented in [161] where the energy shift due to the polarization of LAO seems to continue in the STO layers. We also see that the extrapolating of the dashed line for the case without any capping layers involves an energy $E_0 = 4$ eV, which is higher than the computed gap for the bulk of STO $\Delta_{STO} = 3.6$ eV. There might be an additional energy associated to the creation of the first LAO/STO interface, but it is difficult to extract more from the data. We estimate this energy to 0.4-0.5 eV, which is also the difference in energy between the $m = 1, n = 1$ and the $m = 1, n = 2$ case. It might be due to mechanical constraints.

The metallicity criterion is indeed obtained for the 3+1 structure. The 4+0 structure is not metallic, but the remaining gap is small (0.3 eV), so it can be considered metallic since its amplitude is close to the energy resolution. The 2+2 and 1+3 structures remain insulating with a gap which is too high to be interpreted as 0 within numerical accuracy. There are no substantial differences between the 1+1, 1+2 and 1+3 structures, apart from a slightly different gap between $n = 1$ and $n = 2, 3$. We did these computations with larger sizes of the lateral unit cell ($\sqrt{2} \times \sqrt{2}$ and 2×2) without any significant change in the gaps. The metallicity of these heterostructures must come from another mechanism than a purely electrostatic one. Computations performed using the software VASP in GGA+U lead to the same type of conclusions : the 3+1 structure is metallic while the 1+3 structure is insulating (neither electron gas at the first LAO/STO interface nor hole gas at the free STO surface) in the absence of defects in the structure, though the remaining gap is small. The mechanical relaxation of such heterostructures is very difficult to reach for large lateral size of unit cells in both types of computations. It can alter the numerical results because distortions impact the amplitude of polar energy in heterostructures. Accurate estimations of gaps are critical to accurately determine the metallicity criterion.

V.4.3 Detail of the PDOS in the heterostructure

The energy shift is not the only effect of the mixed chemistry of the heterostructure and the presence of a surface. Underlying electronic reconstruction of the density of states also occurs with the change in the structure. The PDOS of the oxygen and titanium atoms of the bulk of 3.5 unit cell thick slab of STO are shown on Fig. V.5 a and b. If the Ti PDOS is roughly similar, the PDOS of the oxygen changes a lot when going towards the surface, with a displacement of the weight from the peak at -4 eV towards higher energies. This peak is flattened, and the weight goes to unoccupied states : this results in a lowering of the gap.

The PDOS of the oxygen atoms in a STO(bulk)/LAO(4) heterostructure is shown on Fig. V.5 c, as a function of the layer. In the STO side, the oxygen are taken inside the SrO layers, and in the LAO side, they are taken in the LaO layers. The TiO_2 and AlO_2 version of this graph displays similar results. An energy shift corresponding to the slope of Eq. V.2 has been applied to the oxygen of the LaO layers for the sake of comparison. It can be noted that the PDOS of the oxygen in the first LAO layer presents a lot of similarities with the PDOS in the STO bulk. The shape and width of the peak of the PDOS between -5 eV and -3 eV is similar, even if a decrease of the amplitude of the peak around -4.5 eV can be noted. Going further up in the LAO layers results in a progressive deformation of the PDOS, and it is completely different for the topmost layer of LAO (corresponding to the layer number 7 of the structure). This PDOS of the topmost layer is compared with the PDOS of the oxygen atom of the valence band of bulk LAO in Fig. V.5 d, and presents similarities. The bulk computations have been performed for a tetragonal unit cell of LAO with a lateral size of the unit cell equal to the one of STO $a = 3.88\mathring{A}$, and a parameter $c = 3.739\mathring{A}$. This tetragonal distortion takes into account of the adaptation of the LAO unit cell to the lateral size of the substrate of STO. The PDOS of these two oxygen atoms are roughly similar so we can conclude that there is indeed a transition of the electronic structure of the valence band from an STO-like DOS towards a LAO-like DOS.

V.5 Addition of defects : local electrostatics

Oxygen vacancies are known electronic donors in TMO. In particular, the density of carriers at the bare surface of STO can change upon exposition to UV irradiation because

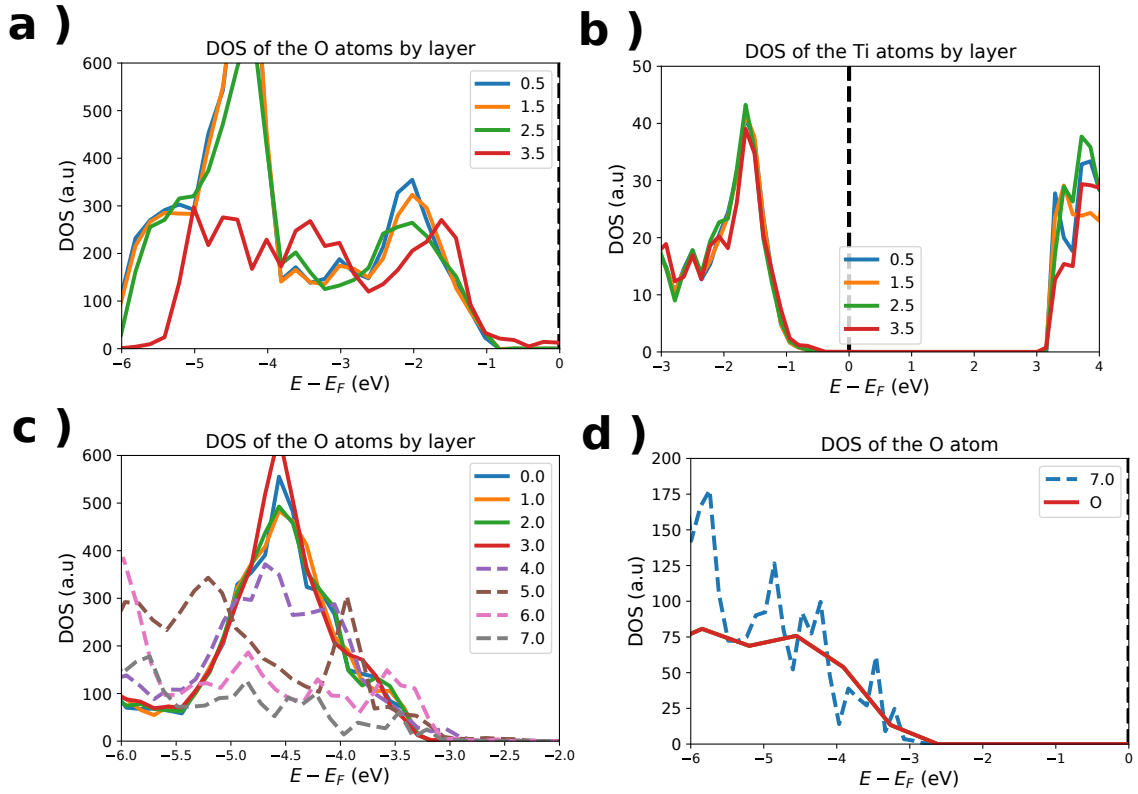

Fig. V.5 a) PDOS of the oxygen atoms in a 1x1 slab of STO thick of 3.5 unit cells as a function of energy and of the layer index (the 0.5 shift is because the atoms are taken in the TiO_2 layers). 0.5 correspond to the center of the sample (bulk-like), while 3.5 correspond to the free surface layer. b) Corresponding PDOS of the Ti atoms. c) PDOS of the oxygen atoms in a STO(bulk)/LAO(4) heterostructure as a function of the energy and the layer. The plain lines are for oxygen atoms belonging to SrO layers while the dashed lines are for oxygen belonging to the LaO layers. The PDOS of the LAO side of the interface are shifted by an energy corresponding to the slope found on Fig. V.4 a) in order to have a common energy reference. d) Comparison of the PDOS of the oxygen atom of the last layer of LaO of the structure of c) (dashed line) with the one of an oxygen in the bulk of LAO (plain line).

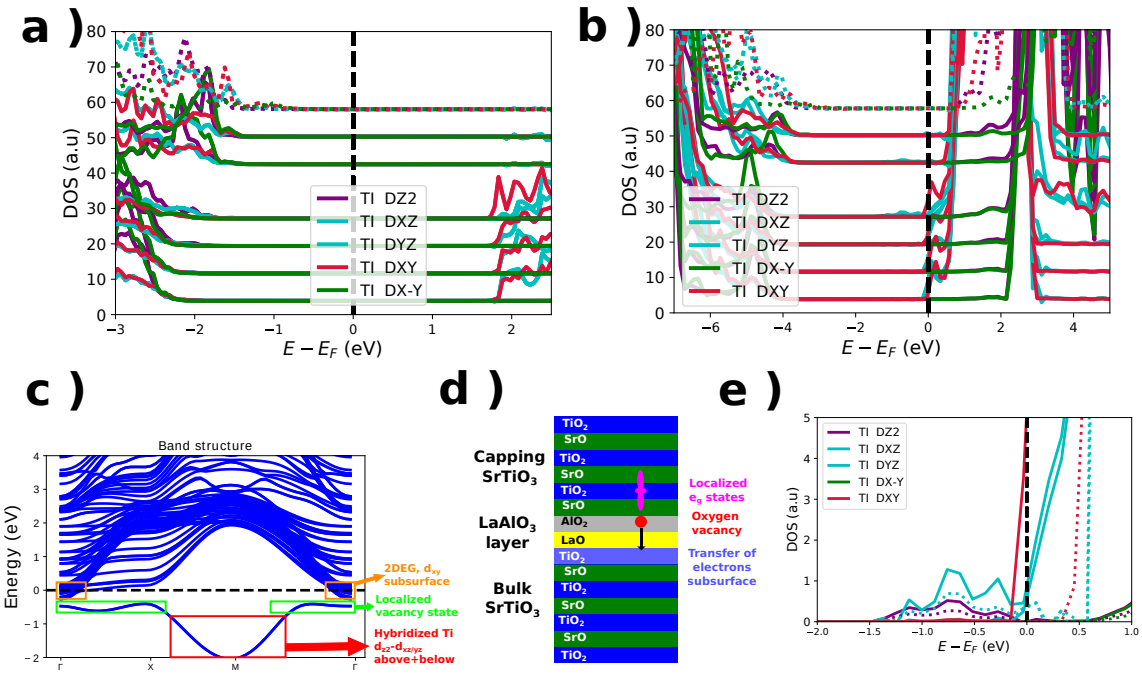

Fig. V.6 a) Orbitally resolved PDOS of a $\sqrt{2} \times \sqrt{2}$ $STO_{bulk}/LAO_1/STO_3$ structure. b) Orbitally resolved PDOS of a 1×1 $STO_{bulk}/LAO_1/STO_3$ structure with an oxygen vacancy in the AlO_2 layer. In a) and b) the PDOS of the topmost layer are in dashed lines. The blank part in the density of states (around 35 in the vertical scale) correspond to the LAO layer, where there are no Ti atoms. The layered structure corresponding is presented in c) where we depict the presence of localized e_g states above the capping layer. An electron transfer happens between the vacancy and the LaO-TiO_2 interface which leads to a metallic state. d) Band structure associated with the DOS of the figure in the top right. We can observe the presence of the 2DEG and the state below which is a vacancy states hybridizing with other t_{2g} levels. e) Detail of the PDOS of b) around the $E - E_F = 0$. In plain lines the PDOS of the TiO_2 layer just below the LAO layer, in dashed lines the PDOS of the TiO_2 layer just above the LAO layer.

light can create oxygen vacancies at the surface [77, 180, 181]. The removal of an oxygen atom from the solid releases 2 free electrons, which screen the effective potential induced by the absence of the oxygen atom. The balance between electrostatic and kinetic energies can lead to metallic states. The formation of oxygen vacancies becomes thermodynamically favorable when more than 4 LAO layers are put on top of the STO substrate [182]. The addition of oxygen vacancies at the bare surface of STO or at the surface of LAO has been shown to drive the system towards metallicity [19]. We add defects in the heterostructures in order to see the impact they have on the metallicity, focusing on the situation with the largest gap (1+3) for it is the less likely to become metallic. The oxygen vacancies are located at the second LAO/STO interface, in the AlO_2 layer, the closest to the capping layer. This is motivated experimentally by the synthesis conditions in which oxygen deficiencies are more likely to occur in the SrO layers. The oxygen-deficient SrO layer captures one of the oxygen atoms of the neighboring AlO_2 layer.

Fig. V.6 a and b show the orbitally resolved PDOS for the ideal 1+3 structure (for a $\sqrt{2} \times \sqrt{2}$ lateral size) and in the presence of an oxygen vacancy in the AlO_2 layer (for a 1×1 lateral size). There is a gap in the ideal structure, and the conduction electrons are located only below the interface. They are of t_{2g} character, as a consequence of the e_g/t_{2g} splitting. The d_{xy} has a greater weight than the $d_{xz/yz}$ near the lower LaO-TiO_2 interface, which is a consequence of the electrostatic field due to the interface. In the presence of oxygen vacancies, the system is metallic, presenting a complicated PDOS near the Fermi energy. However, the nature of the different contributions to the PDOS can be identified : Fig. V.6 e shows a zoom of the Fig. V.6 b near the Fermi energy. The plain lines are the PDOS of the layer below the LAO layer, while the dashed lines are for the layer just above the LAO layer. Just below the Fermi energy, metallic states correspond to the d_{xy} states, and are present in both sides of the interface. These metallic states extend inside the STO bulk, where they present more of a $d_{xz/yz}$ character. Further below the Fermi energy, localized states of mixed $d_{z^2} - d_{xz/yz}$ character appear, corresponding to states located near the oxygen vacancy in AlO_2. Vacancy states can hybridize with the d_{z^2} and $d_{xz/yz}$ orbitals of the Ti atoms at the vertical from the oxygen vacancy because these orbitals have lobes pointing towards the vacancy. The small lateral size of the unit cell can induce hybridizations of the vacancy states through the $d_{xz/yz}$ orbitals and might explain the unexpected dispersion of these states.

This computation also has been carried out for a $\sqrt{2} \times \sqrt{2}$ lateral size but the results were difficult to interpret. Though the system is again found metallic, several states cross the Fermi energy : electron-like states forming a 2DEG as for the 1x1 structure and hole-like states seemingly coming from the hybridization with states located close to the vacancy. We wanted to reduce the concentration of oxygen vacancies in the system in order to limit the unphysical dispersion of these states but the required size of the system exceeded the possibility of our computational resources. In particular, the mechanical relaxation of the structure near the vacancy was impossible to reach. We also studied heterostructures where the vacancy was in the SrO layer above the AlO_2 layer. This scenario would result from the capture of an oxygen atom from the SrO layer towards the oxygen-deficient AlO_2 layer during the synthesis : the interface is again metallic but we observe hole-like states above the interface, which are vacancy states.

The metallicity in the presence of oxygen vacancies is not the end of the story : the $STO_{bulk}/LAO_1/STO_2$ heterostructure is also metallic in the presence of oxygen vacancies, while experiments suggest that it should not be. This could be explained by the fact that the formation of vacancies is not thermodynamically favorable with only two layers of STO capping. However, little to no difference in the energy of formation of the vacancy was found between the cases $n = 2$ and $n = 3$. It was not possible to go to a lower concentration of vacancies due to limited computing power. This work does not include a systematic treatment of oxygen vacancies, which the interested reader can find in more details in [177]. This discrepancy with the experimental results might also be due to the choice of functionals, to a bad guess for the type of defects likely to form in these structures or even from an effect our model does not take into account. In all, this problem remains open and is a nice playground to study the formation of 2DEGs in perovskite heterostructures.

Conclusion

> The man who comes back through the Door in the Wall will never be quite the same as the man who went out. He will be wiser but less sure, happier but less self-satisfied, humbler in acknowledging his ignorance yet better equipped to understand the relationship of words to things, of systematic reasoning to the unfathomable mystery which it tries, forever vainly, to comprehend.
>
> Aldous Huxley,
> *The Doors of Perception*

In this thesis, we study electronic and spintronic properties of Transition Metal Oxides (TMO) heterostructures. The emergence of 2-dimensional electron gases (2DEG) in these structures has been known for more than a decade, and the discovery that these structures can host spintronic properties is noteworthy for the conception of new electronic devices based on these materials. The origin of this gas is still a subject of debates, and we explore the relative impact of the polarity of the interface and of the presence of oxygen vacancies on the formation of the 2DEG in Chapter V. The actual mechanism triggering the emergence of the gas shall influence its behavior under the application of external fields (especially electric). But this is not the end of the story, as this gas presents a strong multi-orbital character, which makes it different from gases in usual semi-conductor heterostructures. This orbital degree of freedom changes the properties of the electronic structure upon doping, and we discuss some of these effects in Chapter II for the [001] and [111] orientation of STO-based interfaces. This modification of the electronic structure upon doping deeply impacts the transport properties, are they topological properties (which we discuss in Chapter III) or spintronic responses (we focus on the Edelstein Effect and Spin Hall Effect of TMO heterostructures in Chapter IV).

In Chapter II we tackle the electrostatic doping of STO interfaces, whose properties are known to be widely gate-tunable. We showed that the electronic spectra of the interfaces can be quantitatively reproduced using a tight-binding model enriched with a Poisson-Schrodinger description of the confinement near the interface. The change in the dielectric constant of STO with temperature impacts the electrostatic confinement near the interface and shall affect both the electronic spectrum and the spatial extension of the 2DEG. We show that the electrostatic doping of the 2DEG in the top and backgating geometry modify the spectrum by the application of a gate voltage : in the backgating geometry, states living away from the interface are more impacted by the potential. If a leakage of a fraction of the charge bound to the interface is expected, overall the gas remains stable, in particular its lower-lying levels. Hall measurements in the [001] and [111] orientations of the LAO/STO interface report the advent of a new population of carriers above a voltage threshold, inducing a Lifshitz transition. Above this transition, the density of the new species of carriers oddly increases at the expense of the first species. We reproduce this behavior introducing electronic correlations in our model of the interface, as they are considered to be the driving force for this unusual behavior to explain measurements in the [001] orientation ; an analysis of electronic correlations at the mean field level in the [111] orientation explains in which conditions correlations can be held responsible for such a behavior. We suspect that disorder, in particular emerging from the surface roughness at the interface, might also explain why the mobilities of the low-lying levels are so low and why their contribution in Hall experiments is less intense than expected.

If the confining potential has known consequences on the spatial density and on the band bending near the interface, the interplay of this potential with disorder leaves open questions. The presence of both surface roughness and sparse oxygen vacancies provides non-equivalent disorder channels with distinct scattering properties. How orbitals and subbands are affected by disorder is of critical importance to evaluate their impact on transport properties. The discrepancy between the number of carriers evaluated in ARPES and in non-linear Hall effect is often explained by the presence of "frozen carriers" : why some carriers are seemingly muted in transport signatures is not well understood yet, but the decrease in the mobility due to the surface roughness near the interface might hinder the observation of a fraction of the carriers, especially of the ones located near the interface. A detailed treatment of disorder and

its interplay with correlations may provide an explanation for the observation of magnetism in some STO samples [56].

Chapter III explains the effects of the topology of band structures on the electronic properties of materials. After a reminder of the vocabulary proper to the topology of band structures, we build quantities such as the Anomalous Hall Conductivity and Spin Hall Conductivity, which both have been observed in recent experiments. They are intimately related to broken symmetries and the multi-orbital nature of the conduction and valence bands of topological insulators or Quantum Spin Hall insulators. In TMO interfaces, these conditions are fulfilled, so that they might host topological properties. In order to reveal these properties, it is necessary to find their experimental signatures and to understand experiments using realistic models. In STO-based systems, the task is difficult for they are both multi-orbital and metallic, blunting the tools available to analyze topological properties.

In Chapter IV we focus on the spintronic responses of TMO heterostructures, in the light of recent experiments demonstrating the presence of the Edelstein Effect [53, 55] and the Spin Hall Effect [54] in STO-based interfaces. We can reproduce experimental results using a tight-binding model and Linear Response Theory, and we relate the spintronic responses to non-trivial spin textures in the Brillouin Zone. The Edelstein Effect originates from winding spin textures which produce two types of response : one is the Rashba-Edelstein effect (the spin-galvanic response of a Rashba-like model [136]), and the other is a multi-band Edelstein effect related to interband spin-orbit couplings. Using the tight-binding model of Chapter II, we build a model for the spin-orbit coupling of STO-based interface that we call Multiband Interfacial Spin-Orbit coupling (MISO) in order to clarify the presence of both intraband and interband couplings. These couplings produce a non-trivial winding of the electron spin in the Brillouin Zone through complex spin-orbital-momentum locking. It is possible to separately compute the spin textures of each band and their impact on the Edelstein response, and the relative strength of the intraband and interband response is influenced by the orbital character of the states. Bands emerging at the Lifshitz transition display very peculiar spin textures that can be explained without the introduction a cubic Rashba spin-orbit interaction. The intrinsic Spin Hall Conductivity of STO-based interfaces can be related to properties of the z direction of the spin polarization, and display similarities with the response of Rashba-like models. The behavior of STO-based systems is shared with other oxides

and we provide tools and quantities helping to understand how to optimize the spintronic responses of TMO-based systems, which is of interest for technological applications.

As far as topological and magneto-transport properties are concerned, disorder should again be of the utmost importance. Indeed, in the Anomalous Hall Effect and Spin Hall Effect (SHE), disorder scattering produces vertex corrections to current operators through two mechanisms, called side-jump and skew-scattering, which can be of the same order of magnitude as the intrinsic contributions : it is acknowledged that the side-jump can cancel the intrinsic contribution of the SHE of the linear Rashba model. Can the multi-orbital nature of the conduction band of STO-based interfaces explain a survival of the SHE signal ? The weak anti-localization and anisotropic magneto-resistance properties of STO interfaces are often interpreted as the signature of a varying Rashba coupling. The form of the MISO coupling might add peculiar scattering channels and bear magneto-transport signatures consistent with the observations of STO-based interfaces. In all, the multi-orbital nature of the 2DEG in TMO heterostructures is a fundamental ingredient to understand its properties, and the possibility to switch from single to multi-band transport upon electrostatic doping allows to nicely observe the signatures of multi-band transport.

In Chapter V, we tackle the *capping problem* using Density Functional Theory : if normally 4 LAO layers deposited on top of a STO substrate are needed to observe a metallic system, recent experiments have shown that the 4 LAO layers can be replaced by m LAO layers and n STO capping layers on top of the STO substrate, as long as $m + n \geq 4$. We show that the LAO layers accumulate polar energy, and the topmost STO capping layer at the free surface shifts the Fermi energy, probably due to the local electrostatic environment of the surface. The gap is indeed reduced in these capped structures, to the point that the system becomes metallic in the 3+1 structure. However, we find that the 2+2 and 1+3 structures are not found to be metallic in computations since the gap does not vanish, in contradiction with the experimental results. The presence of defects may explain the origin of the metallicity but this scenario does not unveil why the number of STO capping layers matters. The respective roles of chemistry and electrostatics in the creation of the 2DEG at the interface between TMO remain to be accurately determined, and the capping problem may help to disentangle the impact of these two factors.

The multi-orbital character of the conduction band is a hallmark of STO-based interfaces,

and is held responsible for a lot of the unusual transport properties. If the presence of multiple carriers is a consequence of the chemistry of the TMO and of the *d*-shell character of the conduction band, the geometry of heterostructures strongly impacts the electronic properties of these carriers. The confinement of the 2DEG near the interface as well as the in-plane electronic transport are different depending on the orbital character of the electrons. Further properties can present this orbital dichotomy : MISO sheds light on the form of the spin-orbit coupling at these interfaces, and on the expected signatures of this multi-orbital character on the responses of the system. The spatial distribution of disorder may also distinguish the scattering properties, as the electronic states living closer to the interface shall be impacted more by surface roughness, diminishing their mobilities to the point that some properties of these carriers may vanish. A detailed model of the local properties near point-like defects such as oxygen vacancies can also help to understand the doping of these interfaces, and whether the actual mechanism triggering the emergence of the 2DEG has a proper signature. The impact of interactions on multi-band electronic systems is also of interest both to discover new phases of matter and to see whether the presence of multiple channels allows the coexistence of unusual electronic properties : might it explain the simultaneous observation of ferromagnetism and superconductivity in some LAO/STO interfaces ?

The presence of multiple bands is also of importance when it comes to topological effects. If topology is usually thought of in insulating systems, it may also lead to interesting signatures in metallic systems. The presence of band crossings in STO-based interface impacts the signature of the spin responses, and might have other noteworthy effects. The ability to control the filling of the 2DEG in STO-based interfaces is of interest to probe the role of band crossings in electronic properties. The compounded effects of these crossings and of couplings with specific symmetries can lead to enhanced responses in unusual sectors : if we tackled the spin responses in this work, the orbital sector is also under scrutiny. The study of heterostructures made with different oxides may also help to better understand these properties by changing the amplitude of the couplings, or even by adding couplings with different symmetries : in magnetic oxides the Time-Reversal symmetry is clearly broken, so that new signatures can emerge from the band structure such as the Anomalous Hall Effect or magneto-electric couplings.

To put in a nutshell, Transition Metal Oxide heterostructures are fascinating systems

with exotic transport properties and provide a rich playground to study complex phases of matter. Their multi-band properties can induce several functionalities inside the same material, and the ability to tune their properties makes them strong contenders for building a next generation of electronic devices.

A – Appendix to Chapter 2

A.1 Orbital operators restricted to the t_{2g} basis

Using the symmetries of the wavefunctions of the t_{2g} orbitals and or the $\hat{\vec{L}}$ operator, one gets the following matrices for the three components of the orbital operators restricted to the t_{2g} basis (d_{yz}, d_{xz}, d_{xy}) :

$$\hat{L}_x = \begin{bmatrix} 0 & 0 & 0 \\ 0 & 0 & i \\ 0 & -i & 0 \end{bmatrix}, \hat{L}_y = \begin{bmatrix} 0 & 0 & -i \\ 0 & 0 & 0 \\ i & 0 & 0 \end{bmatrix}, \hat{L}_z = \begin{bmatrix} 0 & i & 0 \\ -i & 0 & 0 \\ 0 & 0 & 0 \end{bmatrix} \tag{A.1}$$

independently of the direction of the spin. These operators verify the three commutation relations :

$$\begin{aligned} \left[\hat{L}_x, \hat{L}_y\right] &= -i\hat{L}_z \\ \left[\hat{L}_y, \hat{L}_z\right] &= -i\hat{L}_x \\ \left[\hat{L}_z, \hat{L}_x\right] &= -i\hat{L}_y \end{aligned} \tag{A.2}$$

in analogy with the Pauli matrices, but for 3×3 matrices. However they do not posses a closed set of anti-commutation relations ; this complicates a lot the algebraic computations in the t_{2g} basis. The matrix version of the spin-orbit operator is obtained by making the tensorial product of the spin operator with these orbital operator. In the $(d_{yz} \uparrow, d_{yz} \downarrow, d_{xz} \uparrow$

$, d_{xz}\downarrow, d_{xy}\uparrow, d_{xy}\downarrow$) basis, it gives :

$$\mathcal{H}_{bulk}^{SOC} = \lambda_{SO}\begin{pmatrix} 0 & 0 & i & 0 & 0 & -1 \\ 0 & 0 & 0 & -i & 1 & 0 \\ -i & 0 & 0 & 0 & 0 & i \\ 0 & i & 0 & 0 & i & 0 \\ 0 & 1 & 0 & -i & 0 & 0 \\ -1 & 0 & -i & 0 & 0 & 0 \end{pmatrix} = i\lambda_{SO}\begin{pmatrix} 0 & 0 & 1 & 0 & 0 & i \\ 0 & 0 & 0 & -1 & -i & 0 \\ -1 & 0 & 0 & 0 & 0 & 1 \\ 0 & 1 & 0 & 0 & 1 & 0 \\ 0 & -i & 0 & -1 & 0 & 0 \\ i & 0 & -1 & 0 & 0 & 0 \end{pmatrix} \tag{A.3}$$

which can be transformed in the form of Eq. II.5 by using the Pauli matrices.

A.2 Kinetic energy in the [111] orientation

A.2.1 Tight-binding approach

We can build a tight-binding model on the honeycomb lattice of Fig. II.2 a. Using notations similar to [57], we design by $t_\pi, t_\sigma, t_\delta$ respectively the first, second and third nearest-neighbor hopping. The first and third neighbor hoppings change the layer in which the electron is while the second neighbor hopping is intra-layer. This produces a model similar to [39, 77]

$$\begin{aligned}
\epsilon_{0,xy}(k) &= -2t_\sigma \cos(\sqrt{3}k_x\tilde{a}) \\
\epsilon_{0,yz}(k) &= -2t_\sigma \cos(-\frac{\sqrt{3}}{2}k_x\tilde{a} + \frac{3}{2}k_y\tilde{a}) \\
\epsilon_{0,xz}(k) &= -2t_\sigma \cos(\frac{\sqrt{3}}{2}k_x\tilde{a} + \frac{3}{2}k_y\tilde{a}) \\
\epsilon_{1,xy}(k) &= -t_\pi \cos(\frac{\sqrt{3}}{2}k_x\tilde{a})e^{-i\frac{3}{2}k_y\tilde{a}} - t_\delta \\
\epsilon_{1,yz}(k) &= -t_\pi \left[1 + e^{i(\frac{\sqrt{3}}{2}k_x - \frac{3}{2}k_y)\tilde{a}}\right] - t_\delta e^{-i(\frac{\sqrt{3}}{2}k_x + \frac{3}{2}k_y)\tilde{a}} \\
\epsilon_{1,xz}(k) &= -t_\pi \left[1 + e^{-i(\frac{\sqrt{3}}{2}k_x - \frac{3}{2}k_y)\tilde{a}}\right] - t_\delta e^{i(\frac{\sqrt{3}}{2}k_x - \frac{3}{2}k_y)\tilde{a}}
\end{aligned} \tag{A.4}$$

Where $\tilde{a} = \sqrt{\frac{2}{3}}a$ is the unit cell parameter projected in the [111] plane, and k_x, k_y correspond respectively to the directions $[1, -1, 0]$ and $[-1, -1, 2]$. As in graphene, we build the tight-

binding model with a 2x2 Hamiltonian $\mathcal{H}_\nu$ for each orbital ν :

$$\mathcal{H}_\nu = \begin{bmatrix} \epsilon_{0,\nu} & \epsilon_{1,\nu} \\ \epsilon^*_{1,\nu} & \epsilon_{0,\nu} \end{bmatrix} \tag{A.5}$$

Where z^* designs the complex conjugate of z. This 2x2 Hamiltonian has a bonding and anti-bonding state with energies $\epsilon_\pm = \epsilon_{0,\nu} \pm |\epsilon_{1,\nu}|$. It is possible to add an extra potential difference $\delta V \sigma_z$ to the $\mathcal{H}_\nu$ Hamiltonian to account for electrostatic effects near the interface. This additional potential lifts the degeneracy of possible Dirac cones.

A.2.2 Low energy expression

We can derive the spectrum of the model in an alternative manner, using the low-energy development of the kinetic energy and rewriting it in the plane perpendicular to the [111] interface. For low k, the kinetic part of the Hamiltonian of bulk STO is

$$\mathcal{H}_{kin} = \begin{pmatrix} t_2 & t_1 & t_1 \\ t_1 & t_2 & t_1 \\ t_1 & t_1 & t_2 \end{pmatrix} \begin{pmatrix} k_x^2 \\ k_y^2 \\ k_z^2 \end{pmatrix} \tag{A.6}$$

Where the orbital basis is d_{yz}, d_{xz}, d_{xy}. We change the basis of the wavevector to be consistent with the geometry of the [111] interface : we take $(k_1, k_2, k_\perp)$ with $k_1 = \frac{1}{\sqrt{2}}[1, -1, 0]$, $k_2 = \frac{1}{\sqrt{6}}[1, 1, -2]$ and $k_\perp = \frac{1}{\sqrt{3}}[1, 1, 1]$. k_1 and k_2 lie in the plane of the interface while $k_\perp$ is the direction perpendicular to the interface. We invert the relation to get $k_x = \frac{1}{6}\left[3\sqrt{2}, \sqrt{6}, 2\sqrt{3}\right]$, $k_y = \frac{1}{6}\left[-3\sqrt{2}, \sqrt{6}, 2\sqrt{3}\right]$, $k_z = \frac{\sqrt{3}}{3}\left[0, -\sqrt{2}, 1\right]$ and compute the dispersion relations in this basis. Plugging back these expressions in the kinetic energy we get :

$$\begin{aligned} \epsilon_{yz} &= t_1 \left(\frac{k_1}{2} + \frac{\sqrt{3}k_2}{2}\right)^2 + t_c \left(-\frac{\sqrt{3}k_1}{2} + \frac{k_2}{2}\right)^2 + t_\perp k_\perp^2 - t_p k_\perp k_1 - t_q k_\perp k_2 \\ \epsilon_{xz} &= t_1 \left(\frac{k_1}{2} - \frac{\sqrt{3}k_2}{2}\right)^2 + t_c \left(\frac{\sqrt{3}k_1}{2} + \frac{k_2}{2}\right)^2 + t_\perp k_\perp^2 + t_p k_\perp k_1 - t_q k_\perp k_2 \\ \epsilon_{xy} &= t_1 k_1^2 + t_c k_2^2 + t_\perp k_\perp^2 + 2 t_q k_\perp k_2 \end{aligned} \tag{A.7}$$

With $t_\perp = \frac{2t_1+t_2}{3}, t_c = \frac{t_1+2t_2}{3}, t_p = \frac{\sqrt{6}(t_1-t_2)}{3}, t_q = \frac{\sqrt{2}(t_1-t_2)}{3}$. The three orbitals have the same mass along the $\perp$ direction, meaning they are equally affected by the electrostatic confinement. If we forget about the terms including $k_\perp$, we get the in-plane dispersion which yields three elliptic Fermi surfaces rotated one from another by $\frac{2\pi}{3}$ and with the two effective masses t_1 and t_c. The presence of mixed terms $k_\perp k_{1/2}$ has to be handled with care : we show in Appendix A.4 that $t_c \to \frac{4}{3}t_2$ due to terms containing $k_\perp$, giving results consistent with the tight-binding form of the previous paragraph. The parabolic dispersion can be considered as a low energy version of a simpler tight-binding model replacing $(ka)^2 \to 2(1-\cos(ka))$.

A.3 Atomic spin-orbit coupling and trigonal crystal field

In the basis $(X\uparrow, X\downarrow, Y\uparrow, Y\downarrow, Z\uparrow, Z\downarrow)$, the eigenvectors of the atomic spin-orbit coupling defined by Eq. II.5 are :

$$\begin{aligned} D^1_\pm &= \frac{1}{\sqrt{6}}(\pm iX_{\uparrow/\downarrow} + Y_{\uparrow/\downarrow} + 2iZ_{\downarrow/\uparrow}) \\ D^2_\pm &= \frac{1}{\sqrt{2}}(\pm iX_{\uparrow/\downarrow} - Y_{\uparrow/\downarrow}) \\ S_\pm &= \frac{1}{\sqrt{3}}(-iX_{\uparrow/\downarrow} \mp Y_{\uparrow/\downarrow} + iZ_{\downarrow/\uparrow}) \end{aligned} \tag{A.8}$$

The associated eigenvalues are $-\lambda_{SO}$ for the doublet states $D^{1,2}_\pm$ and $2\lambda_{SO}$ for the singlet states $S_\pm$. The two groups of eigenstates + and - are time reversal partners. The atomic spin-orbit energy is often defined as $E_{SO} = 2\lambda_{SO} - (-\lambda_{SO}) = 3\lambda_{SO}$. We chose to keep λ_{SO} to simplify the writing of some formulas.

The eigenstates of the Hamiltonian of the trigonal crystal field defined by Eq. II.4 are :

$$\begin{aligned} D^A &= \frac{1}{\sqrt{3}}(X+Y-2Z) \\ D^B &= \frac{1}{\sqrt{2}}(X-Y) \\ S &= \frac{1}{\sqrt{3}}(X+Y+Z) \end{aligned} \tag{A.9}$$

The structure of the Hamiltonian is similar to the atomic spin-orbit coupling, yielding the eigenvalue $-\Delta_{tcf}$ for the doublet states and $2\Delta_{tcf}$ for the singlet states. The states are of

pure spin character and are degenerate in energy for both direction of the spin.

A.4 Airy functions

We want to solve the Schrodinger equation of an electron in a triangular well

$$-\frac{\hbar^2}{2m}\partial_z^2\psi_n + eFz\psi_n = E_n\psi_n \tag{A.10}$$

Where e is the charge of the electron, m its effective mass and F the amplitude of the electric field. Rescaling of the problem using $u = \frac{z-z_n}{C}$ with $C = \frac{2}{3}\left(\frac{\hbar^2}{2meF}\right)$, $z_n = \frac{E_n}{eF}$ gives the differential equation $\frac{d^2y}{du^2} - uy = 0$, whose two solutions are the Airy functions of the two kinds : $Ai(u) = \frac{1}{\pi}\int_0^\infty \cos(\frac{t^3}{3} + ut)dt$ and $Bi(u) = \frac{1}{\pi}\int_0^\infty e^{-\frac{t^3}{3}+ut} + \sin(\frac{t^3}{3} + ut)dt$. We seek bound states of the problem ; only solutions corresponding to Ai give decaying solutions for $u \to \infty$, so that they are the only physical solution. Solving the eigenvalue problem is equivalent to impose that $\psi_n(z = 0) = 0$, which can be translated into the transcendental equation $Ai(-\frac{z_n}{a}) = 0$. This proves $E_n = c_nK$ with $K = \left(\frac{\hbar^2e^2F^2}{2meF}\right)^{1/3}$ and $c_n \approx \left(\frac{3\pi}{2}(n - \frac{1}{4})\right)^{2/3}$.

In the [111] orientation, Eq. A.7 shows that the dispersion in the direction parallel (k_1, k_2) and perpendicular $k_\perp$ to the interface are entangled. We transform the dispersion relation $\epsilon_{xy}(k)$ of Eq. A.7 into a Schrodinger equation by making the substitution $k_\perp = i\partial_z$, yielding

$$-t_\perp\partial_z^2\psi_n + i2t_qk\partial_z\psi + eFz\psi_n = E_n\psi_n \tag{A.11}$$

If we use the transformation $\psi = e^{i\mu z}\phi$, we see that ϕ obeys the triangular well equation but it adds a kinetic energy $\frac{t_q^2k^2}{t_\perp} \approx -(\frac{t_1}{3} - \frac{2t_2}{3})$ (if $\frac{t_qk}{t_\perp} = \mu$). In the [111] orientation the confinement is not affected by the in-plane dispersion and only renormalizes the effective masses of the in-plane dispersion. With this corrections the new effective model at low energy is

$$\begin{aligned}
\epsilon_{yz} &= t_1\left(\frac{k_1}{2} + \frac{\sqrt{3}k_2}{2}\right)^2 + \frac{4}{3}t_2\left(-\frac{\sqrt{3}k_1}{2} + \frac{k_2}{2}\right)^2 \\
\epsilon_{xz} &= t_1\left(\frac{k_1}{2} - \frac{\sqrt{3}k_2}{2}\right)^2 + \frac{4}{3}t_2\left(\frac{\sqrt{3}k_1}{2} + \frac{k_2}{2}\right)^2 \\
\epsilon_{xy} &= t_1k_1^2 + \frac{4}{3}t_2k_2^2
\end{aligned} \tag{A.12}$$

A.5 Boltzmann equation in a semiclassical approximation

The semi-classical velocity of an electron with wavevector k is given by $v_k = \frac{1}{\hbar}\frac{\partial \epsilon_k}{\partial k}$. In a semi-classical approximation, the current is

$$J = \int q v_k f_k \frac{dk}{2^{d-1}\pi^d} \tag{A.13}$$

Where f_k is the distribution function of electrons with wavevector k. In the absence of fields, $f_k = f_k^0$ is the Fermi-Dirac distribution. There is no net current in this case. In the presence of electric and magnetic fields, the system goes towards a stationary states respecting the Boltzmann equation :

$$\dot{f_k} = \dot{f}_{kfields} + \dot{f}_{kscaterring} + \dot{f}_{kdiffusion} = 0 \tag{A.14}$$

The contribution due to the fields are

$$\dot{f}_{kfields} = -\frac{q}{\hbar}(E + v_k \times B) \cdot \frac{\partial f_k}{\partial k} \tag{A.15}$$

The scattering contribution can be written in a Drude-like version, introducing the scattering time $\tau(k)$

$$\dot{f}_{kscaterring} = -\frac{f_k - f_k^0}{\tau(k)} \tag{A.16}$$

We neglect the diffusion term $\dot{f}_{kdiffusion} = -v_k \cdot \frac{\partial f_k}{\partial r}$ which can be important in the presence of a thermal gradient. The distribution function can be written using perturbation theory in the electric field $f_k = f_k^0 + g_k$. To the leading order :

$$\dot{f}_{kEfield} \approx -\frac{q}{\hbar} E \cdot \frac{\partial f_k^0}{\partial k} = -q \frac{\partial f_k^0}{\partial \epsilon_k} E \cdot v_k \tag{A.17}$$

For the magnetic part, the first term vanishes : $\dot{f}_{kBfield} \approx -\frac{q}{\hbar}(v_k \times B) \cdot \frac{\partial f_k^0}{\partial k} = -q\frac{\partial f_k^0}{\partial \epsilon_k}(v_k \times B) \cdot v_k = 0$, so one has to consider the further term :

$$\dot{f}_{kBfield} = -\frac{q}{\hbar}(v_k \times B) \cdot \frac{\partial g_k}{\partial k} \tag{A.18}$$

Reusing Eq. A.14, one gets :

$$-q\frac{\partial f_k^0}{\partial \epsilon_k}E\cdot v_k = \left(\frac{1}{\tau(k)} + q(v_k\times B)\cdot\frac{\partial}{\partial k}\right)g_k \tag{A.19}$$

This allows to write the correction to the distribution function $g_k = \left[\frac{1}{\tau_k}+D\right]^{-1}(-q\frac{\partial f}{\partial \epsilon_k}E\cdot v_k)$, where D is a differential operator and the inversion must be understood in term of operators. For low magnetic fields, this can be evaluated via perturbation theory $\left[\frac{1}{\tau_k}+D\right]^{-1} = \tau_k - \tau_k^2 D + \tau_k^3 D^2 + ...$ neglecting the change of τ_k with k. In the effective mass approximation $v_k = \frac{k}{m}$ and $D\left[E\cdot v_k\right] = B_z v_k^{\perp}\cdot M^{-1}\cdot E$ where $M^{-1} = \partial_k v_k$ is the effective mass tensor and $v_k^{\perp}$ is the vector $(v_y, -v_x)$. If the effective mass tensor is constant, one gets $D^2 v_k = -B_z^2 v\cdot M^{-2}\cdot E$. After a resummation we get $g_k = -\frac{q\tau}{1+q^2B_z^2\tau^2M^{-2}}\frac{\partial f_k^0}{\partial\epsilon_k}E\cdot(v_k + q\tau M^{-1}B_z v_k^{\perp})$. From this we get the electric conductivity tensor by computing

$$\sigma = \vec{\nabla}_E\int d^2k g_k\vec{v}_k \tag{A.20}$$

Which gives the formulas for the longitudinal and transverse conductivities

$$\begin{aligned}\sigma_{xx} = \sigma_{yy} &= \frac{1}{1+\mu^2B^2}\sigma_0\\ \sigma_{xy} = -\sigma_{yx} &= \frac{\mu B}{1+\mu^2B^2}\sigma_0\end{aligned} \tag{A.21}$$

Where $\mu = \frac{q\tau}{m}$ is the electronic mobility and $\sigma_0 = nq\mu$, where n is the density of carriers. These formulas allow to estimate both the density of carriers and the mobility by low field and high field measurements. The results are often presented in term of the resistivity tensor ρ, which is the inverse of the conductivity tensor, $\rho_{xx} = \frac{\sigma_{xx}}{\sigma_{xx}^2+\sigma_{xy}^2}$ and $\rho_{xy} = \frac{\sigma_{xy}}{\sigma_{xx}^2+\sigma_{xy}^2}$, giving $\rho_{xx} = \frac{1}{nq\mu}$ and $\rho_{xy} = \frac{B}{nq}$. No magneto-resistance effect is expected in this picture since ρ_{xx} does not depend on B. One can use these formulas to estimate both the number of carriers and the mobility of a sample from Hall measurements. The slope of the anomalous resistivity gives the number of carriers. Associated with the value of the longitudinal resistance one can estimate the mobility. Often, these procedure is done in both the low-field and high-field limit.

However, these formulas can only be obtained using several approximations. The first

approximation is the single-band approximation : if several bands are occupied, the contributions of all bands must be summed up, transforming A.21 into a sum of similar terms with a mobility and density of carriers which is not the same for each band. The formula is more involved if the scattering time or the effective mass are not constant inside the Brillouin Zone and the band dispersion cannot be described by only a mobility : these are anisotropy effects. The presence of several band can lead to the emergence of more complex structures linked to the detail of the geometry of the band structure, giving extra scattering processes which correct the velocity operator (and are called the vertex corrections). Another neglected contribution is the anomalous velocity correction which we detail in Chapter III.

When several bands are occupied, the conductivity tensor is the sum of each band contributions, which are parallel channels for conduction. $\sigma = \sum_\nu \frac{\sigma_\nu}{1+\xi_\nu^2} \begin{pmatrix} 1 & \xi_\nu \\ -\xi_\nu & 1 \end{pmatrix}$ with $\xi_\nu = \mu_\nu B$. Inverting this tensor gives

$$\begin{aligned} \rho_{xx} &= \sum_\chi \frac{1}{\left(\sum_\nu \frac{\sigma_\nu}{1+\xi_\nu^2}\right)^2 + \left(\sum_\nu \frac{\xi_\nu \sigma_\nu}{1+\xi_\nu^2}\right)^2} \frac{\sigma_\chi}{1+\xi_\chi^2} \\ \rho_{xy} &= \sum_\chi \frac{1}{\left(\sum_\nu \frac{\sigma_\nu}{1+\xi_\nu^2}\right)^2 + \left(\sum_\nu \frac{\xi_\nu \sigma_\nu}{1+\xi_\nu^2}\right)^2} \frac{\xi_\chi \sigma_\chi}{1+\xi_\chi^2} \end{aligned} \tag{A.22}$$

At very high magnetic fields, $\xi_\nu >> 1$ for all the bands and the transverse resistivity becomes $\rho_{xy}^{hf} = \frac{B}{q n_{2D}}$. This gives an estimate of the number of carriers, often called the "high field" or Hall number of carriers. The slope of $\rho_{xy}(B)$ at low field give a number called the "low field" number of carriers $n_{2D}^{lf} = \frac{\sum_\nu \mu_\nu \sigma_\nu n_\nu}{\sum_\nu \mu_\nu \sigma_\nu}$. This is a mean number of carriers pondered by their relative mobility. It is often considered that this limit reveals the high mobility carriers while the high field limit gives the total number of carriers.

A.6 Stability of the gas

We study the effect of the backgating on a 2DEG via an electrostatic approach. A 2DEG described by a density $\rho(z), z \geq 0$ screens a charge $Q > 0$ located at the origin, ie $\int \rho(z) dz = -Q$. This electronic cloud is screening the potential $V_0(z)$ created by the presence of the charge at the origin. The Poisson equation gives $V_0(z) = -\frac{Q}{\epsilon} z$ for $z \geq 0$. The 2DEG produces

the screening potential

$$V_s(z) = az + b - \int_0^z du \int_0^u dv \frac{\rho(v)}{\epsilon} \tag{A.23}$$

a and b are constants to ensure the boundary conditions, and can be chosen to be 0. Far from the interface, the potential saturates at a constant value V_{max}. We want to model the effects of the addition of a linear potential $V_{gate}(z) = Fz$ on the density $\rho(z)$. We take the following form for the density

$$\rho_{Q,\lambda}(z) = -Q\lambda^2 z e^{-\lambda z} \tag{A.24}$$

This allows to compute the shape of the screening potential and the potential energy of the gas $E_{pot} = \int dz \rho(z)(V_s(z) + V_0(z)) = \frac{5Q^2}{4\epsilon\lambda}$. Screening quickly the charge lowers the energy (the screening length is $\frac{1}{\lambda}$). The fact that in real systems $\lambda \neq 0$ is due to quantum effects linked to the kinetic energy. Taking a LDA-like approximation we can add an additional term proportional to ρ^2 to the energy, leading to an energy $E_{kin} \approx CQ^2\lambda$, where C is a constant. The balance between this energy and the electrostatic energy gives an equilibrium value λ_0, corresponding to a mean spatial extension $z_0 = \frac{1}{\lambda_0}$. We add a backgate potential to this problem and study how Q and λ vary with respect to their equilibrium values. The backgate potential changes the total charge $\tilde{Q} = -Q - \delta Q$ ($Q > 0$) by $\delta Q = \epsilon F_g$ due to the Gauss theorem, where F_g is the electric field due to the back gate voltage $F_g = \frac{V_g}{d}$ where d is the macroscopic thickness of the sample, giving a total energy

$$E_{pot} = \frac{5Q^2 - 2Q\delta Q - 3\delta Q^2}{4\epsilon\lambda} \tag{A.25}$$

The value of λ the total energy $E_{pot}+E_{kin}$ is reached for $\lambda_0^2 = C\frac{5-2x-3x^2}{(1+x)^2}$, where $x = \frac{\delta Q}{Q}$ is the percentage of doping of the system. In Fig. II.8 d we plot the associated spatial extension in arbitrary units to show that the backgating modify the spatial extension of the states inside the well.

A.7 Mean field treatment of interactions

We rewrite the density operator of an electron at site i with spin σ $n_{i,\sigma} = \bar{n}_\sigma + (n_{i,\sigma} - \bar{n}_\sigma)$, where $\bar{n}_\sigma$ denotes the mean density of the electrons with spin σ. Neglecting the quadratic

terms in $(n_{i,\sigma} - \bar{n}_\sigma)$, which are due to quantum fluctuations, we get a mean field form of the Hubbard Hamiltonian :

$$\mathcal{H}_{Hub} = -UN\bar{n}_\uparrow\bar{n}_\downarrow + U\sum_i \bar{n}_\uparrow n_{i,\downarrow} + \bar{n}_\downarrow n_{i,\uparrow} \tag{A.26}$$

Dropping the first term which only concerns the total energy, we see the emergence of an additional effective chemical potential for each band σ $E_{F,\sigma} = U\bar{n}_\sigma$. The sum of Eq. A.26 can be done over wavevectors k instead of sites i using the identity $\sum_i n_{i,\sigma} = \sum_k n_{k,\sigma}$.

For confined states, the z direction is not equivalent to the x, y directions. We use the same transformation by assigning a specific role to the z coordinate $n_{i,\nu} = \bar{n}_{z,\nu} + (n_{i,\nu} - \bar{n}_{z,\nu})$, where ν contains the orbital and spin information, i contains the (x, y, z) coordinates, and $\bar{n}_{z,\nu}$ is the mean value of the population of the orbital ν at the coordinate z (it is a mean value over the corresponding xy plane). Using $\sum_i n_{i,\nu} f(z) = \sum_{k,z} n_{k,z,\nu} f(z)$, with $k = (k_x, k_y)$ a 2-dimensional wavevector, we get the mean field Hubbard term

$$\sum_{i,\nu,\chi} U^{\nu\chi} n_{i\nu} n_{i\chi} = \sum_{k,\nu,\chi} U^{\nu\chi}(\bar{n}_{z\nu} n_{kz\chi} + \bar{n}_{z\chi} n_{kz\nu} - \bar{n}_{z\nu}\bar{n}_{z\chi}) \tag{A.27}$$

If the confinement is decoupled from the in plane dispersion we can write $n_{k,z,\nu} = |\psi_\nu(z)|^2 n_{k\nu}$. We interpret that Eq. A.27 states that the ν index can denote the subband index of a particular orbital, allowing to write $\bar{n}_{z\nu} = p_\nu |\psi_\nu(z)|^2$, where p_ν is the density of the subband ν. The sum over z renormalizes the U constant $U^{\nu\chi} \to U^{\nu\chi} \sum_z |\psi_\nu(z)|^2 |\psi_\chi(z)|^2$. The levels which are the more affected by the interactions have the highest density in this framework, and the interactions between subbands which are not located at the same position in space is minimal.

A model describing correlations in multi-orbital systems is the Hubbard-Kanamori Hamiltonian

$$\begin{aligned}\mathcal{H}_K = U\sum_\nu n_{\nu\uparrow} n_{\nu\downarrow} + U'\sum_{\nu\neq\chi} n_{\nu\uparrow} n_{\chi\downarrow} + (U' - J)\sum_{\nu<\chi,\sigma} n_{\nu\sigma} n_{\chi\sigma} \\ -J\sum_{\nu\neq\chi} c^+_{\nu\uparrow} c_{\nu\downarrow} c^+_{\chi\downarrow} c_{\chi\uparrow} + J\sum_{\nu\neq\chi} c^+_{\nu\uparrow} c^+_{\nu\downarrow} c_{\chi\downarrow} c_{\chi\uparrow}\end{aligned} \tag{A.28}$$

Where $U' = U - 2J$ is an inter-orbital Hubbard coupling and J is the Hund coupling,

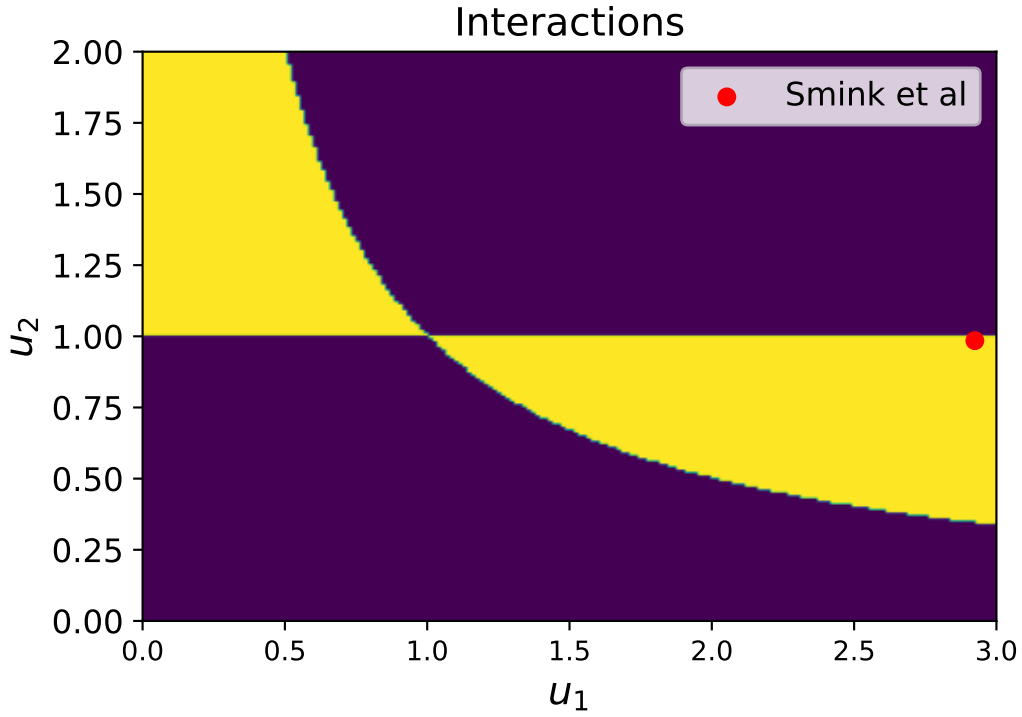

Fig. A.1 The regime where the decrease in the population of the lower subband can happen is in yellow, as a function of $u_1 = \frac{K_1}{U'}$, and $u_2 = \frac{K_1}{U'}$

emerging from the exchange. The last two terms can be neglected at a mean field level which ignores the presence of complex order parameters. Taking the mean field limit, the interaction energy of a level ν is $\epsilon_\nu^{int} = \frac{U}{2} n_\nu + (U' - \frac{J}{2}) \sum_{\chi \neq \nu} n_\chi$. Let us take a minimal model with two levels including the kinetic energy, described by the effective masses m_1, m_2, a gap Δ and an interaction energy coming from Hubbard-Kanamori terms U_1, U_2, U'. The amplitude of the Hubbard term for each band can be distinct $U_1 \neq U_2$. By definition the Fermi wavevectors $k_{F\nu}$ are such that $n_\nu(E_F) = C k_{F\nu}^2$, with $C = \frac{a^2}{4\pi^2}$. Solving $\epsilon_\nu^{tot} = E_F$ gives

$$\begin{aligned} \left[\frac{\hbar^2}{2m_1 C} + U_1\right] n_1 + U' n_2 &= E_F \\ \left[\frac{\hbar^2}{2m_2 C} + U_2\right] n_2 + U' n_1 + \Delta &= E_F \end{aligned} \tag{A.29}$$

Taking the derivative with respect to E_F of both equations, one gets $K_1 \frac{dn_1}{dE_F} = 1 - U' \frac{dn_2}{dE_F}$

and $\frac{dn_2}{dE_F} = \frac{1-U'\frac{dn_1}{dE_F}}{K_2}$, denoting $K_\nu = \frac{\hbar^2}{2m_\nu C} + U_\nu$. This yields

$$\frac{dn_1}{dE_F} = \frac{K_2 - U'}{K_1 K_2 - U'^2} \tag{A.30}$$

There are regimes in which $\frac{dn_1}{dE_F} < 0$ depending on the respective values of U_1, U_2, U', m_1, m_2. The model of [113] is in one such range : they take $U' = 2U_1 = 2U_2 = 1.6$ eV, $m_2 \approx 3m_e > m_1 = 0.7m_e$, giving a point which is in the yellow region of Fig. A.1, which represents the range of parameters where Eq. A.30 is negative. In the [111] orientation, both masses are equal, so if $U_1 = U_2$ then $K_1 = K_2$. Taking $U_1 \neq U_2$, there are values of U' fulfilling $\frac{dn_1}{dE_F} < 0$.

B – Appendix to chapter 4

B.1 Eigenvectors of $\mathcal{H}_{conf} + \mathcal{H}_{SO}$

The total Hamiltonian is composed of 6 bands (3 orbitals times 2 spin degrees of freedom). At the Γ point the orbital degeneracy is lifted because of the interfacial electric field and of the atomic spin-orbit coupling. At the Γ point, the Hamiltonian for the $(d_{yz}\uparrow, d_{xz}\uparrow, d_{xy}\downarrow)$ manifold is

$$M^{SODD} = \begin{pmatrix} 0 & i\lambda_{SO} & -\lambda_{SO} \\ -i\lambda_{SO} & 0 & i\lambda_{SO} \\ -\lambda_{SO} & -i\lambda_{SO} & -\Delta \end{pmatrix} \tag{B.1}$$

Where λ_{SO} is the atomic spin-orbit coupling and $\Delta > 0$ is the confinement gap. Its eigenvalues are : $-\lambda_{SO}, \frac{1}{2}\left(-\Delta + \lambda_{SO} - \sqrt{\Delta^2 + 2\Delta\lambda_{SO} + 9\lambda_{SO}^2}\right), \frac{1}{2}\left(-\Delta + \lambda_{SO} + \sqrt{\Delta^2 + 2\Delta\lambda_{SO} + 9\lambda_{SO}^2}\right)$, associated with the following eigenvectors in the $(d_{yz}\uparrow, d_{xz}\uparrow, d_{xy}\downarrow)$ basis :

$N = \frac{\sqrt{2}}{2}(-i, 1, 0)$

$L = \left(\frac{1}{2}\sqrt{1 - \frac{\zeta+1}{s}}, -\frac{i}{2}\sqrt{1 - \frac{\zeta+1}{s}}, \frac{\sqrt{2}}{2}\sqrt{1 + \frac{\zeta+1}{s}}\right)$

$U = \left(\frac{1}{2}\sqrt{1 + \frac{\zeta+1}{s}}, -\frac{i}{2}\sqrt{1 + \frac{\zeta+1}{s}}, -\frac{\sqrt{2}}{2}\sqrt{1 - \frac{\zeta+1}{s}}\right)$

Using the notations $\zeta = \frac{\Delta}{\lambda_{SO}}$ and $s = \sqrt{\zeta^2 + 2\zeta + 9}$. For the time reversed copy of the Hamiltonian in the $(d_{yz}\downarrow, d_{xz}\downarrow, d_{xy}\uparrow)$ basis

$$M^{SODD} = \begin{pmatrix} 0 & -i\lambda & \lambda \\ i\lambda & 0 & i\lambda \\ \lambda & -i\lambda & -\Delta \end{pmatrix} \tag{B.2}$$

The eigenvalues of the system are the same and the eigenvectors are :
$N = \frac{\sqrt{2}}{2}(i, 1, 0)$
$L = \left(\frac{1}{2}\sqrt{1-\frac{\zeta+1}{s}}, \frac{i}{2}\sqrt{1-\frac{\zeta+1}{s}}, \frac{\sqrt{2}}{2}\sqrt{1+\frac{\zeta+1}{s}}\right)$
$U = \left(\frac{1}{2}\sqrt{1+\frac{\zeta+1}{s}}, \frac{i}{2}\sqrt{1+\frac{\zeta+1}{s}}, -\frac{\sqrt{2}}{2}\sqrt{1-\frac{\zeta+1}{s}}\right)$
The L eigenvectors are almost purely d_{xy} at large $\zeta > 0$ while the U eigenvector are almost purely d_{xy} at large $\zeta < 0$.

B.2 Antisymmetrized form of the Edelstein Effect

We transform Eq. IV.2 to a Fermi surface integral $\kappa_{xy}(E_F) = \sum_\nu \int \frac{d^2k}{4\pi^2} F^\nu(k)\delta(\epsilon_\nu(k) - E_F)$ with $F^\nu(k) = \tau^\nu(k)\langle v_x(k)\rangle_\nu \langle S_y(k)\rangle_\nu$. We switch the wavevector to polar coordinates $dk^2 = kdkd\theta$ and denote by $k_F^\nu(\theta)$ the solutions to the equations $\epsilon_\nu(k) = E_F$, which are called the Fermi wavevectors. Assuming $\tau^\nu(k) = \tau_0$, we get $\kappa_{xy}(\mu) = e\tau_0 \sum_\nu \int d\theta \frac{v_{F,x}^\nu}{|v_F^\nu|} k_F^\nu \langle S_y(k_F^\nu)\rangle_\nu$. For Time Reversal Symmetric systems, Onsager reciprocity theorem implies that $\kappa_{xy} = -\kappa_{yx}$. Thus we focus on the antisymmetric version of the coefficient $\kappa = \kappa_{xy} - \kappa_{yx}$

$$\kappa(E_F) = e\tau_0 \sum_\nu \int k_F^\nu \left(\vec{u}_F^\nu \times \langle \vec{S}(k_F^\nu)\rangle_\nu\right) \cdot \vec{z} d\theta \tag{B.3}$$

Where $\vec{u}_F^\nu = \frac{\vec{v}_F^\nu}{|v_F^\nu|}$ is the unit vector normal to the Fermi surface FS_ν. Denoting by $\vec{w}_F^\nu = \vec{z} \times \vec{u}_F^\nu$ the unit vector tangential to the Fermi surface we obtain Eq. IV.3.

B.3 Anisotropy and Edelstein response of the N bands

The orbital mixing and anisotropy energy are the two possible causes for a splitting of the L, N and U bands and need to be added inside the perturbation theory scheme in order to evaluate the EE and SHE around point B. We write the kinetic energy for each of the bands as $\epsilon_{xz/yz} = (t_0 \pm \delta t \cos(2\theta))a^2k^2$ and $\epsilon_{xy} = (t_0 + \delta t)a^2k^2 - \Delta$ with $t_0 = \frac{t_1+t_2}{2}$ and $\delta t = \frac{t_1-t_2}{2}$. We subtract the diagonal part of the kinetic energy $E_0 = t_0 a^2 k^2$ which defines an effective mass $m^* = \frac{1}{2t_0a^2}$. The d_{xy} band is split by an effective confinement gap $\Delta - \delta t a^2 k^2 \approx \Delta$ near Γ. θ is the polar angle of the wavevector (k_x, k_y). We compute the effective 2x2 Hamiltonian of the N bands considering both the orbital mixing and the anisotropy as perturbations ; this

is valid as long as they are small compared to the gap D between the N and U bands at Γ. We keep track of the perturbations coming from the U bands up to the second order. We could add the perturbations due to the L bands : the effects are similar but the computations including both L and U become more complicated than informative. Moreover, the effects of the bands L on N are less intense than the effects of the bands U on N. We get the effective 2x2 Hamiltonian

$$\mathcal{H}_N = \Lambda_N + D_N\sigma_z + t_n\sigma_y \tag{B.4}$$

Where $\Lambda_N = E_0 + \frac{\alpha^2}{D}a^4k^4 + \frac{B_U^2}{D}a^2k^2$, $D_N = -\frac{2B_U\alpha}{D}a^3k^3\cos(2\theta)$, $t_n = \frac{2\alpha B_U}{D}a^3k^3\sin(2\theta)$ and σ designs the Pauli matrices of the 2 band model. They are not the spin operators which are detailed below. We note $\alpha k^2 = t_\alpha\cos(2\theta)k^2$, $B_U = \sqrt{1-\frac{1+e}{s}}\gamma_{OM}, t_\alpha = \frac{\sqrt{2}}{2}\sqrt{1+\frac{1+e}{s}}\delta t$. The diagonal term E_N contains a reminder of the kinetic energy E_0 of the band N in the absence of anisotropy or orbital mixing ; it dominates the term in B_U^2. The term in α^2k^4 is also smaller but does not have the same symmetry : it is proportional to $\cos^2(2\theta)$ (because $\alpha = t_\alpha\cos(2\theta)$), and gives a four-fold symmetric Fermi surface with a pattern of flower or square depending on its sign. The splitting of the two bands is of order k^3. We denote $A = \frac{2\alpha B_U}{D}a^3k^3$. The Hamiltonian becomes $\mathcal{H}_N = E_N + A\cos(2\theta)\sigma_z - A\sin(2\theta)\sigma_y$. The two levels are $E_N \pm A$ and the corresponding eigenvectors are easy to compute. We can rotate all the operators needed to compute the quantities in the split basis. Inside this two band model, the spin operators are corrected by perturbation theory

$$\begin{aligned}\hat{S}_x &= S_x^0\left[\sin(5\theta)\sigma_z - \cos(5\theta)\sigma_x\right] + \delta S_x\sin(\theta)\\ \hat{S}_y &= -S_y^0\left[\cos(5\theta)\sigma_z + \sin(5\theta)\sigma_x\right] + \delta S_y\cos(\theta)\end{aligned} \tag{B.5}$$

Where $S_x^0 = S_y^0 = \frac{2z\alpha}{D}a^2k^2$ represents the intraband texture and $\delta S_x = -\frac{2zB_U}{D}ak$ the NU interband spin texture. We have $\delta S_x = -\delta S_y = \delta S$. The intraband term is given by $\kappa_N^{intra}(\theta) = \frac{e\tau}{\hbar}\left[S_x^0\sin(5\theta)\sin(\theta) - S_y^0\cos(5\theta)\cos(\theta)\right]\delta k$, yielding $\kappa_N^{intra}(\theta) = \kappa_N^0\cos^2(2\theta)(2\cos^2(2\theta)-1)$ with $\kappa_N^0 = \frac{4ze\tau t_\alpha^2 B_U}{\hbar D^2}m^*a^3k_F^4$. We use $\int\cos^4(x) = 3/8$ and $k_F^2 = \frac{(E_F-E_N)}{a^2t_0}$ to find $\kappa_N^{intra} \approx \frac{2ze\tau}{a\hbar}\frac{t_\alpha^2B_U}{t_0^3}\frac{(E_F-E_N)^2}{D^2}$. Contrarily to the L bands, there is no sharp increase of the response when the band begins to be filled ; the intraband response is negligible. We stress that $t_\alpha m^* = \frac{\sqrt{2}}{2}\sqrt{1+\frac{1+e}{s}}\frac{\delta t}{t_0}$ is linked to the anisotropy of the model. The interband term is given by the length of spin $\delta S = \frac{2zB_U}{D}ak$ with a negative sign multiplied by k. At low filling

$\kappa_N^{inter} = \frac{e\tau}{\hbar}\frac{2zB_U}{D}ak_N^2 \approx \frac{2ze\tau}{a\hbar}\frac{B_U}{t_0}\frac{(E_F-E_N)}{D}$ so there is no sudden increase of the response coming from the interband term either. This term dominates the Edelstein response of the N band at low filling and does not depend on the anisotropy of the model at the lowest order of approximation.

B.4 SHC of the N bands

We want to compute the SHC of the N bands in the vicinity of the point B. We use the perturbation scheme described in the previous section and compute the velocity $\hat{v}_y$ and spin velocity $\hat{v}_x^z$, using that $\hat{S}_z = \sigma_y$ in the N subspace. We have $\hat{v}_x^z = \frac{k_x}{m^*}\hat{S}_z = \frac{k}{m^*}\cos(\theta)\sigma_y$ where m^* is the effective mass of the N bands. We are interested only in the anomalous velocity which allows transitions between the two eigenvectors. There are two sources to this anomalous part : the anisotropy and the orbital mixing anomalous velocities $v_{ani}^a = 4\frac{t_\alpha B_U}{D}a^3k^2\sin(\theta)\sin(4\theta)$ and $v_{OM}^a = 2\frac{t_\alpha B_U}{D}a^3k^2\cos(2\theta)\cos(5\theta)$. The energy splitting is $A = \frac{2t_\alpha B_U}{D}\cos(2\theta)a^3k^3$. Basic algebra gives $\delta k = k_- - k_+ = 2m^*Ck^2 \approx 4m^{*2}C\mu$. Computing the SHC amounts to the integral $I(E_F) = \int_0^{2\pi} d\theta \int_{k_+}^{k_-} \frac{\langle -|v_x^z|+\rangle\langle +|v_y|-\rangle}{D_N^2} kdk$. The k integrand can be rewritten

$$\omega(k,\theta) = -\frac{\frac{k}{m^*}\cos(\theta)\left(4\frac{t_\alpha\beta}{D}k^2\sin(\theta)\sin(4\theta) + 2\frac{t_\alpha\beta}{D}k^2\cos(2\theta)\cos(5\theta)\right)}{(2\frac{t_\alpha\beta}{D})^2k^6\cos^2(2\theta)}k = \frac{\eta(\theta)}{k^2} \qquad \text{(B.6)}$$

The integration gives $\eta(\theta)\frac{\delta k}{k^2} = \eta(\theta)\frac{4m^*t_\alpha B_U}{D}a^3\cos(2\theta)$. There is no divergence of the response for low k. The first angular part is $\frac{\cos(\theta)\sin(\theta)\sin(4\theta)}{\cos(2\theta)} = \sin^2(2\theta)$, giving $1/2$ after integration, the second angular part is $\frac{\cos(4\theta)+\cos(6\theta)}{2}$, giving 0 after integration. The final result is $-\frac{1}{2}\times 2 = -1$.

B.5 SHC : A model for disorder

By adding a constant damping rate Γ to the denominator of the spin-curvature of a Rashba model $\mathcal{H} = \frac{\hbar^2k^2}{2m}\mathbb{I} + \alpha(k_x\sigma_y - k_y\sigma_x)$ we get $\Omega_\pm^z(k) = \mp 2i\hbar^2\frac{k\alpha\sin(\theta)^2}{4m\alpha^2k^2+m\hbar^2\Gamma^2}$, where θ is the polar angle of the wavevector (k_x, k_y). We compute the integral of the curvature over occupied states when the two states are occupied, using $k_{max} - k_{min} = 2\frac{\alpha m}{\hbar^2}$ and $k_{max}^2 \approx k_{min}^2 \approx 2\frac{m\mu}{\hbar^2}$

and find

$$C = \frac{e}{h}\frac{8\alpha^2 m^2 \mu}{8\alpha^2 m^2 \mu + m\hbar^4\Gamma^2} \tag{B.7}$$

In the absence of disorder $C = 1$ as expected. Disorder affects the SHC mostly when $\mu << E_D = \frac{\hbar^4\Gamma^2}{8m\alpha^2}$. It gets reduced with a smaller α, and the filling required to observe a significant signal also increases ; we expect that the contributions from the lowest subband of an 8-band model are washed out by disorder because lower subbands have both a lower α due to their larger confinement gap and a higher Γ due to their proximity to the interface, making them more sensitive to surface roughness scattering.

B.6 Extrinsic contributions to transport

We decompose the contributions to disorder in the scattering rates depending on the order of the disorder potential involved $\omega_{\nu\chi} = \omega^{(2)}_{\nu\chi} + \omega^{(3)}_{\nu\chi} + \omega^{(4)}_{\nu\chi} + ...$ Following [154], we can review the different terms emerging in the Spin Hall response of a system in analogy to what happens for the Anomalous Hall Effect. The total distribution function in the presence of an electric field $\vec{E}$ can be decomposed into

$$f_\nu = f^0(\epsilon_\nu) + g^s_\nu + g^{a1}_\nu + g^{a2}_\nu + g^{adist}_\nu \tag{B.8}$$

where the g_ν 's are non-equilibrium corrections linear in the electric field. They are obtained solving self-consistent master equations. g^s_ν is the well-known correction to the distribution function given by

$$-e\vec{E}\cdot\vec{v}_{0,\nu}\frac{\partial f_0(\epsilon_\nu)}{\partial\epsilon_\nu} = -\sum_\chi \omega^{(2)}_{\nu\chi}(g^s_\nu - g^s_\chi) \tag{B.9}$$

If a single band ν is occupied, this amounts to $-e\vec{E}\cdot\vec{v}_{0,\nu}\frac{\partial f_0(\epsilon_\nu)}{\partial\epsilon_\nu} = -\frac{g_\nu}{\tau_\nu}$, where $\frac{1}{\tau_\nu} = \sum_\chi \omega^{(2)}_{\nu\chi}$ is the total scattering time of band ν associated with the second order processes. This is a correction due to the energy accumulated by the electron displacement between two collisions $v_{0,\nu}\tau_\nu$ inside the electric field. The side-jump mechanism induces another displacement of the electrons due to the side-jump velocity $\vec{v}_{sj,\nu} = \sum_\chi \omega_{\nu\chi}\delta\vec{r}_{\nu\chi}$, where $\delta\vec{r}_{\nu\chi}$ is the coordinate shift

due to the side-jump. The side jump contribution to an operator $\hat{A}$ is given by

$$A_\nu^{sj}(k) = -2\pi \sum_{\eta,p} W_{kp}\delta(\epsilon_{\nu k} - \epsilon_{\eta p}) Im\left[\sum_{\chi\neq\eta} \frac{C_{kp}^{\nu\eta} A_{\eta\chi}(p) C_{pk}^{\chi\nu}}{\epsilon_{\eta p} - \epsilon_{\chi p}} - \sum_{\chi\neq\nu} \frac{C_{pk}^{\eta\nu} A_{\nu\chi}(k) C_{kp}^{\chi\eta}}{\epsilon_{\nu k} - \epsilon_{\chi k}}\right] \quad \text{(B.10)}$$

With $C_{kp}^{\nu\eta} = \langle \nu k | \eta p \rangle$ as a reminder of the evolution of the basis inside the Brillouin Zone, and W_{kp} depends on the scattering properties of the disorder potential between the wavevectors k and p. This produces the anomalous distribution correction

$$-e\vec{E}\cdot\vec{v}_{sj,\nu}\frac{\partial f_0(\epsilon_\nu)}{\partial \epsilon_\nu} = -\sum_\chi \omega_{\nu\chi}(g_\nu^{adist} - g_\chi^{adist}) \quad \text{(B.11)}$$

The corrections g_ν^{a1}, g_ν^{a2} are a rewriting of the corrections of the distribution function in order to account for the higher order perturbation in the disorder $\sum_{l'} \omega_{\nu\chi}^{(3)}(g_\nu^s - g_\chi^s) + \omega_{\nu\chi}^{(2)}(g_\nu^{a1} - g_\chi^{a1}) = 0$ and $\sum_\chi \omega_{\nu\chi}^{(4)}(g_\nu^s - g_\chi^s) + \omega_{\nu\chi}^{(2)}(g_\nu^{a2} - g_\chi^{a2}) = 0$. We have now all the ingredients to write the formula for the transverse conductivity :

$$\sigma_{xy} = \sigma_{xy}^{int} + \sigma_{xy}^{adist} + \sigma_{xy}^{sj} + \sigma_{xy}^{sk1} + \sigma_{xy}^{sk2} \quad \text{(B.12)}$$

Let us review these different contributions to the conductivity. σ_{xy}^{int} is the intrinsic part of the conductivity, which is linked to the Berry curvature via

$$\sigma_{xy}^{int} = e^2 \sum_\nu f^0(\epsilon_\nu)\Omega_\nu \quad \text{(B.13)}$$

σ_{xy}^{adist} is the effect of the anomalous correction to the distribution and its contribution is $\sigma_{xy}^{adist} = \sum_\nu \frac{g_l^{adist}}{E_x} v_{0,\nu}^y$. It is multiplied by the normal part of the velocity $v_{0,\nu}^y = \frac{\partial \epsilon_\nu}{\partial k_y}$. $\sigma_{xy}^{sj} = \sum_\nu \frac{g_\nu^s}{E_x} v_{sj,\nu}^y$ is the side-jump part of the conductivity and is due to the regular correction on the distribution function multiplied by the side-jump velocity. $\sigma_{xy}^{sk1/2} = \sum_\nu \frac{g_\nu^{a1/2}}{E_x} v_{0,\nu}^y$ are the skew-scattering contributions and are the effects of higher order processes of scattering on the external potential in the distribution function ; they involve the regular velocity. Among these five contributions, [154] discards σ_{xy}^{a1} which depends on the impurity concentrations and therefore should be negligible for low disorder. The four others are not negligible and can be of the same order of magnitude. This formalism can be used to compute other response

functions by replacing the velocity by another operator.

Version du 19 novembre 2020, 16:35

Bibliography

[1] G. Moore ; «Cramming More Components Onto Integrated Circuits» ; Proceedings of the IEEE **86**, p. 82–85 (1998). ISSN 0018-9219, 1558-2256. http://ieeexplore.ieee.org/document/658762/. xiii

[2] M. M. Waldrop ; «The chips are down for Moore's law» ; Nature News **530**, p. 144 (2016). http://www.nature.com/news/the-chips-are-down-for-moore-s-law-1.19338 ; section : News Feature. xiii

[3] C. N. R. Rao ; «Transition Metal Oxides» ; p. 36. xiii, 3

[4] J. D. Dunitz & L. E. Orgel ; «Properties of Transition Metal Oxides-I Distortions from cubic symmetry» ; p. 10. xiii, 3

[5] J. Dunitz & L. Orgel ; «Electronic properties of transition-metal oxides-II» ; Journal of Physics and Chemistry of Solids **3**, p. 318–323 (1957). ISSN 00223697. https://linkinghub.elsevier.com/retrieve/pii/0022369757900355. xiii, 3

[6] W. J. Burke & R. J. Pressley ; «Stress induced ferroelectricity in SrTiO3» ; Solid State Communications **9**, p. 191–195 (1971). ISSN 0038-1098. http://www.sciencedirect.com/science/article/pii/0038109871901153. xiii, 3

[7] G. Khaliullin & S. Maekawa ; «Orbital Liquid in Three-Dimensional Mott Insulator : ${\mathrm{LaTiO}}_{3}$» ; Physical Review Letters **85**, p. 3950–3953 (2000). https://link.aps.org/doi/10.1103/PhysRevLett.85.3950 ; publisher : American Physical Society. xiii, 3

[8] B. Keimer, D. Casa, A. Ivanov, J. W. Lynn, M. v. Zimmermann, J. P. Hill, D. Gibbs, Y. Taguchi & Y. Tokura ; «Spin Dynamics and Orbital State in ${\mathrm{LaTiO}}_{3}$» ; Physical Review Letters **85**, p. 3946–3949 (2000). https:

//link.aps.org/doi/10.1103/PhysRevLett.85.3946 ; publisher : American Physical Society. xiii, 3

[9] V. Eyert ; «The metal-insulator transitions of VO2 : A band theoretical approach» ; Annalen der Physik **11**, p. 650–704 (2002). xiii, 3

[10] G. Zhang, E. Gorelov, E. Koch & E. Pavarini ; «Importance of exchange anisotropy and superexchange for the spin-state transitions in RCoO${}_{3}$ ($R=$ rare earth) cobaltates» ; Physical Review B **86**, p. 184 413 (2012). https://link.aps.org/doi/10.1103/PhysRevB.86.184413 ; publisher : American Physical Society. xiii, 3

[11] V. G. Bhide, D. S. Rajoria, Y. S. Reddy, G. R. Rao, G. V. S. Rao & C. N. R. Rao ; «Localized-to-Itinerant Electron Transitions in Rare-Earth Cobaltates» ; Physical Review Letters **28**, p. 1133–1136 (1972). https://link.aps.org/doi/10.1103/PhysRevLett.28.1133 ; publisher : American Physical Society. xiii, 3

[12] S. Middey, J. Chakhalian, P. Mahadevan, J. Freeland, A. Millis & D. Sarma ; «Physics of Ultrathin Films and Heterostructures of Rare-Earth Nickelates» ; Annual Review of Materials Research **46**, p. 305–334 (2016). https://doi.org/10.1146/annurev-matsci-070115-032057 ; _eprint : https ://doi.org/10.1146/annurev-matsci-070115-032057. xiii, 3

[13] K. Rościszewski & A. M. Oleś ; «Spin-orbital order in LaMnO$_3$: $d-p$ model study» ; arXiv :1903.10557 [cond-mat] (2019)http://arxiv.org/abs/1903.10557. xiii

[14] H. Kroemer ; «Nobel Lecture : Quasielectric fields and band offsets : teaching electrons new tricks» ; Reviews of Modern Physics **73**, p. 783–793 (2001). https://link.aps.org/doi/10.1103/RevModPhys.73.783 ; publisher : American Physical Society. xiv

[15] A. Ohtomo & H. Y. Hwang ; «A high-mobility electron gas at the LaAlO 3 /SrTiO 3 heterointerface» ; Nature **427**, p. 423–426 (2004). ISSN 1476-4687. https://www.nature.com/articles/nature02308. xiv, 5, 9, 88

[16] L. W. Martin, Y. H. Chu & R. Ramesh ; «Advances in the growth and characterization of magnetic, ferroelectric, and multiferroic oxide thin films» ; Mate-

rials Science and Engineering R: Reports **68**, p. 89–133 (2010). ISSN 0927-796X. https://escholarship.org/uc/item/1gm2n89d. xiv, 4, 9

[17] J. A. Sulpizio, S. Ilani, P. Irvin & J. Levy ; «Nanoscale Phenomena in Oxide Heterostructures» ; Annual Review of Materials Research **44**, p. 117–149 (2014). https://doi.org/10.1146/annurev-matsci-070813-113437. xiv, 9, 12

[18] Y.-Y. Pai, A. Tylan-Tyler, P. Irvin & J. Levy ; «Physics of SrTiO $_3$ -based heterostructures and nanostructures : a review» ; Reports on Progress in Physics **81**, p. 036 503 (2018). ISSN 0034-4885, 1361-6633. http://stacks.iop.org/0034-4885/81/i=3/a=036503?key=crossref.06c63fe1885f96d4761f31cf08fe4e99. xiv, 9

[19] S. Lemal, N. C. Bristowe & P. Ghosez ; «Polarity-field driven conductivity in SrTiO$_3$/LaAlO$_3$: a hybrid functional study» ; arXiv :2005.12771 [cond-mat] (2020)http://arxiv.org/abs/2005.12771 ; arXiv : 2005.12771. xiv, 4, 9, 101

[20] A. V. Boris, Y. Matiks, E. Benckiser, A. Frano, P. Popovich, V. Hinkov, P. Wochner, M. Castro-Colin, E. Detemple, V. K. Malik, C. Bernhard, T. Prokscha, A. Suter, Z. Salman, E. Morenzoni, G. Cristiani, H.-U. Habermeier & B. Keimer ; «Dimensionality Control of Electronic Phase Transitions in Nickel-Oxide Superlattices» ; Science **332**, p. 937–940 (2011). ISSN 0036-8075, 1095-9203. https://www.sciencemag.org/lookup/doi/10.1126/science.1202647. xiv, 4, 9

[21] K. S. Takahashi, M. Kawasaki & Y. Tokura ; «Interface ferromagnetism in oxide superlattices of CaMnO3/CaRuO3» ; Applied Physics Letters **79**, p. 1324–1326 (2001). ISSN 0003-6951. https://aip.scitation.org/doi/abs/10.1063/1.1398331 ; publisher : American Institute of Physics. xiv, 4, 9

[22] P. Schütz, D. Di Sante, L. Dudy, J. Gabel, M. Stübinger, M. Kamp, Y. Huang, M. Capone, M.-A. Husanu, V. Strocov, G. Sangiovanni, M. Sing & R. Claessen ; «Dimensionality-driven metal-insulator-transition in spin-orbit coupled SrIrO$_3$» ; Physical Review Letters **119**, p. 256 404 (2017). ISSN 0031-9007, 1079-7114. http://arxiv.org/abs/1706.09694 ; arXiv : 1706.09694. xiv, 4, 10

[23] D. J. Groenendijk, C. Autieri, J. Girovsky, M. C. Martinez-Velarte, N. Manca, G. Mattoni, A. M. R. V. L. Monteiro, N. Gauquelin, J. Ver-

BEECK, A. F. OTTE, M. GABAY, S. PICOZZI & A. D. CAVIGLIA ; «Spin-orbit semimetal SrIrO$_3$ in the two-dimensional limit» ; Physical Review Letters **119**, p. 256 403 (2017). ISSN 0031-9007, 1079-7114. http://arxiv.org/abs/1706.08901 ; arXiv : 1706.08901. xiv, 4, 10

[24] J. M. KOSTERLITZ & D. J. THOULESS ; «Ordering, metastability and phase transitions in two-dimensional systems» ; Journal of Physics C: Solid State Physics **6**, p. 1181–1203 (1973). ISSN 0022-3719 ; publisher : IOP Publishing. xiv, 47

[25] F. D. M. HALDANE ; «Model for a Quantum Hall Effect without Landau Levels : Condensed-Matter Realization of the "Parity Anomaly"» ; Physical Review Letters **61**, p. 2015–2018 (1988). https://link.aps.org/doi/10.1103/PhysRevLett.61.2015 ; publisher : American Physical Society. xiv, 47

[26] J. M. KOSTERLITZ ; «Topological Defects and Phase Transitions» ; p. 15. xiv, 47

[27] F. D. M. HALDANE ; «Topological Quantum Matter» ; International Journal of Modern Physics B **32**, p. 1830 004 (2018). ISSN 0217-9792, 1793-6578. https://www.worldscientific.com/doi/abs/10.1142/S0217979218300049. xiv, 47

[28] M. KÖNIG, S. WIEDMANN, C. BRÜNE, A. ROTH, H. BUHMANN, L. W. MOLENKAMP, X.-L. QI & S.-C. ZHANG ; «Quantum Spin Hall Insulator State in HgTe Quantum Wells» ; Science **318**, p. 766–770 (2007). ISSN 0036-8075, 1095-9203. https://science.sciencemag.org/content/318/5851/766. xiv, 47

[29] B. A. BERNEVIG, T. L. HUGHES & S.-C. ZHANG ; «Quantum Spin Hall Effect and Topological Phase Transition in HgTe Quantum Wells» ; Science **314**, p. 1757–1761 (2006). ISSN 0036-8075, 1095-9203. https://science.sciencemag.org/content/314/5806/1757. xiv, 47, 53

[30] M. Z. HASAN & C. L. KANE ; «Topological Insulators» ; Reviews of Modern Physics **82**, p. 3045–3067 (2010). ISSN 0034-6861, 1539-0756. http://arxiv.org/abs/1002.3895 ; arXiv : 1002.3895. xiv, 47

[31] J. E. MOORE ; «The birth of topological insulators» ; Nature **464**, p. 194–198 (2010). ISSN 1476-4687. https://www.nature.com/articles/nature08916 ; number : 7286 Publisher : Nature Publishing Group. xiv, 47

[32] L. Fu, C. L. Kane & E. J. Mele ; «Topological Insulators in Three Dimensions» ; Physical Review Letters **98**, p. 106 803 (2007). https://link.aps.org/doi/10.1103/PhysRevLett.98.106803 ; publisher : American Physical Society. xiv, 47

[33] L. Fu & C. L. Kane ; «Topological insulators with inversion symmetry» ; Physical Review B **76**, p. 045 302 (2007). https://link.aps.org/doi/10.1103/PhysRevB.76.045302 ; publisher : American Physical Society. xiv, 47

[34] A. Y. Kitaev ; «Unpaired Majorana fermions in quantum wires» ; Physics-Uspekhi **44**, p. 131–136 (2001). ISSN 1063-7869 ; publisher : Uspekhi Fizicheskikh Nauk (UFN) Journal. xiv, 48

[35] L. Fu & C. L. Kane ; «Superconducting Proximity Effect and Majorana Fermions at the Surface of a Topological Insulator» ; Physical Review Letters **100**, p. 096 407 (2008). https://link.aps.org/doi/10.1103/PhysRevLett.100.096407 ; publisher : American Physical Society. xiv, 48

[36] S. Nadj-Perge, I. K. Drozdov, J. Li, H. Chen, S. Jeon, J. Seo, A. H. MacDonald, B. A. Bernevig & A. Yazdani ; «Observation of Majorana fermions in ferromagnetic atomic chains on a superconductor» ; Science **346**, p. 602–607 (2014). ISSN 0036-8075, 1095-9203. https://science.sciencemag.org/content/346/6209/602 ; publisher : American Association for the Advancement of Science Section : Research Article. xiv, 48

[37] D.-H. Choe, H.-J. Sung & K. J. Chang ; «Understanding topological phase transition in monolayer transition metal dichalcogenides» ; Physical Review B **93**, p. 125 109 (2016). https://link.aps.org/doi/10.1103/PhysRevB.93.125109 ; publisher : American Physical Society. xv, 48

[38] Y. Ma, L. Kou, X. Li, Y. Dai, S. C. Smith & T. Heine ; «Quantum spin Hall effect and topological phase transition in two-dimensional square transition-metal dichalcogenides» ; Physical Review B **92**, p. 085 427 (2015). https://link.aps.org/doi/10.1103/PhysRevB.92.085427 ; publisher : American Physical Society. xv, 48

[39] D. Xiao, W. Zhu, Y. Ran, N. Nagaosa & S. Okamoto ; «Interface engineering of quantum Hall effects in digital transition metal oxide heterostructures» ; Nature Com-

munications **2**, p. 596 (2011). ISSN 2041-1723. https://www.nature.com/articles/ncomms1602 ; number : 1 Publisher : Nature Publishing Group. xv, 16, 48, 110

[40] M. Kargarian & G. A. Fiete ; «Topological Crystalline Insulators in Transition Metal Oxides» ; Physical Review Letters **110**, p. 156 403 (2013). https://link.aps.org/doi/10.1103/PhysRevLett.110.156403 ; publisher : American Physical Society. xv, 48

[41] P. Jadaun, L. F. Register & S. K. Banerjee ; «Rational design principles for giant spin Hall effect in 5d-transition metal oxides» ; arXiv :1909.07544 [cond-mat] (2019)http://arxiv.org/abs/1909.07544. xv

[42] S. Bader & S. Parkin ; «Spintronics» ; Annual Review of Condensed Matter Physics **1**, p. 71–88 (2010). ISSN 1947-5454, 1947-5462. http://www.annualreviews.org/doi/10.1146/annurev-conmatphys-070909-104123. xv, 59

[43] A. Fert ; «The origin, development and future of spintronics» ; Uspekhi Fizicheskih Nauk **178**, p. 1336 (2008). ISSN 0042-1294, 1996-6652. http://ufn.ru/ru/articles/2008/12/f/. xv, 59

[44] A. Manchon, H. C. Koo, J. Nitta, S. M. Frolov & R. A. Duine ; «New perspectives for Rashba spin–orbit coupling» ; Nature Materials **14**, p. 871–882 (2015). ISSN 1476-4660. https://www.nature.com/articles/nmat4360. xv, 59

[45] T. Kimura, Y. Otani, T. Sato, S. Takahashi & S. Maekawa ; «Room Temperature Reversible Spin Hall Effect» ; Physical Review Letters **98**, p. 156 601 (2007). ISSN 0031-9007, 1079-7114. http://arxiv.org/abs/cond-mat/0609304. xv, 59

[46] J. H. Ryoo, C.-H. Park & I. Souza ; «Computation of intrinsic spin Hall conductivities from first principles using maximally-localized Wannier functions» ; Physical Review B **99**, p. 235 113 (2019). ISSN 2469-9950, 2469-9969. http://arxiv.org/abs/1906.07139. xv, 60

[47] C.-F. Pai, L. Liu, Y. Li, H. W. Tseng, D. C. Ralph & R. A. Buhrman ; «Spin transfer torque devices utilizing the giant spin Hall effect of tungsten» ; Applied Physics Letters **101**, p. 122 404 (2012). ISSN 0003-6951. https://aip.scitation.org/doi/abs/10.1063/1.4753947 ; publisher : American Institute of Physics. xv, 59

[48] C. Hahn, G. de Loubens, O. Klein, M. Viret, V. V. Naletov & J. Ben Youssef ; «Comparative measurements of inverse spin Hall effects and magnetoresistance in YIG/Pt and YIG/Ta» ; Physical Review B **87**, p. 174 417 (2013). https://link.aps.org/doi/10.1103/PhysRevB.87.174417 ; publisher : American Physical Society. xv, 59

[49] A. Manchon, J. Železný, I. M. Miron, T. Jungwirth, J. Sinova, A. Thiaville, K. Garello & P. Gambardella ; «Current-induced spin-orbit torques in ferromagnetic and antiferromagnetic systems» ; arXiv :1801.09636 [cond-mat] (2018)http://arxiv.org/abs/1801.09636. xv, 59, 64

[50] H. Li, H. Gao, L. P. Zârbo, K. Výborný, X. Wang, I. Garate, F. Doğan, A. Čejchan, J. Sinova, T. Jungwirth & A. Manchon ; «Intraband and interband spin-orbit torques in non-centrosymmetric ferromagnets» ; Physical Review B **91** (2015). ISSN 1098-0121, 1550-235X. http://arxiv.org/abs/1501.03292. xv, 59, 70

[51] J. Sinova, D. Culcer, Q. Niu, N. A. Sinitsyn, T. Jungwirth & A. H. MacDonald ; «Universal Intrinsic Spin-Hall Effect» ; Physical Review Letters **92** (2004). ISSN 0031-9007, 1079-7114. http://arxiv.org/abs/cond-mat/0307663. xv, 60, 64

[52] A. D. Caviglia, M. Gabay, S. Gariglio, N. Reyren, C. Cancellieri & J.-M. Triscone ; «Tunable Rashba Spin-Orbit Interaction at Oxide Interfaces» ; Physical Review Letters **104**, p. 126 803 (2010). https://link.aps.org/doi/10.1103/PhysRevLett.104.126803. xv, 5, 6, 42, 60, 78

[53] E. Lesne, Y. Fu, S. Oyarzun, J. C. Rojas-Sánchez, D. C. Vaz, H. Naganuma, G. Sicoli, J.-P. Attané, M. Jamet, E. Jacquet, J.-M. George, A. Barthélémy, H. Jaffrès, A. Fert, M. Bibes & L. Vila ; «Highly efficient and tunable spin-to-charge conversion through Rashba coupling at oxide interfaces» ; Nature Materials **15**, p. 1261–1266 (2016). ISSN 1476-4660. https://www.nature.com/articles/nmat4726. xv, 60, 62, 105

[54] F. Trier, D. C. Vaz, P. Bruneel, P. Noël, A. Fert, L. Vila, J.-P. Attané, A. Barthélémy, M. Gabay, H. Jaffrès & M. Bibes ; «Electric-Field Control of Spin Current Generation and Detection in Ferromagnet-Free SrTiO3-Based Nanodevices» ; Nano Letters **20**, p. 395–401 (2020). ISSN 1530-6984. https://doi.org/10.

1021/acs.nanolett.9b04079 ; publisher : American Chemical Society. xv, 60, 63, 65, 105

[55] D. C. Vaz, P. Noël, A. Johansson, B. Göbel, F. Y. Bruno, G. Singh, S. McKeown-Walker, F. Trier, L. M. Vicente-Arche, A. Sander, S. Valencia, P. Bruneel, M. Vivek, M. Gabay, N. Bergeal, F. Baumberger, H. Okuno, A. Barthélémy, A. Fert, L. Vila, I. Mertig, J.-P. Attané & M. Bibes ; «Mapping spin–charge conversion to the band structure in a topological oxide two-dimensional electron gas» ; Nature Materials p. 1–7 (2019). ISSN 1476-4660. https://www.nature.com/articles/s41563-019-0467-4. xv, 60, 61, 62, 68, 105

[56] J. A. Bert, B. Kalisky, C. Bell, M. Kim, Y. Hikita, H. Y. Hwang & K. A. Moler ; «Direct imaging of the coexistence of ferromagnetism and superconductivity at the LaAlO 3 /SrTiO 3 interface» ; Nature Physics **7**, p. 767–771 (2011). ISSN 1745-2481. https://www.nature.com/articles/nphys2079 ; number : 10 Publisher : Nature Publishing Group. xviii, 6, 7, 105

[57] W. A. Harrison ; *Electronic Structure and the Properties of Solids : The Physics of the Chemical Bond* (Courier Corporation) (2012) ; ISBN 978-0-486-14178-7. 2, 110

[58] V. M. Goldschmidt ; «Die Gesetze der Krystallochemie» ; Naturwissenschaften **14**, p. 477–485 (1926). ISSN 1432-1904. https://doi.org/10.1007/BF01507527. 3

[59] M. A. Peña & J. L. G. Fierro ; «Chemical Structures and Performance of Perovskite Oxides» ; Chemical Reviews **101**, p. 1981–2018 (2001). ISSN 0009-2665. https://doi.org/10.1021/cr980129f ; publisher : American Chemical Society. 3

[60] E. Pytte ; «Theory of Perovskite Ferroelectrics» ; Physical Review B **5**, p. 3758–3769 (1972). https://link.aps.org/doi/10.1103/PhysRevB.5.3758 ; publisher : American Physical Society. 4

[61] V. Železný, E. Cockayne, J. Petzelt, M. F. Limonov, D. E. Usvyat, V. V. Lemanov & A. A. Volkov ; «Temperature dependence of infrared-active phonons in ${\mathrm{CaTiO}}_{3} :$ A combined spectroscopic and first-principles study» ; Physical Review B **66**, p. 224 303 (2002). https://link.aps.org/doi/10.1103/PhysRevB.66.224303 ; publisher : American Physical Society. 4

[62] J. Jensen & A. R. Mackintosh ; «Structures and Excitations» ; p. 413. 4

[63] J. B. Goodenough ; «Spin-Orbit-Coupling Effects in Transition-Metal Compounds» ; Physical Review **171**, p. 466–479 (1968). https://link.aps.org/doi/10.1103/PhysRev.171.466 ; publisher : American Physical Society. 4

[64] W. S. Choi, M. F. Chisholm, D. J. Singh, T. Choi, G. E. Jellison & H. N. Lee ; «Wide bandgap tunability in complex transition metal oxides by site-specific substitution» ; Nature Communications **3**, p. 689 (2012). ISSN 2041-1723. https://www.nature.com/articles/ncomms1690 ; number : 1 Publisher : Nature Publishing Group. 4

[65] M. V. Ganduglia-Pirovano, A. Hofmann & J. Sauer ; «Oxygen vacancies in transition metal and rare earth oxides : Current state of understanding and remaining challenges» ; Surface Science Reports **62**, p. 219–270 (2007). ISSN 0167-5729. http://www.sciencedirect.com/science/article/pii/S0167572907000295. 4

[66] D. G. Schlom, L.-Q. Chen, C.-B. Eom, K. M. Rabe, S. K. Streiffer & J.-M. Triscone ; «Strain Tuning of Ferroelectric Thin Films» ; Annual Review of Materials Research **37**, p. 589–626 (2007). https://doi.org/10.1146/annurev.matsci.37.061206.113016 ; _eprint : https ://doi.org/10.1146/annurev.matsci.37.061206.113016. 4

[67] S. Thiel ; «Tunable Quasi-Two-Dimensional Electron Gases in Oxide Heterostructures» ; Science **313**, p. 1942–1945 (2006). ISSN 0036-8075, 1095-9203. https://www.sciencemag.org/lookup/doi/10.1126/science.1131091. 5, 88, 89

[68] S. Gariglio, M. Gabay, J. Mannhart & J. M. Triscone ; «Interface superconductivity» ; Physica C: Superconductivity and its Applications **514**, p. 189–198 (2015). ISSN 0921-4534. http://www.sciencedirect.com/science/article/pii/S0921453415000556. 5

[69] L. Yu & A. Zunger ; «A polarity-induced defect mechanism for conductivity and magnetism at polar–nonpolar oxide interfaces» ; Nature Communications **5**, p. 5118 (2014). ISSN 2041-1723. https://www.nature.com/articles/ncomms6118 ; number : 1 Publisher : Nature Publishing Group. 6

[70] N. Reyren, S. Thiel, A. D. Caviglia, L. F. Kourkoutis, G. Hammerl, C. Richter, C. W. Schneider, T. Kopp, A.-S. Rüetschi, D. Jaccard, M. Gabay, D. A.

Muller, J.-M. Triscone & J. Mannhart ; «Superconducting Interfaces Between Insulating Oxides» ; Science **317**, p. 1196–1199 (2007). ISSN 0036-8075, 1095-9203. https://science.sciencemag.org/content/317/5842/1196 ; publisher : American Association for the Advancement of Science Section : Report. 6

[71] A. Fête, S. Gariglio, A. D. Caviglia, J.-M. Triscone & M. Gabay ; «Rashba induced magnetoconductance oscillations in the LaAlO${}_{3}$-SrTiO${}_{3}$ heterostructure» ; Physical Review B **86**, p. 201 105 (2012). https://link.aps.org/doi/10.1103/PhysRevB.86.201105. 6

[72] L. Li, C. Richter, J. Mannhart & R. C. Ashoori ; «Coexistence of magnetic order and two-dimensional superconductivity at LaAlO 3 /SrTiO 3 interfaces» ; Nature Physics **7**, p. 762–766 (2011). ISSN 1745-2481. https://www.nature.com/articles/nphys2080 ; number : 10 Publisher : Nature Publishing Group. 6

[73] A. D. Caviglia, S. Gariglio, N. Reyren, D. Jaccard, T. Schneider, M. Gabay, S. Thiel, G. Hammerl, J. Mannhart & J.-M. Triscone ; «Electric field control of the LaAlO 3 /SrTiO 3 interface ground state» ; Nature **456**, p. 624–627 (2008). ISSN 1476-4687. https://www.nature.com/articles/nature07576. 6

[74] A. M. R. V. L. Monteiro, M. Vivek, D. J. Groenendijk, P. Bruneel, I. Leermakers, U. Zeitler, M. Gabay & A. D. Caviglia ; «Band inversion driven by electronic correlations at the (111) ${\mathrm{LaAlO}}_{3}/{\mathrm{SrTiO}}_{3}$ interface» ; Physical Review B **99**, p. 201 102 (2019). https://link.aps.org/doi/10.1103/PhysRevB.99.201102 ; publisher : American Physical Society. 10, 37, 38, 39, 44, 46

[75] S. Sarkar & S. Sarkar ; «Tunneling in Graphene SymFETs» ; arXiv :1805.09659 [cond-mat] (2018)http://arxiv.org/abs/1805.09659 ; arXiv : 1805.09659. 12

[76] «Introduction to Crystal Field Theory» ; (2013). https://chem.libretexts.org/Bookshelves/Inorganic_Chemistry/Modules_and_Websites_(Inorganic_Chemistry)/Crystal_Field_Theory/Introduction_to_Crystal_Field_Theory ; library Catalog : chem.libretexts.org. 12

[77] T. C. Rödel, F. Fortuna, S. Sengupta, E. Frantzeskakis, P. L. Fèvre, F. Bertran, B. Mercey, S. Matzen, G. Agnus, T. Maroutian, P. Lecoeur & A. F.

Santander-Syro ; «Universal Fabrication of 2D Electron Systems in Functional Oxides» ; Advanced Materials **28**, p. 1976–1980 (2016). ISSN 09359648. http://doi.wiley.com/10.1002/adma.201505021. 14, 19, 101, 110

[78] M. Vivek ; *Topological states on surfaces and interfaces of perovskite transition metal oxides* ; Thèse de doctorat ; Université Paris Saclay (COmUE) (2018). https://tel.archives-ouvertes.fr/tel-01890133. 16

[79] E. O. Kane ; «Band structure of indium antimonide» ; Journal of Physics and Chemistry of Solids **1**, p. 249–261 (1957). ISSN 0022-3697. http://www.sciencedirect.com/science/article/pii/0022369757900136. 18, 78

[80] G. Khalsa & A. H. MacDonald ; «Theory of the SrTiO${}_{3}$ surface state two-dimensional electron gas» ; Physical Review B **86**, p. 125 121 (2012). https://link.aps.org/doi/10.1103/PhysRevB.86.125121. 19

[81] G. Khalsa, B. Lee & A. H. MacDonald ; «Theory of ${t}_{2g}$ electron-gas Rashba interactions» ; Physical Review B **88**, p. 041 302 (2013). https://link.aps.org/doi/10.1103/PhysRevB.88.041302. 19

[82] Z. Zhong, A. Tóth & K. Held ; «Theory of spin-orbit coupling at LaAlO${}_{3}$/SrTiO${}_{3}$ interfaces and SrTiO${}_{3}$ surfaces» ; Physical Review B **87**, p. 161 102 (2013). https://link.aps.org/doi/10.1103/PhysRevB.87.161102 ; publisher : American Physical Society. 19, 21, 78

[83] S. McKeown Walker, A. de la Torre, F. Bruno, A. Tamai, T. Kim, M. Hoesch, M. Shi, M. Bahramy, P. King & F. Baumberger ; «Control of a Two-Dimensional Electron Gas on ${\mathrm{SrTiO}}_{3}(111)$ by Atomic Oxygen» ; Physical Review Letters **113**, p. 177 601 (2014). https://link.aps.org/doi/10.1103/PhysRevLett.113.177601 ; publisher : American Physical Society. 19, 42

[84] A. F. Santander-Syro, F. Fortuna, C. Bareille, T. C. Rödel, G. Landolt, N. C. Plumb, J. H. Dil & M. Radović ; «Giant spin splitting of the two-dimensional electron gas at the surface of SrTiO3» ; Nature Materials **13**, p. 1085–1090 (2014). ISSN 1476-1122, 1476-4660. http://www.nature.com/articles/nmat4107. 21

[85] S. M. Walker, S. Riccò, F. Y. Bruno, A. de la Torre, A. Tamai, E. Golias, A. Varykhalov, D. Marchenko, M. Hoesch, M. S. Bahramy, P. D. C. King,

J. Sánchez-Barriga & F. Baumberger ; «Absence of Giant Spin Splitting in the Two-Dimensional Electron Liquid at the Surface of SrTiO$_3$ (001)» ; Physical Review B **93**, p. 245 143 (2016). ISSN 2469-9950, 2469-9969. http://arxiv.org/abs/1603.00181. 21

[86] E. B. Guedes, S. Muff, M. Fanciulli, A. P. Weber, M. Caputo, Z. Wang, N. C. Plumb, M. Radović & J. H. Dil ; «Single spin-polarised Fermi surface in SrTiO$_3$ thin films» ; arXiv :1908.07379 [cond-mat] (2019)http://arxiv.org/abs/1908.07379. 21

[87] M. Vivek, M. O. Goerbig & M. Gabay ; «Topological states at the (001) surface of ${\mathrm{SrTiO}}_{3}$» ; Physical Review B **95**, p. 165 117 (2017). https://link.aps.org/doi/10.1103/PhysRevB.95.165117 ; publisher : American Physical Society. 21, 57

[88] C. Şahin, G. Vignale & M. E. Flatté ; «Strain engineering of the intrinsic spin Hall conductivity in a ${\mathrm{SrTiO}}_{3}$ quantum well» ; Physical Review Materials **3**, p. 014 401 (2019). https://link.aps.org/doi/10.1103/PhysRevMaterials.3.014401 ; publisher : American Physical Society. 21

[89] Z. Zhang & J. T. Yates ; «Band Bending in Semiconductors : Chemical and Physical Consequences at Surfaces and Interfaces» ; Chemical Reviews **112**, p. 5520–5551 (2012). ISSN 0009-2665. https://doi.org/10.1021/cr3000626 ; publisher : American Chemical Society. 25

[90] F. Stern ; «Self-Consistent Results for n-Type Si Inversion Layers» ; Physical Review B **5**, p. 4891–4899 (1972). https://link.aps.org/doi/10.1103/PhysRevB.5.4891 ; publisher : American Physical Society. 25

[91] J. Coignus ; *Etude de la conduction électrique dans les diélectriques à forte permittivité utilisés en microélectronique* ; Thèse de doctorat ; Institut National Polytechnique de Grenoble - INPG (2010). https://tel.archives-ouvertes.fr/tel-00557752. 25

[92] A. Fete ; *Magnetotransport experiments at the LaAlO3/SrTiO3 interface* ; PhD Thesis ; University of Geneva (2014). https://archive-ouverte.unige.ch/unige:38284. 25, 31, 38

[93] J. Biscaras ; *Supraconductivité bi-dimensionnelle à l'interface d'Oxydes de Titane* ; These de doctorat ; Paris 6 (2012). https://www.theses.fr/2012PA066639. 25, 33, 36

[94] A. E. M. Smink, J. C. de Boer, M. P. Stehno, A. Brinkman, W. G. van der Wiel & H. Hilgenkamp ; «Gate-tunable band structure of the LaAlO$_3$-SrTiO$_3$ interface» ; Physical Review Letters **118**, p. 106 401 (2017). ISSN 0031-9007, 1079-7114. http://arxiv.org/abs/1610.02299 ; arXiv : 1610.02299. 25, 37, 38, 39, 44

[95] K. Pesz & R. W. Munn ; «Densities of states and anisotropy in tight-binding models» ; Journal of Physics C: Solid State Physics **19**, p. 2499–2507 (1986). ISSN 0022-3719 ; publisher : IOP Publishing. 28

[96] M. Stengel ; «First-Principles Modeling of Electrostatically Doped Perovskite Systems» ; Physical Review Letters **106**, p. 136 803 (2011). https://link.aps.org/doi/10.1103/PhysRevLett.106.136803 ; publisher : American Physical Society. 28

[97] H. Wang, G. Wang, S. Chang & Q. Huang ; «Accelerated solution of poisson-schrodinger equations in nanoscale devices by anderson mixing scheme» ; Micro Nano Letters **4**, p. 122–127 (2009). ISSN 1750-0443 ; conference Name : Micro Nano Letters. 29

[98] K. V. Reich, M. Schecter & B. I. Shklovskii ; «Accumulation, inversion, and depletion layers in ${\mathrm{SrTiO}}_{3}$» ; Physical Review B **91**, p. 115 303 (2015). https://link.aps.org/doi/10.1103/PhysRevB.91.115303 ; publisher : American Physical Society. 29

[99] C. Ang & Z. Yu ; «dc electric-field dependence of the dielectric constant in polar dielectrics : Multipolarization mechanism model» ; Physical Review B **69**, p. 174 109 (2004). https://link.aps.org/doi/10.1103/PhysRevB.69.174109 ; publisher : American Physical Society. 29

[100] J. Hemberger, P. Lunkenheimer, R. Viana, R. Böhmer & A. Loidl ; «Electric-field-dependent dielectric constant and nonlinear susceptibility in SrTiO 3» ; Physical Review B **52**, p. 13 159–13 162 (1995). ISSN 0163-1829, 1095-3795. https://link.aps.org/doi/10.1103/PhysRevB.52.13159. 31

[101] J. H. Barrett ; «Dielectric Constant in Perovskite Type Crystals» ; Physical Review **86**, p. 118–120 (1952). https://link.aps.org/doi/10.1103/PhysRev.86.118 ; publisher : American Physical Society. 31

[102] R. C. Neville, B. Hoeneisen & C. A. Mead ; «Permittivity of Strontium Titanate» ; Journal of Applied Physics **43**, p. 2124–2131 (1972). ISSN 0021-8979. https://aip.scitation.org/doi/abs/10.1063/1.1661463 ; publisher : American Institute of Physics. 31

[103] A. Raslan, P. Lafleur & W. A. Atkinson ; «Temperature-dependent band structure of ${\mathrm{SrTiO}}_{3}$ interfaces» ; Physical Review B **95**, p. 054 106 (2017). https://link.aps.org/doi/10.1103/PhysRevB.95.054106 ; publisher : American Physical Society. 31

[104] M. Basletic, J.-L. Maurice, C. Carrétéro, G. Herranz, O. Copie, M. Bibes, E. Jacquet, K. Bouzehouane, S. Fusil & A. Barthélémy ; «Mapping the spatial distribution of charge carriers in LaAlO3/SrTiO3 heterostructures» ; Nature Materials **7**, p. 621–625 (2008). ISSN 1476-1122, 1476-4660. http://www.nature.com/articles/nmat2223. 31

[105] A. M. R. V. L. Monteiro, D. J. Groenendijk, I. Groen, J. de Bruijckere, R. Gaudenzi, H. S. J. van der Zant & A. D. Caviglia ; «Two-dimensional superconductivity at the (111)LaAlO$_3$/SrTiO$_3$interface» ; Physical Review B **96**, p. 020 504 (2017). ISSN 2469-9950, 2469-9969. http://arxiv.org/abs/1703.04742 ; arXiv : 1703.04742. 32

[106] P. Rout, E. Maniv & Y. Dagan ; «Link between the Superconducting Dome and Spin-Orbit Interaction in the (111) ${\mathrm{LaAlO}}_{3}/\mathrm{SrTi}{\mathrm{O}}_{3}$ Interface» ; Physical Review Letters **119**, p. 237 002 (2017). https://link.aps.org/doi/10.1103/PhysRevLett.119.237002 ; publisher : American Physical Society. 32, 38

[107] K. Song, S. Ryu, H. Lee, T. R. Paudel, C. T. Koch, B. Park, J. K. Lee, S.-Y. Choi, Y.-M. Kim, J. C. Kim, H. Y. Jeong, M. S. Rzchowski, E. Y. Tsymbal, C.-B. Eom & S. H. Oh ; «Direct imaging of the electron liquid at oxide interfaces» ; Nature Nanotechnology **13**, p. 198–203 (2018). ISSN 1748-3395. https://www.nature.com/

articles/s41565-017-0040-8/ ; number : 3 Publisher : Nature Publishing Group. 32

[108] J. Biscaras, N. Bergeal, S. Hurand, C. Grossetête, A. Rastogi, R. C. Budhani, D. LeBoeuf, C. Proust & J. Lesueur ; «Two-Dimensional Superconducting Phase in ${\mathrm{LaTiO}}_{3}/{\mathrm{SrTiO}}_{3}$ Heterostructures Induced by High-Mobility Carrier Doping» ; Physical Review Letters **108**, p. 247 004 (2012). https://link.aps.org/doi/10.1103/PhysRevLett.108.247004 ; publisher : American Physical Society. 33

[109] A. Joshua, S. Pecker, J. Ruhman, E. Altman & S. Ilani ; «A universal critical density underlying the physics of electrons at the $LaAlO_3$/$SrTiO_3$ interface» ; Nature Communications **3**, p. 1129 (2012). ISSN 2041-1723. https://www.nature.com/articles/ncomms2116. 37, 38

[110] C. Cancellieri, M. L. Reinle-Schmitt, M. Kobayashi, V. N. Strocov, P. R. Willmott, D. Fontaine, P. Ghosez, A. Filippetti, P. Delugas & V. Fiorentini ; «Doping-dependent band structure of LaAlO${}_{3}$/SrTiO${}_{3}$ interfaces by soft x-ray polarization-controlled resonant angle-resolved photoemission» ; Physical Review B **89**, p. 121 412 (2014). https://link.aps.org/doi/10.1103/PhysRevB.89.121412 ; publisher : American Physical Society. 38, 91

[111] C. Bell, S. Harashima, Y. Kozuka, M. Kim, B. G. Kim, Y. Hikita & H. Y. Hwang ; «Dominant Mobility Modulation by the Electric Field Effect at the ${\mathrm{LaAlO}}_{3}/{\mathrm{SrTiO}}_{3}$ Interface» ; Physical Review Letters **103**, p. 226 802 (2009). https://link.aps.org/doi/10.1103/PhysRevLett.103.226802 ; publisher : American Physical Society. 38

[112] Z. Chen, H. Yuan, Y. Xie, D. Lu, H. Inoue, Y. Hikita, C. Bell & H. Y. Hwang ; «Dual-Gate Modulation of Carrier Density and Disorder in an Oxide Two-Dimensional Electron System» ; Nano Letters **16**, p. 6130–6136 (2016). ISSN 1530-6984, 1530-6992. https://pubs.acs.org/doi/10.1021/acs.nanolett.6b02348. 38

[113] A. E. M. Smink, M. P. Stehno, J. C. de Boer, A. Brinkman, W. G. van der Wiel & H. Hilgenkamp ; «Correlation between Superconductivity, Band Filling and Electron Confinement at the LaAlO${}_{3}$-SrTiO${}_{3}$ Interface» ; Physical Review

B **97**, p. 245 113 (2018). ISSN 2469-9950, 2469-9969. http://arxiv.org/abs/1801.02881 ; arXiv : 1801.02881. 39, 44, 45, 46, 120

[114] T. Ando, A. B. Fowler & F. Stern ; «Electronic properties of two-dimensional systems» ; Reviews of Modern Physics **54**, p. 437–672 (1982). https://link.aps.org/doi/10.1103/RevModPhys.54.437 ; publisher : American Physical Society. 39

[115] U. Khanna, P. K. Rout, M. Mograbi, G. Tuvia, I. Leermakers, U. Zeitler, Y. Dagan & M. Goldstein ; «Symmetry and correlation effects on band structure explain the anomalous transport properties of (111) LaAlO$_3$/SrTiO$_3$» ; arXiv :1901.10931 [cond-mat] (2019)http://arxiv.org/abs/1901.10931. 41, 46

[116] A. Georges, L. d. Medici & J. Mravlje ; «Strong Correlations from Hund's Coupling» ; Annual Review of Condensed Matter Physics **4**, p. 137–178 (2013). https://doi.org/10.1146/annurev-conmatphys-020911-125045 ; _eprint : https ://doi.org/10.1146/annurev-conmatphys-020911-125045. 45

[117] H. Weng, X. Dai & Z. Fang ; «From Anomalous Hall Effect to the Quantum Anomalous Hall Effect» ; (2015). 49

[118] M. O. Goerbig ; «Quantum Hall Effects» ; arXiv :0909.1998 [cond-mat] (2009)http://arxiv.org/abs/0909.1998 ; arXiv : 0909.1998. 49

[119] G. Montambaux ; «Semiclassical quantization of skipping orbits» ; The European Physical Journal B **79**, p. 215–224 (2011). ISSN 1434-6036. https://doi.org/10.1140/epjb/e2010-10584-y. 49

[120] C. W. J. Beenakker, H. van Houten & B. J. van Wees ; «Skipping orbits, traversing trajectories, and quantum ballistic transport in microstructures» ; Superlattices and Microstructures **5**, p. 127–132 (1989). ISSN 0749-6036. http://www.sciencedirect.com/science/article/pii/0749603689900815. 49

[121] J. Kondo ; «Anomalous Hall Effect and Magnetoresistance of Ferromagnetic Metals» ; Progress of Theoretical Physics **27**, p. 772–792 (1962). ISSN 0033-068X. https://academic.oup.com/ptp/article-lookup/doi/10.1143/PTP.27.772. 49

[122] C.-Z. Chang & M. Li ; «Quantum anomalous Hall effect in time-reversal-symmetry breaking topological insulators» ; Journal of Physics: Condensed Matter **28**, p. 123 002 (2016). ISSN 0953-8984 ; publisher : IOP Publishing. 49

[123] Wikipedia ; «Topology» ; (2020). https://en.wikipedia.org/w/index.php?title=Topology&oldid=965847258 ; page Version ID : 965847258. 50

[124] D. Xiao, M.-C. Chang & Q. Niu ; «Berry phase effects on electronic properties» ; Reviews of Modern Physics **82**, p. 1959–2007 (2010). https://link.aps.org/doi/10.1103/RevModPhys.82.1959 ; publisher : American Physical Society. 50

[125] T. Kato ; «On the Adiabatic Theorem of Quantum Mechanics» ; Journal of the Physical Society of Japan **5**, p. 435–439 (1950). ISSN 0031-9015. https://journals.jps.jp/doi/abs/10.1143/JPSJ.5.435 ; publisher : The Physical Society of Japan. 50

[126] D. J. Thouless, M. Kohmoto, M. P. Nightingale & M. den Nijs ; «Quantized Hall Conductance in a Two-Dimensional Periodic Potential» ; Physical Review Letters **49**, p. 405–408 (1982). https://link.aps.org/doi/10.1103/PhysRevLett.49.405 ; publisher : American Physical Society. 52

[127] F. D. M. Haldane ; «Berry Curvature on the Fermi Surface : Anomalous Hall Effect as a Topological Fermi-Liquid Property» ; Physical Review Letters **93**, p. 206 602 (2004). https://link.aps.org/doi/10.1103/PhysRevLett.93.206602 ; publisher : American Physical Society. 56

[128] R. Resta ; «X-ray circular dichroism versus orbital magnetization» ; Physical Review Research **2**, p. 023 139 (2020). ISSN 2643-1564. http://arxiv.org/abs/2003.04256 ; arXiv : 2003.04256. 56

[129] A. Marrazzo & R. Resta ; «Local Theory of the Insulating State» ; Physical Review Letters **122**, p. 166 602 (2019). https://link.aps.org/doi/10.1103/PhysRevLett.122.166602 ; publisher : American Physical Society. 56

[130] M. Gradhand, D. V. Fedorov, F. Pientka, P. Zahn, I. Mertig & B. L. Györffy ; «First-principle calculations of the Berry curvature of Bloch states for charge and spin transport of electrons» ; Journal of Physics: Condensed Matter **24**, p. 213 202 (2012). ISSN 0953-8984 ; publisher : IOP Publishing. 57

[131] G. Y. Guo, S. Murakami, T.-W. Chen & N. Nagaosa ; «Intrinsic Spin Hall Effect in Platinum : First-Principles Calculations» ; Physical Review Letters **100**, p. 096 401 (2008). https://link.aps.org/doi/10.1103/PhysRevLett.100.096401. 59

[132] L. Zhu & R. A. Buhrman ; «Maximizing the spin-orbit torque efficiency of Pt/Ti multilayers by optimization of the tradeoff between the intrinsic spin Hall conductivity and carrier lifetime» ; arXiv :1908.06528 [cond-mat] (2019)http://arxiv.org/abs/1908.06528. 59

[133] A. Hoffmann ; «Spin Hall Effects in Metals» ; IEEE Transactions on Magnetics **49**, p. 5172–5193 (2013). ISSN 0018-9464, 1941-0069. http://ieeexplore.ieee.org/document/6516040/. 60

[134] T. S. Ghiasi, A. A. Kaverzin, P. J. Blah & B. J. van Wees ; «Charge-to-Spin Conversion by the Rashba-Edelstein Effect in 2D van der Waals Heterostructures up to Room Temperature» ; arXiv :1905.01371 [cond-mat, physics :physics] (2019)http://arxiv.org/abs/1905.01371. 60

[135] L. Li, J. Zhang, G. Myeong, W. Shin, H. Lim, B. Kim, S. Kim, T. Jin, S. A. Cavill, B. S. Kim, C. Kim, J. Lischner, A. Ferreira & S. Cho ; «Gate-Tunable Reversible Rashba-Edelstein Effect in a Few-Layer Graphene/2H-TaS2 Heterostructure at Room Temperature» ; ACS Nano p. acsnano.0c01037 (2020). ISSN 1936-0851, 1936-086X. http://arxiv.org/abs/1906.10702 ; arXiv : 1906.10702. 60

[136] V. M. Edelstein ; «Spin polarization of conduction electrons induced by electric current in two-dimensional asymmetric electron systems» ; Solid State Communications **73**, p. 233–235 (1990). ISSN 0038-1098. http://www.sciencedirect.com/science/article/pii/003810989090963C. 60, 61, 105

[137] P. Bruneel & M. Gabay ; «Spin texture driven spintronic enhancement at the $\mathrm{La}\mathrm{Al}{\mathrm{O}}_{3}/\mathrm{Sr}\mathrm{Ti}{\mathrm{O}}_{3}$ interface» ; Physical Review B **102**, p. 144 407 (2020). https://link.aps.org/doi/10.1103/PhysRevB.102.144407 ; publisher : American Physical Society. 60

[138] C. Kittel ; «On the Theory of Ferromagnetic Resonance Absorption» ; Physical Review **73**, p. 155–161 (1948). https://link.aps.org/doi/10.1103/PhysRev.73.155 ; publisher : American Physical Society. 62

[139] S. P. Dash, S. Sharma, R. S. Patel, M. P. de Jong & R. Jansen ; «Electrical creation of spin polarization in silicon at room temperature» ; Nature **462**, p.

491–494 (2009). ISSN 0028-0836, 1476-4687. http://www.nature.com/articles/nature08570. 62

[140] M. Tran, H. Jaffrès, C. Deranlot, J.-M. George, A. Fert, A. Miard & A. Lemaître ; «Enhancement of the Spin Accumulation at the Interface between a Spin-Polarized Tunnel Junction and a Semiconductor» ; Physical Review Letters **102**, p. 036 601 (2009). ISSN 0031-9007, 1079-7114. https://link.aps.org/doi/10.1103/PhysRevLett.102.036601. 62

[141] D. A. Abanin, A. V. Shytov, L. S. Levitov & B. I. Halperin ; «Nonlocal Charge Transport Mediated by Spin Diffusion in the Spin-Hall Effect Regime» ; Physical Review B **79** (2009). ISSN 1098-0121, 1550-235X. http://arxiv.org/abs/0708.0455. 62

[142] A. Mook, R. R. Neumann, A. Johansson, J. Henk & I. Mertig ; «Origin of the Magnetic Spin Hall Effect : Spin Current Vorticity in the Fermi Sea» ; arXiv :1910.13375 [cond-mat] (2019)http://arxiv.org/abs/1910.13375. 62, 67

[143] T. Maassen, I. J. Vera-Marun, M. H. D. Guimarães & B. J. van Wees ; «Contact induced spin relaxation in Hanle spin precession measurements» ; Physical Review B **86**, p. 235 408 (2012). ISSN 1098-0121, 1550-235X. http://arxiv.org/abs/1210.0093. 62

[144] R. J. Elliott ; «Theory of the Effect of Spin-Orbit Coupling on Magnetic Resonance in Some Semiconductors» ; Physical Review **96**, p. 266–279 (1954). ISSN 0031-899X. https://link.aps.org/doi/10.1103/PhysRev.96.266. 63

[145] Y. Yafet ; «g Factors and Spin-Lattice Relaxation of Conduction Electrons» ; dans «Solid State Physics», , tome 14p. 1–98 (Elsevier) (1963) ; ISBN 978-0-12-607714-8. https://linkinghub.elsevier.com/retrieve/pii/S0081194708602593. 63

[146] P. Boross, B. Dóra, A. Kiss & F. Simon ; «A unified theory of spin-relaxation due to spin-orbit coupling in metals and semiconductors» ; Scientific Reports **3**, p. 1–5 (2013). ISSN 2045-2322. https://www.nature.com/articles/srep03233 ; number : 1 Publisher : Nature Publishing Group. 63

[147] L. Smrcka & P. Streda ; «Transport coefficients in strong magnetic fields» ; Journal of Physics C: Solid State Physics **10**, p. 2153–2161 (1977). ISSN

0022-3719. http://stacks.iop.org/0022-3719/10/i=12/a=021?key=crossref.00d9133e41a1e687da57f6c2d2ea44a9. 64

[148] P. Stieda ; «Theory of quantised Hall conductivity in two dimensions» ; p. 6. 64

[149] K. Shen, G. Vignale & R. Raimondi ; «Inverse Edelstein Effect» ; Physical Review Letters **112** (2014). ISSN 0031-9007, 1079-7114. http://arxiv.org/abs/1311.6516. 66

[150] G. Vignale & I. V. Tokatly ; «Theory of the nonlinear Rashba-Edelstein effect : The clean electron gas limit» ; Physical Review B **93**, p. 035 310 (2016). ISSN 2469-9950, 2469-9969. https://link.aps.org/doi/10.1103/PhysRevB.93.035310. 66

[151] N. A. Sinitsyn, A. H. MacDonald, T. Jungwirth, V. K. Dugaev & J. Sinova ; «Anomalous Hall effect in a two-dimensional Dirac band : The link between the Kubo-Streda formula and the semiclassical Boltzmann equation approach» ; Physical Review B **75**, p. 045 315 (2007). ISSN 1098-0121, 1550-235X. https://link.aps.org/doi/10.1103/PhysRevB.75.045315. 67, 83

[152] N. A. Sinitsyn, Q. Niu, J. Sinova & K. Nomura ; «Disorder effects in the AHE induced by Berry curvature» ; Physical Review B **72** (2005). ISSN 1098-0121, 1550-235X. http://arxiv.org/abs/cond-mat/0502426. 67, 83

[153] S. Okamoto, T. Egami & N. Nagaosa ; «Critical spin fluctuation mechanism for the spin Hall effect» ; arXiv :1905.10929 [cond-mat] (2019)http://arxiv.org/abs/1905.10929. 67

[154] N. A. Sinitsyn ; «Semiclassical theories of the anomalous Hall effect» ; Journal of Physics: Condensed Matter **20**, p. 023 201 (2007). ISSN 0953-8984 ; publisher : IOP Publishing. 67, 83, 125, 126

[155] J.-M. Jancu, R. Scholz, E. A. de Andrada e Silva & G. C. La Rocca ; «Atomistic spin-orbit coupling and k.p parameters in III-V semiconductors» ; Physical Review B **72**, p. 193 201 (2005). ISSN 1098-0121, 1550-235X. https://link.aps.org/doi/10.1103/PhysRevB.72.193201. 78

[156] C. Yin, P. Seiler, L. M. K. Tang, I. Leermakers, N. Lebedev, U. Zeitler & J. Aarts ; «Tuning Rashba spin-orbit coupling at LaAlO3/SrTiO3 interfaces by band filling» ; arXiv :1904.03731 [cond-mat] (2019)http://arxiv.org/abs/1904.03731. 78

[157] Y. Gan, Y. Zhang, D. V. Christensen, N. Pryds & Y. Chen ; «Gate-tunable Rashba spin-orbit coupling and spin polarization at diluted oxide interfaces» ; arXiv :1908.11167 [cond-mat] (2019)http://arxiv.org/abs/1908.11167. 78

[158] A. Crépieux & P. Bruno ; «Theory of the anomalous Hall effect from the Kubo formula and the Dirac equation» ; Physical Review B **64** (2001). ISSN 0163-1829, 1095-3795. http://arxiv.org/abs/cond-mat/0101376. 83

[159] S. Bhowal & S. Satpathy ; «Electric field tuning of the anomalous Hall effect at oxide interfaces» ; arXiv :1812.08950 [cond-mat] (2018)http://arxiv.org/abs/1812.08950. 85

[160] J.-M. Triscone ; «Origin of the conduction in polar/non-polar heterostructures : the case of SrTiO3 capped LaAlO3/SrTiO3 interfaces» ; Unpublished . 87, 88, 89

[161] Y. Kwak, W. Han, T. D. N. Ngo, D. Odkhuu, J. Kim, Y. Heon, N. Park, S. H. Rhim, M.-H. Jung, J. Suh, S.-B. Shim, S. Choi, Y.-J. Doh, J. S. Lee, J. Song & J. Kim ; «Interplay between superconductivity and magnetism in one-unit-cell LaAlO3 capped with SrTiO3» ; p. 23. 87, 89, 92, 97

[162] M. Tomczyk, G. Cheng, H. Lee, S. Lu, A. Annadi, J. P. Veazey, M. Huang, P. Irvin, S. Ryu, C.-B. Eom & J. Levy ; «Micrometer-Scale Ballistic Transport of Electron Pairs in ${\mathrm{LaAlO}}_{3}/{\mathrm{SrTiO}}_{3}$ Nanowires» ; Physical Review Letters **117**, p. 096 801 (2016). https://link.aps.org/doi/10.1103/PhysRevLett.117.096801 ; publisher : American Physical Society. 88

[163] R. Pentcheva, R. Arras, K. Otte, V. G. Ruiz & W. E. Pickett ; «Termination control of electronic phases in oxide thin films and interfaces : LaAlO $_3$ /SrTiO $_3$ (001)» ; Philosophical Transactions of the Royal Society A: Mathematical, Physical and Engineering Sciences **370**, p. 4904–4926 (2012). ISSN 1364-503X, 1471-2962. https://royalsocietypublishing.org/doi/10.1098/rsta.2012.0202. 89, 91

[164] R. Arras, V. G. Ruiz, W. E. Pickett & R. Pentcheva ; «Tuning the two-dimensional electron gas at the LaAlO 3 / SrTiO 3 (001) interface by metallic contacts» ; Physical Review B **85**, p. 125 404 (2012). ISSN 1098-0121, 1550-235X. https://link.aps.org/doi/10.1103/PhysRevB.85.125404. 89

[165] D. C. Vaz, E. Lesne, A. Sander, H. Naganuma, E. Jacquet, J. Santamaria, A. Barthélémy & M. Bibes ; «Tuning Up or Down the Critical Thickness in LaAlO3/SrTiO3 through In Situ Deposition of Metal Overlayers» ; Advanced Materials **29**, p. 1700 486 (2017). ISSN 1521-4095. https://www.onlinelibrary.wiley.com/doi/abs/10.1002/adma.201700486 ; _eprint : https ://onlinelibrary.wiley.com/doi/pdf/10.1002/adma.201700486. 89

[166] E. Lesne, N. Reyren, D. Doennig, R. Mattana, H. Jaffrès, V. Cros, F. Petroff, F. Choueikani, P. Ohresser, R. Pentcheva, A. Barthélémy & M. Bibes ; «Suppression of the critical thickness threshold for conductivity at the LaAlO 3 /SrTiO 3 interface» ; Nature Communications **5**, p. 4291 (2014). ISSN 2041-1723. https://www.nature.com/articles/ncomms5291 ; number : 1 Publisher : Nature Publishing Group. 89

[167] R. Pentcheva, M. Huijben, K. Otte, W. E. Pickett, J. E. Kleibeuker, J. Huijben, H. Boschker, D. Kockmann, W. Siemons, G. Koster, H. J. W. Zandvliet, G. Rijnders, D. H. A. Blank, H. Hilgenkamp & A. Brinkman ; «Parallel electron-hole bilayer conductivity from electronic interface reconstruction» ; Physical Review Letters **104**, p. 166 804 (2010). ISSN 0031-9007, 1079-7114. http://arxiv.org/abs/0912.4671 ; arXiv : 0912.4671. 89, 91

[168] M. Caputo, M. Boselli, A. Filippetti, S. Lemal, D. Li, A. Chikina, C. Cancellieri, T. Schmitt, J.-M. Triscone, P. Ghosez, S. Gariglio & V. N. Strocov ; «Artificial quantum confinement in LaAl O 3 / SrTi O 3 heterostructures» ; Physical Review Materials **4**, p. 035 001 (2020). ISSN 2475-9953. https://link.aps.org/doi/10.1103/PhysRevMaterials.4.035001. 90

[169] P. Hohenberg & W. Kohn ; «Inhomogeneous Electron Gas» ; Physical Review **136**, p. B864–B871 (1964). ISSN 0031-899X. https://link.aps.org/doi/10.1103/PhysRev.136.B864. 90

[170] R. Dovesi, V. R. Saunders, C. Roetti, R. Orlando, C. M. Zicovich-Wilson, F. Pascale, B. Civalleri, K. Doll, N. M. Harrison, I. J. Bush, P. D'Arco, M. Llunell, M. Causà, Y. Noel, L. Maschio, A. Erba, M. Rérat & S. Casassa ; «CRYSTAL17» ; (2017)https://iris.unito.it/retrieve/handle/2318/1709158/

525194/crystal17.pdf ; accepted : 2019-08-09T18 :08 :45Z Company : ITA Distributor : ITA Institution : ITA Label : ITA Publisher : Gruppo di Chimica Teorica, Dipartimento di Chimica. 91

[171] R. Dovesi, A. Erba, R. Orlando, C. M. Zicovich-Wilson, B. Civalleri, L. Maschio, M. Rérat, S. Casassa, J. Baima, S. Salustro & B. Kirtman ; «Quantum-mechanical condensed matter simulations with CRYSTAL» ; WIREs Computational Molecular Science **8**, p. e1360 (2018). ISSN 1759-0884. https://onlinelibrary.wiley.com/doi/abs/10.1002/wcms.1360 ; _eprint : https ://onlinelibrary.wiley.com/doi/pdf/10.1002/wcms.1360. 91

[172] Z. Wu & R. E. Cohen ; «More accurate generalized gradient approximation for solids» ; Physical Review B **73**, p. 235 116 (2006). https://link.aps.org/doi/10.1103/PhysRevB.73.235116 ; publisher : American Physical Society. 91

[173] J. P. Perdew, K. Burke & M. Ernzerhof ; «Generalized Gradient Approximation Made Simple» ; Physical Review Letters **77**, p. 3865–3868 (1996). https://link.aps.org/doi/10.1103/PhysRevLett.77.3865 ; publisher : American Physical Society. 91

[174] M. L. Reinle-Schmitt, C. Cancellieri, D. Li, D. Fontaine, M. Medarde, E. Pomjakushina, C. W. Schneider, S. Gariglio, P. Ghosez, J.-M. Triscone & P. R. Willmott ; «Tunable conductivity threshold at polar oxide interfaces» ; Nature Communications **3**, p. 932 (2012). ISSN 2041-1723. https://www.nature.com/articles/ncomms1936 ; number : 1 Publisher : Nature Publishing Group. 91

[175] P. Delugas, A. Filippetti, V. Fiorentini, D. I. Bilc, D. Fontaine & P. Ghosez ; «Spontaneous 2-Dimensional Carrier Confinement at the n-Type ${\mathrm{SrTiO}}_{3}/{\mathrm{LaAlO}}_{3}$ Interface» ; Physical Review Letters **106**, p. 166 807 (2011). https://link.aps.org/doi/10.1103/PhysRevLett.106.166807 ; publisher : American Physical Society. 91

[176] C. Cancellieri, D. Fontaine, S. Gariglio, N. Reyren, A. D. Caviglia, A. Fête, S. J. Leake, S. A. Pauli, P. R. Willmott, M. Stengel, P. Ghosez & J.-M. Triscone ; «Electrostriction at the ${\mathrm{LaAlO}}_{3}/{\mathrm{SrTiO}}_{3}$ Interface» ; Physical Review Letters **107**, p. 056 102 (2011). https://link.aps.org/doi/10.1103/PhysRevLett.107.056102 ; publisher : American Physical Society. 91

[177] S. Lemal ; *Low dimensional d states electron systems : insights from first principles* ; Thèse de doctorat ; Université de Liège, Belgique. 91, 92, 102

[178] M. Cardona ; «Optical Properties and Band Structure of SrTi${\mathrm{O}}_{3}$ and BaTi${\mathrm{O}}_{3}$» ; Physical Review **140**, p. A651–A655 (1965). https://link.aps.org/doi/10.1103/PhysRev.140.A651 ; publisher : American Physical Society. 93

[179] R. A. Cowley ; «Lattice Dynamics and Phase Transitions of Strontium Titanate» ; Physical Review **134**, p. A981–A997 (1964). https://link.aps.org/doi/10.1103/PhysRev.134.A981 ; publisher : American Physical Society. 95

[180] E. Frantzeskakis, T. C. Rödel, F. Fortuna & A. F. Santander-Syro ; «2D surprises at the surface of 3D materials : confined electron systems in transition metal oxides» ; Journal of Electron Spectroscopy and Related Phenomena **219**, p. 16–28 (2017). ISSN 03682048. http://arxiv.org/abs/1610.03221 ; arXiv : 1610.03221. 101

[181] S. McKeown Walker, F. Y. Bruno & F. Baumberger ; «ARPES Studies of Two-Dimensional Electron Gases at Transition Metal Oxide Surfaces» ; dans C. Cancellieri & V. N. Strocov (rédacteurs), «Spectroscopy of Complex Oxide Interfaces : Photoemission and Related Spectroscopies», Springer Series in Materials Science ; p. 55–85 (Springer International Publishing, Cham) (2018) ; ISBN 978-3-319-74989-1. https://doi.org/10.1007/978-3-319-74989-1_4. 101

[182] Y. Li, S. N. Phattalung, S. Limpijumnong & J. Yu ; «Oxygen-vacancy-induced charge carrier in n-type interface of LaAlO3 overlayer on SrTiO3 (001) : interface vs bulk doping carrier» ; arXiv :0912.4805 [cond-mat] (2009)http://arxiv.org/abs/0912.4805 ; arXiv : 0912.4805. 101

université PARIS-SACLAY | ÉCOLE DOCTORALE Physique en île-de-France (EDPIF)

Titre : Propriétés électroniques et spintroniques des interfaces entre oxydes de métaux de transition

Mots clés : Oxydes de métaux de transition, transport anormal, surfaces, interfaces

Résumé : Cette thèse porte sur les propriétés de transport anormal des oxydes de métaux de transition, en particulier de la surface de $SrTiO_3$ ou de l'interface entre $SrTiO_3$ et $LaAlO_3$. Dans ces systèmes on observe l'apparition de gaz d'électrons bidimensionnels. Des mesures d'Effet Hall non linéaire indiquent que ces gaz sont constitués de plusieurs sortes de porteurs de charge, et que leurs populations varient de manière non monotone sous l'effet du dopage électrostatique. L'effet des propriétés électrostatiques et des corrélations électroniques sur ces variations sont discutées.

Celles-ci sont à l'origine de réponses remarquables en ce qui concerne la conversion du spin en charge dans ces systèmes à l'aide d'un modèle de liaisons fortes et de la théorie de la réponse linéaire. Les effets conjoints du spin-orbite atomique et de la brisure de symétrie d'inversion à l'interface verrouille les nombres quantiques de spin, de caractère orbital et d'impulsion des électrons, et induit des textures de spin complexe dans l'espace réciproque. Ces textures sont responsables de l'apparition des effets Edelstein et Hall de spin dans ces hétérostructures et sont caractéristiques de la nature multi-orbitale de ces systèmes électroniques.

Enfin nous conduirons une étude ab initio des hétérostructures STO/LAO/STO pour expliquer les observations expérimentales de nouvelles manières de former un gaz d'électrons à ces interfaces d'oxydes. Nous discuterons des rôles respectifs de la chimie, de l'électrostatique et des défauts dans l'apparition de ce gaz.

Title : Electronic and spintronic properties of the interfaces between transition metal oxides

Keywords : Transition metal oxides, anomalous transport, surfaces, interfaces

Abstract : The anomalous transport properties of transition metal oxides, in particular the surface of $SrTiO_3$ or at the interface between $SrTiO_3$ and $LaAlO_3$ is investigated in this thesis. These systems host two-dimensional electron gases. Nonlinear Hall Effect measurements suggest that several species of carriers are present in these systems, and that their population is varying on a nontrivial manner upon electrostatic doping. The role of the electrostatics properties of the electron gas and of the electronic correlations are discussed in this light.

Next we discuss the spin to charge conversion of these systems thanks to tight-binding modeling and linear response theory. The complex interplay between atomic spin-orbit coupling and the inversion symmetry breaking at the interface leads to a complex spin-orbital-momentum locking of the electrons, inducing spin textures. These spin textures are responsible for the appearance of the Edelstein and Spin Hall Effect in these heterostructures and are characteristic of the multi-orbital character of these electronic systems.

Finally an ab initio study of STO/LAO/STO heterostructures is performed to explain experimental evidence of new ways to produce an electron gas at this interface. The respective roles of the chemistry, electrostatics and defects are discussed.